Van der Waals complexes containing open-shell monomers

by

Jacek Kłos

A dissertation submitted in partial fulfillment
of the requirements for the degree of
Doctor
(Chemistry)
in The University of Warsaw

Warsaw, 2001

To my family

ACKNOWLEDGEMENTS

I am very obliged to my supervisor, prof. Grzegorz Chałasiński for his support during my research, guidance, invaluable advices and inspiring discussions.

I am gratuful to prof. Maria M. Szczęśniak for her support and fruitful discussions, interest and numerous advices during my work.

I would like to thank Dr Rudolf Burcl for many interesting discussions and advices.

I gratefully acknowledge all members of Quantum Chemistry Laboratory for memorable and kind athmosphere during my work.

I am very thankful to my Mother, aunt Barbara and Grandmother Zofia for their help and understanding.

I would like to thank my wife Catalina for her support.

I acknowledge Adam Górecki for discussions.

TABLE OF CONTENTS

Proemial

The nature of weak intermolecular interactions between atoms and molecules is investigated. There is a great deal of interest in such atom-molecule complexes because of their importance in the description of astrophysical phenomena in interstellar clouds and in the description of entrance channels to chemical reactions. This Thesis is focused mainly on interactions involving open-shell moieties.

Before going into details, it is crucial to have a basic understanding of the concepts that define the basis of the theoretical description of processes of interest here.

Molecules and clusters of molecules may be viewed as aggregates of electrons and nuclei. Nuclei are much heavier than electrons so their motion is much slower. One can thus consider the motion of electrons in a molecule as if the nuclei had fixed positions in space. The motion of the nuclei, on the other hand, is in an mean field due to the fast motion of electrons. This allows us to separate the motion of the electrons and the nuclei. This approximation is well known as the Born-Oppenheimer (BO) approximation.

Solving the Schrödinger equation for the electronic motion for a set of fixed positions of the nuclei gives as a result, using mathematical technics, the potential energy hypersurface - electronic energy for all possible nuclear positions in space. The global minimum value of the potential energy hypersurface determines the equilibrium structure of the molecular system.

There are cases, where the BO approximation breaks down and the idea of single potential energy surfaces is not longer valid. In Thesis such cases are considered, where for open-shell systems one needs more than one potential energy hypersurface for their proper description.

The potential energy hypersurface can be, in general, divided into two regions, a short range region, where there is strong overlap of the monomers wave funtctions, and a long range part, where the overlap is negligible. The short range is dominated by the so-called exchange interaction and it becomes repulsive at small separations of the monomers in the dimer. This exchange interaction has purely quantum origin as a consequence of the Pauli principle.

The long range interaction energy is determined by three contributions, electrostatic, induction and dispersion contribution. The latter one is quantum mechanical in nature. Those three contributions are called together Van der Waals forces. If the system is kept together by this weak interactions it is called a Van der Waals complex.

Electronic structure calculations wich have no use of empirical parameters are called *ab initio* methods. The basic method is the Hartree-Fock method wich uses one-electron approximation and than there are many methods to account for correlation of motions of the electrons.

Since the nuclei have finit mass, one can be interested in dynamics of the molecular skeleton. This dynamics requires knowledge of the potential hypersurface(s) determined from *ab initio* calculations or, alternatively, from other sources including experimental one as well. The dynamical calculations solve the Schrödinger equation for the nuclear motion. As a result we have ro-vibrational energies and wave functions of the states of the molecular system. Gaining

information about wave functions one can calculate a set of molecular properties using quantum mechanical theorems concerning observables.

CHAPTER I

Introduction

An understanding of reactive interactions at the fundamental level has been one of the central goals of physical chemistry. As has been recognized since the early days of transition state theory, the shape of the Potential Energy Surface (PES) dictates the reaction rate and the processes of energy disposal in the products. Today's reaction dynamics makes the connection between the overall shape and the particular features of the PES, such as barriers or local wells, and a success or failure of reactive events.[1] The understanding of this relationship allows us not only to predict the probability of reactive events, but also opens up a possibility of influencing the course of reactions by selectively modifying certain regions of PES.[2] One way to achieve a control of the reaction outcome is by orienting molecules and their orbitals as they approach one another.[3] Such attempts give rise to the emerging field of stereodynamics.[4] Another way of achieving prealigned systems is via the formation of a van der Waals system.[5]

In these exciting developments the interactions involving open-shell radicals or excited state species are invaluable model systems. A modeling of PESs of reactive interactions from the first principles is a very challenging proposition. Such a modeling must include the long-range part, which in the opinion of some[5] represents "one of the hardest regions to study, both experimentally and theoretically". Furthermore, it should be able to cope with the areas of incipient chemical bonding, where our understanding is incomplete at best. Finally, it must include the transition-state region where the expertise in all the types of interactions: covalent, non-covalent, and intermediate between them, is required. Recent advances in crossed beam techniques coupled with spectroscopic methods have allowed for the monitoring of the reaction dynamics at a completely state-resolved level of detail.[6,7] High resolution supersonic jet spectroscopic techniques have been successfully employed to probe weakly bound molecules trapped in the wells due to the van der Waals or hydrogen-bond interactions.[8,9] The measurements of photofragment angular distributions resulting from the state-specific excitation have allowed the determination of dissociation energies in hydrogen-bonded complexes, such as $(HF)_2$ and its deuterated analogs.[10] State-to-state studies of laser excited vibrational transitions in prereactive molecular beams show that vibration excitation is sufficient to send reactants over the reaction barrier.[11]

The open-shell species play a particularly important role in these studies because they open reactive channels on the PES making them much more complex. The long-range forces which operate in the entrance and exit channels can significantly affect the outcomes of chemical reactions. For example, orienting the reactants as they approach one another can increase the probability of reactive collisions. Conversely, if an entrance channel contained an attractive

well before the barrier, the formation of long-lived collision complexes could lower the reaction probability. The elucidation of the effect the open-versus closed-shell species have in the interaction potential, and consequently, on the reaction dynamics is, thus, of fundamental importance. The interactions involving open-shell species are, in principle, more anisotropic than closed-shell interactions. The presence of unpaired electrons may induce a new type of electronic anisotropy which is absent in the closed-shell case. For example, the interactions between two closed-shell atoms are fully angle-independent (isotropic), whereas the interactions between closed-shell and P-state atoms display angular dependence in many ways similar to that which is present in molecules. This electronic anisotropy plays a fundamental role in determining the strength and directionality of intermolecular forces, and leads to their description in terms of a manifold of potential energy surfaces.[12]

Generally PESs can either be extracted from the spectroscopic measurements via the so-called inversion procedures or calculated from first principles (*ab initio*) by solving an approximate electronic Schrödinger equation. However, in the case of open-shell interactions the inversion is very difficult because the spectroscopy does not sample a single PES, and it may be further complicated by the presence of the spin-orbit coupling and a possible breakdown of the Born-Oppenheimer approximation.[13] In such circumstances, the *ab initio* approaches for the calculations of PESs for open-shell interactions represent an invaluable resource.

Over the last decade, the interest in open-shell Van der Waals complexes has been steadily growing, as documented by recent experimental[14,15] and theoretical [16,17] review papers. Yet, the area is far from being well-travelled, and the relevant literature is scarce. The most important developments in the *ab initio* theory of such complexes came esentially from two centers: from Alexander, Werner, and collaborators, and from Cybulski, Chałasiński, Szczęsniak, and collaborators. In the seminal papers on H_2+B and H_2+O, Alexander and coll. applied supermolecular MRCI approach to calculations of adiabatic and nonadiabatic PESs. Since then, this approach has been applied to a variety of systems .[18–20] However, the major problem with the MRCI method is the virtual impossibility of ensuring consistent treatment of the cluster and constituent monomers. It should be stressed, however, that this is often the only viable approach when one has to deal with a manifold of closely lying PESs, especially of the same symmetry. Cybulski and coll. proposed a different approach. In the Cl_2+He paper[21] , an intermolecular version of unrestricted Moller-Plesset perturbation theory was described and implemented. Its combination with the UCCSD(T) was succeessfully applied to many open-shell Van der Waals species:He-CH,[22]Ar-O_2,[23] Ar-NH,[24] He-NO,[25] Ar-OH.[26] The method proved to be very accurate but revealed problems when dealing with several states of the same symmetry, especially in the presence of avoided crossing.

1.1 The goals and the structure of thesis

The major theme of this thesis is application of *ab initio* methods to model the manifold PESs arising in the interaction of an open-shell atom with a closed-shell system; in particular, in the case of an open-shell cluster which involves two states of the same symmetry.

To realize this goal a variety of systems have been selected, which are appropriate as representative models, but also interesting per se, accessible to experimental determination of calculated properties.

The first class of complexes was composed of closed-shell systems, for which the templates of PES and fitting techniques were proposed and mastered. It included Ar-HCN and Ar-CO_2

Van der Waals systems. Comparison with the experimental measurements of the spectra and bulk properties asserted to the very good quality of *ab initio results*. These works are described in Chapters II and III, respectively.

The second class included atom-Rg complexes (Rg-Rare Gas). These systems serve as a bridge between the Van der Waals interaction and chemical bond. Since they are relatively simple, one may perform calculations which are at the high-end of the state-of-the-art *ab initio approach*. Their accuracy if not surpassing is certainly not worse than that of experimental determinations. This work is described in Chapter IV

The third class included halogen-molecule complexes: Cl+HCl, Cl+H_2, F+H_2 and Br+H_2 which are well known models that are widely used in simulations of abstraction reactions. In contrast to previous studies of these sytems, which aimed at globally valid PESs with compromised accuracy in the Van der Waals region - in this Thesis the focus has been on obtaining very accurate description of the Van der Waals complex in the entrance channel to the reaction, and neglecting the reactive region itself. These works are described in Chapters V, VI, VII and VIII. They constitute the most important contribution to this Thesis.

CHAPTER II

Structure and dynamics of Ar-HCN Van der Waals complex

2.1 Introduction

Complexes of a rare gas atoms with the HCN molecule have been the subject of many studies by both experimentalists and theorists - see e.g. the bibliography of the recent of Toczyłowski et al. [27] In the context of this Thesis, the Ar-HCN complex, as well as the Ar-CO_2 complex described in the next Chapter have provided a testing grounds to design and master algorithms and techniques of modeling PES from accurate *ab initio* calculations. Their closed-shell rather than open-shell character is irrelevant since the templates for and fitting of the PES are general as the major components of the interaction: exchange, electrostatics, induction and dispersion are essentially the same. More importantly, in contrast to open-shell systems, there is a plethora of experimental data to verify the *ab initio* results.

In order to obtain the spectra, the Author implemented a collocation algorithm, calculated several lowest rovibration levels, and analysed rovibration wave functions. The agreement with the experimental proved to be good, and the paper has become the important reference for later experimental works, e.g. Ref. [28] Recently, the potential for Ar-HCN has been quantitatively improved upon by Toczyłowski et al.,[27] but the major results of our paper have remained valid.

2.2 Collocation dynamics

Calculations of rotation vibration eigenvalues and eigenfunctions were performed using the collocation method[29,30] The Hamiltonian for the Ar-HCN complex in the body-fixed reference frame can be written in the form:[31]

$$\hat{H} = -\frac{\hbar^2}{2\mu R^2}\frac{\partial}{\partial R}R^2\frac{\partial}{\partial R} + \frac{\hbar^2}{2\mu R^2}\left(\hat{\mathbf{J}} - \hat{\mathbf{j}}\right)^2 + \hat{H}_x + V\left(R,\theta\right) \tag{2.1}$$

where μ is the reduced mass of the complex calculated from the masses of the HCN molecule and the Ar atom, $\hat{\mathbf{l}} = \hat{\mathbf{J}} - \hat{\mathbf{j}}$ is the angular momentum operator associated with the end-over-end rotation of the complex, $\hat{\mathbf{J}}$ is the total angular momentum operator of the complex, $\hat{\mathbf{j}}$ is the angular momentum operator of the HCN molecule, $\hat{H}_x$ is the rotational Hamiltonian of the free monomer, and $V\left(R,\theta\right)$ is the intermolecular potential. The intramolecular coordinates of HCN were kept constant in all calculations and were assumed to be separable from the intermolecular coordinates.

2.3 *Ab initio* potential

The *ab initio* points were fitted to a two-dimensional model potential that was divided into the short $V_{sh}(R,\theta)$ and the asymptotic $V_{as}(R,\theta)$ parts,

$$V(R,\theta) = V_{sh}(R,\theta) + V_{as}(R,\theta) \tag{2.2}$$

The short range potential consisted of the exponential function,

$$V_{sh}(R,\theta) = \sum_{l=0}^{5}\sum_{j=0}^{2} g_{lj} R^l e^{-\alpha(\theta)R+\beta(\theta)} \frac{1}{\sqrt{2j+1}} P_j^0(\cos\theta) \tag{2.3}$$

Nonlinear parameters in the exponent depend on the angular variable in the following way

$$\alpha(\theta) = \sum_{j=0}^{L} \alpha_j \frac{1}{\sqrt{2j+1}} P_j^0(\cos\theta) \tag{2.4}$$

and

$$\beta(\theta) = \sum_{j=0}^{L} \beta_j \frac{1}{\sqrt{2j+1}} P_j^0(\cos\theta) \tag{2.5}$$

In all expansions $L = 5$.

The asymptotic part included a damped-dispersion expansion, that was truncated at the R^{-7} term, i.e., $n_{max} = 7$,

$$V_{as}(R,\theta) = \sum_{n=6}^{n_{max}} \sum_{\substack{j=0,2,... \\ \text{or} j=1,3,...}}^{j_{max}} D_n(\beta(\theta) R) \frac{C_{n,j}}{R^n} \frac{1}{\sqrt{2j+1}} P_j^0(\cos\theta) \tag{2.6}$$

where D_n function was the damping function of Tang-Toennies[32] and for

$$D_n(x) = 1 - e^{-x} \sum_{k=0}^{n} \frac{x^k}{k!} \tag{2.7}$$

Dispersion coefficients C_{nj} were obtained from a least squares fit. The maximum absolute error of the fit did not exceed 0.75%. The contour plot of the PES is shown in Publication I (see Sec. 2.6). The fitting was performed with the modified code of Bukowski et al.[24] The chosen functional form was found to provide an accurate representation of *ab initio* results, and that is why it was adopted. For example, the fitted surface showed the existence of a small barrier between two local minima, which was later verified by *ab initio* calculations. The root-mean-square and the maximum errors of the fit amount to 0.16 and 0.54 cm^{-1}, respectively.

2.4 Strategy of solving eigenvalue problem for Hamiltonian

The strategy of solving the eigenvalue problem for the Hamiltonian given by Eq. 2.1 is that of Peet and Yang.[33] A trial wave function of the dimer must be expanded in a basis set that provides a good description of the dynamics for $J = 0, 1, 2$. A direct product basis of a

normalized Legendre polynomial in $\cos\theta$ and distributed Gaussians in R is suitable in this case, and the wave function Ψ takes the form 2.8

$$\Psi(R,\theta) = \sum_{\epsilon=0}^{J} \sum_{\Omega=\epsilon}^{J} \sum_{i=1}^{N_R} \sum_{n=\Omega}^{N_T-1} C_{\epsilon in\Omega} \varphi_i(R) P_n^{\Omega}(\cos\theta) \tag{2.8}$$

where

$$\varphi_i(R) = \sqrt[4]{\frac{2A_i}{\pi}} e^{-A_i(R-R_i)^2} \tag{2.9}$$

and the parameters A_i are specified by the recipe of Hamilton and Light. [29] Inserting the trial wave function into Schrödinger equation with Hamiltonian 2.1 gives equation from which the expansion coefficient and eigenvalues can be determined:

$$\sum_{\epsilon=0}^{J} \sum_{\Omega=\epsilon}^{J} \sum_{i=1}^{N_R} \sum_{n=\Omega}^{N_T-1} (H-E) \varphi_i(R) P_n^{\Omega}(\cos\theta) C_{\epsilon in\Omega} = 0 \tag{2.10}$$

The traditional way of solving eigenvalue problem in 2.10 is to multiply the equation by $\varphi_{i'}(R) P_{n'}^{\Omega}(\cos\theta)$ and integrate over coordinates. This procedure require integration of the potential V to obtain potential matrix elements within basis functions of expansion of 2.8. Following Peet and Yang [33] collocation method simplifies the step of determination of Hamiltonian matrix elements by forcing equation 2.10 to be exact at $N_R \times N_T$ grid points. This gives collocation method eigenvalue problem in form of 2.11 solved by direct diagonalization:

$$\sum_{\epsilon=0}^{J} \sum_{\Omega=\epsilon}^{J} \sum_{i=1}^{N_R} \sum_{n=\Omega}^{N_T-1} (H-E) \varphi_i(R_{i'}) P_n^{\Omega}(\cos\theta_{n'}) C_{\epsilon in\Omega} = 0$$
$$i' = 1, \ldots, N_R; \qquad n' = 0, \ldots, N_T - 1 \tag{2.11}$$

The number of angular, N_T , and radial, N_R , functions was equal to (10,30) and (30,65) in two consecutive runs. The largest difference for the first six eigenvalues was less than 0.0042 cm^{-1}. The collocation points in an angular variable were chosen to be the Gauss Legendre points of the order N_T . Gaussian-type radial functions were equally distributed between 3.0 and 16.0 a_0 .

2.5 Eigenvalues and Eigenfunctions

The energies of eigenstates from collocation calculations are reported in Publication I along with contours of several lowest eigenfunctions.

It is useful to view squares of eigenfunctions multiplied by the Jacobian $R^2 \sin\theta$. This quantity is present in calculations of various expectations values and is defined below:

$$\rho_{jJ\nu}(R,\theta) = \Psi^{\star}_{jJ\nu}(R,\theta) \Psi_{jJ\nu}(R,\theta) R^2 \sin\theta \tag{2.12}$$

Figure 2.1 shows the ground state ρ_{000} density for the Ar-HCN system. It is clearly seen that the Ar atom is located in the vicinity of the colinear global minimum on the potential energy surfaces. The peak of this density is narrow and it id cause by fact that Ar atom is quite heavy.

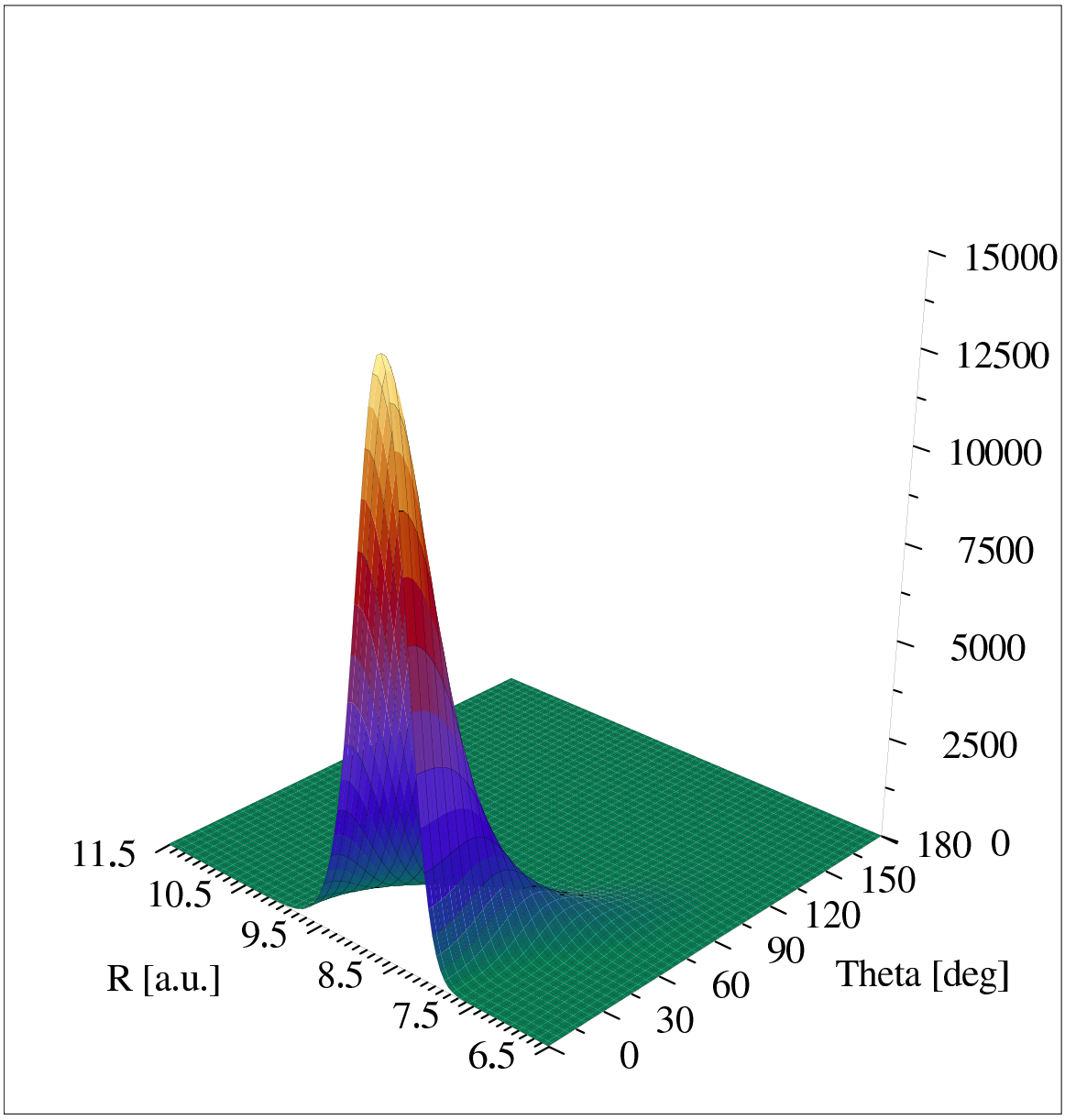

Figure 2.1: ρ_{000} for the Ar-HCN van der Waals complex

2.6 Publication I: *J. Chem. Phys*, 110, 1416 (1999)

JOURNAL OF CHEMICAL PHYSICS VOLUME 110, NUMBER 3 15 JANUARY 1999

An *ab initio* study of the Ar–HCN complex

Sławomir M. Cybulski[a] and Jacques Couvillion
Department of Chemistry and Biochemistry, Miami University, Oxford, Ohio 45056

Jacek Kłos and Grzegorz Chałasiński
Department of Chemistry, University of Warsaw, Pasteura 1, 02-093 Warszawa, Poland

(Received 5 August 1998; accepted 15 October 1998)

The potential energy surfaces for the ground state of the Ar–HCN complex have been calculated at several levels of theory, including the single and double excitation coupled-cluster method with noniterative perturbational treatment of triple excitation CCSD(T). Calculations have been performed using the augmented correlation-consistent polarized triple zeta basis set supplemented with bond functions (aug-cc-pVTZ+bf). The global minimum with a well depth of approximately 141 cm^{-1} has been found for the linear Ar–H–C–N geometry ($\Theta=0.0°$) with the distance R between the Ar atom and the center of mass of the HCN molecule equal to $8.52a_0$. In addition, the potential energy surface has been found to contain a long channel that extended from the bent configuration at $R=7.39a_0$ and $\Theta=59.7°$ (a well depth of 126 cm^{-1}) toward the T-shaped configuration with $R=7.16a_0$ and $\Theta=107.5°$ (a well depth of 121 cm^{-1}). The interaction energies have been analyzed using perturbation theory of intermolecular forces. The location of the global minimum is determined by the anisotropy of the dispersion and induction effects. The ground vibrational state dissociation energy D_0 determined by the collocation method has been found to be 105 cm^{-1}. The wave number of the Σ_1 bend amounts to 4.2 cm^{-1}, somewhat below the experimental value (5.5 cm^{-1}). © *1999 American Institute of Physics.* [S0021-9606(99)30303-2]

I. INTRODUCTION

The Ar–HCN van der Waals complex, along with the isoelectronic Ar–HCCH, are the simplest prototype systems for exploring characteristic force fields around rod-like molecules. Ar–HCN has been the subject of extensive experimental studies. Originally, pure rotational transitions in the ground state Σ_0 were measured by Leopold *et al.*,[1] and refined and extended later by other researchers.[2,3] The lowest excited Σ_1 and Π_1 bending states were measured by Cooksy *et al.*[4] and Drucker *et al.*[5] The combined data for Σ_0, Σ_1, and Π_1 states reflect virtually the entire angular coordinate along the radial minimum of the potential and provide a reliable benchmark for *ab initio* calculations.

The high resolution spectroscopic experiments have stimulated several theoretical investigations with various empirical,[2] semiempirical,[6] and *ab initio* models.[7,8] In particular, a state-of-the-art *ab initio* potential energy surface (PES) obtained with a large basis set at the fourth-order (MP4) level of Møller–Plesset perturbation theory has been recently reported by Tao *et al.*[8] The rovibrational transition energies and spectroscopic constants calculated using the potential energy function fitted to the MP4 interaction energies agreed very well with the experimental results. It was, however, concluded that "considerable errors, especially in the potential anisotropy, still exist in the MP4 potential."[8] It was also suggested that the monomer-bending vibration has a considerable effect on the potential anisotropy.

Taking into account the intramolecular vibrations is, however, a challenging problem for *ab initio* calculations and requires one to deal with a six-dimensional problem instead of a two-dimensional one. Before one can seriously address this, it is worthwhile to improve the results for a rigid monomer model. In other words, to establish how the refinement of electron correlation treatment and a further extension of the basis set affects the potential and the related spectroscopic properties.

The goal of this work was to improve the quality of the PES of the Ar–HCN complex. To accomplish this, we applied the supermolecule single and double excitation coupled-cluster theory with noniterative perturbational treatment of triple excitation CCSD(T),[9] in combination with an augmented correlation-consistent triple zeta (aug-cc-pVTZ) basis set,[10–12] supplemented with a set of bond functions. Symmetry-adapted intermolecular Møller–Plesset perturbation theory (I-MPPT) formalism[13] was used to understand the source of intermolecular interaction and anisotropy in Ar–HCN. In addition, the rovibrational characteristics of the ground and excited Σ_1 and Π_1 bending vibrational states were calculated by means of the collocation dynamics.[14–17]

II. METHODOLOGY

The interaction energy in every order of supermolecule Møller–Plesset perturbation theory (MPPT) and its infinite-order coupled-cluster (CC) generalizations is obtained as the difference between the value of the energy of the complex (E_{AB}) and the sum of the energies of its constituents (E_A+E_B)

$$\Delta E=E_{AB}-(E_A+E_B). \tag{1}$$

[a]Electronic mail: cybulssm@muohio.edu

Interaction energies at different levels of theory will be identified by appropriate superscripts, e.g., $\Delta E^{\mathrm{CCSD(T)}}$ will denote the interaction energy at the CCSD(T) level of theory. In the case of the MP2 interaction energy, which is given by

$$\Delta E^{\mathrm{MP2}}=\Delta E^{\mathrm{SCF}}+\Delta E^{(2)}; \tag{2}$$

also, the second-order correlation correction, $\Delta E^{(2)}$, will be examined.

The SCF supermolecule interaction energy as well as the second- and higher-order correlation corrections to ΔE^{SCF} can be related to the sum of the appropriate electrostatic, induction, dispersion, and exchange energies obtained from intermolecular Møller–Plesset perturbation theory. Details of this approach which makes it possible to analyze the supermolecule results in terms of physically meaningful contributions to the interaction energy can be found elsewhere,[18–20] so here we only give a brief summary. The contributing energies in the I-MPPT expansion are denoted by $\epsilon^{(ij)}$, where i and j refer to the order of the intermolecular interaction operator and the intramolecular correlation operator, respectively.

ΔE^{SCF} is most conveniently analyzed as the sum of the Heitler–London energy (ΔE^{HL}) and the SCF deformation energy ($\Delta E^{\mathrm{SCF}}_{\mathrm{def}}$),

$$\Delta E^{\mathrm{SCF}}=\Delta E^{\mathrm{HL}}+\Delta E^{\mathrm{SCR}}_{\mathrm{def}}, \tag{3}$$

where ΔE^{HL} denotes the sum of the electrostatic ($\epsilon^{(10)}_{\mathrm{es}}$) and exchange ($\epsilon^{\mathrm{HL}}_{\mathrm{ex}}$) energies,

$$\Delta E^{\mathrm{HL}}=\epsilon^{(10)}_{\mathrm{es}}+\epsilon^{\mathrm{HL}}_{\mathrm{ex}}, \tag{4}$$

and $\Delta E^{\mathrm{SCF}}_{\mathrm{def}}$ denotes the induction energy properly restrained by intermolecular exchange effects. At distances where intermolecular overlap is small and the intermolecular exchange effects can be neglected, $\Delta E^{\mathrm{SCF}}_{\mathrm{def}}$ can be approximated by the second-order induction energy with response effects ($\epsilon^{(20)}_{\mathrm{ind},r}$).

In addition to the electrostatic, exchange, and deformation energies, $\Delta E^{(2)}$ also includes the dispersion energy so an analysis of the supermolecule MP2 results must be based on Eqs. (3) and (4) and the following relationship:

$$\Delta E^{(2)}=\epsilon^{(12)}_{\mathrm{es},r}+\epsilon^{(20)}_{\mathrm{disp}}+\Delta E^{(2)}_{\mathrm{ex}}+\Delta E^{(2)}_{\mathrm{def}}, \tag{5}$$

where $\epsilon^{(12)}_{\mathrm{es},r}$ denotes the second-order electrostatic correlation energy with response effects and $\epsilon^{(20)}_{\mathrm{disp}}$ denotes the second-order dispersion energy. The remaining terms, $\Delta E^{(2)}_{\mathrm{ex}}$ and $\Delta E^{(2)}_{\mathrm{def}}$, describe, respectively, the second-order deformation correlation correction to the SCF deformation and the second-order exchange correlation.

The coordinate system used for the Ar–HCN complex is shown in Fig. 1. R denotes the distance between the center of mass of the HCN molecule and the Ar atom, and Θ corresponds to the angle between the R vector and the bond axis of HCN. $\Theta=0°$ corresponds to the Ar–H–C–N colinear arrangement. The equilibrium structure of HCN remains somewhat uncertain[21] and several different sets of CH and CN bond lengths can be found in the literature. We used the equilibrium distances given by Strey and Mills,[22] which are essentially the same as the earlier values of Winnewisser *et al.*[23] and very similar to the most recent values of Carter

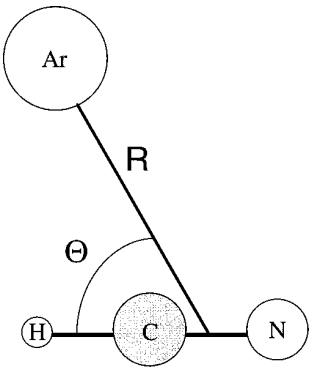

FIG. 1. The coordinate system used for Ar–HCN.

et al.[21] The H–C and C–N bond lengths were set at 1.0655 and 1.1532 Å, respectively, and were kept constant in all calculations.

Calculations of the potential energy surface of the Ar–HCN complex were performed at the CCSD(T) level of theory using the frozen core approximation. Automatically, we also obtained the MP2 and CCSD results. The counterpoise method of Boys and Bernardi[24] was used to avoid the basis set superposition error (BSSE). Supermolecule calculations, for the most part, were performed with MOLPRO 96 program,[25] with the exception of a few cases when GAUSSIAN 94 package[26] was used. Perturbation calculations were performed with TRURL 94 program.[27]

In our preliminary calculations we tested two different basis sets: a well-tempered basis set (WT) similar to the one used by Tao *et al.*,[8] and the augmented correlation-consistent triple zeta (aug-cc-pVTZ) basis set of Dunning *et al.*[10–12] Both basis sets were supplemented with a set of bond functions [3*s*3*p*2*d*][28] centered in the middle of the R vector. We will denote these basis sets as WT+bf and aug-cc-pVTZ+bf. The former contained the following contractions: H: [5s3p1d], C and N: [7s5p3d], and Ar: [7s4p2d1f]. The latter contained the original contractions of Dunning *et al.*:[10–12] H: [4s3p2d], C and N: [5s4p3d2f], and Ar: [6s5p3d2f]. Overall, the WT+bf and aug-cc-pVTZ+bf basis sets contained, respectively, 151 and 187 contracted Gaussian functions. Despite the use of bond functions the differences between the interaction energies obtained with these two basis sets were rather large. For example, in the vicinity of the global minimum at $R=8.6a_0$ and $\Theta=0°$, we found from calculations in which all electrons were correlated that $\Delta E^{\mathrm{CCSD(T)}}$ was equal to $-597\mu E_h$ when the WT+bf basis set was used and to $-641\mu E_h$ when the aug-cc-pVTZ+bf basis set was used. The latter value is expected to be closer to the complete basis set limit, but we did not perform calculations with any larger basis sets to verify this. Indirect evidence comes from a comparison of binding energies of the Ar–HF complex. It was found[29] that the aug-cc-pVTZ+bf basis set gave the binding energy only 0.34% smaller in magnitude than the value obtained with a lot larger aug-cc-pV5Z basis set.[30] Furthermore, the use of the aug-cc-pVQZ+bf basis set resulted in the lowering of the aug-cc-pVTZ+bf interaction energy by only 0.50%. It thus appears that the aug-cc-pVTZ+bf basis set is an excellent

1418 J. Chem. Phys., Vol. 110, No. 3, 15 January 1999 Cybulski *et al.*

compromise between the quality and efficiency of calculations and because of that we adopted it in the present work.

III. COLLOCATION DYNAMICS

Calculations of rotation–vibration eigenvalues and eigenfunctions were performed using the collocation method.[14–17] The Hamiltonian for the Ar–HCN complex in the body-fixed reference frame can be written in the form[31]

$$\hat{H}=-\frac{\hbar^2}{2\mu R^2}\frac{\partial}{\partial R}R^2\frac{\partial}{\partial R}+\frac{\hbar^2}{2\mu R^2}(\hat{J}-\hat{j})^2+\hat{H}_x+V(R,\Theta), \tag{6}$$

where μ is the reduced mass of the complex calculated from the masses of the HCN molecule and the Ar atom, $\hat{l}=\hat{J}-\hat{j}$ is the angular momentum operator associated with the end-over-end rotation of the complex, $\hat{J}$ is the total angular momentum operator of the complex, $\hat{j}$ is the angular momentum operator of the HCN molecule, $\hat{H}_x$ is the rotational Hamiltonian of the free monomer, and $V(R,\Theta)$ is the intermolecular potential. The intramolecular coordinates of HCN were kept constant in all calculations and were assumed to be separable from the intermolecular coordinates.

The *ab initio* points were fitted to a two-dimensional model potential that was divided into the short range $V_{sh}(R,\Theta)$ and the asymptotic $V_{as}(R,\Theta)$ parts,

$$V(R,\Theta)=V_{sh}(R,\Theta)+V_{as}(R,\Theta). \tag{7}$$

The short range potential consisted of the exponential function,

$$V_{sh}(R,\Theta)=G(R,\Theta)e^{D(\Theta)-B(\Theta)R}, \tag{8}$$

where $D(\Theta)$, $B(\Theta)$, and $G(R,\Theta)$ were all expansions in Legendre polynomials, $P_l^0(\cos\Theta)$. Their explicit forms were

$$X(\Theta)=\sum_{l=0}^{L}x^{0l}P_l^0(\cos\Theta), \tag{9}$$

for $D(\Theta)$ and $B(\Theta)$ ($X=D$ or B) and

$$G(R,\Theta)=\sum_{l=0}^{L}(g_0^l+g_1^lR+g_2^lR^2+g_3^lR^3)P_l^0(\cos\Theta). \tag{10}$$

In all expansions $L=5$.

The asymptotic part included a damped-dispersion expansion, that was truncated at the R^{-7} term, i.e., $n_{max}=7$,

$$V_{as}(R,\Theta)=\sum_{n=6}^{n_{max}}\sum_{\substack{l=0,2,\ldots\\ \text{or } l=1,3,\ldots}}^{n-4}f_n[B(\Theta)R]\frac{C_n^{0l}}{R^n}\frac{1}{\sqrt{2l+1}}P_l^0(\cos\Theta), \tag{11}$$

and included the Tang–Toennies damping function (f_n),[32]

$$f_n(x)=1-e^{-x}\sum_{k=0}^{n}\frac{x^k}{k!}, \tag{12}$$

and dispersion coefficients C_n^{0l} obtained from a least squares fit. The maximum absolute error of the fit did not exceed 0.75%. The parameters of the potential functional form are available upon request from the authors. The fitting was performed with the modified code of Bukowski *et al.*[33,34] The chosen functional form was found to provide an accurate representation of *ab initio* results, and that is why it was adopted. For example, the fitted surface showed the existence of a small barrier between two local minima, which was later verified by *ab initio* calculations. The root-mean-square and the maximum errors of the fit amount to 0.16 and 0.54 cm^{-1}, respectively. We have also refitted the *ab initio* results of Tao *et al.*, since their representation was less accurate.

The strategy of solving the eigenvalue problem for the Hamiltonian given by Eq. (6) is that of Peet and Yang.[16] A trial wave function of the dimer must be expanded in a basis set that provides a good description of the dynamics for $J=0,1,2$. A direct product basis of a normalized Legendre polynomial in $\cos\Theta$ and distributed Gaussians in R is suitable in this case, and the wave function Ψ takes the form

$$\Psi(R,\Theta)=\sum_{\epsilon=0}^{J}\sum_{\Omega=\epsilon}^{J}\sum_{i=1}^{N_R}\sum_{n=\Omega}^{N_T-1}C_{\epsilon in\Omega}\varphi_i(R)P_n^{\Omega}(\cos\Theta), \tag{13}$$

where

$$\varphi_i(R)=\sqrt[4]{\frac{2A_i}{\pi}}e^{-A_i(R-R_i)^2}, \tag{14}$$

and the parameters A_i are specified by the recipe of Hamilton and Light.[14] The number of angular, N_T, and radial, N_R, functions was equal to (10,30) and (30,65) in two consecutive runs. The largest difference for the first six eigenvalues was less than 0.0042 cm^{-1}. The collocation points in an angular variable were chosen to be the Gauss–Legendre points of the order N_T. Gaussian-type radial functions were equally distributed between 3.0 and 16.0a_0.

IV. RESULTS AND DISCUSSION

A. Features of total PES

The interaction energies at the SCF, MP2, CCSD, and CCSD(T) levels of theory obtained with the aug-cc-pVTZ+bf basis set are reported in Table I. We give this extensive set to allow other researchers to use the original results for developing their own model potentials. Our calculations probed the potential energy surface most extensively for intermolecular distances in the interval from 7.0a_0 to 10.0a_0, and 11 angles in the range from 0° to 180°. For some angles, calculations were performed for additional distances of 6.0, 6.5, 12.0, and 15.0a_0. Several additional calculations were done in the vicinity of the global minimum ($R\approx 8.5a_0$, $\Theta=0°$). The PES, which is shown in Fig. 2, was fitted to the analytic function described earlier. The global minimum with a well depth of approximately 141 cm^{-1} ($642\mu E_h$) was found on the CCSD(T) surface for the linear Ar–H–C–N geometry ($\Theta=0.0°$) at $R=8.52a_0$. The well depth found in a frozen core calculation is smaller than the well depth found in a core–valence electron-correlated calculation by approximately 1% and larger basis sets are not expected to change this. The error due to basis set incom-

TABLE I. SCF, MP2, CCSD, and CCSD(T) interaction energies (in μE_h) of the Ar–HCN complex at different values of Θ and R.

$\Theta(^\circ)$	$R(a_0)$	ΔE^{SCF}	ΔE^{MP2}	ΔE^{CCSD}	$\Delta E^{CCSD(T)}$
0	7.0	8962.1	5076.4	5864.9	5321.9
	7.5	3196.3	820.5	1269.8	923.7
	8.0	1028.9	−442.6	−177.5	−397.9
	8.4	356.5	−658.2	−478.6	−632.4
	8.5	261.9	−664.0	−500.6	−641.2
	8.6	186.5	−659.4	−510.0	−638.6
	8.7	126.8	−646.6	−509.8	−627.5
	9.0	14.2	−580.0	−473.4	−563.9
	10.0	−57.8	−320.6	−269.6	−309.1
	12.0	−21.4	−89.0	−73.6	−83.3
	15.0	−5.8	−19.8	−16.3	−18.3
20	7.0	6036.4	2826.5	3451.6	3004.6
	7.5	2162.0	178.2	548.5	262.5
	8.0	692.0	−551.8	−323.3	−506.7
	8.5	168.0	−625.0	−478.7	−597.0
	9.0	−0.7	−517.4	−419.2	−496.4
	10.0	−46.7	−281.3	−232.6	−267.2
40	7.0	2313.5	165.9	594.4	299.7
	7.5	824.4	−540.4	−265.3	−457.3
	8.0	255.5	−623.0	−443.1	−568.7
	8.5	52.2	−525.2	−402.6	−485.5
	9.0	−12.3	−398.9	−313.7	−369.2
	10.0	−26.8	−210.8	−167.5	−193.6
60	6.5	2341.3	−69.5	472.1	153.6
	7.0	905.5	−630.2	−280.6	−488.7
	7.5	327.1	−659.3	−433.6	−569.9
	8.0	103.1	−542.1	−392.0	−482.2
	8.5	21.3	−410.2	−306.7	−367.2
	9.0	−5.5	−300.3	−227.2	−268.4
	10.0	−12.2	−156.8	−120.0	−140.1
	12.0	−5.3	−48.5	−37.0	−42.9
	15.0	−1.7	−11.7	−9.2	−10.6
80	6.0	3723.5	468.4	1249.9	841.2
	6.5	1512.9	−519.1	−30.5	−294.5
	7.0	594.2	−691.3	−379.7	−551.3
	7.5	221.3	−605.2	−403.0	−515.5
	8.0	74.3	−468.4	−333.4	−408.2
	8.5	18.9	−343.8	−253.1	−303.5
	9.0	−0.5	−247.7	−185.8	−220.3
	10.0	−6.8	−121.3	−98.4	−115.1
90	6.0	3555.0	358.9	1134.7	738.4
	6.5	1439.4	−544.6	−61.9	−317.2
	7.0	563.7	−686.7	−380.2	−545.9
	7.5	209.3	−593.4	−394.6	−503.3
	8.0	69.9	−456.0	−324.3	−396.5
	8.5	17.4	−335.9	−245.7	−294.4
	9.0	−0.9	−241.8	−180.4	−213.8
	10.0	−6.8	−128.6	−95.9	−112.7
	12.0	−3.0	−44.0	−30.2	−35.6
	15.0	−0.7	−6.3	−7.3	−8.3
100	6.0	3693.0	448.0	1239.4	840.1
	6.5	1484.8	−523.5	−32.9	−290.0
	7.0	576.3	−687.2	−376.2	−543.0
	7.5	211.0	−599.2	−397.7	−507.0
	8.0	68.5	−462.6	−328.5	−401.2
	8.5	15.4	−339.7	−249.3	−298.4
	9.0	−2.8	−246.8	−183.3	−217.0
	10.0	−8.1	−129.5	−97.5	−114.3
120	6.5	2004.3	−234.6	308.2	19.5
	7.0	763.8	−646.5	−303.2	−490.8
	7.5	271.5	−633.3	−410.8	−533.8
	8.0	82.7	−509.8	−361.7	−443.3
	8.5	14.2	−381.9	−281.2	−336.1
	9.0	−8.3	−278.5	−208.7	−246.2
	10.0	−13.1	−147.7	−111.4	−129.9
	12.0	−5.2	−46.5	−34.5	−40.0
	15.0	−1.0	−11.5	−8.0	−9.4

TABLE I. (*Continued.*)

$\Theta(^\circ)$	$R(a_0)$	ΔE^{SCF}	ΔE^{MP2}	ΔE^{CCSD}	$\Delta E^{CCSD(T)}$
140	7.0	1285.6	−375.7	15.4	−209.4
	7.5	455.6	−611.7	−358.3	−505.6
	8.0	139.7	−558.7	−390.2	−487.5
	8.5	25.8	−439.9	−325.1	−390.2
	9.0	−11.2	−327.9	−247.9	−292.1
	10.0	−19.7	−174.9	−133.9	−155.3
160	7.0	2060.3	157.0	584.4	323.2
	7.5	735.4	−485.1	−209.1	−380.0
	8.0	232.2	−565.3	−381.8	−494.4
	8.5	50.3	−480.2	−355.0	−429.9
	9.0	−9.6	−369.2	−281.7	−332.2
	10.0	−25.6	−199.7	−155.3	−179.3
180	7.0	2474.3	469.5	909.3	632.8
	7.5	885.9	−397.8	−114.3	−295.1
	8.0	282.7	−555.4	−366.8	−485.8
	8.1	219.2	−552.1	−377.7	−487.3
	8.5	64.5	−492.7	−363.9	−442.9
	9.0	−7.8	−384.9	−294.9	−348.0
	10.0	−28.0	−210.9	−164.1	−189.3
	12.0	−11.4	−63.7	−49.4	−56.4
	15.0	−2.1	−14.2	−10.8	−12.3

pleteness is more difficult to estimate, but a comparison with the estimated complete basis set limit values of interaction energies that van Mourik and Dunning obtained for Ar–HF suggests that it should not exceed a few percent. In addition to the global minimum, the PES contains a long channel that extends between two local minima: one for the angular configuration at $R=7.39a_0$ and $\Theta=59.7^\circ$ (a well depth of 126 cm^{-1}) and another one for the T-shaped configuration at $R=7.16a_0$ and $\Theta=107.5^\circ$ (a well depth of 121 cm^{-1}). These two minima are separated by a barrier that *ab initio* calculations predict to be only 0.2 cm^{-1} higher than the more shallow minimum. Our fitted surface gives a barrier of 1 cm^{-1}. Whether such a low barrier really exists will have to be verified by more sophisticated calculations.

Our results are in good qualitative and quantitative agreement with the results of Tao *et al.*,[8] in part because of the fortunate cancellation of two effects. On one hand, the magnitude of the interaction energy at the MP4 level of theory, ΔE^{MP4}, is overestimated compared to $\Delta E^{CCSD(T)}$. On

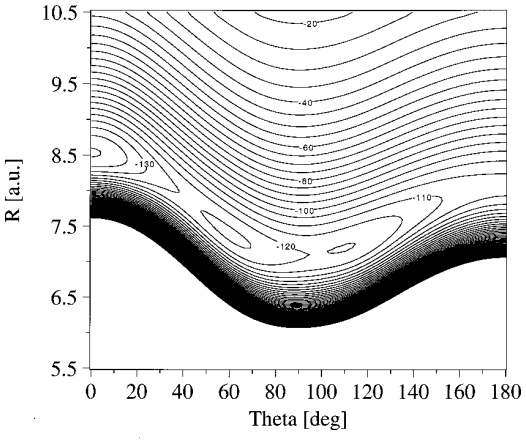

FIG. 2. Potential energy surface of the Ar–HCN complex.

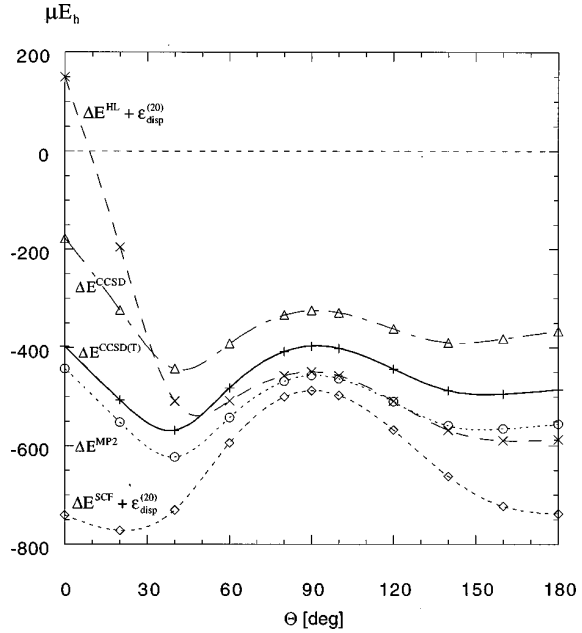

FIG. 3. The angular dependence of the interaction energy at different levels of theory at $R=8.0a_0$.

the other hand, the WT+bf basis set underestimates the strength of the interaction compared to the aug-cc-pVTZ+bf basis. These two effects partially cancel each other and at the MP4 level of theory with their version of the WT+bf basis set Tao *et al.*[8] obtained at $R=8.5a_0$ the MP4 interaction energy of -133.8 cm^{-1} ($-609.6\mu E_h$) that is smaller by 7 cm^{-1} (5%) in comparison with our CCSD(T) result of -140.7 cm^{-1} ($-641.2\mu E_h$). But our value of ΔE^{MP4} obtained with the aug-cc-pVTZ+bf basis set is equal to -146.9 cm^{-1} ($-669.2\mu E_h$) and differs from the result of Tao *et al.* by approximately 10%. The depth of global minima appears to be the biggest discrepancy between our CCSD(T) surface and the MP4 surface of Tao *et al.*[8] Other differences are smaller and, for example, the radial minimum at $\Theta=90.0°$ found by Tao *et al.* is 19.5 cm^{-1} above the global minimum, which can be compared with our value of 20 cm^{-1} and with 15 cm^{-1} from the fit of the ground state transition data.[6] As with the CCSD(T) PES, the fit of the MP4 PES of Tao *et al.* shows two minima in the 50°–120° region separated by a barrier of 1 cm^{-1}.

B. Decomposition of the interaction energy

The angular dependence of the MP2, CCSD, and CCSD(T) supermolecule interaction energies at $R=8.0a_0$ is given in Fig. 3, and in Table II. This distance is shorter than the radial minimum at $\Theta=0.0°$ but longer than the one at $\Theta=90.0°$. At $\Theta=180.0°$ it is quite close to the radial minimum. As can be seen in Fig. 3, each curve contains two minima. The more pronounced one corresponds to the Ar atom positioned between the H and C atoms of HCN ($\Theta\approx45°$), and a very shallow one ($\Theta\approx140°-150°$) corresponds to Ar positioned between C and N. The strength of the interaction is overestimated at the MP2 and underestimated at the CCSD level of theory, in comparison to the

TABLE II. Interaction energies (in μE_h) at various levels of MP and CC theory at the approximate global and local minima on the PES of the Ar–HCN complex. All correlated supermolecule results are from frozen core calculations, with the exception of the ΔE^{MP2} values given in parentheses. All perturbation results are from calculations in which all electrons were correlated.

Energy	$R=8.5$, $\Theta=0°$	$R=7.0$, $\Theta=90°$	$R=8.1$, $\Theta=180°$
ΔE^{SCF}	261.9	563.7	219.2
$\Delta E^{(2)}$	−925.9	−1250.4	−771.3
ΔE^{MP2}	−664.0	−686.7	−552.1
	(−671.4)	(−694.7)	(−559.3)
ΔE^{MP3}	−545.9	−453.4	−376.7
ΔE^{MP4}	−669.2	−578.9	−521.0
ΔE^{CCSD}	−500.6	−380.2	−377.7
$\Delta E^{\mathrm{CCSD(T)}}$	−641.2	−545.9	−487.3
$\epsilon_{\mathrm{ex}}^{\mathrm{HL}}$	863.2	987.7	514.3
$\epsilon_{\mathrm{es}}^{(10)}$	−143.0	−311.0	−157.8
$\Delta E_{\mathrm{def}}^{\mathrm{SCF}}$	−458.3	−112.9	−137.2
$\epsilon_{\mathrm{ind},r}^{(20)}$	−534.1	−473.1	−234.3
$\epsilon_{\mathrm{es},r}^{(12)}$	−55.9	9.9	−50.1
$\epsilon_{\mathrm{disp}}^{(20)}$	−1050.7	−1392.2	−927.8

CCSD(T) results. Figure 3 also includes two curves obtained by adding the second-order dispersion energy, $\epsilon_{\mathrm{disp}}^{(20)}$, to ΔE^{HL} and ΔE^{SCF}. Neither of these approximations can be considered good, although the sum of ΔE^{HL} and $\epsilon_{\mathrm{disp}}^{(20)}$ compares favorably with ΔE^{MP2} for angles greater than 60°. The reason for its failure for angles smaller than 60° is the neglect of the induction energy, which becomes quite important for the linear Ar–HCN geometry and its immediate vicinity, as can be seen in Fig. 4.

Figure 4 also shows clearly that the most anisotropic are the dispersion and exchange energies and it is mainly their interplay that shapes the overall surface. A more refined picture can be obtained by considering the induction energy, whose role in certain regions of the PES was already mentioned, and the electrostatic energy that is shown in Fig. 3 as the sum of $\epsilon_{\mathrm{es}}^{(10)}$ and $\epsilon_{\mathrm{es},r}^{(12)}$. Because of its purely charge-overlap character, the electrostatic energy is the least important component of the interaction energy, but its magnitude is far from negligible, especially for the linear Ar–HCN geometry.

A complex nature of the interaction is further illustrated in Table II, which contains supermolecule and perturbation energies for the approximate global minimum ($R=8.5a_0$, $\Theta=0°$) and for two radial minima ($R=7.0a_0$, $\Theta=90°$, and $R=8.1a_0$, $\Theta=180°$). Our calculations confirm the finding of Tao *et al.*[8] that at the MP2 level of theory, the T-shaped structure is lower in energy than the linear Ar–HCN geometry. It is only at the MP3 and higher levels of theory that their relative positions are reversed. The key to the understanding of this effect is the third-order correlation correction $\Delta E^{(3)}$, whose partitioning, unfortunately, has not been implemented so far. For the T-shaped geometry, because of the short separation between Ar and the carbon atom of HCN, the magnitude of the exchange, dispersion, and also electrostatic energy is larger than for either of the linear arrangements. This can be contrasted with the interaction of rare gases with diatomic molecules, where at the radial

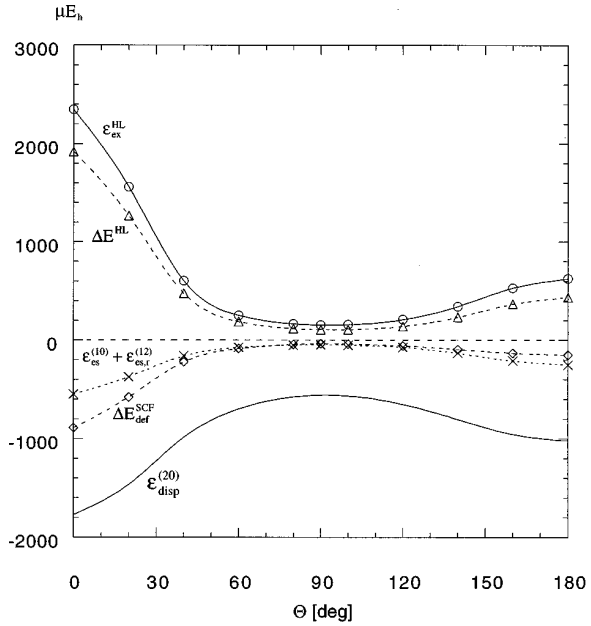

FIG. 4. The angular dependence of contributions to ΔE^{SCF} and $\Delta E^{(2)}$ at $R=8.0a_0$.

minima the magnitude of the exchange and dispersion energies are commonly greater for the linear than for the T-shaped geometry.[35]

C. Rovibrational energy levels

To make comparisons of our potential with the experiment as well as with the previous *ab initio* work, we calculated some spectroscopic constants and rovibrational energy levels using the collocation method. In Table III we compare the equilibrium (D_e) and ground-vibrational-state (D_0) dissociation energies, equilibrium (R_e), and vibrationally averaged (R_0) intermolecular distances, the values of $\langle P_1(\cos(\Theta))\rangle$ and $\langle P_2(\cos(\Theta))\rangle$, and the rotational constants B in the rigid rotor approximation. In Table IV we collect calculated and observed term values of the ground state, and the lowest excited Σ_1 and Π_1 bending states.

TABLE III. Spectroscopic constants of Ar–HCN calculated with the present CCSD(T) and the Tao *et al.*[8] potentials, and from the experimental work of Drucker *et al.*[5] The values of the rotational B constant are for the free-rotor approximation.

	Tao *et al.* (Ref. 8) MP4 (Σ_0)	Tao *et al.* (Ref. 8) MP4 (Σ_0)[a]	This work CCSD(T) (Σ_0)	Experiment (Σ_0)
D_e (cm^{-1})	135.9	134.4	140.8	
R_e (a_0)	8.617	8.58	8.52	
D_0 (cm^{-1})	102.13	100.72	105.0	
$\langle R\rangle$(a_0)		8.116	8.109	8.183
$\langle P_1(\cos(\Theta))\rangle$	0.853	0.827	0.856	0.875
$\langle P_2(\cos(\Theta))\rangle$	0.578	0.572	0.635	0.607
B (MHz)	1579	1700.18	1702.78 (1655.38)[b]	1610

[a]Results obtained with the potential obtained by fitting the MP4 energies of Tao *et al.* (Ref. 8) to the function given by Eqs. (7)–(13).
[b]The results obtained with the rigid body diffusion quantum Monte Carlo method (Refs. 36, 37).

TABLE IV. Calculated and observed term values (cm^{-1}) of the ground state, and the lowest excited Σ_1 and Π_1 bending states of ArHCN.

State	J	Tao *et al.* (Ref. 8) MP4[a]	Tao *et al.* (Ref. 8) MP4[b]	This work CCSD(T)	Observed (Ref. 5)[c]
Σ_0	1	0.1053	0.1109	0.1112	0.1073
	2	0.3156	0.3326	0.3335	0.3218
Σ_1	0	5.0496	4.2470	4.2391	5.4964
	1	5.1735	4.3670	4.3644	5.6225
	2	5.4216	4.6080	4.6153	5.8755
Π_1^e	1	5.7977	4.6718	4.8567	6.1339
	2	6.0633	4.9406	5.1241	6.4046

[a]The results from Table V of Tao *et al.* (Ref. 8).
[b]Results obtained with the potential obtained by fitting the MP4 energies of Tao *et al.* (Ref. 8) to the function given by Eqs. (7)–(13).
[c]Experimental results as reported in Table V of Tao *et al.* (Ref. 8).

Overall, our calculated values in Tables III and IV are in good agreement with the experimental measurements, although quantitatively the deviations are still significant. The calculated frequencies for the $J=0\rightarrow 1$ transitions from the ground state to the Σ_1 and Π_1 bending states amount to 4.2 and 4.9 cm^{-1} and can be compared with the experimental values of 5.50 and 6.13 cm^{-1}.[8] Our calculation gives a differential energy $\Pi_1-\Sigma_1$ of 0.62 cm^{-1}, with the Σ_1 state being lower than the Π_1 state, which can be compared with the experimental value of 0.57 cm^{-1}. The rotational constant in the rigid-body approximation amounts to 1702.8 MHz, and is somewhat larger than the experimental value of 1610 MHz. The agreement with experiment can be improved by using the rigid-body quantum Monte Carlo (RBDQMC) method, which gives $B=1655.4$ MHz.[36,37]

The new constants and frequencies based on the CCSD(T) potential are in certain cases farther away from the experimental values than the previous *ab initio* results based on the MP4 potential reported by Tao *et al.*[8] In particular, our frequencies are visibly smaller than those reported in Ref. 8. However, the discrepancy between our results and those of Tao *et al.* disappeared almost completely when we recalculated the frequencies using the potential energy func-

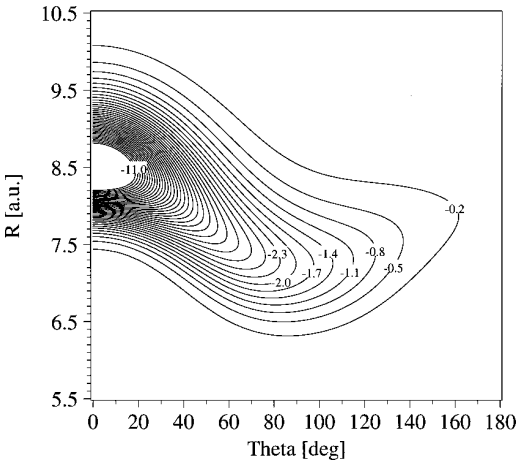

FIG. 5. The ground state Σ_0 rovibrational wave function.

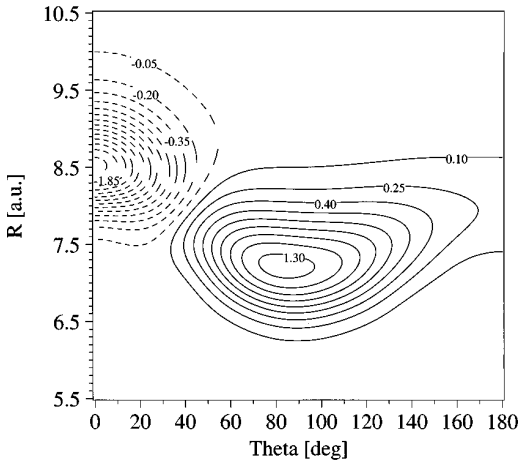

FIG. 6. The bending excited state Σ_1 rovibrational wave function for $J=1$.

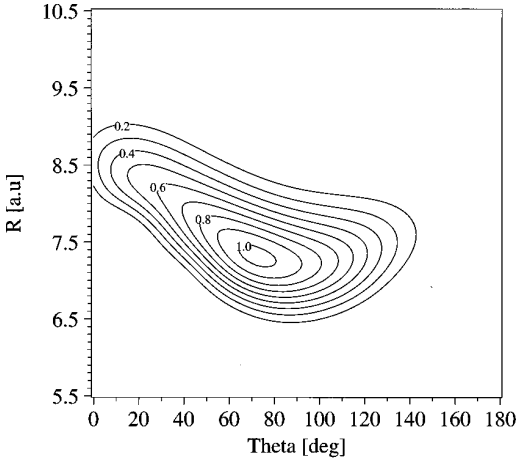

FIG. 7. The bending excited state Π_1 rovibrational wave function for $J=1$.

tion given by Eqs. (7)–(13) fitted to their MP4 interaction energies. A comparison of the original results of Tao *et al.* and those that we obtained with the new fit of their *ab initio* MP4 energies can be found in Tables III and IV. The sensitivity of some quantities to the specific form of the potential is quite high, and it would be very useful, in our opinion, to examine the issue for a larger set of systems and different functional forms of fitted intermolecular potentials. Because some potentials are obtained by approximation and some other ones by interpolation methods, it would be equally useful to perform a study of the reliability of different functions. Such studies have not yet been done, so in order to perform meaningful comparisons it is essential to report detailed results of *ab initio* calculations, as has been done in the present work as well as in the work of Tao *et al.*,[8] rather than fitted potential functions.

To shed some light on the dynamics of the system, it is instructive to visualize the wave functions of the three vibrational states. The ground-state rovibrational wave function shows large-amplitude bending of Ar, which, as shown in Fig. 5, samples a long channel extending toward the T-shaped region. This is in striking contrast to the ground state of the Ar–HF complex,[38] where the Ar atom is largely localized around the collinear Ar–H–F configuration. The function for the Σ_1 bending state is presented in Fig. 6. This state is only 4.2 cm^{-1} higher in energy than the ground state and has a large amplitude for both the collinear Ar–H–C–N configuration as well as for the T-shaped geometry, with a nodal plane around 60°. It also involves the Ar–N–C–H configuration. An analogous state for the Ar–H–F complex is largely localized around two collinear geometries, Ar–H–F and Ar–F–H. Finally, the Π_1 rovibrational wave function is displayed in Fig. 7. This one is clearly localized around the T-shaped geometry, yet it also the involves Ar–H–C–N configuration.

V. SUMMARY AND CONCLUSIONS

We have calculated the potential energy surface for the Ar–HCN complex at the CCSD(T) level of theory using the aug-cc-pVTZ+bf basis set. This PES has been obtained at a higher level of theory and with a better basis set than the MP4 surface of Tao *et al.*,[8] and can therefore serve as a benchmark for a rigid-monomer model. In comparison with the earlier results,[8] the equilibrium interaction energy that we have found, $D_e=140.8$ cm^{-1}, is deeper by 6.4 cm^{-1}, and the equilibrium intermolecular distance, $R=8.52$ Å, is shorter by 0.06 Å. Spectroscopic constants that we have obtained using the collocation method are similar to those obtained by Tao *et al.*,[8] partially because of the fortunate cancellation of errors inherent in the MP4 surface. Good agreement with the previous theoretical results means that, unfortunately, agreement with experimental results is still not completely satisfactory. This is seen for the average values of R, $P_1(\cos\Theta)$, $P_2(\cos\Theta)$, the rotational constant B, and, most noticeably, for the bending frequencies that differ from the experimental results by 25%. A plausible explanation of these findings is that the error committed by using the rigid-monomer potential is smaller than the effect of the intramonomer vibrations.

ACKNOWLEDGMENTS

S.M.C. acknowledges the support of National Science Foundation (Grant No. CHE-9616683). J.K. and G.C. acknowledge support by the Polish Committee for Scientific Research KBN (Grant No. 12-501-07-BW-1383/32/97) and partial support by the National Science Foundation (Grant No. CHE-9527099).

[1] K. R. Leopold, G. T. Fraser, F. J. Lin, D. D. Nelson, and W. Klemperer, J. Chem. Phys. **81**, 4922 (1984).
[2] T. D. Klots, C. E. Dykstra, and H. S. Gutowsky, J. Chem. Phys. **90**, 30 (1989).
[3] R. E. Bumgarner and G. A. Blake, Chem. Phys. Lett. **161**, 308 (1989).
[4] A. L. Cooksy, S. Drucker, J. Faeder, C. A. Gottlieb, and W. Klemperer, J. Chem. Phys. **95**, 3017 (1991).
[5] S. Drucker, A. L. Cooksy, and W. Klemperer, J. Chem. Phys. **98**, 5158 (1993).
[6] D. Yaron and W. Klemperer, J. Chem. Phys. **95**, 1907 (1991).
[7] D. C. Clary, C. E. Dateo, and T. Stoecklin, J. Chem. Phys. **93**, 7666 (1990).

[8] F.-M. Tao, S. Drucker, and W. Klemperer, J. Chem. Phys. **102**, 7289 (1995).
[9] K. Raghavachari, G. W. Trucks, J. A. Pople, and M. Head-Gordon, Chem. Phys. Lett. **157**, 479 (1989).
[10] T. H. Dunning, Jr., J. Chem. Phys. **90**, 1007 (1989).
[11] R. A. Kendall, T. H. Dunning, Jr., and R. J. Harrison, J. Chem. Phys. **96**, 6796 (1992).
[12] D. E. Woon and T. H. Dunning, Jr., J. Chem. Phys. **98**, 1358 (1993).
[13] B. Jeziorski, R. Moszynski, and K. Szalewicz, Chem. Rev. **94**, 1887 (1994).
[14] I. P. Hamilton and J. C. Light, J. Chem. Phys. **84**, 306 (1986).
[15] W. Yang and A. C. Peet, Chem. Phys. Lett. **153**, 98 (1988).
[16] A. C. Peet and W. Yang, J. Chem. Phys. **90**, 1746 (1989).
[17] W. Yang and A. C. Peet, J. Chem. Phys. **92**, 522 (1990).
[18] G. Chałasiński and M. M. Szczęśniak, Mol. Phys. **63**, 205 (1988).
[19] S. M. Cybulski, G. Chałasiński, and R. Moszynski, J. Chem. Phys. **92**, 4357 (1990).
[20] G. Chałasiński and M. M. Szczęśniak, Chem. Rev. **94**, 1723 (1994).
[21] S. Carter, I. M. Mills, and N. C. Handy, J. Chem. Phys. **97**, 1606 (1992).
[22] G. Strey and I. M. Mills, Mol. Phys. **26**, 129 (1973).
[23] G. Winnewisser, A. G. Maki, and D. R. Johnson, J. Mol. Spectrosc. **39**, 149 (1971).
[24] S. F. Boys and F. Bernardi, Mol. Phys. **19**, 553 (1970).
[25] MOLPRO is a package of *ab initio* programs written by H.-J. Werner and P. J. Knowles, with contributions from J. Almlof, R. D. Amos, A. Berning, M. J. O. Deegan, F. Eckert, S. T. Elbert, C. Hampel, R. Lindh, W. Meyer, A. Nicklass, K. Peterson, R. Pitzer, A. J. Stone, P. R. Taylor, M. E. Mura, P. Pulay, M. Schuetz, H. Stoll, T. Thorsteinsson, and D. L. Cooper.
[26] M. J. Frisch, G. W. Trucks, H. B. Schlegel, P. M. W. Gill, B. G. Johnson, M. A. Robb, J. R. Cheesman, T. A. Keith, G. A. Petersson, J. A. Montgomery, K. Raghavachari, M. A. Al-Laham, V. G. Zakrzewski, J. V. Ortiz, J. B. Foresman, J. Cioslowski, B. B. Stefanov, A. Nanayakkara, M. Challacombe, C. Y. Peng, P. Y. Ayala, W. Chen, M. W. Wong, J. L. Andres, E. S. Replogle, R. Gomperts, R. L. Martin, D. J. Fox, J. S. Binkley, D. J. Defrees, J. Baker, J. P. Stewart, M. Head-Gordon, C. Gonzalez, and J. A. Pople, GAUSSIAN 94, Revision B.3 (Gaussian, Inc., Pittsburgh, PA, 1995).
[27] S. M. Cybulski, TRURL 94 package, Rochester MI, 1994.
[28] F.-M. Tao and Y.-K. Pan, J. Chem. Phys. **97**, 4989 (1992).
[29] K. W. Chan, T. D. Power, J. Jai-nhuknan, and S. M. Cybulski, J. Chem. Phys. **110**, 860 (1999).
[30] T. van Mourik and T. H. Dunning, Jr., J. Chem. Phys. **107**, 2451 (1997).
[31] J. M. Hutson, Adv. Mol. Vibrat. Coll. Dyn. **1A**, 1 (1991).
[32] K. T. Tang and J. P. Toennies, J. Chem. Phys. **80**, 3726 (1984).
[33] R. Bukowski, B. Jeziorski, and K. Szalewicz (unpublished).
[34] R. A. Kendall, G. Chałasiński, J. Klos, R. Bukowski, M. W. Severson, M. M. Szczęśniak, and S. M. Cybulski, J. Chem. Phys. **108**, 3235 (1998).
[35] J. Sadlej, G. Chałasiński, and M. M. Szczesniak, J. Mol. Struct.: THEOCHEM **307**, 187 (1994).
[36] V. Buch, J. Chem. Phys. **97**, 726 (1992).
[37] P. Sandler, J. oh Jung, M. M. Szczęśniak, and V. Buch, J. Chem. Phys. **101**, 1378 (1994).
[38] A. E. Thornley and J. M. Hutson, J. Chem. Phys. **101**, 5578 (1994).

CHAPTER III

Structure and dynamics of Ar-CO_2 Van der Waals complex

3.1 Introduction

Similarly to Ar-HCN, the Ar-CO_2 complex has provided another testing grounds to design and master algorithms and techniques of modeling PES from accurate *ab initio* calculations. The system is also of great interst on its own. The structure, dynamics, and properties of the Van der Waals complexes of rare gases with the CO_2 molecule are important in the field of the atmospheric chemistry and astrophysics.

In the literature, there is a great number of studies of Ar-CO_2 Van der Waals complex cf. the bibliography in Szalewicz et al .[34] The latter paper appeared when this work has already been completed. Szalewicz et al. reported thorough a study of the spectroscopic properties of this complex, in a good agreement with the Author's results. Therefore, below the Author takes the liberty to present only those results which have not been supereseded by the work of Szalewicz et al. These include:

- collocation dynamics for J=0
- calculations of the second virial coefficients

It is worthwhile to stress that calculations of the quantum corrections to the second virial coefficient for this system have not been reported before.

3.2 Methodology of *ab initio* calculations

The Ar-CO_2 complex is described in Jacobi system of coordinates which is shown in Figure 3.1. The variable R denotes the distance between the carbon atom and the argon atom, and θ denotes the angle between the $\vec{R}$ vector and the carbon dioxide bond axis. The CO_2 monomer geometry was fixed at $r_{CO} = 1.1612$ Å [35] and kept rigid during calculations. Calculations of the PES were performed with the augmented correlation-consistent polarized valence-triple-zeta (aug-cc-pVTZ) basis set functions supplemented with an additional set of bond functions. The set of bond functions $3s3p2d$ of Tao and Pan,[36] with the exponents:sp 0.9, 0.3, 0.1;d 0.6, 0.2, was used. Radial grid was chosen to be [5.5, 6.0, 6.5, 7.0, 7.5, 8.0, 8.5, 9.0, 9.5, 10.0, 11.0, 12.0, 14.0] a_0 and angular grid to be [0, 20, 40, 60, 80, 90] degrees. The position of the bond functions varied according to

$$\sin\theta\left(\frac{R}{2}\right) + \cos\theta\left(\frac{R + r_{CO}}{2}\right) \tag{3.1}$$

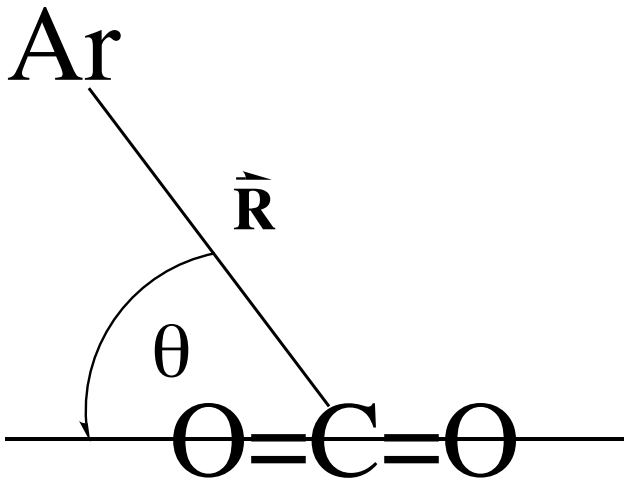

Figure 3.1: Jacobi coordinates.

The varied position of the bond functions prevented their location to be too close to the O atom for the collinear arrangement. The interaction energy was calculated using supermolecular approach. This method derives the interaction energy as the difference between the energies of the dimer AB and the monomers A and B

$$\Delta E^{(n)} = E_{AB}^{(n)} - E_A^{(n)} - E_B^{(n)} \tag{3.2}$$

Energies of the monomers were calculated in the dimer centered basis set for the sake of removal of the basis set superposition error.

3.3 Fitting of *ab initio* points to analytical expression

The CCSD(T)/aug-cc-pVTZ+322 *ab initio* interaction energies calculated using Eq. 3.2 were chosen as the data for fitting procedure. The analytical expression applied in the approximation procedure is the sum of a short-range term and a long-range term, dependent on (R,θ) Jacobi coordinates:

$$V(R,\theta) = V_{sh}(R,\theta) + V_{as}(R,\theta) \tag{3.3}$$

where

$$V_{sh}(R,\theta) = \sum_{l=0}^{3}\sum_{j=0}^{2} g_{l(2j)} R^l e^{-\alpha(\theta)R+\beta(\theta)} \frac{1}{\sqrt{4j+1}} P_{2j}^0(\cos\theta) \tag{3.4}$$

Nonlinear parameters in the exponent depend on the angular variable in the following way

$$\alpha(\theta) = \sum_{j=0}^{2} \alpha_{2j} \frac{1}{\sqrt{4j+1}} P_{2j}^0(\cos\theta) \tag{3.5}$$

and

$$\beta(\theta) = \sum_{j=0}^{2} \beta_{2j} \frac{1}{\sqrt{4j+1}} P_{2j}^0(\cos\theta) \tag{3.6}$$

The long-range part was chosen to be a damped electrostatic-dispersion-induction term:

$$V_{as}(R,\theta) = \sum_{n=0,j=0}^{1} D_n(\beta(\theta)R)\frac{C_{2n+6,2j}}{R^{2n+6}}\frac{1}{\sqrt{4j+1}}P_{2j}^{0}(\cos\theta) \tag{3.7}$$

where the D_n function was the damping function of Tang-Toennies[32]

$$D_n(x) = 1 - e^{-x}\sum_{k=0}^{n}\frac{x^k}{k!} \tag{3.8}$$

The fitting strategy was carried out in two steps:

1. Linear least-square method to determine initial α_j and β_j parameters.The logarithm of the SCF interaction energies was fit to determine the exponent of the V_{sh} formula

2. Non-linear least-square method optimized all parameters simultaneously including Van der Waals C_{nl} coefficients.

Table 3.1 collects optimized parameters. The largest absolute deviation from the *ab initio* data for the values were below 20000 μE_h was 0.84 μE_h. The rms (root-mean-square) for the whole set of data was 583 μE_h, and the biggest errors were located in the highly repulsive region of the PES. Units of variables of the fit are a_0 for R, degrees for θ and mE_h for the energy.

3.3.1 Features of PES

The global minimum of the Ar-CO_2 CCSD(T) PES is the T-shaped minimum located at R_e=6.515 a_0 and θ=90°, and its well depth equals to 193.41cm^{-1}. Recently Misquita, Bukowski and Szalewicz[34] reported SAPT and CCSD(T) calculations with various basis sets. Their CCSD(T) well depth is approximately 2 cm^{-1}deeper than reported in this work. The saddle point of the PES obtained in this work is located at the collinear geometry for R=8.75 a_0 . The barier height between the T-shaped and the collinear arrangement is equal to 86.45 cm^{-1}. Figure 3.2 shows the contour plot of the PES.

3.4 Collocation dynamics for J=0.

The Author chose the collocation method to simulate the dynamics of the Ar-CO_2 complex on the CCSD(T) PES. The 2-D collocation method is straightforward to program, because it does not require integrals of the potential with the functions of the basis set in which diagonalization is performed. The details of the method are described in Chapter II.

The basis set for hamiltonian diagonalization consisted of 30 Legendre polynomials for the angular variable and 65 gaussian functions for the radial variable. The radial functions were evenly spaced starting from R= 3.0 a_0 to 13.0 a_0 . This basis set was sufficient for convergence of the eigenvalues of the hamiltonian for quantum number of total angular momentum $J = 0$. Table 3.2 contains first 10 eigenvalues (there were more than 60 eigenvalues) relatively to the value of D_0. The first excited state which corresponds to van der Waals bending vibration lies 27.2 cm^{-1}above the ground state energy. This value is in very good agreement with experimentally[37] determined number, which is 27.818 cm^{-1}.

Table 3.1: Optimal parameters for the Ar-CO_2 CCSD(T) fit.

Parameter	Value
α_j coefficients	
α_0	1.46397162544828174
α_2	0.391491797617520787
α_4	0.155567987018096210
β_j coefficients	
β_0	15.2232403266627312
β_2	5.76080669549135482
β_4	1.22247614415686789
g_{lj} coefficients	
g_{00}	0.264066050850794952E-01
g_{02}	-0.861020166743013404E-01
g_{04}	0.145185301547874311E-01
g_{10}	0.652917566349019325E-02
g_{12}	0.509475095154112365E-01
g_{14}	-0.207548129507051302E-01
g_{20}	-0.236174077765420294E-02
g_{22}	-0.661253538537006583E-02
g_{24}	0.437585840196362107E-02
g_{30}	0.167270478365487348E-03
g_{32}	0.190893693304583425E-03
g_{34}	-0.238397882323656684E-03
C_{nj} coefficients	
C_{60}	-47390.2605932150254
C_{62}	-91885.9499599325354
C_{80}	-15350113.0129258446
C_{82}	-11343314.1745753922

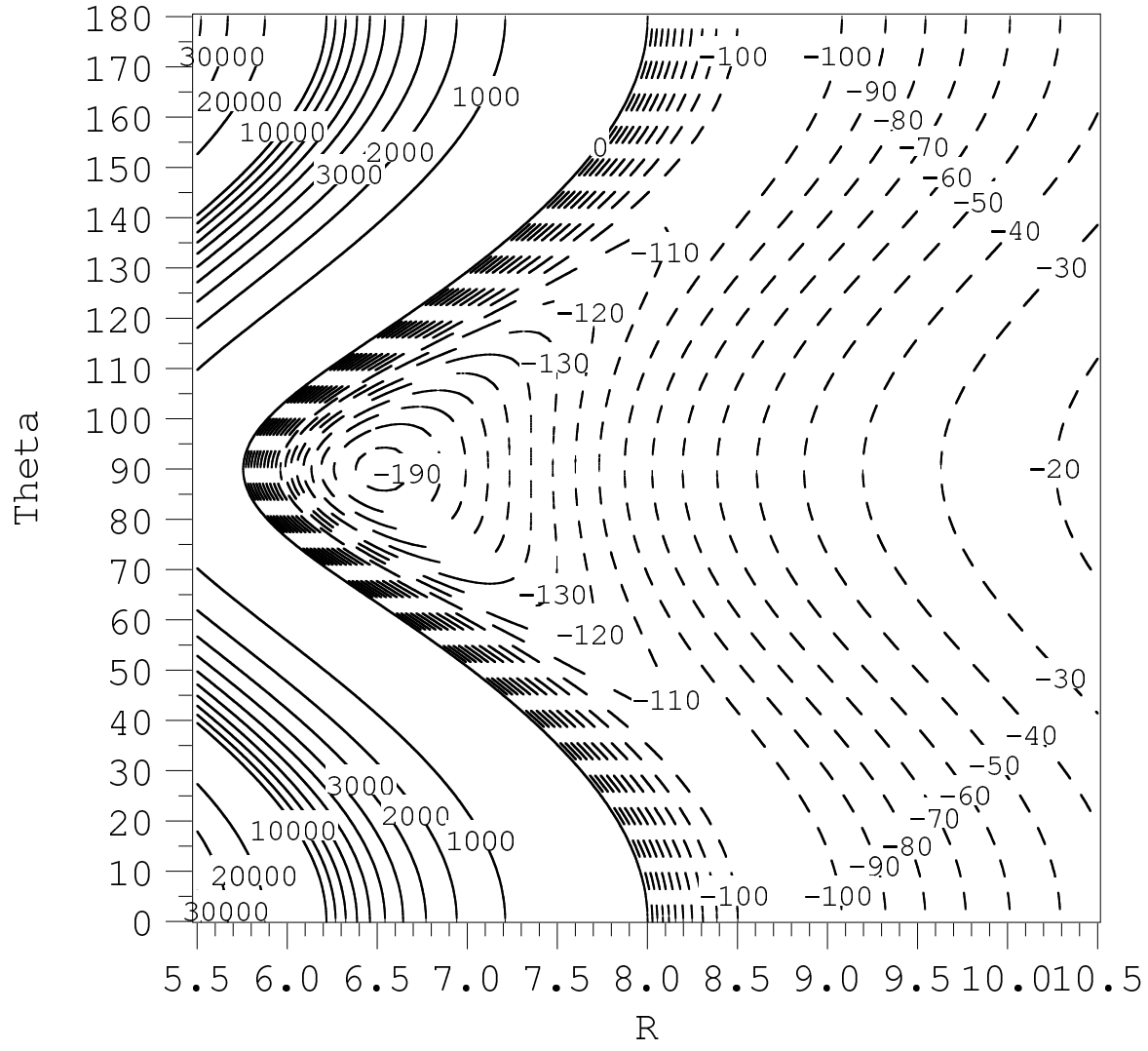

Figure 3.2: Contour of the Ar-CO_2 CCSD(T) PES.

Table 3.2: Eigenvalues for Ar-CO_2 in the case of $J = 0$. The values are reported relatively to D_0=157.6 cm^{-1}.

Number	Energy [cm^{-1}]
0	0.0
1	27.222
2	33.315
3	51.183
4	52.210
5	61.293
6	65.601
7	66.440
8	69.829
9	70.155
10	76.720

3.5 Second virial coefficient. Classical approach with first-order quantum corrections.

3.5.1 Classical formula of second virial coefficient for atom-linear molecule case.

Classical formula for the second virial coefficient for an atom-linear molecule system is well known[38] and is shown below

$$B_{AB}^{(0)}(T) = N_A \pi \iint \left(1 - e^{-\frac{V(R,\theta)}{kT}}\right) R^2 \sin\theta \, dR d\theta \tag{3.9}$$

The subscript AB denotes a system composed of an atom A and a linear molecule B. N_A is Avogadro's constant in [mol^{-1}], k - Boltzmann's constant [$\frac{J}{K}$]. The dependence of the second virial coefficient on the interaction energy in the system is included in the exponent of the exponential function. Variables R and θ are Jacobi coordinates, the same as described in section 3.2. Variable T is the temperature expressed in Kelvin.

Classical formula 3.9 is valid for the temperatures for wich exchange processes are negligible. For temperatures below 11 K or when system contains light molecules one has to switch to the quantum description of the second virial coefficient.

3.5.2 First order radial and angular quantum corrections to second virial coefficient.

Inclusion of quantum corrections to the classical expression 3.9 is important for lower temperatures. As it will be seen, these corrections are fairly small for higher temperatures and satisfactory agreement with experiment can be riched using only formula 3.9.

First-order quantum corrections can be divided into the radial component and the angular component .[38] The radial component is described by equation 3.10 and the angular one by 3.11.

$$B_{ABr}^{(1)}(T) = \frac{N_A \pi}{12\,(kT)^3} \frac{\hbar^2}{2\mu} \iint e^{-\frac{V(R,\theta)}{kT}} \left(\frac{\partial V(R,\theta)}{\partial R}\right)^2 R^2 \sin\theta \, dR d\theta \tag{3.10}$$

$$B^{(1)}_{ABa}(T) = \frac{N_A \pi}{12\,(kT)^3} \iint e^{-\frac{V(R,\theta)}{kT}} \left(\frac{\hbar^2}{2\mu R^2} + \frac{\hbar^2}{2I_B} \right) \times \sum_{j_B} j_B\,(j_B+1)\, V_{j_B}(R)\, P_{j_B}(\cos\theta)\, R^2 \sin\theta\, dR d\theta \tag{3.11}$$

The reduced mass of the AB supermolecule is denoted by μ and the moment of inertia of the B molecule by I_B. Finally, the second virial coefficient is equal to sum of the classical part and quantum corrections:

$$B_{AB}(T) = B^{(0)}_{AB}(T) + B^{(1)}_{ABr}(T) + B^{(1)}_{ABa}(T) \tag{3.12}$$

In the angular correction the interaction potential V is expanded in the body fixed frame in terms of Legendre polynomials. The corrections can be easily calculated using numerical quadrature commonly used for evaluation of the classic second virial coefficients.

3.6 Numerical calculations and results

To calculate the second virial coefficient for the Ar-CO_2 complex one has to evaluate integrals in expressions 3.9, 3.10 and 3.11. 500 point Gauss-Legendre numerical quadrature have been chosen. The results converged within 0.0001 $[\frac{cm^3}{mol}]$.

In the case of the classical part the radial range was $R \in [1,\ 500]\ a_0$. Between $R = 0.0$ and $R = 1.0\ a_0$ the integral 3.9 was calculated analytically assuming that potential's highly repulsive wall causes vanishing of the exponential term in expression 3.9. Table 3.3 contains results obtained from calculations described above using CCSD(T) PES. Comparison of final second virial coefficient in this work with theoretical and experimental values reported by Hutson *et al*[39] is in Table 3.4.

The plot 3.3 presents some of these results in a graphical way. It can be seen that the agreement between calculated $B(T)$ values using CCSD(T) PES and experimental ones is excellent for tamperatures over 250 K. The rest of the results below 250 K are located within experimental error bars except for two lowest temperature in data range.

Table 3.3: Results of classical second virial coefficients calculations and first order quantum corrections for the Ar-CO_2 Van der Waals complex. Values in $\frac{cm^3}{mol}$

T[K]	$B^{(0)}$	$B_r^{(1)}$	$B_a^{(1)}$
213.0	-80.96	0.3575	0.1706
223.0	-73.40	0.3209	0.1524
242.0	-61.22	0.2662	0.1255
262.0	-50.80	0.2234	0.1046
276.0	-44.62	0.1998	0.09307
288.2	-39.84	0.1825	0.08466
296.0	-37.04	0.1727	0.07991
303.2	-34.61	0.1644	0.07591
313.2	-31.47	0.1539	0.07087
323.1	-28.58	0.1446	0.06512
333.2	-25.86	0.1361	0.06232
365.0	-18.46	0.1141	0.05184

Table 3.4: Comparison of calculated in this work second virial coefficients values with previously reported theoretical and experimental values by Hutson. Values in $\frac{cm^3}{mol}$. Numbers in parenthesis denote experimental error bars.

T[K]	B	$B_{Spl.Rep.}$	B^{exp}
213.0	-80.43	-88.30	-93.30(10)
223.0	-72.92	-80.20	-84.50(10)
242.0	-60.83	-67.30	-67.20(10)
262.0	-50.47	-56.30	-53.80(10)
276.0	-44.33	-49.70	-48.70(7)
288.2	-39.57	-44.70	-40.33(7)
296.0	-36.79	-41.70	-37.05(7)
303.2	-34.37	-39.10	-34.21(7)
313.2	-31.24	-35.80	-31.20(7)
323.1	-28.38	-32.80	-28.30(7)
333.2	-25.66	-29.90	-25.80(7)
365.0	-18.29	-22.00	-19.60(7)

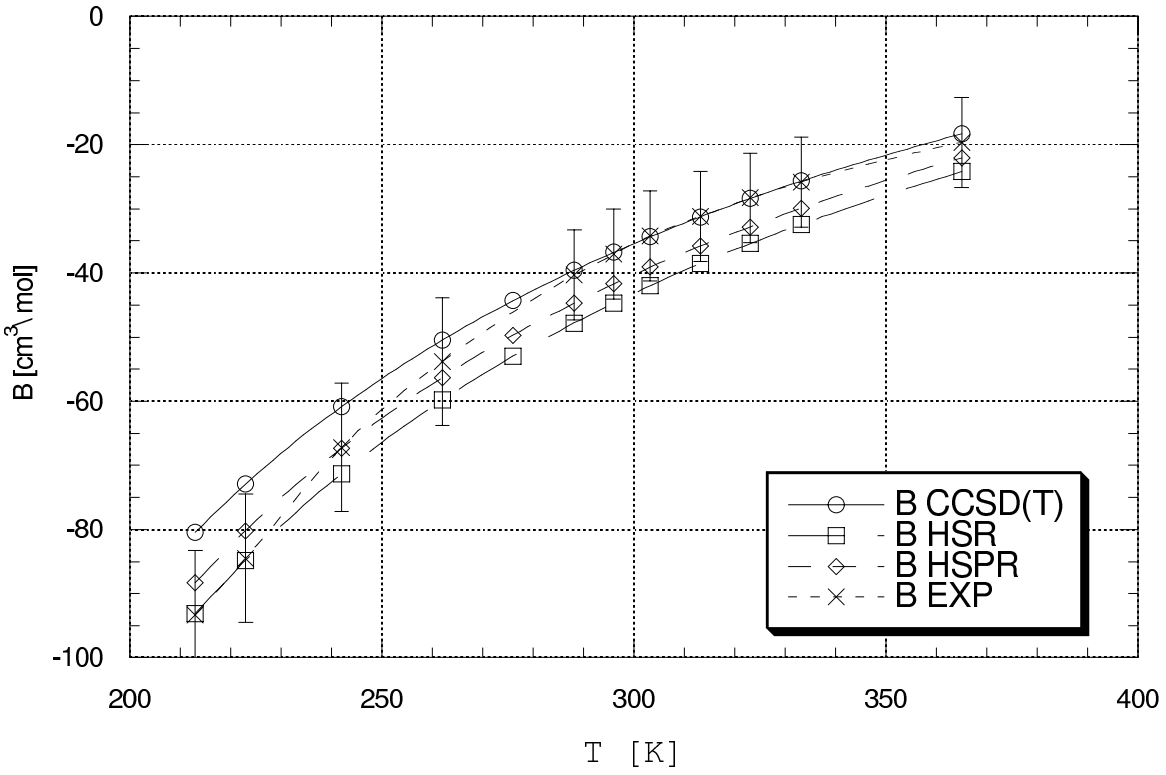

Figure 3.3: Plot of the calculated second virial coefficient for Ar-CO_2 versus temperature. The HSR abbreviation denotes Hutson Single Repulsion model and HSPR -Hutson Split Repulsion Model.

CHAPTER IV

Structure and spectroscopy of Rg-S(^{3}P) Van der Waals complexes

4.1 Preface

From the most general perspective, rare gas-atom interactions are the simplest models of the open-shell Van der Waals complexes. Very accurate *ab initio* calculations and reliable modeling are possible for these interactions, and the resulting potentials may be used to simulate experimentaly determined properties, first of all collision properties. For this reason the Author has undertaken the study of the Rg-S(^{3}P) interactions, in collaboration with the renowned experimental group of professor Aquilanti from Perugia. As a result, excellent *ab initio* potentials have been modeled that accurately reproduced a variety of collision properties of these systems. The *ab initio* potentials appear to be competitive to the exeperimentaly determined ones.

4.2 Introduction

The studies of weak interatomic interactions are important for understanding transport, collision, and relaxation phenomena in the gas phase, modeling the structure and dynamics of clusters and condensed phases, and gaining a greater insight into the nature of van der Waals bonding. The analysis of open-shell interactions is of especially interest because it allows one to investigate the interaction anisotropy arising from a non-spherical electron density distribution in the open-shell systems. The anisotropy of interaction manifests itself in the splitting of degenerate electronic states of the open-shell atom upon the interaction with an external particle. The difference in the corresponding interaction potentials can often be attributed to contribution from the incipient bonding, the embryo of the covalent chemical bonding. The role of fine structure effects like the spin-orbit coupling is important for the processes of collisional energy redistribution in plasmas, discharges, laser media, *etc.*. It is not surprising therefore that many researchers focused their recent attention on an accurate description of van der Waals interactions with account of relativistic effects.

At present, there are three basic routes to accurate modeling of weak interaction potentials (here "weak" means a few hundreds of wavenumbers or less). First of all, the interaction potentials for some weakly bound atom-atom systems can be generated from analysis of atomic scattering in molecular beams.

It is well understood that the scattering data uniquely determine the interaction potential ,[40] although this may not be generally true for open-shell atoms where the collision dynamics

is governed by several coupled potentials. The interactions in such systems can, however, be studied with the help of some more sophisticated techniques like magnetic field selection.

Spectroscopic measurements is an alternative approach to experimental determination of interaction potentials in weakly bound systems. The experimental measurements, however, meet with certain difficulties when applied for studies of the lowest electronic states in the complexes. The weak binding energy makes it difficult to generate the species in concentrations high enough to obtain well-resolved excitation spectra. Measurements of bound-free laser induced fluorescence are more instructive for studying the low-lying states (see, *e.g.*, Refs.[41–43]).

However, selection rules do not usually allow the experiments to probe all the states correlating with the first dissociation limit, and the anisotropy of interaction can not be investigated in full details. One solution is to use the photoelectron spectroscopy of weakly-bound anions, especially high-resolution zero electron kinetic energy (ZEKE) spectroscopy, (see, *e.g.*,Refs.[44–46]). Due to the higher binding energy of anions and less strict selection rules, this approach is very promising. It is, however, yet to be widely explored.

Finally, the interaction potentials of van der Waals complexes can be computed from first principles using the *ab initio* electronic structure theory. Although the calculations for weakly-bound open-shell systems are still considered as the state-of-the-art level of theory ,[17] many authors proved them to be successful for a number of systems.

The only reliable interaction potentials for the Rg-S(^{3}P) systems are the scattering potentials obtained recently from molecular beam experiments .[47] Several recent *ab initio* calculation for the heavy Kr-S [48] and Xe-S[49] systems have been mainly designed to treat the states correlating with excited atomic limits and do not provide an accurate description of low-lying electronic states. The purposes of the present paper are

(i) to evaluate accurate *ab initio* potentials for Rg-S systems (Rg=He-Xe) and test the accuracy of the atomic model for spin-orbit (SO) coupling;

(ii) compare the *ab initio* and scattering potentials and test the correlation rules for Rg-S systems;

(iii) investigate the dynamics of intramultiplet mixing in Rg + S(^{3}P$_j$) inelastic collisions and make a qualitative comparison to the results obtained previously for the Rg + O(^{3}P$_j$) collisions.

4.3 *Ab initio* interaction potentials

4.3.1 Non-relativistic potentials

In the non-relativistic approximation, the interaction of an S(^{3}P) atom with Rg gives rise to two states of $^3\Pi$ and $^3\Sigma^-$ symmetry. Their electronic configurations are $p_x^2 p_y^1 p_z^1$ and $p_x^1 p_y^1 p_z^2$, respectively. In the latter case the Rg atom is bound to the S atom by purely van der Waals interaction with doubly occupied p_z orbital. In the $^3\Pi$ configuration the Rg atom interacts primarily with the singly occupied orbital and the incipient chemical bonding contributes to the binding energy.

The supermolecular approach is used to calculate interaction energies of the He, Ne, Ar, Kr and Xe with the sulfur atom. The interaction energy is expressed as

$$\Delta E\left(R\right) = E_{AB}\left(R\right) - E_A^{DCBS}\left(R\right) - E_B^{DCBS}\left(R\right) \tag{4.1}$$

where quantity E^l_{AB} is the energy of the dimer AB, and $E^{l,DCBS}_A$ and $E^{l,DCBS}_B$ are energies of monomers A and B, respectively, calculated with dimer centered basis set (DCBS). Interaction energies were corrected for basis set superposition error (BSSE) by using counterpoise procedure of Boys and Bernardi.[50]

Calculations of the non-relativistic potentials are performed with augmented correlation consistent quadruple zeta basis set denoted as aug-cc-pVQZ (hereafter, VQZ) augmented by the [3s3p2d] set of bond functions. The bond functions are centered at the midpoint between the sulfur atom and the rare gas atom and have the exponents sp: 0.9, 0.3, 0.1; d: 0.6, 0.2. The resulting basis set is denoted by VQZ+332. In the case of the Xe-S system, the relativistic effective core potential ECP46MWB is used for the Xe atom and the VQZ basis set for the S atom with the same 332 bond functions are employed.

The post-Hartree-Fock interaction energies are obtained at the unrestricted coupled cluster UCCSD(T) level of theory, based on the single reference RHF wave function, as described in Ref.[51,52]

The resulting set of *ab initio* potentials is designated below by UCCSD(T)/VQZ+332 (UCCSD(T)/VQZ/ECP+332 for Xe-S). Only the valence shell is correlated. The internuclear distance R was varied in the range [1.25 Å, 12.0 Å] for He-S, [1.5 Å, 12.0 Å] for Ne-S, [1.75 Å, 12 Å] for Ar-S, [2.0 Å, 12.0 Å] for Kr-S, and [2.0Å, 15.0 Å] for Xe-S. The spin contamination $\langle S^2 - S_z^2 - S_z \rangle = 0.002$ is small for all complexes under consideration. It does not change with the distance and is the same as for the separated S monomer. Tables 4.1, 4.2, 4.3, 4.4, 4.5 collect UCCSD(T)/VQZ+332 interaction energies for the He-S, Ne-S, Ar-S, Kr-S and Xe-S system, respectively.

For the Ne-S system, the most accurate scattering data are available .[47] Therefore, we perform a more extensive *ab initio* analysis for this system. First, we use an extended aug-cc-pV5Z basis supplemented with a larger [3s3p2d2f1g] set of bond functions with the exponents (sp: 0.9, 0.3, 0.1; d: 0.6, 0.2; f: 0.3). This basis set is denoted by V5Z+33221. Second, another version of the coupled cluster method which includes triples at the fourth order, UCCSD[T] ,[53,54] with the same V5Z+33221 basis set is applied. Finally, the calculations which correlate all shells of Ne and S except for only the innermost 1s orbitals are performed. This calculations are referred to as UCCSD[T]/fc(1s)/V5Z+33221.

All of the electronic structure calculations were performed with MOLPRO 2000 suite of programs.[53]

4.3.2 Comparison of scattering and *ab initio* potentials

The scattering and *ab initio* potentials are shown in Figure 4.1 , and the zero points and equilibrium parameters of the potentials are collected in Table 4.6.

In general, the *ab initio* data for Rg=Ne-Xe fall within the error bars of the scattering experiments .[47] Comparison of our *ab initio* results with the parameters of the scattering potentials reveals the following trends. For all Rg atoms except Ar, the agreement is markedly better for the excited $^3\Sigma^-$ state than for the ground $^3\Pi$ one. The *ab initio* calculations predict shorter equilibrium distances and smaller interaction energies in the ground states, although the theoretical value of D_e for Xe is overestimated by *ca.* 20 cm^{-1}. The *ab initio* calculations of the excited states also result in slightly shorter R_e but lead to the D_e values in an excellent agreement with experimental data. The ArS system is an exception. The computed binding energy of ArS slightly overestimates the result of the measurements.

Table 4.1: UCCSD(T) interaction energies for He-S μEh

R [Å]	$^3\Pi$	$^3\Sigma$
1.25	228287.73173	405826.40699
1.50	108528.34263	205195.08385
1.75	49467.55102	97590.16230
2.00	21446.17721	44643.57845
2.25	8791.74654	19836.20829
2.50	3352.53865	8563.17892
2.75	1134.19751	3562.38825
3.00	287.24466	1398.31956
3.25	-3.88463	491.36093
3.50	-83.08998	129.33648
3.75	-88.83492	-3.14905
4.00	-73.74386	-42.95151
4.25	-56.12838	-47.91688
4.50	-41.32519	-41.60347
5.00	-22.02390	-25.25055
5.50	-12.09241	-14.30979
6.00	-6.96486	-8.21750
6.50	-4.20348	-4.88989
7.00	-2.64210	-3.02751
8.00	-1.15333	-1.28593
9.00	-.55848	-.61522
10.00	-.29354	-.32214
12.00	-.09889	-.11530

Table 4.2: UCCSD(T) interaction energies for Ne-S μEh

R [Å]	$^3\Pi$	$^3\Sigma$
1.50	251737.68239	375413.15293
1.75	113680.82509	185830.48054
2.00	48216.19186	84630.17802
2.25	19339.17124	36762.81145
2.50	7221.14854	15352.96948
2.75	2381.66656	6101.73700
3.00	570.70732	2229.56438
3.25	-35.62268	676.27485
3.50	-191.70566	95.26977
3.75	-195.88513	-93.04295
4.00	-159.42628	-132.08416
4.25	-119.90217	-120.66058
4.50	-87.55584	-96.72794
5.00	-46.24039	-54.73074
5.50	-25.28147	-29.98380
6.00	-14.50358	-16.81312
6.50	-8.70769	-9.82645
7.00	-5.44984	-6.02456
8.00	-2.37298	-2.58005
9.00	-1.13802	-1.23911
10.00	-0.59376	-0.64659
12.00	-0.19952	-0.21654

Table 4.3: UCCSD(T) interaction energies for Ar-S μEh

R [Å]	$^3\Pi$	$^3\Sigma$
1.75	249942.48836	409454.71997
2.00	116052.49874	213774.99206
2.25	51713.46460	104955.20851
2.50	21766.30614	48986.76144
2.75	8306.47841	21692.09036
3.00	2557.82661	8945.10685
3.25	303.63754	3255.76842
3.50	-443.90630	862.59720
3.75	-591.22024	-51.77176
4.00	-530.73913	-335.68911
4.25	-420.24105	-371.19162
4.50	-315.78021	-322.74644
5.00	-170.08980	-195.92633
5.50	-92.62758	-110.26190
6.00	-52.58782	-62.61141
6.50	-31.27481	-36.79967
7.00	-19.42832	-22.51558
8.00	-8.35697	-9.41194
9.00	-4.01739	-4.43117
10.00	-2.09693	-2.28469
12.00	-0.68853	-0.74036

Table 4.4: UCCSD(T) interaction energies for Kr-S μEh

R [Å]	$^3\Pi$	$^3\Sigma$
2.00	153612.80302	279354.62719
2.25	69407.49511	143787.45565
2.50	30072.99977	70455.06133
2.75	12062.30598	32811.69966
3.00	4078.61644	14343.41491
3.25	760.76663	5676.69249
3.50	-448.51754	1820.22099
3.75	-760.35340	232.87005
4.00	-730.42200	-332.72301
4.25	-598.77116	-467.19777
4.30	-569.95027	-469.34307
4.50	-459.26547	-438.58120
5.00	-252.15137	-282.41133
5.50	-137.89109	-162.03985
6.00	-78.13873	-92.48071
6.50	-46.28861	-54.32639
7.00	-28.61489	-33.16154
8.00	-12.19610	-13.80295
9.00	-5.82708	-6.47791
10.00	-3.03399	-3.33097
12.00	-0.98860	-1.07104

Table 4.5: UCCSD(T) interaction energies for Xe-S μEh

R [Å]	$^3\Pi$	$^3\Sigma$
2.00	209893.13141	361606.31440
2.25	94983.36749	198139.01786
2.50	41443.04437	104003.26104
2.75	17041.71095	52014.21816
3.00	6137.41977	24611.04456
3.25	1437.02052	10812.81890
3.50	-414.15349	4192.45619
3.75	-986.05463	1200.26077
4.00	-1025.15523	-34.38665
4.25	-877.49042	-460.08147
4.30	-840.74688	-494.22940
4.50	-692.15433	-539.21929
5.00	-391.35552	-398.94068
5.50	-215.19020	-238.83002
6.00	-120.75091	-137.66384
6.50	-70.42009	-80.58816
7.00	-42.92932	-48.83022
8.00	-17.98470	-20.09112
9.00	-8.51424	-9.37881
10.00	-4.40723	-4.81135
12.00	-1.43173	-1.55534
15.00	-0.37275	-0.40076

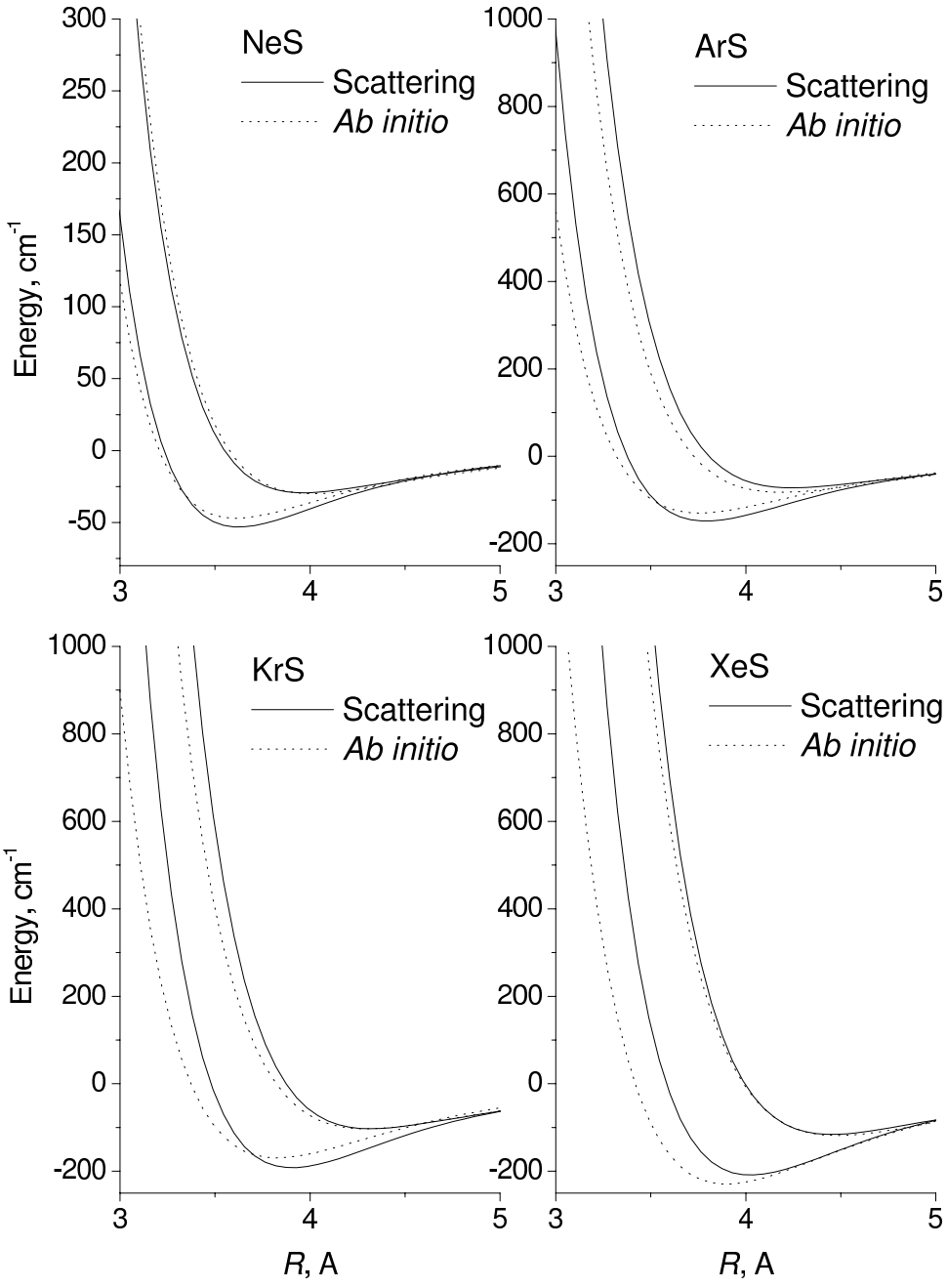

Figure 4.1: Scattering and *ab initio* potentials.

Table 4.6: The zeroes σ ($V(\sigma) = 0$), Å, equilibrium distances R_e, Å, and well depths D_e, cm^{-1} for the scattering and *ab initio* potentials of the $^3\Pi$ and $^3\Sigma^-$ states of the Rg-S systems

System	Parameters	Scattering		UCCSD(T)/VQZ+332	
		$^3\Pi$	$^3\Sigma^-$	$^3\Pi$	$^3\Sigma^-$
HeS	σ	-	-	3.244	3.739
	R_e	-	-	3.653	4.188
	D_e	-	-	19.94	10.60
NeS	σ	3.23 ± 0.13	3.55 ± 0.14	3.223	3.589
				3.212[a]	3.580[a]
				3.206[b]	3.575[b]
				3.206[c]	3.575[c]
	R_e	3.62 ± 0.14	3.97 ± 0.16	3.625	4.024
				3.614[a]	4.013[a]
				3.608[b]	4.008[b]
				3.604[c]	4.003[c]
	D_e	53.2 ± 13	29.0 ± 7	44.60	29.03
				46.17[a]	29.48[a]
				47.03[b]	29.97[b]
				47.55[c]	30.24[c]
ArS	σ	3.38 ± 0.10	3.81 ± 0.11	3.319	3.726
	R_e	3.79 ± 0.11	4.24 ± 0.13	3.755	4.186
	D_e	148.4 ± 22	72.6 ± 11	129.76	82.15
KrS	σ	3.48 ± 0.10	3.87 ± 0.12	3.373	3.822
	R_e	3.91 ± 0.12	4.32 ± 0.13	3.826	4.295
	D_e	192.0 ± 29	103.2 ± 15	169.49	103.01
XeS	σ	3.58 ± 0.11	4.00 ± 0.12	3.418	3.988
	R_e	4.02 ± 0.12	4.45 ± 0.13	3.897	4.482
	D_e	209.7 ± 31	115.3 ± 17	229.45	118.43

[a] UCCSD(T)/V5Z+33221 calculations [b] UCCSD[T]/V5Z+33221 calculations [c] UCCSD[T]/fc(1s)/V5Z+33221 calculations

Calculations with bigger basis sets for Ne-S indicate that the UCCSD(T)/VQZ+332 calculations are not fully converged with respect to the both basis set size and the level of correlation treatment (although the convergence error is only on the order of 5%). Interestingly, all factors (the use of extended basis set, the implementation of the UCCSD[T] method, and the account for the correlation of inner shells) increase the binding energy in the $^3\Pi$ state improving the agreement with the scattering data. The same holds true for the $^3\Sigma^-$ state, but the net effect is much less significant. At the same time, the improvements of the *ab initio* calculations systematically shorten the equilibrium distances in both electronic state, increasing the deviation from the experimental results. The effect of the basis set size is most significant.

It is also instructive to compare qualitative trends in potential parameters in the sequence of Rg atoms. According to our *ab initio* calculations, He-S is a distinguished system with relatively long equilibrium distances in both electronic states. Indeed, passing to Ne, significantly reduces R_e which then monotonically increases when Rg changes from Ne to Xe. The same trend is represented by the scattering potentials.

The degree of interaction anisotropy can be qualitatively characterized by the decrease of the equilibrium distance $\delta R_e = |R_e(^3\Pi) - R_e(^3\Sigma^-)|$ $/R_e(^3\Pi)$ and increase of the binding energy $\delta D_e = |D_e(^3\Pi) - D_e(^3\Sigma^-)|/D_e$ $(^3\Pi)$ upon the excitation from the $^3\Sigma^-$ to $^3\Pi$ state. If we consider the latter state as having purely van der Waals bonding, these differences reflect the contribution of the incipient chemical bond formed by an unfilled p_z orbital. For the scattering potentials, neither δR_e nor δD_e exhibit definite trend when Rg changes from He to Xe, varying in the ranges 45-51% and 10-12%, respectively. In contrast, the *ab initio* results show a clear and consistent propensity in the Ne-Xe sequence with He-S being again a distinguished system. The relative anisotropy steadily increases from Ne to Xe undergoing the largest change for Xe.

The behavior of the short- and long-range potential branches is also worth to discuss. According to Figure 4.1, repulsive walls of the *ab initio* potentials are generally slightly softer, especially in the ground state. The leading C_6 coefficients of the long-range $1/R^n$ expansion are presented in Table 4.7. For both electronic states, the coefficients of scattering potentials systematically exceed the *ab initio* values. As far as only $1/R^6$ term is retained in the scattering potentials, it is likely that C_6 coefficient effectively accumulates all the attraction, which is distributed among high-order expansion coefficients in the *ab initio* potentials. The interaction anisotropy, *i.e.*, the ratio of C_6 coefficients for $^3\Pi$ and $^3\Sigma^-$ states is also different. Evaluation of scattering potentials was relied on the fixed ratio $C_{6,\Pi}/C_{6,\Sigma} = 1.185$ [47] as estimated from the ratio of static polarizabilities of sulfur atom .[55] *Ab initio* interaction is much less anisotropic. The C_6 ratio increases from Ne to Xe reaching the maximum value of 1.102 (He-S interaction is again an exception being more anisotropic than Ne-S and Ar-S ones). Although the UCCSD(T)/VQZ+332 calculations tend to overestimate the C_6 anisotropy as is evident from refined calculations on Ne-S, the disagreement with scattering data is still too big. One can take into account two possible reasons. First, the overall anisotropy of the long-range *ab initio* potentials is higher due to the difference of the high-order dispersion-interaction terms. Second, the relation of C_6 coefficient with the static polarizabilities used in the construction of scattering potentials is an approximate one.

Table 4.7: The C_6 coefficients of the asymptotic long-range expansions of the Rg-S interactions in the $^3\Pi$ and $^3\Sigma^-$ states, eV Å^6

System	Potential	$C_{6,\Pi}$	$C_{6,\Sigma}$	$C_{6,\Pi}/C_{6,\Sigma}$
HeS	UCCSD(T)/VQZ+332	7.08	7.72	1.090
NeS	scattering	17.90	21.20	1.185
	UCCSD(T)/VQZ+332	15.19	15.46	1.018
	UCCSD(T)/V5Z+33221	15.27	15.99	1.047
	UCCSD[T]/V5Z+33221	15.55	16.20	1.042
	UCCSD[T]/fc(1s)/V5Z+33221	15.75	16.48	1.046
ArS	scattering	63.11	74.77	1.185
	UCCSD(T)/VQZ+332	51.76	53.45	1.033
KrS	scattering	87.61	103.79	1.185
	UCCSD(T)/VQZ+332	76.33	80.30	1.052
XeS	scattering	131.88	156.24	1.185
	UCCSD(T)/VQZ+332	118.54	107.57	1.102

4.3.3 Analytical fits

The UCCSD(T)/aug-cc-pVQZ+332 (ECP46MWB(Xe)+ aug-cc-pVQZ(S)+332 in case of Xe-S system) results for Rg-S interaction for $^3\Sigma$ and $^3\Pi$ states were approximated by analytic expression of Degli Esposti-Werner type[56] composed from the short-range term (V_{sh}), and the asymptotic long-range part (V_{as}):

$$V(R) = V_{sh}(R) + V_{as}(R) \tag{4.2}$$

where

$$V_{sh}(R) = \sum_{l=0}^{8} g_l R^l e^{-\alpha(R-\beta)} \tag{4.3}$$

The long-range part were chosen to be a damped dispersion term:

$$V_{as}(R) = -\frac{1}{2}\left[1 + \tanh(\gamma + \delta R)\right] \sum_{n=0}^{4} \frac{C_{2n+6}}{R^{2n+6}} \tag{4.4}$$

The nonlinear α, β, γ, δ and the linear g_l and C_i parameters were optimized using the Levenberg-Marquardt least square method. The RMS values for each curve of the $^3\Sigma$ and $^3\Pi$ of Rg-S systems are collected in Table. 4.8.
The maximum of absolute error was equal to 0.2 μEh for Xe-S system in the vicinity of the sign change.

4.4 Total scattering cross sections

Table 4.8: The RMS of fits. Unit in μEh

Rg-S	$^3\Sigma$	$^3\Pi$
He-S	0.0033	0.0011
Ne-S	0.025	0.016
Ar-S	0.020	0.0115
Kr-S	0.0084	0.008
Xe-S	0.046	0.105

4.4.1 Computational details

To calculate absolute total scattering cross sections (ATCS) we use the same model as was implemented for the analysis of molecular beam measurements in Ref.[47] The SO coupling is approximated by its atomic contribution

$$\hat{H}_{SO} = a\hat{L}\hat{S}, \tag{4.5}$$

where $\hat{L}$ and $\hat{S}$ are the orbital and spin electronic angular momenta of the open-shell atom and the SO constant a is related to the energies of $j = 1$ and $j = 0$ atomic sublevels with respect to $j = 2$ one Δ_1=396.2 cm^{-1} and Δ_0=573.4 cm^{-1} .[57] It should be noted that if Eq.(4.5) is strictly valid, Δ_1/Δ_0 should be 2/3. The experimental values of the SO splittings are used in the calculations. Using the minimum atomic basis set to describe the wave functions of the Rg-S electronic states correlating to Rg + S(^{3}P) asymptotic limits ,[58] one can easily evaluate the matrix of the relativistic Hamiltonian, see, *e.g.*, .[59–64] Neglecting the Coriolis and radial diabatic couplings, one can resort to adiabatic approximations which allows us to consider scattering on six uncoupled relativistic potentials. The individual ATCS for each potential are calculated using the effective quasiclassical [65] and exact quantum approaches as functions on the center-of-mass (c.m.) velocity. Both methods led to essentially the same results. After the summation of individual cross sections with weights corresponding to the experimental conditions ,[47] the total ATCS is transformed to the laboratory frame to account for the spreading of the laboratory velocity of the beam and thermal motion of the projectile.

Before discussing the results of these calculations, it is worth to address the validity of the electronic structure model. For Rg+O(^{3}P) collisions, we have found that the interaction with the electronic states correlating with excited electronic states of oxygen atom does not influence the scattering dynamics significantly ,[66] although small contribution from the S(^{1}D) atom itself could not be excluded .[47] It is interesting to check here the quality of the atomic approximation to the SO coupling (4.5).

For this purpose, the direct calculation of the SO coupling matrix elements between the $^3\Pi$ and $^3\Sigma^-$ states of the Ne-S and Xe-S are performed using the method of diagonalization of the $\hat{H}_{el} + \hat{H}_{SO}$ operator [67] implemented in the MOLRPO2000 suite of programs .[53] The Ne and S atoms are described using the uncontracted VQZ basis set, while for the Xe atom we adopt the pseudopotential Stuttgart ECP46MWB(spdf) basis set. The complete Breit-Pauli SO Hamiltonian ($\hat{H}_{SO}$) is expressed in the basis of adiabatic states of the $\hat{H}_{el}$ Hamiltonian. In the case of Ne-S, only two states correlating with the ^{3}P state of the sulfur atom are included in the diagonalization procedure. For the Xe-S system, this basis set is also augmented by the states originating from the ^{1}S and ^{1}D states of the sulfur atom.

Asymptotic values of the SO coupling matrix element are equal to 193.1 and 194.5 cm^{-1} for the minimum and extended bases of the adiabatic states. The corresponding splittings are Δ_1=386.2, Δ_0=579.3 cm^{-1} and Δ_1=389.0, Δ_0=583.5 cm^{-1}, respectively. The latter values are closer to experimental data (with an absolute error within 10%). The calculated SO matrix elements are plotted in Figure 4.2.

The matrix elements are almost independent of the interatomic separation down to relatively short internuclear distances and then show a rapid decrease. For Ne-S, this fall-off happens at a rather small distance, which is well outside the region of importance for collision dynamics. However, for Xe-S the deviation from the atomic model starts quite close to the zero of the $^3\Pi$ potential. The test calculations performed with the *ab initio* R-dependent couplings demonstrate that this does not affect significantly the total scattering cross sections discussed below. It should be noted, however, that the effect on the high-energy collisions can be more important.

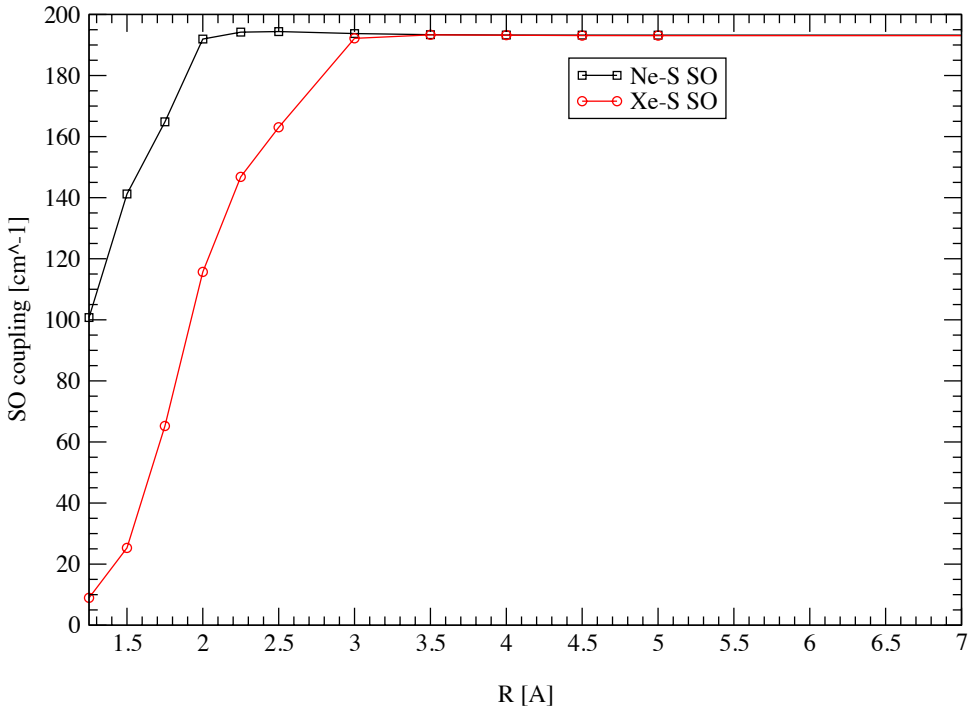

Figure 4.2: R-dependent SO matrix elements for the Ne-S and the Xe-S systems.

CHAPTER V

Ab initio calculations of adiabatic and diabatic potential energy surfaces of $Cl(^2P)\cdots HCl(^1\Sigma^+)$ Van der Waals complex

[J. Chem. Phys. **115**, 3085 (2001)]

5.1 Preface

This Chapter describes supermolecular *ab initio* calculations of the Cl+HCl Van der Waals complexes. It developes several new ideas necessary to apply a CCSD(T) potential for first 3 states arising from the interaction of HCl with the ground state (^{2}P) chlorine atom. In particular, the issue of basis set superposition error related to rotation of singly-occupied orbitals in three ghost monomer states has been addressed and solved. Another novelty is related to consequent use of the CCSD(T) method to calculate interaction energies of all three states, despite two have the same symmetry. The adiabatic and diabatic PESs for this system represent the first state-of-the-art characterization of the complex in the literature. Previous semiempirical[68] and recent *ab initio* (Jungvirth) potential are of considerable lower quality. It is expected that the paper will prompt experimental determination of the spectra of Cl-HCl - still a highly nontrivial task.[69,70]

5.2 Introduction

The reactions between halogen atoms and hydrogen halide molecules are important prototypes in the study of chemical reaction dynamics. They can be studied in greater detail experimentally, and have also been used as testing ground for theories of reactive scattering. In particular, for almost two decades, there has been a great deal of interest in the hydrogen exchange reaction $Cl(^2P)+HCl\rightarrow ClH+Cl(^2P)$.[71–77]

The transition state of this reaction has been probed by photodetachement spectroscopy of the negative ion $ClHCl^-$,[78–80] and this triggered further theoretical work .[81–90]

It is now widely recognized that long-range intermolecular forces influence the rate and outcome of chemical reactions by trapping and/or orienting the reactants as they approach one another .[15,69,91–93] Perhaps the most spectacular case is provided by the Cl+HD reaction, where, as shown by Scouteris et al.,[93] the entrance valley plays a decisive role in the strong preference for the production of DCl.

However, little is known about long-range forces between reactive species. Most theoretical studies of chemical reactions have used interaction potentials specifically designed to reproduce the transition state region, paying relatively little attention to the Van der Waals region in the entrance channel, and to the possibility of formation of weakly bound pre-reactive complexes. The series of pioneering studies of halogen atoms and hydrogen halide molecules by Hutson and coll.[68,94,95] represent first attempts to address this problem at the semiempirical level. They also underscore a great need for the state-of-the-art *ab initio* potential energy surfaces for the Cl-HCl system to examine quality of the semiempirical model.

Probing the Cl+HCl complex experimentally has barely started. In 1995 Zhao et al. reported state-resolved rotational energy transfer in open shell collisions $Cl(^2P_{3/2})$+HCl.[70] More recently, in 1999, spectroscopical probe of the pre-reactive complex Cl-HCl by bond-specific photodissociation of $(HCl)_2$ has been studied by Liu et al.[69]

From the *ab initio* point of view the Cl+HCl reaction represents a serious challenge. If one neglects the spin-orbit (SO) coupling, the electronic ^{2}P ground state of the Cl atom is triply degenerate. Interaction with the HCl molecule removes this degeneracy, and, in general, three orthogonal states arise. Two of them are of the same ^{2}A′ reflection symmetry, and correspond to two orthogonal assignments of the five Cl 3p electrons: $p_x^2p_yp_z^2$ and $p_x^2p_y^2p_z$, with p_z and p_y orbitals lying in the Cl-H-Cl plane. The remaining orthogonal state is of the ^{2}A″ reflection symmetry, and corresponds to the $p_xp_y^2p_z^2$ assignment of the Cl free atom with p_x othogonal to the triatomic plane. For the collinear configuration of the atoms there are a non-degenerate $^2\Sigma^+$ state and a doubly degenerate $^2\Pi$ state. The latter is related to the singly occupied orbital of the Cl monomer perpendicular to the HCl bond axis. On bending the Cl-HCl complex, the $^2\Sigma^+$ state correlates with one of A′ symmetry, whilst the $^2\Pi$ state splits into one state of the A′ symmetry and another of the A″ symmetry.

At long range, the $^2\Pi$ potential energy surface (PES) of the collinear Cl-HCl complex lies lower in energy than the $^2\Sigma^+$ PES. This is because the singly occupied p orbital of the $^2\Pi$ state is perpendicular to the ClHCl molecular axis, so that the p orbital pointing towards the positively polarised H in HCl is doubly occupied, giving rise to a more favourable concerted dipole-quadrupole and quadrupole-quadrupole interactions, than does the converse ($^2\Sigma^+$) arrangement of the singly and doubly occupied orbitals.[68] However, in the transition state region for the reaction, the $^2\Sigma^+$ PES lies lower in energy than the $^2\Pi$ PES. This is because there is stronger exchange repulsion between the doubly occupied p orbital lying along the molecular axis ($^2\Pi$) and HCl, than is the case when the singly occupied p orbital lies along the molecular axis ($^2\Sigma^+$). As a result, there is a crossing of the $^2\Sigma^+$ and $^2\Pi$ PESs at some intermediate collinear geometry. For non-collinear geometries, this real crossing becomes avoided, producing a conical intersection between the 1A′ and 2A′ (hereafter we omit the superscript of multiplicity). This situtation is very similar to the H_2 + F and H_2 + Cl reactive systems.[96,97] It is worthwhile to note, that other crossings are expected at another collinear, nonreactive approach Cl···Cl-H. To the best of our knowledge, they have not been investigated so far.

Many electronic-structure investigations have been made of the Cl+H
Cl system. However, most of *ab initio* studies of the potential surfaces have considered only the ground adiabatic PES, and have concentrated primarily upon the transition-state region, with much less attention devoted to the Van der Waals region. The lowest adiabatic PES has been studied by Gonzales et al.[88] at the spin-projected second order Møller-Plesset (MP2) level of theory. Maierle et al.[90] evaluated all three states at the admittedly very modest multi-configurational self-consisted field (MCSCF) level of theory, as evidenced by their two-fold

underestimation of the barrier. The most advanced and refined calculations to date of all three PES by the restricted coupled cluster singles, doubles and non-iterative triples (RCCSD(T)) and multireference configuration interaction (MRCI) treatments are those of Dobbyn et al.[87] However, even these authors composed the global potential by combining the fitted *ab initio* surface with empirical long range and short range potentials of Ref.[68]

Indeed, the only information on the Van der Waals region so far comes from Dubernet and Hutson.[68] They combined the multipole-expanded electrostatic potentials with the semiempirical Ar-Cl(^{2}P) and Ar-HCl potentials, from which they extracted only the appropriate coefficients.[68] This simple but ingenious approach provided the three semiempirical adiabatic states which indicated the presence of a well region sufficient to support bound states. They also estimated the spectral range where the stretching and bending frequencies should occur. Unfortunately, no experimental spectra of this complex have yet been detected. The empirical surfaces of Dubernet and Hutson have been widely used in reactions not involving chlorine,[94,95] but the *ab initio* verification has never been done.

The aim of our work is to calculate PESs of the Cl+HCl reaction in the Van der Waals region, by using the state of the art *ab initio* technology. By contrast with the previous work, we attempt to evaluate the three PES only in the region of weak interaction, to achieve the highest accuracy possible, while skipping the region of strong interaction and of transistion state. Such a focal approach enables us to summon all our expertise regarding the *ab initio* calculations of intermolecular forces, in particular about basis set requirements, removal of a basis set superposition error (BSSE), level of correlation treatment, and size consistency.[16,17] We use the supermolecular approach within the (RCCSD(T)) formalism, and very efficient augmented correlation consistent polarized basis sets supplemented with bond functions to ensure saturation of basis set and highest level of electron correlation treatment. We generate the adiabatic PESs by using the RCCSD(T) method. Since the RCCSD(T) is bound to fail in the regions of curve crossings, we carry out parallel calculations at the MRCI level of theory. In particular, we evaluate non-adiabatic couplings between adiabatic states at the MRCI level, and then we use the results to transform adiabatic PESs to the diabatic basis.

5.3 Computational methods

5.3.1 Geometries and basis sets

The Cl-HCl complex is described in Jacobi coordinates (R, θ). The R variable denotes the distance between the center of mass of the HCl monomer and the Cl atom, and θ denotes the angle between the $\vec{R}$ vector and the HCl bond axis. $\theta = 0°$ corresponds to the Cl$\cdots$H-Cl collinear sequence. The HCl monomer was kept rigid during calculations and its interatomic separation was set at $r = 1.275$ Å. This value is slightly different from the bond length given by Huber and Herzberg[98] which is 1.27455 Å. The axis of the system of coordinates are shown on Figure refcl2h-fig1ab. The origin of the system is placed at the center of mass of the HCl molecule. The bond axis of the HCl molecule was set along the y axis of the coordinate system and the x axis as perpendicular to the triatomic plane.

Calculations of the potential energy surfaces were performed with the augmented correlation-consistent polarized valence-triple-zeta (aug-cc-pvTZ) basis function set of Dunning et al. [99–101] supplemented with an additional set of bond functions. The set of bond functions [3s3p2d] of Tao and Pan ,[36] with the exponents:sp 0.9, 0.3, 0.1;d 0.6, 0.2, was used. Bond functions were

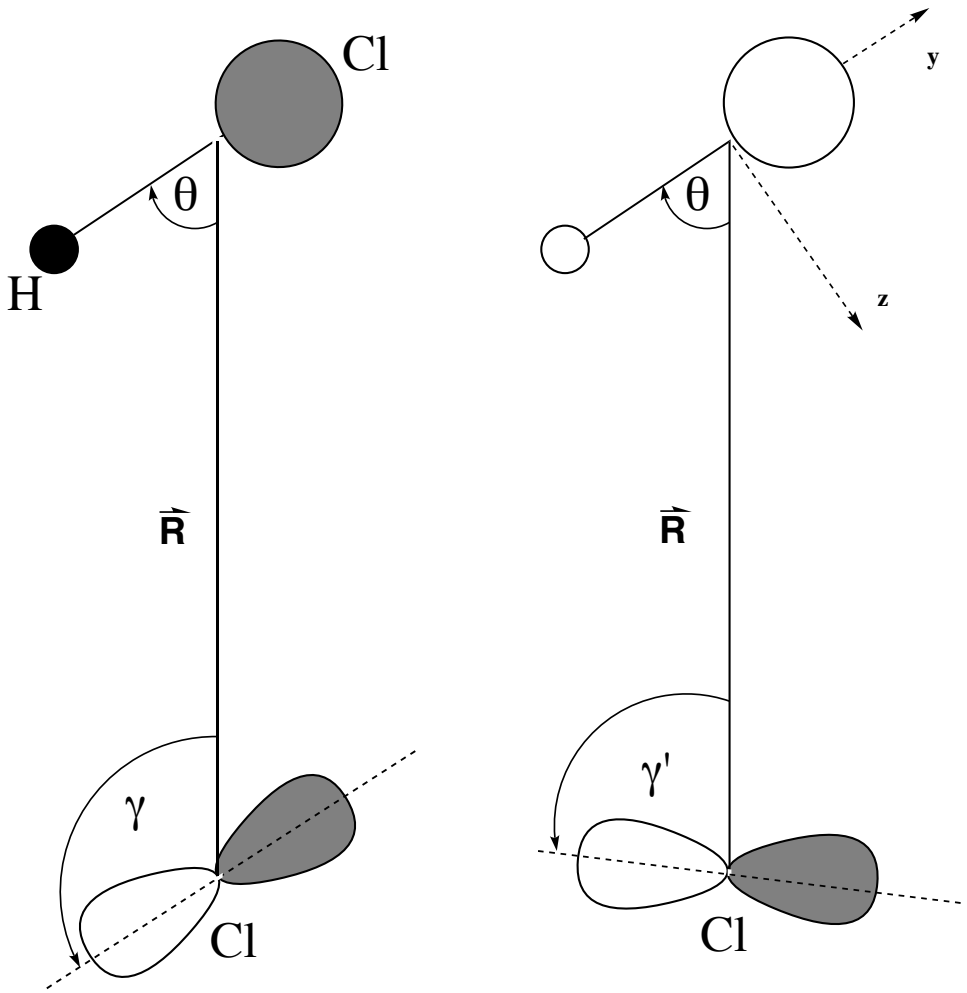

Figure 5.1: The example of the orientation of the singly occupied orbital (a) in the dimer, and (b) in the monomer.

centered in the middle of the distance of the Cl atom from the center of mass of the HCl molecule. The basis set is denoted as aug-cc-pvTZ+(332). It was shown to be both effective and economical for a number of Van der Waals complexes which included rare gas atoms.[23,24,102]

5.3.2 *Ab initio* adiabatic potential energy surfaces

All calculations reported in this paper were performed using MOLPRO package.[53] The supermolecular method was used in calculations of three adiabatic potential energy surfaces. This method derives the interaction energy as the difference between the energies of the dimer AB and the monomers A and B

$$\Delta E^{(n)} = E_{AB}^{(n)} - E_A^{(n)} - E_B^{(n)} \tag{5.1}$$

The superscript (n) denotes the level of *ab initio* theory. In this paper the RCCSD(T) method [51,52] is used, because of its ability to recover practically all correlation contributions for the Van der Waals interaction. *Lege artis*, previous studies employed RCCSD(T) only for the lowest states of each symmetry, $1A'$ and $1A''$. The single reference coupled cluster techniques are not able to calculate globally valid $2A'$ PES, the second state of the A' symmetry, nor give any information about the nonadiabatic couplings between the $1A'$ and $2A'$ states. However, locally in the Van der Waals region, where the A' states are mostly well separated, the excited $2A'$ state can be adequately represented by a single Slater determinant. Indeed, according to Szalay and Gauss, an excited state described by a single-electron promotion to a singly occupied open-shell (from one p orbital to another, orthogonal p orbital) should be amenable to single-reference teatment.[103] To make sure that one-determinantal reference is valid, we performed the diagnostic of the T_1 quantity.[104,105] T_1 is related to the norm of singles amplitude vector. The T_1 value seldom exceeded the threshold of 0.02 which confirmed that for almost whole Van der Waals region one-determinantal reference worked.

If the *ab initio* theory is size-consistent, such as the RCCSD(T)[51] method is, to avoid BSSE it is enough that all of the components in Eq. 5.1 are calculated in the whole basis set of the dimer. This is equivalent to the counterpoise (CP) correction method of Boys and Bernardi .[50,106,107] The CP procedure is straightforward as long as one considers single non-degenerate electronic states for the dimer and for the monomers. However, in the case of degenerate open-shell monomers the procedure becomes more involved. This is because the degeneracy of the monomer energies is removed by the effect of partner's orbitals, and each dimer state is related to a different CP monomer state. If the dimer and CP monomer states are of different electronic symmetry, as it is, for example, for He(^{1}S)+NO($X^2\Pi$)[25] or Ar(^{1}S)+OH($X^2\Pi$)[26] systems, one can still easily match, by using symmetry, the proper monomer energy with the dimer energy. If not, the situation is more complex, as will be described below.

Some calculations of the state energies and the calculations of the $1A'$- $2A'$ mixing angle were performed at the MRCI level of theory. These calculations began with the determination of the state-averged CASSCF orbitals which assumed the Cl-moiety-related orbitals as follows: the 1s orbital frozen, the 2s and 2p orbitals doubly occupied, and the 3s and 3p orbitals active. The state averaging included all three states: $1A'$, $2A'$ and $1A''$. Subsequent MRCI calculations employed the full valence CI wavefunction with respect to the CASSCF active space. Additional tests, which augmented the active space with the σ^* orbital, were also performed, but revealed no significant effect. The MRCI was a 2-state calculation.

5.3.3 Approximate counterpoise correction for adiabatic states

The proper counterpoise-corrected (CP) monomer state to be used in Eq. 5.1 is when the orientation of the singly occupied orbital in the Cl monomer is identical to that as in the Cl-HCl dimer. This is easy to ensure for the $1A''$ state, but not necessarily for the $1A'$ and $2A'$ states. The difference between orbital orientations in the dimer and the open-shell monomer is schematically depicted in Fig.1. The orientation of the singly occupied orbital depends on the variables (R, θ). There are arrangements where the difference between the dimer and the Cl monomer orientations is small, but there are also geometries where it is difficult to decide which of the Cl monomer energies has to be chosen for proper removal of the BSSE. To alleviate the difficulty Alexander, in his paper on B(^{2}P)-H_2[108] system, proposed: first to transform adiabatic energies, calculated with dimer centered basis set (DCBS), to diabatic ones, and next calculate interaction energy for diabats only.

Since only adiabatic states diagonalize the hamiltonian, and the diabatization procedure is neither unique nor exact, we belive that one should have an alternative procedure for removal of BSSE at the adiabatic level. Hence in this paper we calculated CP-corrected interaction energy at the adiabatic level. To this end we obtained the Cl monomer energies which at the RHF level correspond to the orientation of the dimer orbital defining the $1A'$ and $2A'$ states. First, the ground CP state of A' symmetry was obtained. The second A' state was achieved by rotation of the singly occupied orbital in the RHF reference wavefunction to the orthogonal orientation in the triatomic plane. RHF calculations were followed by RCCSD(T) calculations. To calculate adiabatic interaction energies for both of the A' states we "rotated" the Cl monomer RCCSD(T) energies to be related to the same orientation of the singly occupied orbital as in the dimer. The definition of the orientation angle γ for the $1A'$ dimer and γ' for the monomer are shown in Fig.1a and Fig.1b, respectively. The rotation was performed according to Eq.(11a) and Eq.(11b) of Ref.[108] It should be noted that, strictly speaking, such a rotation introduces coupling between monomer CP states, so the Cl monomer energies after rotation are not rigorously adiabatic. As long as difference $\gamma - \gamma'$ is small we can neglect the nondiagonal term. The Cl monomer energies for CP corrected potentials were calculated as follows

$$E^{Cl}_{1A'}(\gamma) = \cos^2(\gamma - \gamma')\, E^{Cl}(\gamma') + \sin^2(\gamma - \gamma')\, E^{Cl}(90^\circ - \gamma') \tag{5.2}$$

$$E^{Cl}_{2A'}(90^\circ - \gamma) = \sin^2(\gamma - \gamma')\, E^{Cl}(\gamma') + \cos^2(\gamma - \gamma')\, E^{Cl}(90^\circ - \gamma') \tag{5.3}$$

and the energy $E^{Cl}(\gamma')$ denotes the RCCSD(T) Cl monomer energy corresponding to the orientation of the RHF singly occupied orbital described by angle γ'. The $\gamma - \gamma'$ difference was calculated from the orientations of the orbitals at the RHF level. The γ angle for the dimer corresponds to the mixing angle in the adiabatic-diabatic transformation. Finally, the three CP corrected adiabatic RCCSD(T) potentials for Cl-HCl complex are obtained from the formulae

$$V_{1A'} = E^{Cl-HCl}_{1A'} - E^{Cl}_{1A'} - E^{HCl} \tag{5.4}$$
$$V_{2A'} = E^{Cl-HCl}_{2A'} - E^{Cl}_{2A'} - E^{HCl} \tag{5.5}$$
$$V_{1A''} = E^{Cl-HCl}_{1A''} - E^{Cl}_{1A''} - E^{HCl} \tag{5.6}$$

To reveal what effect has the approximate CP procedure on the interaction energy, we compared the results calculated with the rotated monomers energies and without such a rotation, for

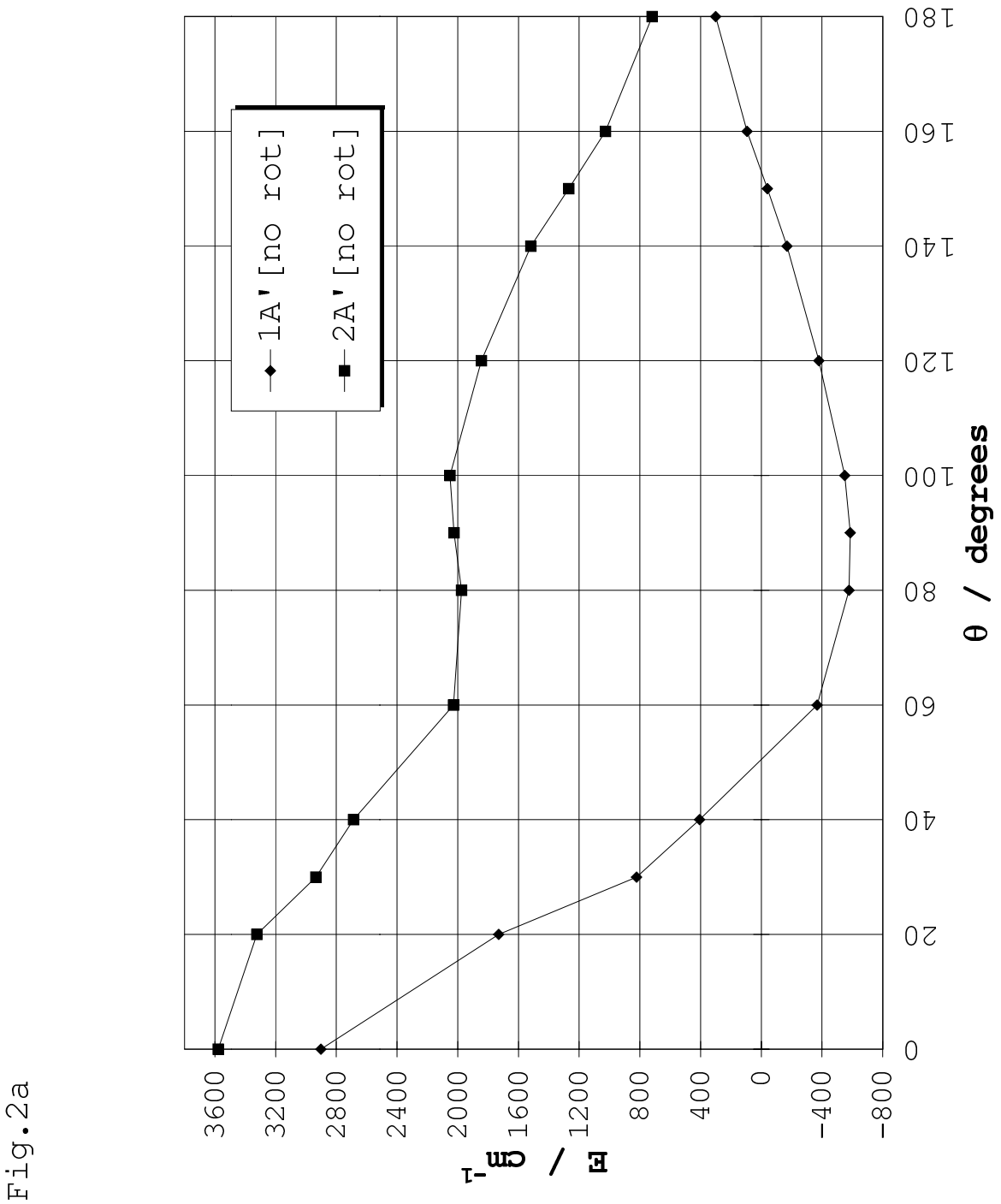

Fig.2a

Figure 5.2: The anisotropies of A′ states for $R = 3.0$ Å obtained directly (without rotation of Cl monomer energies). Energy in cm^{-}1.

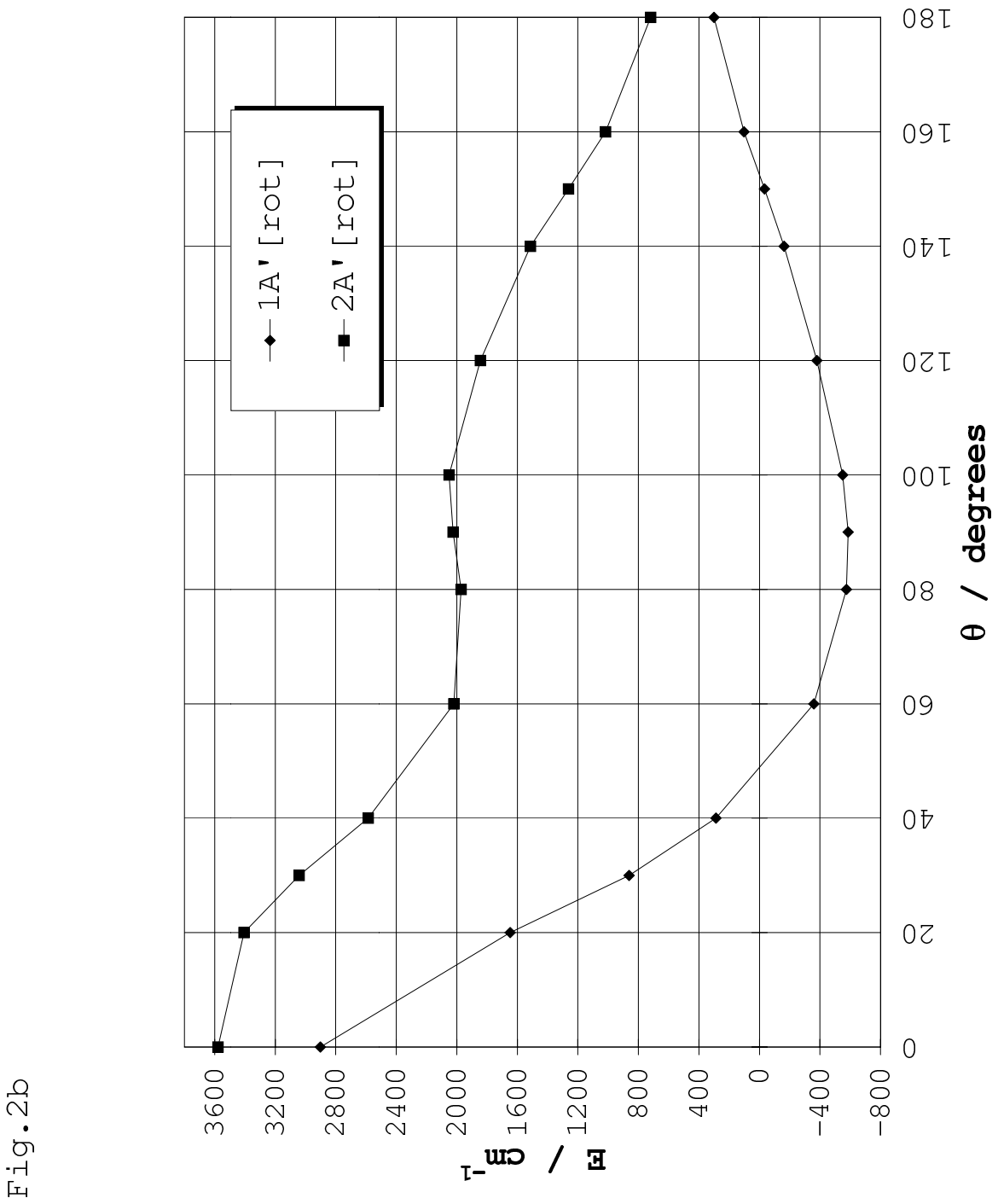

Figure 5.3: The anisotropies of A′ states for $R = 3.0$ Å using rotated Cl monomer energies. Energy in cm^{-}1.

$R = 3.0$ Å. Figure 5.2 shows anisotropy for both A′ states obtained directly and Figure 5.3 with rotation of the monomers.

The curves obtained without rotation are less smooth than the curves for rotated monomer energies. Quantitative differences are small, but this example shows that the rotation procedure improves the quality of the adiabatic PESs. On the other hand the BSSE itself is not small and must be removed.

5.4 Adiabatic-diabatic transformation

The diabatic surfaces provide more convenient representations for simulations of the Van der Waals spectra of the system. These potentials contain information about couplings between the adiabatic wavefunctions of the same symmetry. The adiabatic-diabatic transformation yields diabatic states for which the non-adiabatic coupling matrix elements approximately vanish. The diabatic states are obtained by an unitary orthogonal transformation of adiabatic states[108,109]

$$\begin{bmatrix} \Psi_1^d \\ \Psi_2^d \end{bmatrix} = \begin{bmatrix} \cos\gamma & \sin\gamma \\ -\sin\gamma & \cos\gamma \end{bmatrix} \begin{bmatrix} \Psi_1^a \\ \Psi_2^a \end{bmatrix} , \tag{5.7}$$

where the transformation angle γ depends on the nuclear coordinates. The resulting diabatic wavefunctions are no longer eigenstates of the electronic Hamiltonian. The Hamiltonian in the diabatic (p_x, p_y, p_z) basis is not diagonal and the matrix elements are

$$\begin{aligned} H_{11} &= \cos^2\gamma V_{1A'} + \sin^2\gamma V_{2A'} \\ H_{22} &= \sin^2\gamma V_{1A'} + \cos^2\gamma V_{2A'} \\ H_{12} &= (V_{1A'} - V_{2A'})\cos\gamma\sin\gamma \end{aligned} \tag{5.8}$$

The fourth diabatic state, H_{33}, is exactly equal to the 1A″ adiabatic state.

The transformation angle γ, the so-called 'mixing angle', may be defined as the angle between the vector of singly occupied p orbital and the $\vec{R}$ vector. It is shown in Fig.1a. This angle is a function of Jacobi coordinates of the system, and depends on the orientation of the HCl molecule. Within a two-state model the mixing angle can in principle be obtained by numerical integration of the non-adiabatic coupling matrix elements (NACMEs) using the relation

$$\frac{\partial\gamma\,(R,\theta)}{\partial q} = \left\langle 1A' \left| \frac{\partial}{\partial q} \right| 2A' \right\rangle . \tag{5.9}$$

This is quite computationally demanding procedure, which suffers from the fact that the NACMEs are strongly varying functions of the geometry and have poles at the conical intersections. Also, in real systems the integration is not entirely path independent, due to the admixture of further states.[110] Eq. 5.9 is only valid for the two-state model, and diabatization procedure is approximate in any case for polyatomic molecules. Therefore, we used a less expensive method which determines the mixing angle directly with reasonably accuracy.[111] This method is based on the transition angular momentum connecting the 1A″ state with two states of the A′ symmetry. We calculated matrix elements of the $\hat{L}_y$ operator at the MRCI(SD) [112,113] level of theory within the same basis set (cf. Sec. II A) and determined the mixing angle from the following formula

$$\gamma = \tan^{-1}\left[\frac{\left|\left\langle 1A' \left| \hat{L}_y \right| 1A'' \right\rangle\right|}{\left|\left\langle 2A' \left| \hat{L}_y \right| 1A'' \right\rangle\right|}\right] \tag{5.10}$$

The γ angle from the MRCI calculations was subsequently used to transform the RCCSD(T) surfaces. The relief map of the γ^{MRCI} mixing angle is shown in Fig 5.4.

This figure clearly shows three regions where the A′ states avoid crossing each other, and the points where the Σ^+ and Π states cross. These are the regions where the mixing is the strongest and the angle in Eq. 5.7 reaches 45°. The conical intersection occurs at the reactive side, Cl· · ·H-Cl, $\theta = 0°$, $R \approx 3.0$ Å, but also at the "nonreactive" side H-Cl· · ·Cl, $\theta = 180°$, at two distances, 3.25 and 6.0 Å. These intersections are related to the crossings of Σ^+ and Π, which switch there. The "reactive" conical intersection has been known for a long time. The "nonreactive" one has not been reported previously. In general case, γ from different methods are not the same, since the PESs differ. For the Cl-HCl complex, however, the γ^{MRCI} and γ^{RHF} were found remarkably close except for the region near the H-Cl· · ·Cl collinear arrangement, cf. the plot of the difference $\gamma^{MRCI} - \gamma^{RHF}$, Fig. 5.5. The $\gamma^{RCCSD(T)}$, which was not explicitely evaluated, is expected to be even closer to the γ^{MRCI} angle.

We expect that for the systems for which the anisotropy of the PES is qualitatively correctly reproduced at the SCF level of theory this rule should hold. For such a system the anisotropy is driven by electrostatic and induction interactions. Fig.4 reveals that there are significant differences between γ^{MRCI} and γ^{RHF} only in the region where the 2A′ potential exhibits a minimum. This is the region near the conical intersection, and we assume that the RHF approach followed by RCCSD(T) procedure is not valid here. It should be stressed that adiabats of the A′ symmetry could not be described properly in this region as they become nearly degenerate.

5.5 Fits

The RCCSD(T)/aug-cc-pvTZ+(332) results for the $V_{1A'}$, $V_{2A'}$ and $V_{1A''}$ potentials were approximated by an analytic expression composed of the short-range term (V_{sh}), and the asymptotic long-range part (V_{as}):[24,114]

$$V(R,\theta) = V_{sh}(R,\theta) + V_{as}(R,\theta) \tag{5.11}$$

where

$$V_{sh}(R,\theta) = G(R,\theta)\, e^{d(\theta) - Rb(\theta)} \tag{5.12}$$

Terms $d(\theta)$ and $b(\theta)$ were expanded in normalized Legendre polynomials $P_l^0(\cos\theta)$, respectively, to the order L_d and L_b, and term

$$G(R,\theta) = \sum_{l=0}^{L_G} \sum_{i=0}^{3} g_{il} R^i P_l^0(\cos\theta) \tag{5.13}$$

to the order of L_G. The long-range part was chosen to be a damped asymptotic expansion that included both induction (R^{-4}) and dispersion (R^{-6} and higher) components

$$V_{as}(R,\theta) = \sum_{n=4}^{10} \sum_{l} f_n(Rb(\theta)) \cdot \frac{C_{nl}}{R^n} P_l^0(\cos\theta) \tag{5.14}$$

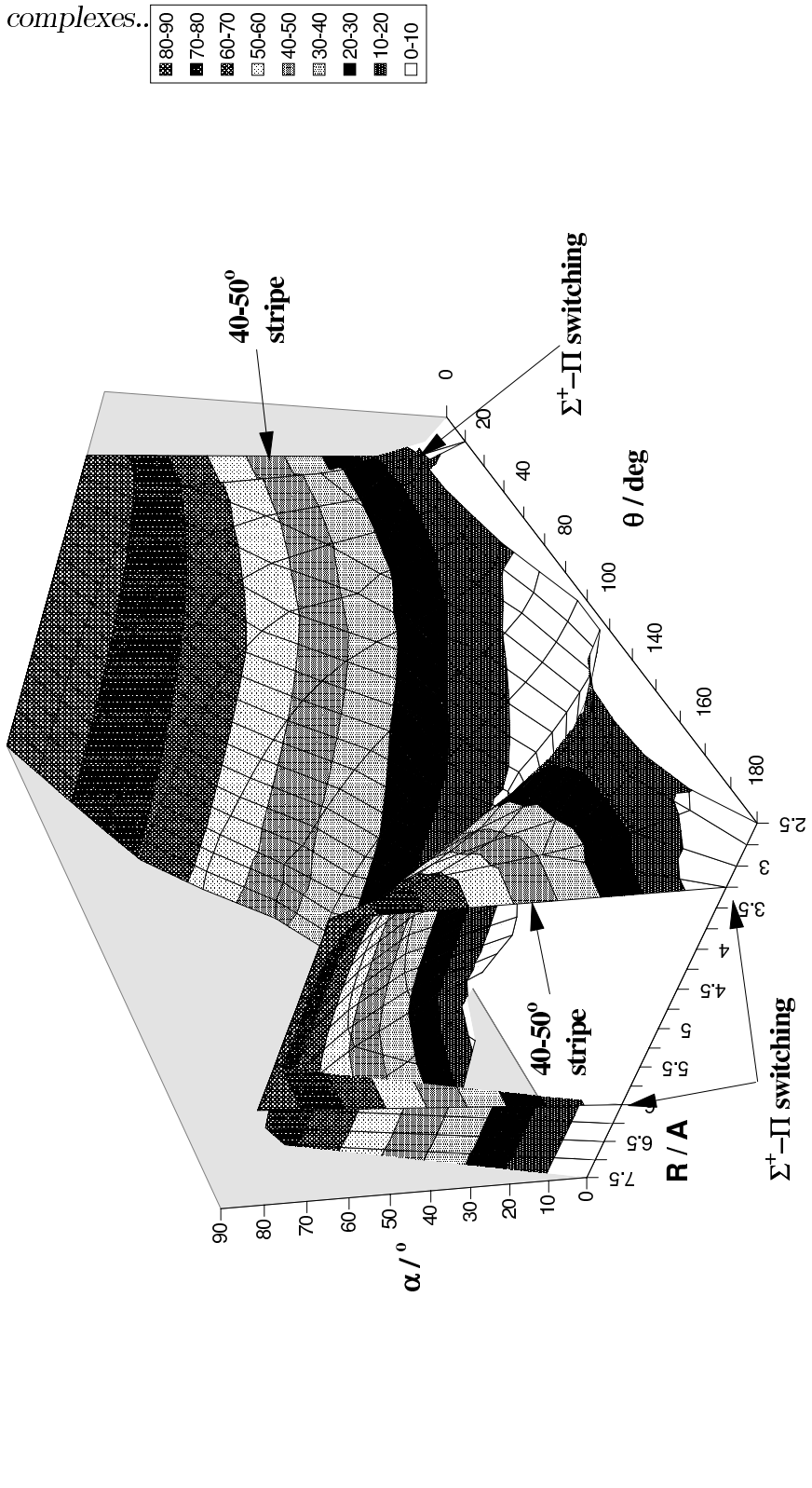

Figure 5.4: The relief map of the geometric dependency of the mixing angle γ calculated at the MRCI level. Angle in degrees.

Fig.4

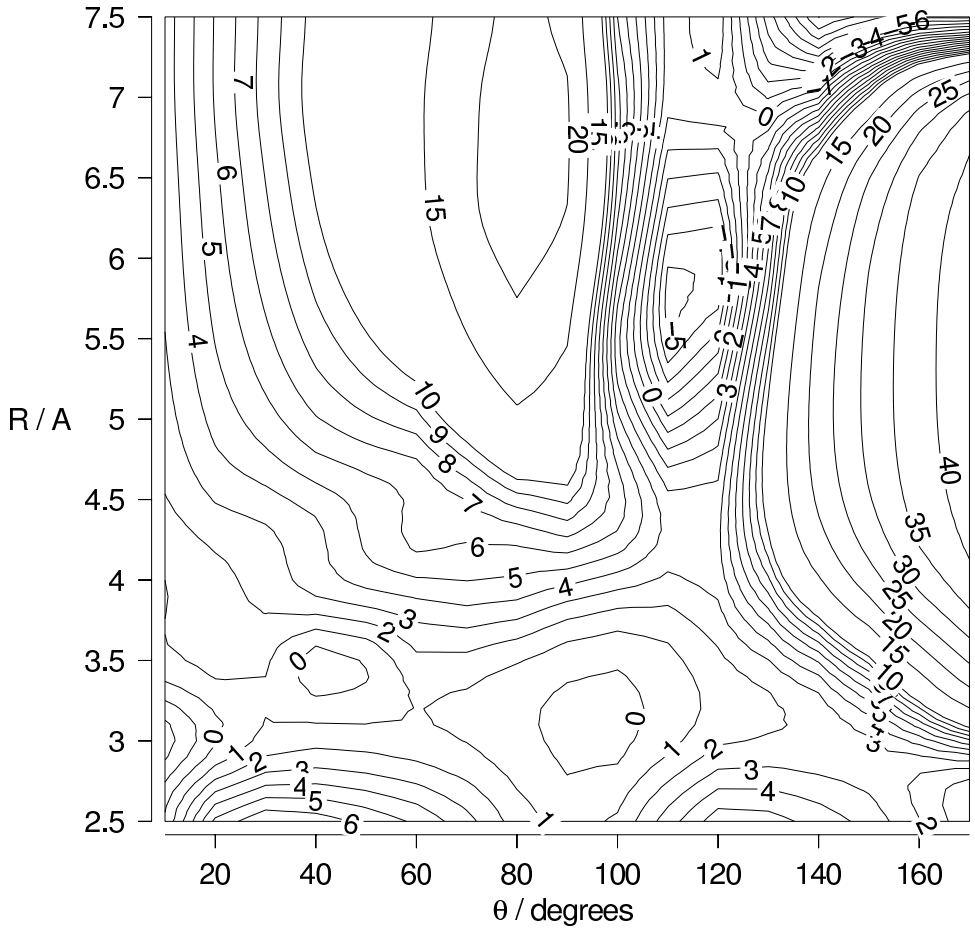

Figure 5.5: Contour of the $\gamma^{MRCI} - \gamma^{RHF}$ difference. Angle in degrees.

where f_n function was the damping function of Tang-Toennies[32]

$$f_n(x) = 1 - e^{-x} \sum_{k=0}^{n} \frac{x^k}{k!} \tag{5.15}$$

Van der Waals coefficients start from $C_{4,0}$ and end at $C_{10,0}$. In the case of the non-diagonal diabatic matrix element, H_{12}, we used associated Legendre polynomials of the second rank $P_l^2(x)$ in Eq. 5.13, to ensure correct behaviour at the colinear arrangements. The Eq. 5.14 for the long-range part was slightly modified, and included also the $P_l^2(x)$ polynomials:

$$V_{as}^{H_{12}}(R,\theta) = \sum_{n=4}^{10} f_n(Rb(\theta)) \cdot \frac{C_{nn-2}}{R^n} P_{n-2}^2(\cos\theta) \tag{5.16}$$

The errors of the fits in the Van der Waals region and the long range do not exceed 1% generally. There were errors of several percents for some geometries depending on the surface. In the highly repulsive area, for very small values of the R distance, errors of fitting may exceed 10%. Above fits were obtained for purpose of graphical representation of potential surfaces.

5.6 Results and discussion

5.6.1 Topology of adiabatic potentials

Contours of fits of the 1A′, 2A′ and 1A″ adiabats are shown, respectively, in Figs. 5.6, 5.7,and 5.8.

The 1A′ surface has two minima. The global minimum occurs for the T-shaped geometry ($R = 3.08$ Å, $\theta = 88°$ and $D_e = 600.4$ cm^{-1}). There is also a local minimum at the collinear geometry ($R = 3.90$ Å, $\theta = 0°$ and $D_e = 438.2$ cm^{-1}). The HCl$\cdots$Cl geometry corresponds to a saddle point at $R = 3.73$ Å , and the interaction energy at the saddle point is elevated 425 cm^{-1} above the global minimum.

The topology of the 2A′ potential shows only one minimum at the collinear geometry ($R = 3.68$ Å, $\theta = 180°$ and $D_e = 126.0$ cm^{-1}). The region for the angular variable θ less than 60° is repulsive. The attractive area of this PES occures when the free Cl atom approaches the HCl molecule from the chlorine side.

The 1A″ potential has two collinear minima. The minimum for $\theta = 0°$ is the same as collinear minimum of the 1A′ surface. The minimum for the HCl$\cdots$Cl arrangement is characterized by $R = 3.72$ Å and $D_e = 180.0$ cm^{-1}.

5.6.2 Diabatic potentials

The *ab initio* diabatic PESs were constructed using energies from the RCCSD(T) calculations and the mixing angle from the MRCI(SD) method. Figs. 5.9, 5.10, 5.11 represent respectively contours of the H_{11}, H_{22} and H_{12} diabatic PESs.

The H_{11} diabat reveals only one minimum for the T-shaped arrangement of the atoms. The position of this minimum is at $R = 3.07$ Å , $\theta = 92°$, and the well depth is 602 cm^{-1}. The region in the neighborhood of the collinear Cl$\cdots$H-Cl geometries are in general repulsive.

The H_{22} and H_{33} diabats have two collinear minima, for Cl$\cdots$H-Cl and H-Cl$\cdots$Cl arrangements. Table 5.6 lists the locations and well depths.

Fig.5a

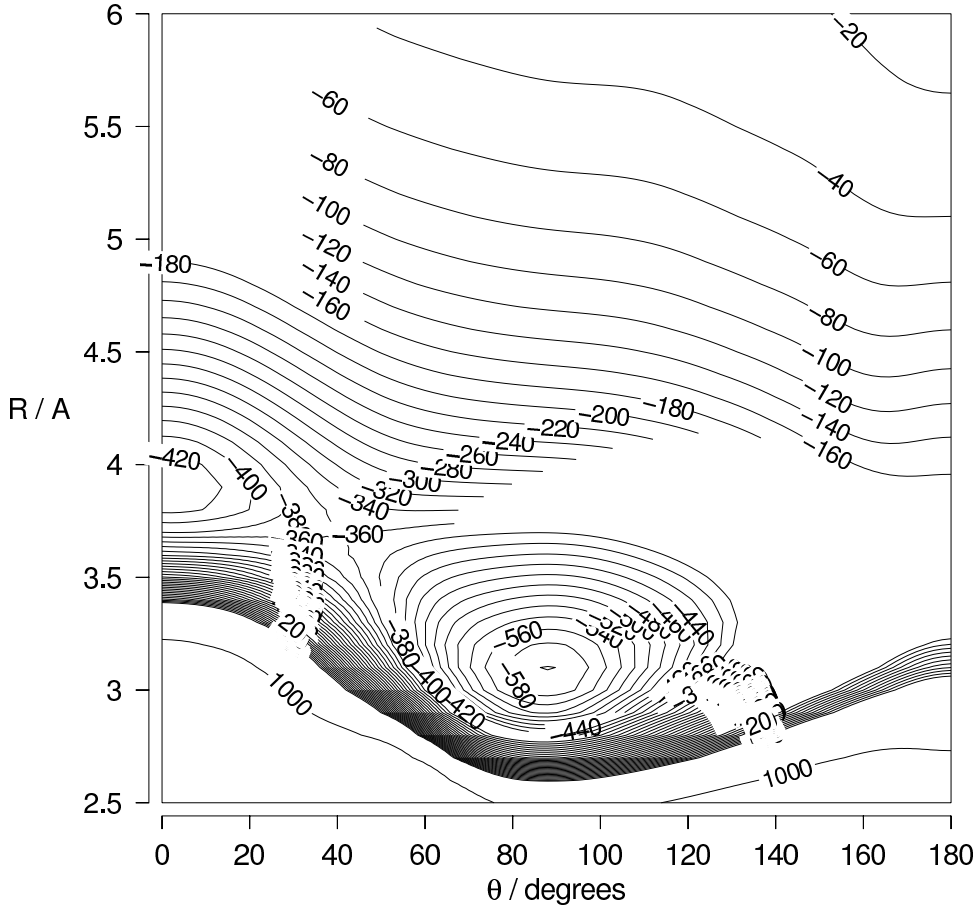

Figure 5.6: Contour of the fit of the 1A′ RCCSD(T) surface. Energy in cm^{-1}.

Fig.5b

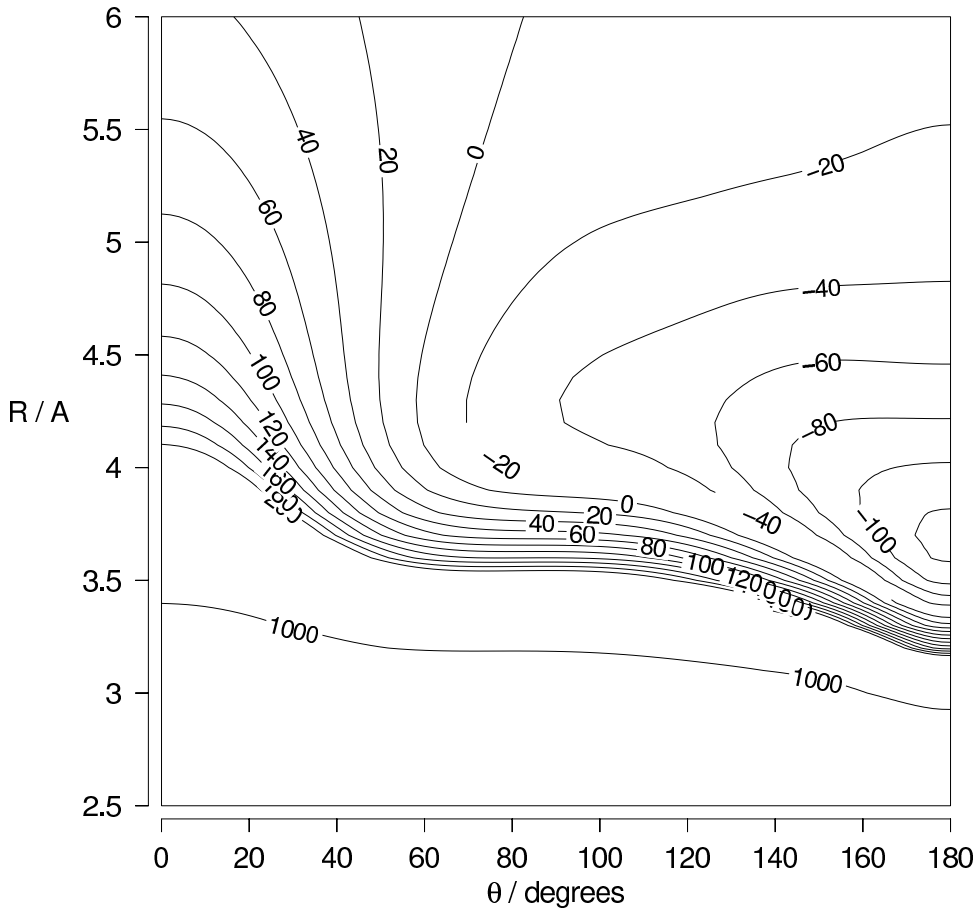

Figure 5.7: Contour of the fit of the 2A′ RCCSD(T) surface. Energy in cm^{-1}.

Fig.5c

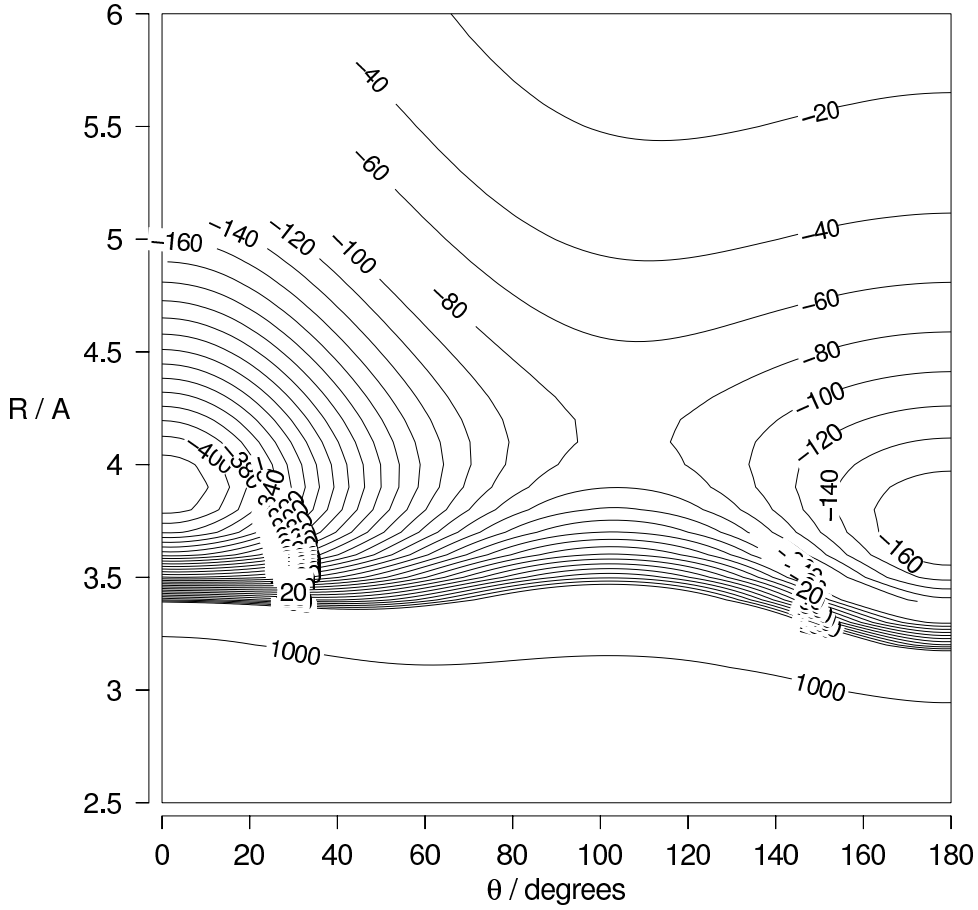

Figure 5.8: Contour of the fit of the 1A″ RCCSD(T) surface. Energy in cm^{-1}.

Fig.6a

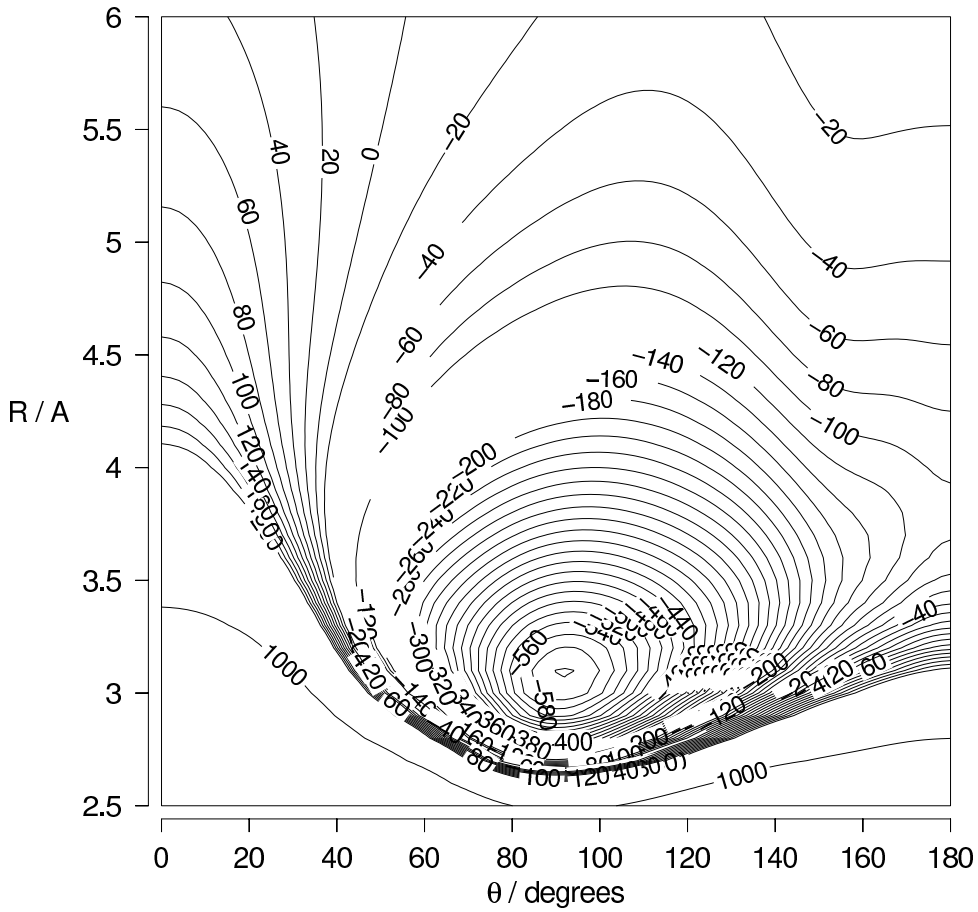

Figure 5.9: Contour of the fit of the 1A′ RCCSD(T) surface. Energy in cm^{-1}.

Fig.6b

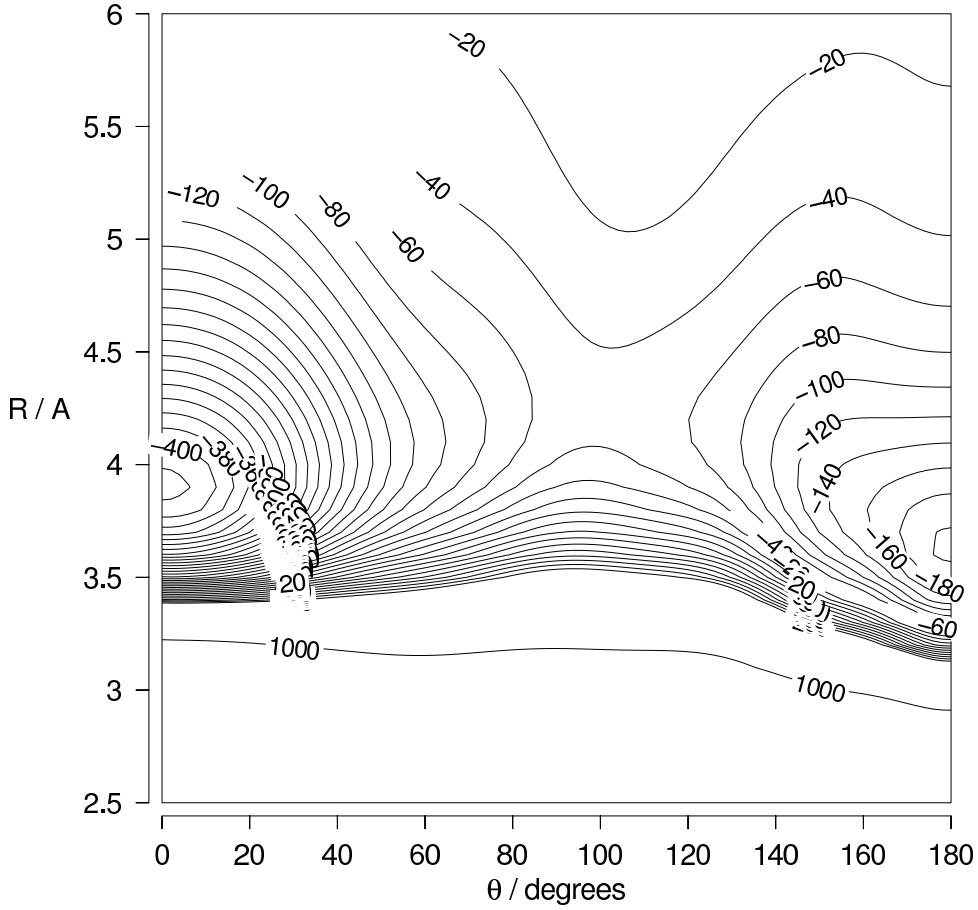

Figure 5.10: Contour of the fit of the 2A′ RCCSD(T) surface. Energy in cm^{-1}.

Fig.6c

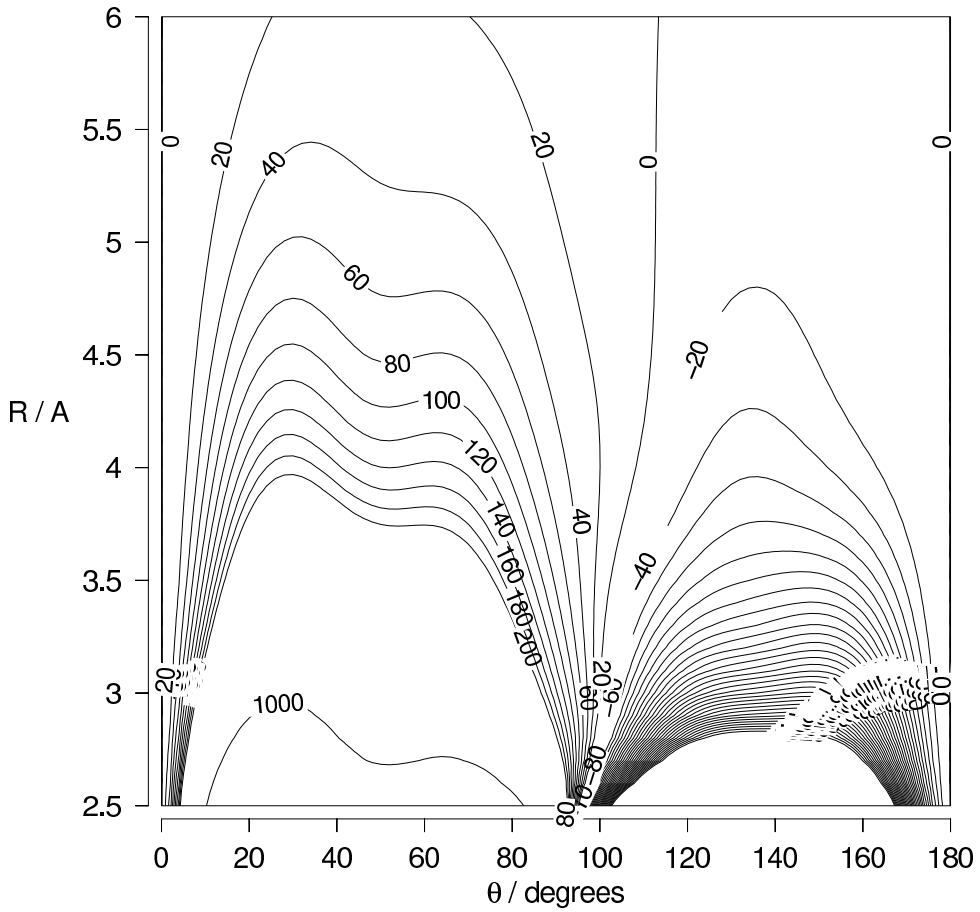

Figure 5.11: Contour of the fit of the 1A″ RCCSD(T) surface. Energy in cm^{-1}.

The non-diagonal term of the hamiltonian in the diabatic basis, H_{12}, has a positive part for geometries with $\theta < 90°$ and a negative region for $\theta > 90°$. The H_{12} diabat vanishes for the collinear arrangements of the atoms.

To qualitatively analyze the anisotropy of the diabatic potentials, we modeled the electrostatic interaction for the H_{11}, H_{22} and H_{33} diabats. The Cl-HCl complex was treated as the diatom-diatom system, so the position of the singly occupied orbital of the Cl atom was described by two angles (θ_a,ϕ). The orientation of the HCl diatom was described by θ_b angle. The electrostatic model accounts for the dipole-dipole, dipol-quadrupole terms, and the quadrupole-quadrupole interaction components. Since the Cl atom has no dipol moment, we used the following formulae:[115]

$$V\left(R,\theta_a,\theta_b,\phi\right) = V_{d_b-\Theta_a} + V_{\Theta_a-\Theta_b} \tag{5.17}$$

where

$$V_{d_i-\Theta_j}\left(R,\theta_i,\theta_j,\phi\right) = \frac{3}{2}\frac{d_i\Theta_j}{R^4}\left(\cos\theta_i\left(3\cos^2\theta_j - 1\right) + \sin\theta_i \sin 2\theta_j \cos\phi\right) \tag{5.18}$$

$$\begin{aligned} V_{\Theta_i-\Theta_j}\left(R,\theta_i,\theta_j,\phi\right) = \frac{3}{4}\frac{\Theta_i\Theta_j}{R^5}(1 - 5\cos^2\theta_i - 5\cos^2\theta_j + \\ 17\cos^2\theta_i cos^2\theta_j + 2\sin^2\theta_i \sin^2\theta_j \cos^2\phi \\ +16\sin\theta_i\cos\theta_i\sin\theta_j\cos\theta_j\cos\phi) \end{aligned} \tag{5.19}$$

and $i \neq j \in \{a,b\}$

The value Θ_a of the quadrupole of the Cl atom was set at 2.214 DÅ , and d_b and Θ_b of HCl were equal 1.1996 D and 3.707 DÅ, respectively. The quadruple moment of HCl was taken at the center of mass. To obtain electrostatic models of the diabatic potentials we appropriately set the (θ_a, ϕ) pair of angles, i.e. for the H_{11} diabat we have (0,0) (singly occupied orbital along the R direction), for the H_{22} diabat-(90,0) (singly occupied orbital perpendicular to the R direction, and lying in the triatomic plane), for the H_{33} diabat-(90,90) (singly occupied orbital perpendicular to the triatomic plane). Note that the H_{33} surface is the same as the $1A''$ adiabat. Figs. 5.12, 5.13, 5.14 represent contours of the modeled electrostatics in the H_{11}, H_{22} and H_{33} diabats, respectively.

The electrostatic modeling correctly predicts the pattern for anisotropies of the long-range diabatic PESs. One may distinguish 3 regions related roughly to 3 forms: Cl···H-Cl, T-shaped and H-Cl···Cl. The electrostatic model predicts stabilization for T-shaped of the H_{11} diabat and stabilization for collinear forms of the H_{22} and H_{33} diabats. However, quantitatively the electrostatic model is poor unless the intermolecular distance becomes large.

5.6.3 Comparison of restricted and unrestricted approach

To reveal differences between the restricted and unrestricted coupled cluster methods we calculated, at selected points, the adiabatic interaction energies using both approaches. At first, we calculated the reference wavefunction at the RHF level of theory. Next, the RCCSD(T) or UCCSD(T)[51] method were used. Both calculations started with the RHF orbitals. The results are shown in Table 5.1 for $R = 4.25$ Å and $\theta = 90°$. The UCCSD(T) result for $2A'$ state is

Fig.7a

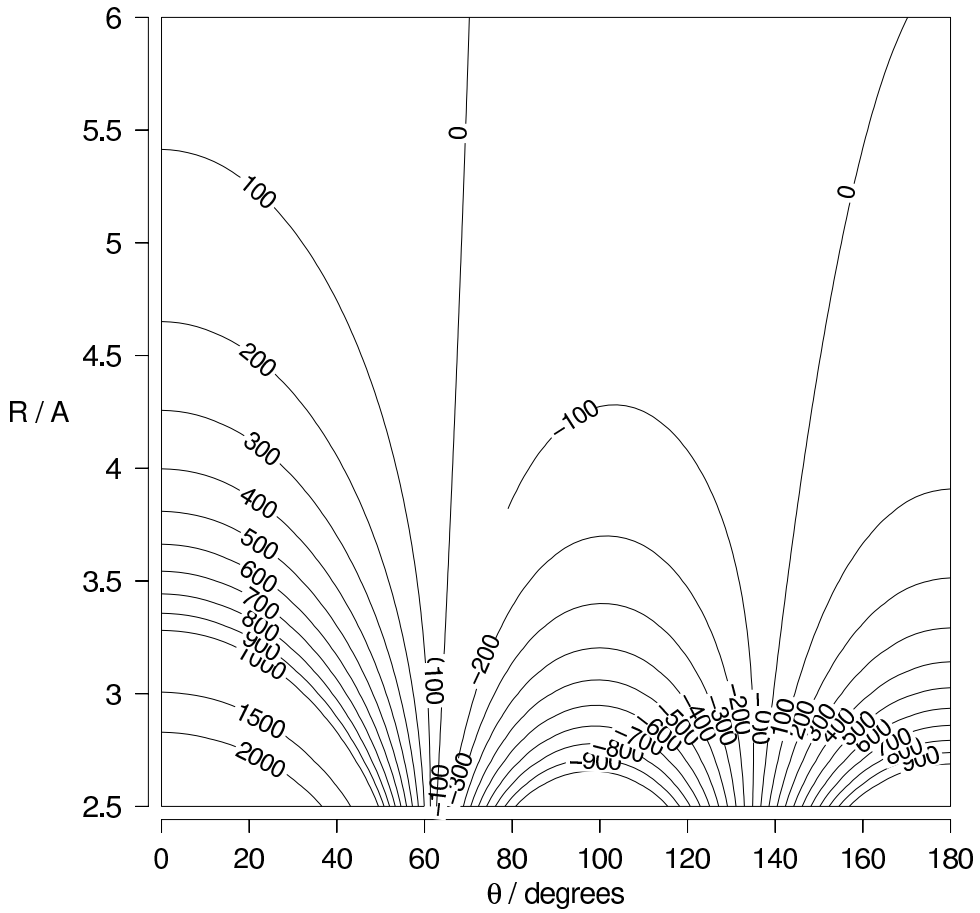

Figure 5.12: Contour of the electrostatic model of the H_{11} diabat. Energy in cm^{-1}.

Fig.7b

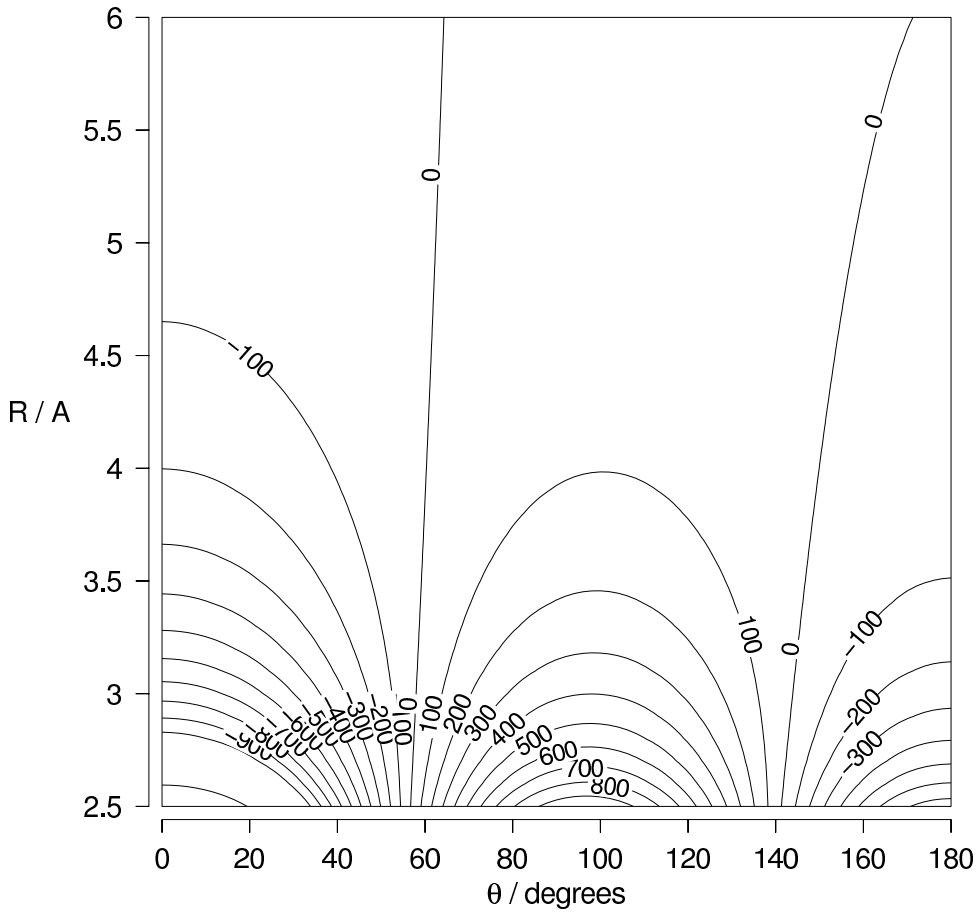

Figure 5.13: Contour of the electrostatic model of the H_{22} diabat. Energy in cm^{-1}.

Fig.7c

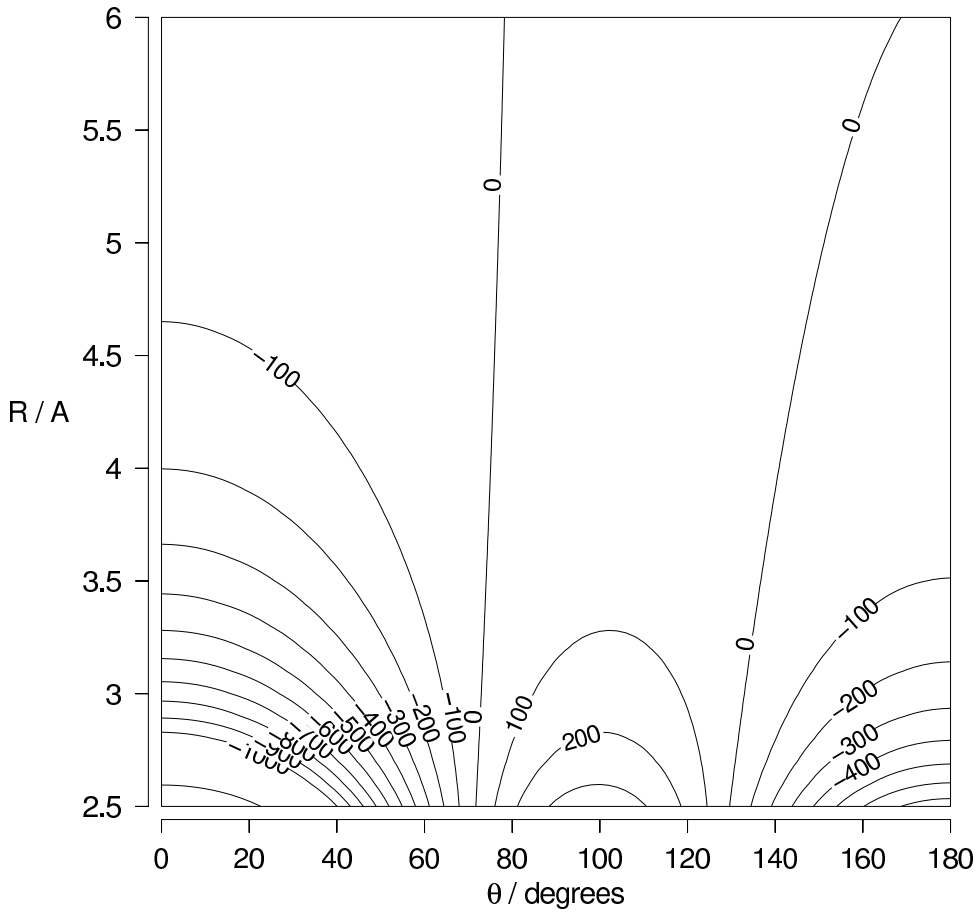

Figure 5.14: Contour of the electrostatic model of the H_{33} diabat. Energy in cm^{-1}.

not shown because of divergence of the UCCSD(T) calculations in this case. This comparison shows that both, restricted and unrestricted, approaches give similar results.

5.6.4 Role of bond functions

The role of bond function in intermolecular interaction calculations is to improve the description of the intermolecular electron correlation effect - the dispersion energy .[16,116] In order to elucidate the effect of bond functions, we calculated the cut through the 1A′ adiabat at $\theta = 90°$ without application of those functions. Fig. 5.15 shows how bond functions affect the values of the interaction energy. The global minimum of 1A′ is about 20% shallower than the result obtained with bond functions (586 cm^{-1}), and equals to 464 cm^{-1}.

The position of this minimum also changed to $R = 3.25$ Å. Bond functions move the position of the global minimum towards the center of mass of the HCl molecule. The effect of further extension of the correlation-consistent basis set was also checked. To this end, we performed calculations at two characteristic points: at ($R = 4.0$Å, $\theta = 0°$) - the Π-state minimum - and at ($R = 2.5$Å, $\theta = 0°$) - in the repulsive wall. Two basis sets were used: an aug-cc-pvQZ+(33221) basis [(33221) stands for 3s3p2d2f1g], which proved extremly accurate for rare gas complexes with molecules,[27,117–119]

and the largest correlation-consistent set available, aug-cc-pv5Z. The results are listed in Table 5.7, and compared with those obtained with aug-cc-pvTZ+(332), used throughout this study. One can see that these large basis sets changed the interaction energies in the region of the well only slightly. In the Π-state minimum region one obtaines the lowering of about 1% and 2% for the Σ^+ and Π states, respectively. In the repulsive wall the changes are somewhat larger, a lowering of 4-5% and 3% for the Σ^+ and Π states , respectively. It is also interesting to note that the bond functions appear to be efficient in the minimum region, but high up in the repulsive wall the aug-cc-pv5Z basis provides lower result than the aug-cc-pvQZ+(33221) basis. This is due to the fact that bond function are effective in recovering the inter-monomer (dispersion) correlation, but are not appropriate for the intra-monomer correlation corrections .[116]

5.6.5 Comparison of RCCSD and CASSCF/MRCI results

As stated in Sec. II B, application of the single reference RCCSD(T) approach to the second state of the A′ symmetry is not illegitemate as long as the states are well separated, and differ by a single electron promotion to single occupied open shell - in our case from one p orbital to another p orbital. An independent verification of the adopted approach is therefore necessary, and may be achieved by parallel evaluation of the PES's by means of the MRCI technique. In particular, if the CC approach is to be trusted, the MRCI(SD) size consistency- [120,121] and counterpoise-corrected results should agree well with the CCSD results obtained with the same basis set.

To corroborate the RCCSD and RCCSD(T) calculations we used CASSCF[122,123] followed by the MRCI(SD) calculations. We used the aug-cc-pvTZ+(332) basis set, the same as previously described in section II A. To correct for the BSSE and size consistency error the MRCI(SD) results were calculated as follows:[108]

$$V(R,\theta) = E_{Cl-HCl}(R,\theta) - E_{Cl}(R,\theta) - E_{HCl}(R,\theta) - \Delta_{SC} \tag{5.20}$$

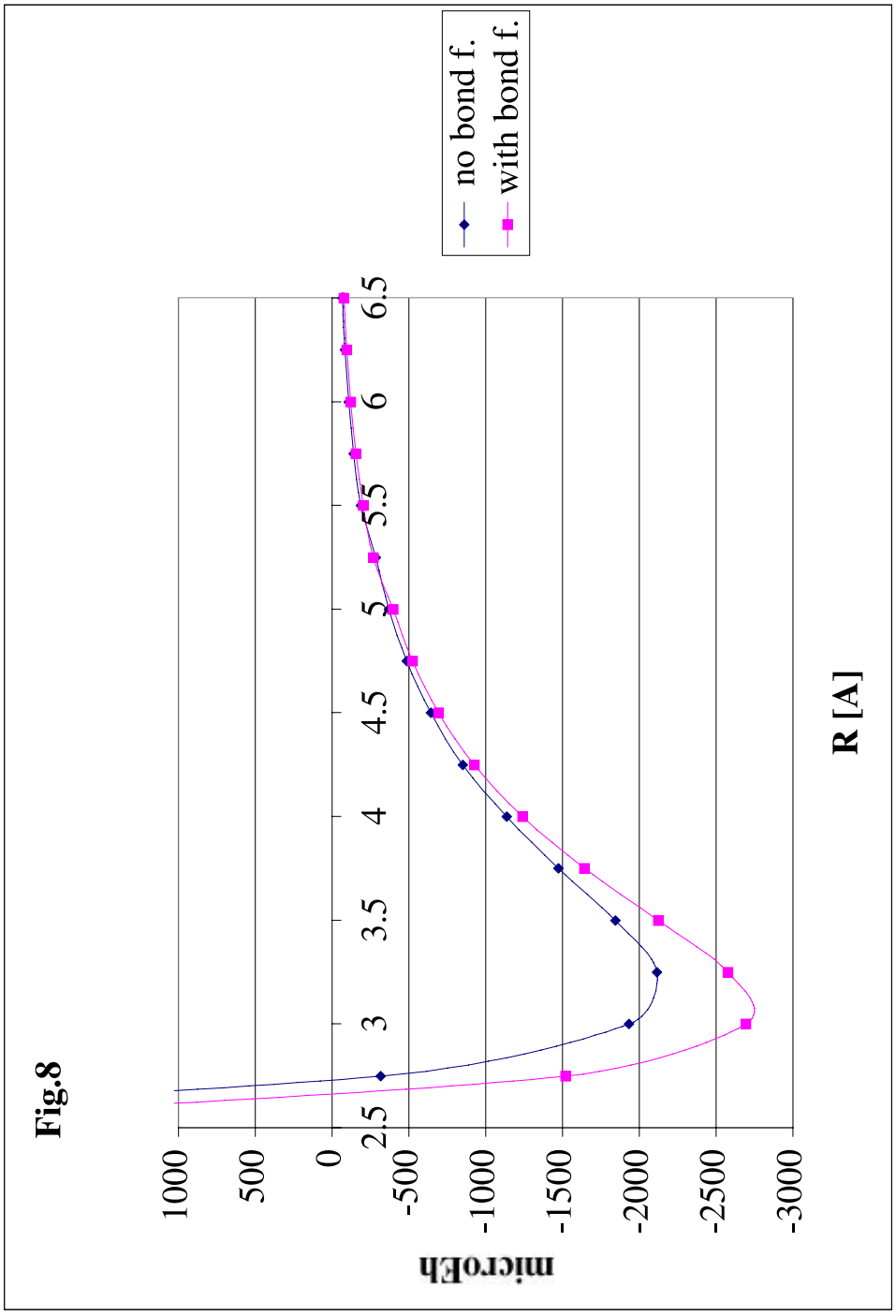

Figure 5.15: The influence of bond function on well depth. The cut for $\theta = 90°$. Energy in μEh.

where

$$\Delta_{SC} = E_{Cl-HCl}(\infty) - E_{Cl}(\infty) - E_{HCl}(\infty) \tag{5.21}$$

and all energies in Eq. 5.20 were calculated with DCBS. The active space was limited to the valence shell and composed from $3s$ and $3p$ orbitals. In Table 5.2, 5.3, 5.4, 5.5

we report the results for both A′ states for $R = 3.0$ Å and $R = 4.25$ Å , and for the set of values of angular variable.

The agreement between the multireference CI results and the restricted CCSD numbers are in general satisfactory. For the $2A'$ state there are differences in the attractive region. The RCCSD curve has a minimum at the collinear HCl···Cl geometry while the multireference results show minimum for somewhat bent geometries. Note that the MRCI may be somewhat distorted by neglecting rotation part of the CP correction, see Sec.IIC. The whereabouts of collinear geometries should be more strongly influenced by close proximity of the conical intersection. However, location of the crossing points Σ^+-Π that are the closest to the center of mass of the HCl molecule practically does not change with applied computational method. For the $\theta = 0°$ collinear arrangement, the crossing point between Σ^+ and Π curves occures at $R = 3.1$ Å. The RCCSD and MRCI+Q method give the same location of the crossing point. The Fig. 5.16 shows the crossing points for $\theta = 0°$ at the RCCSD and the RCCSD(T) levels of theory. Inclusion of triples contributions has practically no effect on the location of the crossing point.

In case of the short-range Σ^+-Π crossing point at the distance $R = 3.4$ Å for the angular orientation $\theta = 180°$, the level of applied theory has also practically no influence on its location. There is an additional, long-range crossing point far from the HCl molecule and its location noticeably changes when different methods are applied. Fig. 5.17 shows that the location of this point is in the range of $R = 5.75$ Å and $R = 6.0$ Å depending on method.

Additionally entire diabatic surfaces were calculated using the MRCI+Q method with the smaller aug-cc-pVDZ basis set augmented with the same set of the bond functions, (332), as in the coupled cluster calculations. Anisotropy of the H_{11} and the H_{22} surfaces are qualitatively similar to anisotropies of the RCCSD(T) diabats. Figs. 5.18 and 5.19 show contours of the H_{11} and H_{22} diabats respectively.

5.6.6 Comparison with semiempirical model of Dubernet and Hutson

Dubernet and Hutson presented a semiempirical PES of the Cl-HCl complex derived from the known potentials for Ar-HCl, Ar-Cl and Ar-Ar systems. The PES was used to predict Van der Waals spectra for the Cl-HCl complex.[68] The overall anisotropies of the *ab initio* adiabatic surfaces are very similar to the semiempirical ones (see right panel of Fig. 1 in Ref.[68]). The most significant difference is in the position of the global minimum of the ground 1A′ surface. The DH (Dubernet and Hutson) 1A′ adiabat has the global minimum for the Cl···H-Cl collinear geometry ($\theta = 0°$) with the well depth of 383 cm^{-1}. The global minimum of the 1A′ RCCSD(T) surface occurs at a T-shaped arrangement of the atoms ($\theta = 90°$), and has a depth of 586 cm^{-1}. The DH surface has a local minimum for the T-shaped geometry, but shallower (347 cm^{-1}) than *ab initio* one. The position of the T-shaped minimum on the RCCSD(T) 1A′ surface is 0.5 Å closer to the center of mass of the HCl molecule in comparison to the DH adiabat. The Tab. 5.6 collects positions and well depths of the 1A′ DH and RCCSD(T) surface.

The DH and *ab initio* 2A′ surfaces are qualitatively similar. The excited 2A′ state has a minimum near the HCl···Cl collinear arrangement for DH ($\theta \approx 150°$). The RCCSD(T) 2A′ surface has global minimum located exactly for HCl···Cl collinear arrangement. The well depth

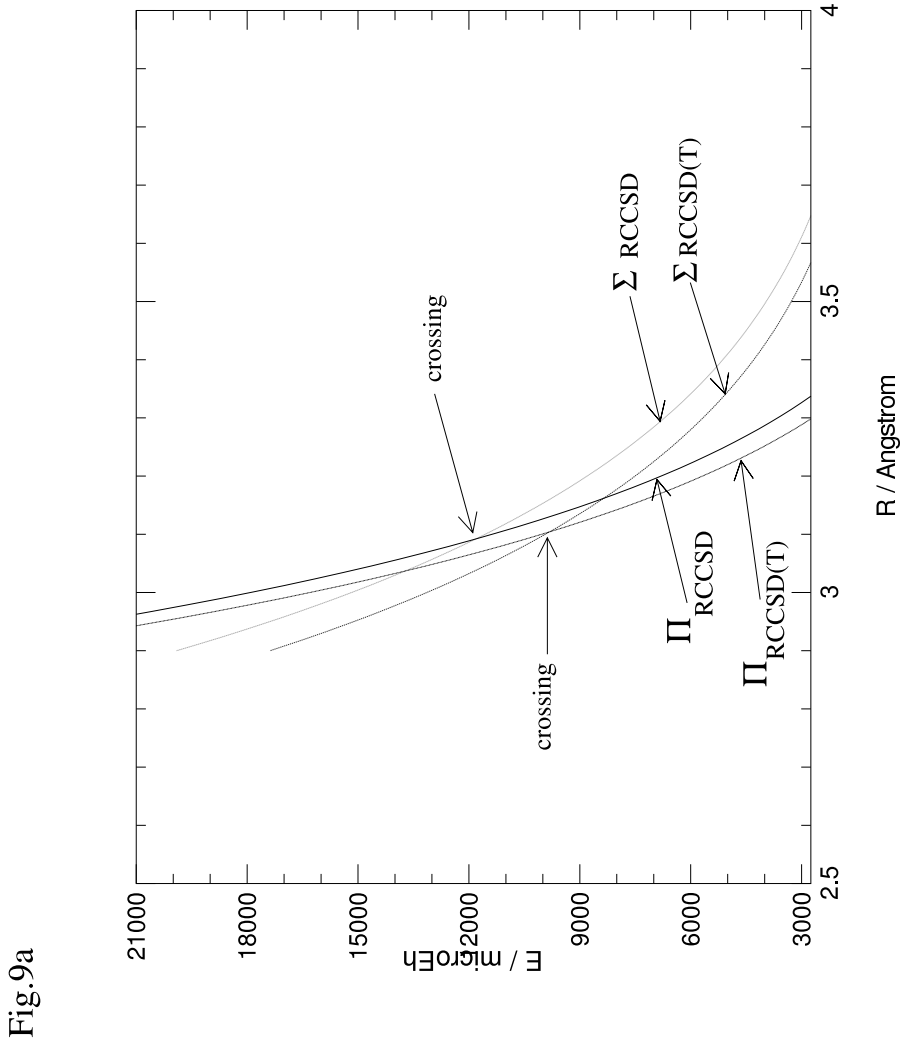

Figure 5.16: The Σ^+-Π crossing point for $\theta = 0°$ at RCCSD and RCCSD(T) level of theory. Energy in μEh.

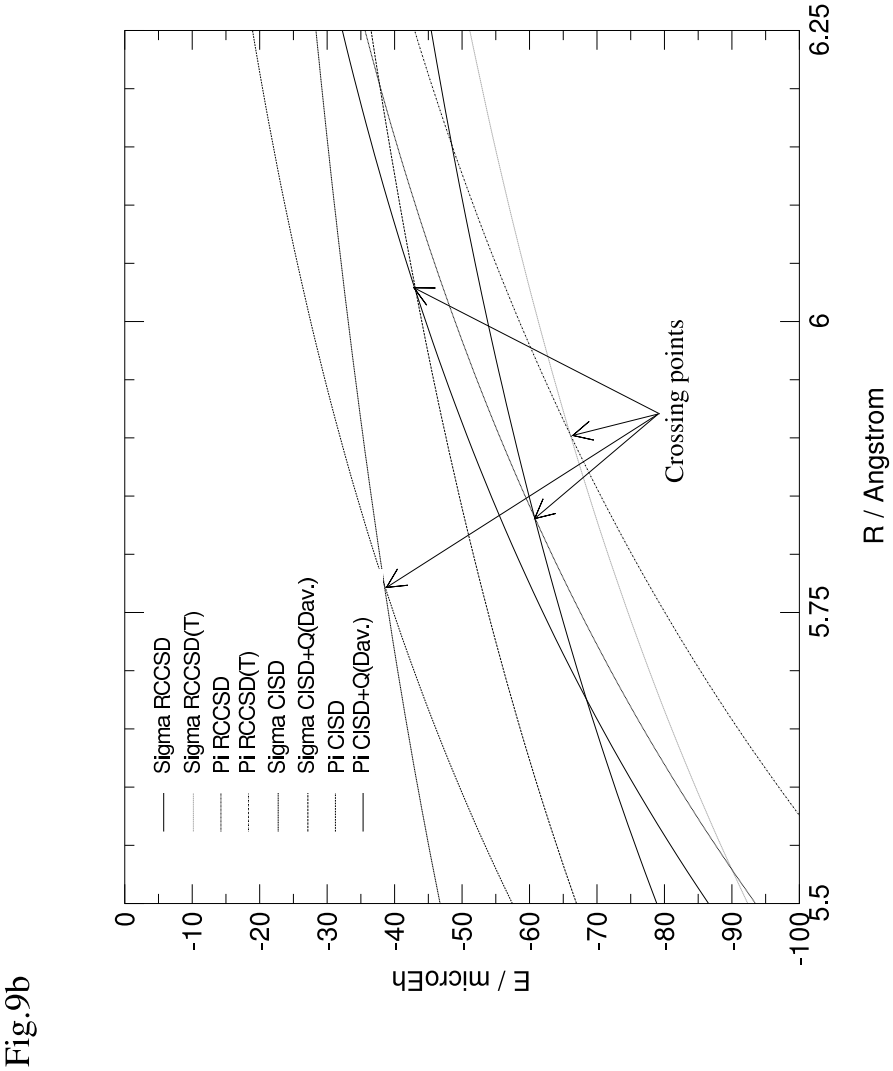

Figure 5.17: The Σ^+-Π crossing point for $\theta = 180°$ at long range at CC and MRCI level of theory. Energy in μEh.

Fig.10a

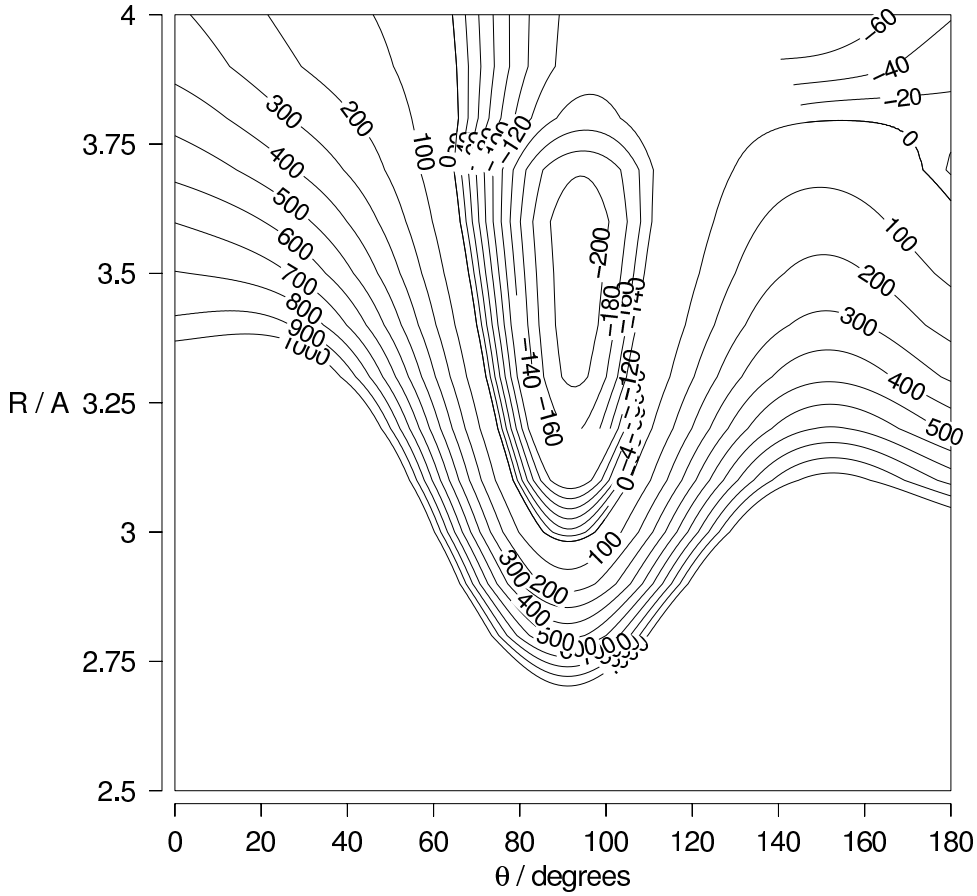

Figure 5.18: Contour of the H_{11} MRCI+Q/aug-cc-pvDZ+(332) diabat. Energy in cm^{-1}.

Fig.10b

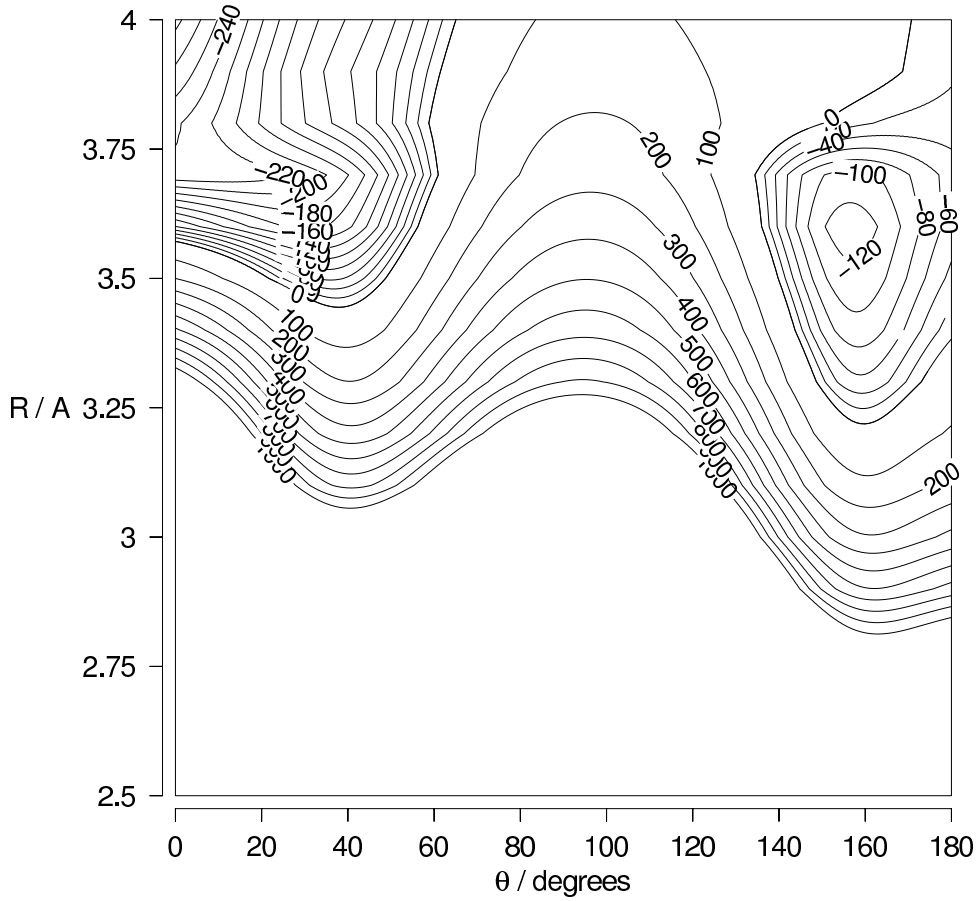

Figure 5.19: Contour of the H_{22} MRCI+Q/aug-cc-pvDZ+(332) diabat. Energy in cm^{-1}.

of the RCCSD(T) surface is almost twice as large as the well depth of the DH model. The values are reported in Tab. 5.6.

The 1A″ surface is very similar in both approaches. In this case the doubly occupied p orbital points towards the HCl molecule, and the Cl-HCl surface should be very similar to that of the closed shell Ar-HCl complex. In Tab. 5.6 we reported data of the minima of the 1A″ state for comparison with DH values.

Our *ab initio* diabats are in general deeper in comparison with the diabats obtained by Dubernet and Hutson.[68] However, the overall anisotropy is very similar. The position of the T-shaped global minimum of the *ab initio* H_{11} diabat differs somewhat from the location of global minimum on the DH diabat. The RCCSD(T) method moves this minimum 0.5 Å closer to the center of mass of the HCl molecule. The well depth of the *ab initio* H_{11} surface is deeper by 265 cm^{-1}. The Tab. 5.6 contains locations and well depths of the RCCSD(T) diabats and DH ones, for H_{11} and H_{22} surfaces. The well depths for the collinear arrangements in the H_{22} and the H_{33} diabat are in the close agreement with the semiempirical surfaces of Dubernet and Hutson.

5.7 Summary

We presented *ab initio* RCCSD(T) adiabatic potential energy surfaces for the Van der Waals Cl-HCl complex. The global minimum of the ground adiabatic state occurs for a T-shaped geometry with a well depth of 600 cm^{-1}. The Dubernet and Hutson semiepirical ground state potential has the global minimum at a collinear Cl···H-Cl geometry with a well depth of 383 cm^{-1}. Despite these quantitative differences, qualitatively the shapes of the ground 1A′ as well as the excited 2A′ and 1A″ PES's are remarkably similar, attesting the physical foundation of the Dubernet and Hutson model.

The non-adiabatic couplings were calculated at the MRCI(SD) level of theory, and used to obtain the RCCSD(T) diabatic surfaces. Anisotropies of the adiabats and the diabats are similar in both ab initio and semiempirical approaches, but due to much deeper well depths of *ab initio* PESs in general, they can certainly give different patterns of the Van der Waals spectrum.

The regions close to the conical intersections revealed, obviously, problems with the RHF/ RCCSD(T) approach, but in general RCCSD(T) proved to be quite robust. We found three conical intersections: one "reactive" at the collinear Cl···H-Cl arrangement and two "nonreactive" at H-Cl···Cl. The second "nonreactive" conical intersection is located quite far from the center of mass of the HCl molecule: at $R \approx 6.0$ Å.

The Σ^+-Π crossing at the reactive Cl···HCl arrangement is due to the fact that the contact through the doubly-occupied orbital is favored by the dipole-quadrupole and quadrupole-quadrupole attraction - then the Π state lies below the Σ^+ state. In the short-range, however, this arrangement causes larger exchange repulsion, which eventually elevates the Σ^+ over the Π state. Such a switch of balance, which results in Σ^+-Π crossings, was also observed for e.g. Ar···O^- [59] and Ar···Cl .[124]

The Σ^+-Π crossings at the nonreactive HCl···Cl arrangement are due to a somewhat more complex balance. Asymptotically, the Cl(quadrupole)···HCl(dipole) interaction favors the Σ^+ state. However, at smaller, but still relatively large R the Cl(quadrupole)···HCl(quadrupole) becomes sizeable and dominates, favoring the Π state. This rationalizes the long-range crossing.

In the short-range, however, the Π symmetry creates more exchange repulsion, which again elevates the Σ^+ above the Π state.

Table 5.1: Comparison of the restricted and unrestricted CC results at $R = 4.25$Å, $\theta = 90°$ in $[cm^{-1}]$

State	RCCSD	RCCSD(T)	UCCSD	UCCSD(T)
$1A'$	-181.02	-201.44	-183.68	-204.04
$2A'$	-14.77	-37.64	not conv.	not conv.
$1A''$	-59.21	-81.76	-59.34	-81.90

Table 5.2: Comparison of the RCCSD and MRCI(SD)+Q results for $1A'$ state at $R = 3.0$Å, in $[cm^{-1}]$

θ	RCCSD	RCCSD(T)	MRCI(SD)+Q(Davidson)	MRCI(SD)+Q(Pople)
0	3330.37	2883.79	3272.16	3264.66
20	2039.27	1646.97	2060.61	2048.53
40	590.37	287.76	526.87	517.89
60	-113.33	-359.41	-141.97	-
80	-348.25	-574.78	-366.16	-375.96
90	-364.90	-586.03	-378.49	-388.00
120	-	-380.35	-52.62	-212.86
140	19.74	-163.76	1.24	-6.08
160	266.09	102.40	239.11	233.08
180	451.66	299.20	432.95	427.39

Table 5.3: Comparison of the RCCSD and MRCI(SD)+Q results for $2A'$ state at $R = 3.0$Å, in $[cm^{-1}]$

θ	RCCSD	RCCSD(T)	MRCI(SD)+Q(Davidson)	MRCI(SD)+Q(Pople)
0	3930.42	3577.35	3878.29	3870.5
20	3741.56	3406.67	3598.93	3594.18
40	2804.85	2585.45	2800.26	2789.84
60	2184.39	2019.62	2179.21	-
80	2123.49	1971.55	2117.09	2105.94
90	2175.63	2023.9	2165.03	2154.03
120	-	1844.24	1907.25	2048.59
140	1664.89	1513.32	1657.49	1647.64
160	1166.74	1017.2	1164.84	1155.84
180	868.12	718.10	861.22	853.32

Table 5.4: Comparison of the RCCSD and MRCI(SD)+Q results for 1A′ state at $R = 4.25$Å, in $[cm^{-1}]$

θ	RCCSD	RCCSD(T)	MRCI(SD)+Q(Davidson)	MRCI(SD)+Q(Pople)
0	-322.03	-362.59	-319.87	-324.02
20	-288.79	-324.97	-326.49	-329.37
40	-229.48	-258.03	-258.4	-261.22
60	-193.15	-216.64	-208.75	-211.47
80	-182.52	-203.66	-185.1	-187.85
90	-181.02	-201.44	-178.65	-181.44
120	-158.75	-177.62	-154.3	-157.07
140	-129.51	-147.67	-135.47	-138.01
160	-101.21	-119.31	-132.51	-134.62
180	-101.39	-121.31	-97.79	-100.50

Table 5.5: Comparison of the RCCSD and MRCI(SD)+Q results for 2A′ state at $R = 4.25$Å, in $[cm^{-1}]$

θ	RCCSD	RCCSD(T)	MRCI(SD)+Q(Davidson)	MRCI(SD)+Q(Pople)
0	202.38	165.91	200.78	197.23
20	161.06	127.66	199.46	195.22
40	81.74	53.67	113.46	109.45
60	20.02	-4.77	40.81	37.07
80	-8.42	-31.79	-0.01	-3.62
90	-14.77	-38.59	-10.7	-14.31
120	-32.08	-54.1	-29.09	-32.65
140	-47.89	-68.98	-34.21	-37.59
160	-63.78	-83.72	-24.76	-27.85
180	-58.41	-75.22	-55.66	-57.69

Table 5.6: Locations and well depths of adiabatic and diabatic surfaces. Comparison of the RCCSD(T) and DH results.

Method	Location	D_e[cm^{-1}]
	$1A'$	
RCCSD(T)[a]	$R = 3.08$Å , $\theta = 88°$	600
Dubernet, Hutson[b]	$R \approx 3.60$Å , $\theta \approx 90°$	347
RCCSD(T)	$R = 3.90$Å , $\theta = 0°$	438
Dubernet, Hutson	$R \approx 3.90$Å , $\theta = 0°$	383
	$2A'$	
RCCSD(T)	$R = 3.68$Å , $\theta = 180°$	126
Dubernet, Hutson	$R \approx 4.20$Å , $\theta \approx 150°$	50
	A''	
RCCSD(T)	$R = 3.90$Å , $\theta = 0°$	438
Dubernet, Hutson	$R \approx 3.90$Å , $\theta = 0°$	383
RCCSD(T)	$R = 3.72$Å , $\theta = 180°$	180
Dubernet, Hutson	$R \approx 3.70$Å , $\theta = 180°$	200
	H_{11}	
RCCSD(T)	$R = 3.07$Å , $\theta = 92°$	602
Dubernet, Hutson	$R \approx 3.60$Å , $\theta = 100°$	335
	H_{22}	
RCCSD(T)	$R = 3.90$Å , $\theta = 0°$	427
Dubernet, Hutson	$R \approx 3.90$Å , $\theta = 0°$	383
RCCSD(T)	$R = 3.63$Å , $\theta = 180°$	205
Dubernet, Hutson	$R \approx 3.70$Å , $\theta = 180°$	200

[a] this work [b] Values from Ref.[68]

Table 5.7: Basis set effects for the colinear arrangement $\theta = 0°$. Energies in cm^{-1}.

Distance [Å]	aug-cc-pvTZ+(332)	aug-cc-pvQZ+(33221)	aug-cc-pv5Z
$^2\Pi$			
2.5	22279.2	21690.3	21495.4
4.0	-429.2	-438.6	-436.6
$^2\Sigma^+$			
2.5	14040.7	13526.5	13354.4
4.0	236.5	233.4	234.9

CHAPTER VI

Perturbational analysis of the interaction energy of the $Cl(^2P)\cdots HCl(^1\Sigma^+)$ Van der Waals complex

6.1 Introduction

The purpose of this Chapter is to report and analyze components of the interaction energy of the $Cl(^2P)$ atom with the HCl molecule in its ground state by means of Cybulski et al's perturbational formalism. Supermolecular calculations of the PESs [125] for this system together with perturbational analysis done in this Chapter provide a complete insight into the nature of the van der Waals forces in the entrance channel to the Cl+HCl→Cl+HCl reaction.

6.2 Methodology of Intermolecular Unrestricted Møller-Plesset Perturbation Theory (I-UMPPT)

The supermolecular MP perturbation theory derives the interaction energy corrections as the differences between the dimer (supermolecule) correction and the sum of monomer corrections in every order of perturbation theory.[21]

$$\Delta E^{(n)} = E_{\mathrm{AB}}^{(n)} - E_{\mathrm{A}}^{(n)} - E_{\mathrm{B}}^{(n)} \qquad n = \mathrm{UHF}, 2, 3, 4, \ldots \tag{6.1}$$

Superscript UHF stands for Unrestricted Hartree-Fock level.

Let us denote the sum of corrections up to the n-th order as $\Delta E\,(n)$. In the language of SAPT (Symmetry Adapted Perturbation Theory) each $\Delta E^{(n)}$ component includes well defined contributions to the interaction energy of the system. These contributions are of electrostatic, induction, dispersion and exchange character when expressed in double perturbation expansion form.

Application of SAPT to open-shell systems requires a properly generalized formalizm. To this end Cybulski et al. developed the IUMBPT.

6.2.1 Components of $\Delta E^{\mathbf{UHF}}$

The UHF correction can be divided into two terms:

$$\Delta E^{\mathrm{UHF}} = \Delta E^{\mathrm{HL}} + \Delta E_{\mathrm{def}}^{\mathrm{UHF}} \tag{6.2}$$

The first term of sum in equation (6.2) denotes Heitler-London contribution and the remaining term is UHF deformation contribution. $\Delta E^{\rm HL}$ is defined in the following way

$$\Delta E^{\rm HL} = \frac{\langle \mathcal{A}{\rm AB}|\hat{H}|\mathcal{A}{\rm AB}\rangle}{\langle {\rm AB}|\mathcal{A}{\rm AB}\rangle} - \frac{\langle {\rm A}|\hat{H}_{\rm A}|{\rm A}\rangle}{\langle {\rm A}|{\rm A}\rangle} - \frac{\langle {\rm B}|\hat{H}_{\rm B}|{\rm B}\rangle}{\langle {\rm B}|{\rm B}\rangle} \tag{6.3}$$

where $\mathcal{A}$ is the antisymmetrizer for the dimer AB. A and B are UHF wave functions of the monomers A and B, respectively. $\hat{H_{\rm AB}}$, $\hat{H}_{\rm A}$ and $\hat{H}_{\rm B}$ are the dimer and monomer Hamiltonians, respectively. The Heitler-London term (6.3) is divided into electrostatic, $\epsilon_{\rm es}^{(10)}$ and exchange, $\epsilon_{\rm exch}^{\rm (HL)}$ contributions. These components are defined as

$$\epsilon_{\rm es}^{(10)} = \langle {\rm AB}|\hat{V}|{\rm AB}\rangle \tag{6.4}$$

$$\epsilon_{\rm exch}^{\rm HL} = \Delta E^{\rm HL} - \epsilon_{\rm es}^{(10)} \tag{6.5}$$

The operator $\hat{V}$ is intermolecular interaction operator. The UHF-deformation term defined in (6.2) has its origin in mutual electric polarization restrained by the Pauli principle.[21]

6.2.2 Partitioning of the second order correction: $\Delta E^{(2)}$

The second-order supermolecular interaction energy can be divided into the following terms:

$$\Delta E^{(2)} = \epsilon_{\rm es,r}^{(12)} + \epsilon_{\rm disp}^{(20)} + \Delta E_{\rm def}^{(2)} + \Delta E_{\rm exch}^{(2)} \tag{6.6}$$

where $\epsilon_{\rm es,r}^{(12)}$ is the second-order electrostatic correlation energy with response effects, $\epsilon_{\rm disp}^{(20)}$ is the second-order UHF dispersion energy. The remaining terms in equation (6.6) describe, respectively, the second order deformation correlation correction to the UHF deformation and the second-order exchange correlation.

6.3 *Ab initio* calculations of I-UMPPT corrections

Calculations of perturbation intertaction terms were performed with the Dimer Centered Basis Set (DCBS). This is equivalent to the counterpoise (CP) correction method of Boys and Bernardi.[50,106,107] The CP procedure is straightforward as long as one considers single non-degenerate electronic states for the dimer and for the monomers. However, in the case of degenerate open-shell monomers the procedure becomes more involved. This is because the degeneracy of the monomer energies is removed by the effect of partner's orbitals, and each dimer state is related to a different CP monomer state. If the dimer states are of different electronic symmetry, as it is, for example, for He(^{1}S)+NO($X^2\Pi$)[25] or Ar(^{1}S)+OH($X^2\Pi$)[26] systems, one can still easily match, by using symmetry, the proper monomer energy with the dimer energy. If not, the situation is more complex as described in Ref.[125]

There is also, in addition, spin contamination problem, which arises in UHF calculations for open-shell complexes. To obtain reliable interaction energy and its components one has to be sure that the spin contamination for monomers and dimer is practically the same. In our DCBS calculations Cl monomer and dimer had the same spin contamination $S^2 = 0.7602$.

The calculations were performed using GAUSSIAN 92[126] suite of programs and intermolecular perturbation theory package TRURL 94[127] which includes I-UMPPT corrections.

6.3.1 Basis set and geometries

The Cl-HCl complex is described in Jacobi coordinates (R, θ). The R variable denotes the distance between the center of mass of the HCl monomer and the Cl atom, and θ denotes the angle between the $\vec{R}$ vector and the HCl bond axis. $\theta = 0°$ corresponds to the Cl···H-Cl collinear sequence. The HCl monomer was kept rigid during calculations and its interatomic separation was set at $r = 1.275$ Å. The origin of the system is placed at the center of mass of the HCl molecule. Calculations of the perturbation components were performed with the augmented correlation-consistent polarized valence-triple-zeta (aug-cc-pvTZ) basis function set of Dunning et al. [99–101] supplemented with an additional set of bond functions. The set of bond functions [3*s*3*p*2*d*] of Tao and Pan ,[36] with the exponents:*sp* 0.9, 0.3, 0.1;*d* 0.6, 0.2, was used. Bond functions were centered in the middle of the distance of the Cl atom from the center of mass of the HCl molecule. The basis set is denoted as aug-cc-pvTZ+(332).

6.4 Decomposition of the interaction energy

The radial and angular dependence of the Heitler-London exchange, electrostatic and dispersion contributions to Cl-HCl interaction energies of 1A′,2A′ and A″ is shown by contour plots. In the next subsections, we will characterize features of the interaction energy components, and construct PESs at the HL exchange plus dispersion level of theory.

6.4.1 ΔE (HL) energy

The ΔE^{HL} term for states 1A′, 2A′ and A″ is shown in Figures 6.1, 6.2 and Figure 6.3, respectively. This Heitler-London term has strong angular anisotropy and largely determines the topology of interaction potentials in the short range, in the very long range and for the Cl·ClH arrangement. For the 1A′ state there is a wide basin of negative energies starting from $R = 4.25$ Å. The global minimum occures for the collinear geometry at $R = 4.5$ Å and its well is 77 cm^{-1} deep, entirely due to electrostatics. The T-shaped minimum around $\theta = 80 - 90°$ is also present with the well depth of 50 cm^{-1}. Contrary to the HL contribution for the 1A′ state, the 2A′ HL energy is repulsive for the whole range of geometries. It is less repulsive for the geometries where Cl atom approaches HCl molecule from its chlorine atomic subunit. This is because the electrostatic interactions favor this region.

6.4.2 First order electrostatic correction: $\epsilon_{\mathrm{es}}^{(10)}$

The first-order electrostatic contribution for the 1A′, 2A′ and A″ states is shown in Figures 6.4, 6.5 and Figure 6.6, respectively. For the ground state of the Cl-HCl van der Waals complex, $\epsilon_{\mathrm{es}}^{(10)}$ is attractive in a wide range of geometries. This is because the quadrupole-quadrupole interaction is attractive for this orientation of the Cl quadrupole with its negative end pointing towards the positive end of the HCl quadrupole.

For the 2A′ state there are regions of repulsive electrostatic interaction. For the collinear arrangement they correspond to the Σ state, where energy of the Σ state is more repulsive then the Π state.

For the excited A″ state there is an island of repulsive electrostatics for the region of angles θ greater than 90°, starting approximately from $R = 4.5$ Å. The reason for this feature is unfavorable orientation of the Cl monomer quadrupole. In this range of geometries the Cl

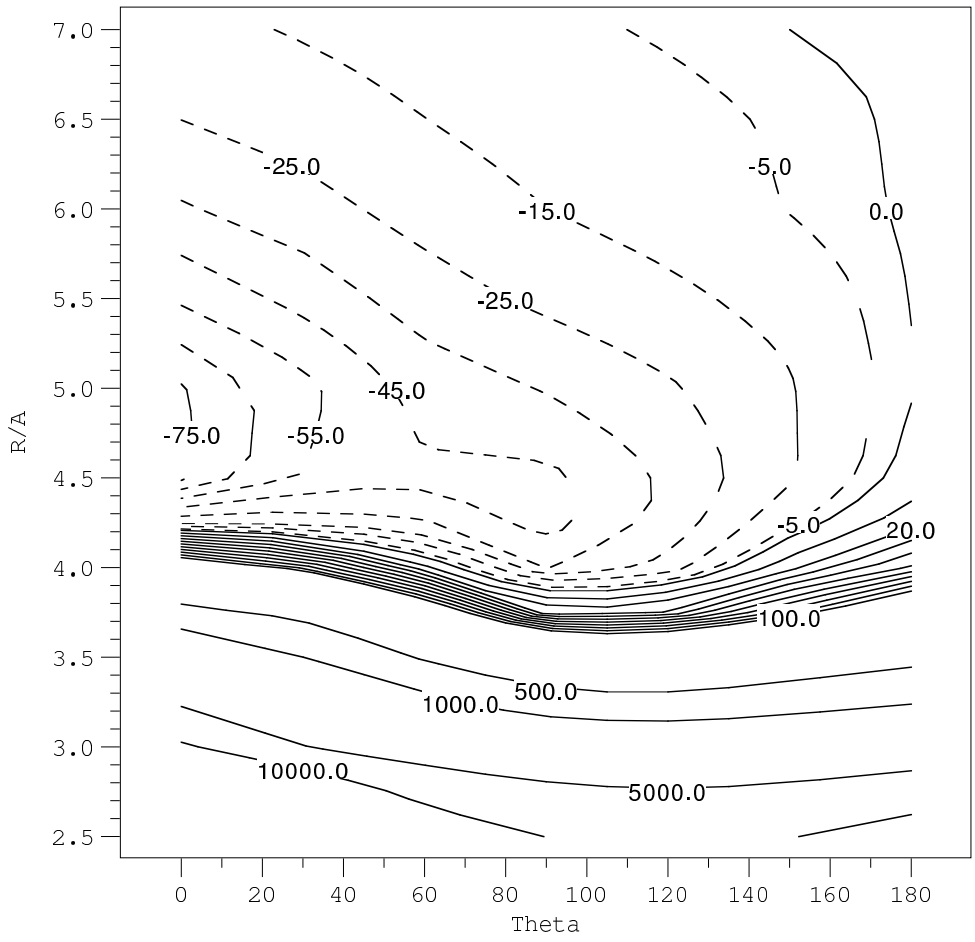

Figure 6.1: Contour plot of Heitler-London energy for the 1A′ state. Energy unit [cm^{-1}]

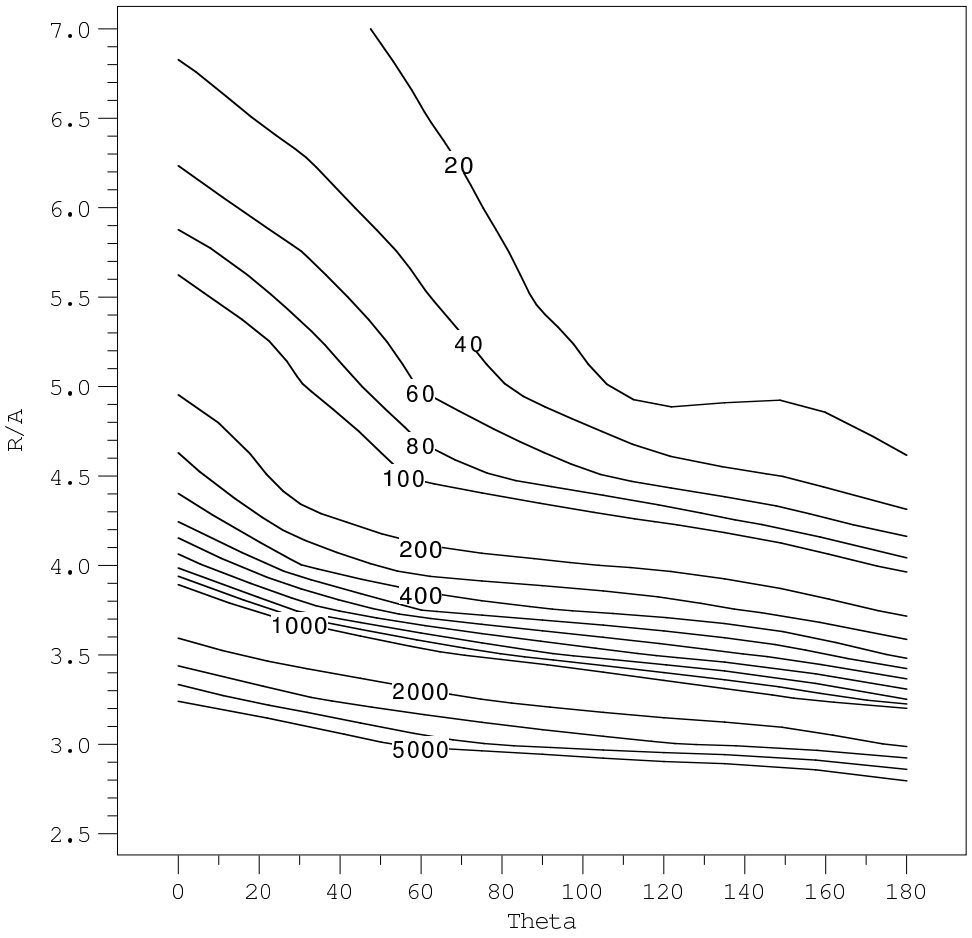

Figure 6.2: Contour plot of Heitler-London energy for the 2A′ state. Energy unit [cm^{-1}]

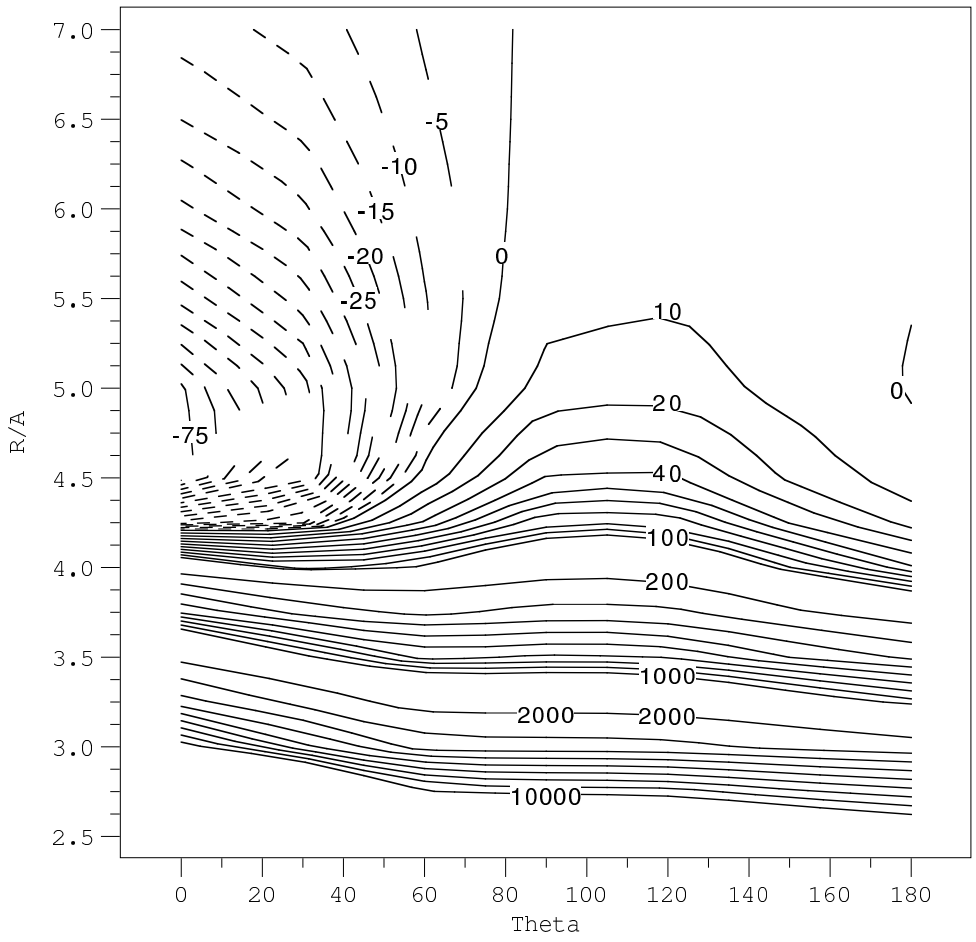

Figure 6.3: Contour plot of Heitler-London energy for the A″ state. Energy unit [cm^{-1}]

quadrupole has its negative lobes pointing towards the negative lobes of the HCl quadrupole and it makes electrostatic interaction repulsive.

6.4.3 Second-order dispersion correction: $\epsilon^{(20)}_{\mathbf{disp}}$

The second-order dispersion term, $\epsilon^{(20)}_{\rm disp}$, is shown in Figures 6.7, 6.8 and Figure 6.9 for the 1A′, 2A′ and A″ states, respectively. This term is only weakly anisotropic, and is similar for all of these three adiabatic states. Dispersion energy is deeper near the collinear arrangement, for $\theta = 0°$. The dispersion term is important in the intermediate range and for the Cl·Cl-H arrangements.

For the 1A′ state the dispersion term and electrostatic term are both attractive and of similar magnitude. For the 2A′ state the electrostatics is repulsive, and it can be seen that the minimum on the 2A′ HL energy plus dispersion term surface is driven by the second order dispersion correction.

6.4.4 Sum of Heitler-London energy and second order dispersion correction

The HL-exchange term and the dispersion correction can be used to construct approximate PESs for three diabatic states. They are given in Figures 6.10, 6.11 and in Figure 6.12 for the 1A′, 2A′ and A″ adiabats, respectively. Incidentally, they qualitatively resemble the adiabatic PESs from RCCSD(T) calculations.[125]

The 1A′ $\Delta E\,(\mathrm{HL}) + \epsilon^{(20)}_{\rm disp}$ surface has two minima. The global one of the T-shaped character and is located at $R = 3.5$ Å and $\theta = 120°$ and its well depth is 400 cm^{-1}. The second local minimum with the well depth equal to 319 cm^{-1} is located at the collinear geometry for $\theta = 0°$ and $R = 4.0$ Å. This is in qualitative agreement with the supermolecular RCCSD(T) PES presented in Ref. [125] However, the global minimum well of RCCSD(T) 1A′ PES is almost 200 cm^{-1} deeper and located closer to the HCl molecule than perturbational PES reported here.

The 2A′ $\Delta E\,(\mathrm{HL}) + \epsilon^{(20)}_{\rm disp}$ surface has one minimum for the collinear geometry for $\theta = 180°$ and $R = 3.75$ Å. This minimum is 126 cm^{-1} deep and, incidentally, it is in excellent agreement with the RCCSD(T) adiabatic PES (Figure 5b in Ref. [125]).

The A″ perturbational PES has two minima located at collinear geometries for $\theta = 0°$ and $\theta = 180°$. The global minimum has the same location and well depth as local collinear minimum of the 1A′ adiabatic surface. The local minimum occures at the chlorine side of the HCl molecule at $R = 3.75$ Å and is 226 cm^{-1} deep. This is in qualitative agreement with the RCCSD(T) PES.

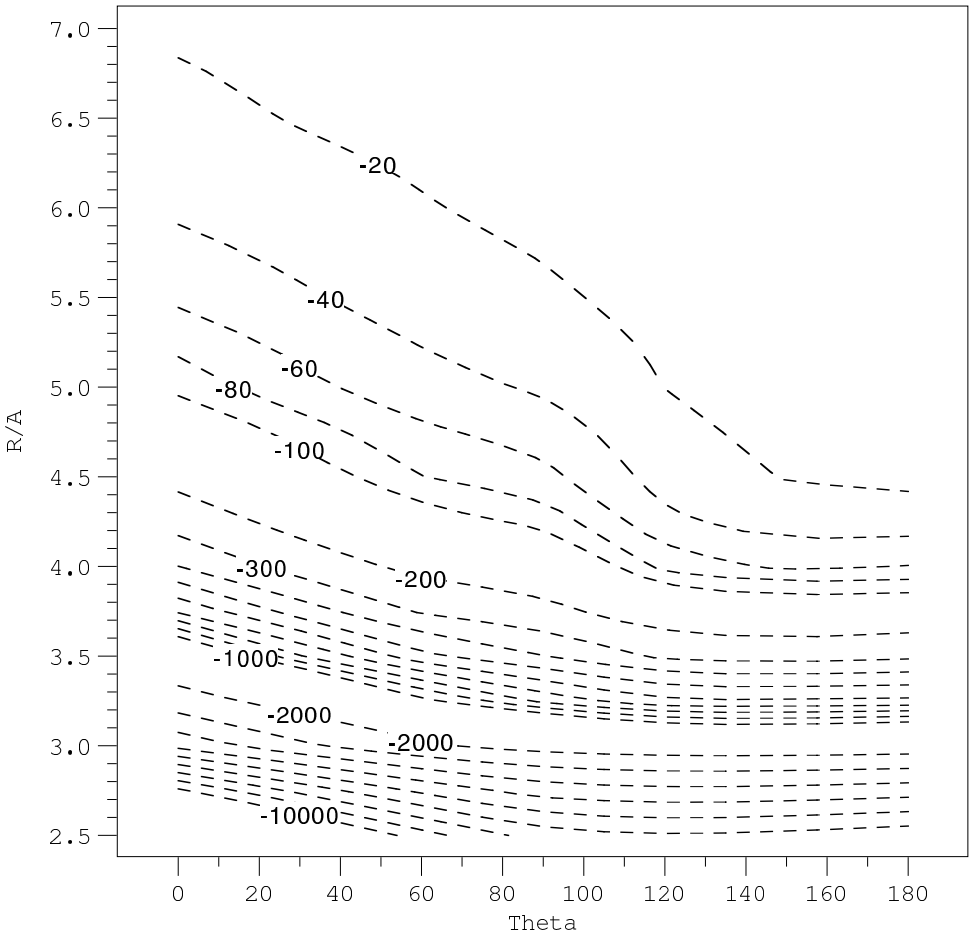

Figure 6.4: Contour plot of the first-order electrostatic correction for the $1A'$ state. Energy unit [cm^{-1}]

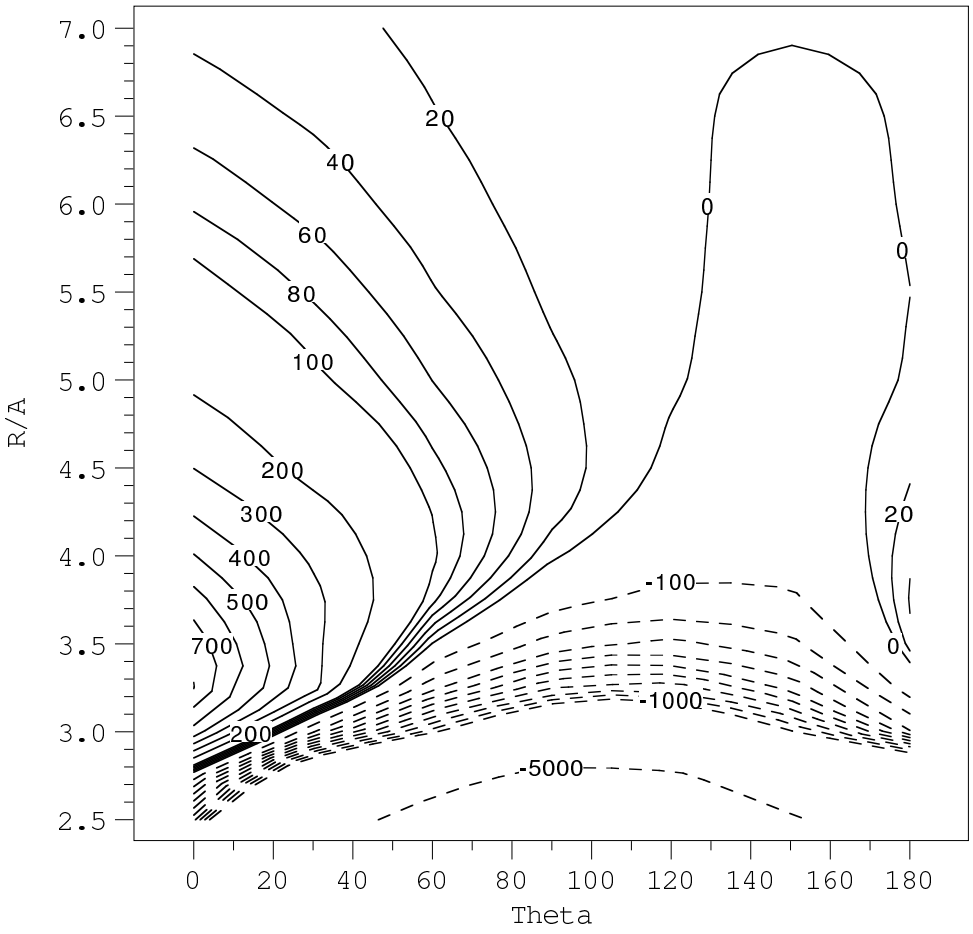

Figure 6.5: Contour plot of the first-order electrostatic correction for the 2A′ state. Energy unit [cm^{-1}]

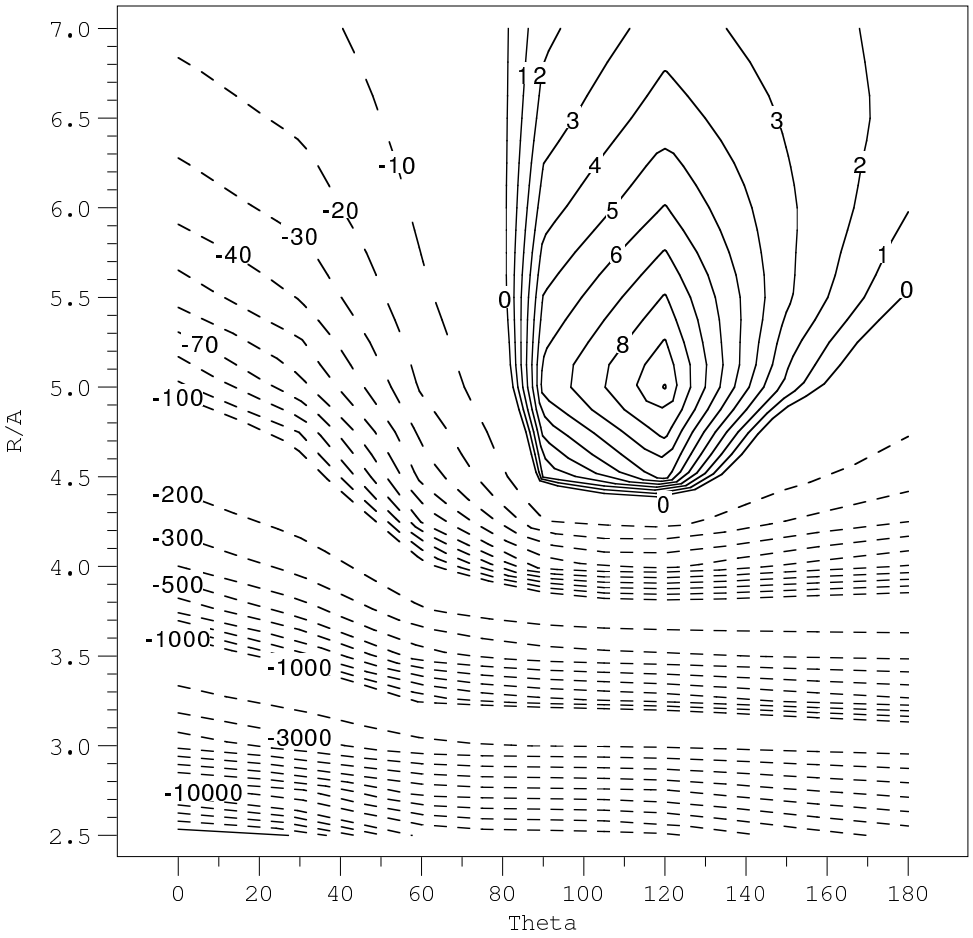

Figure 6.6: Contour plot of the first-order electrostatic correction for the A″ state. Energy unit [cm^{-1}]

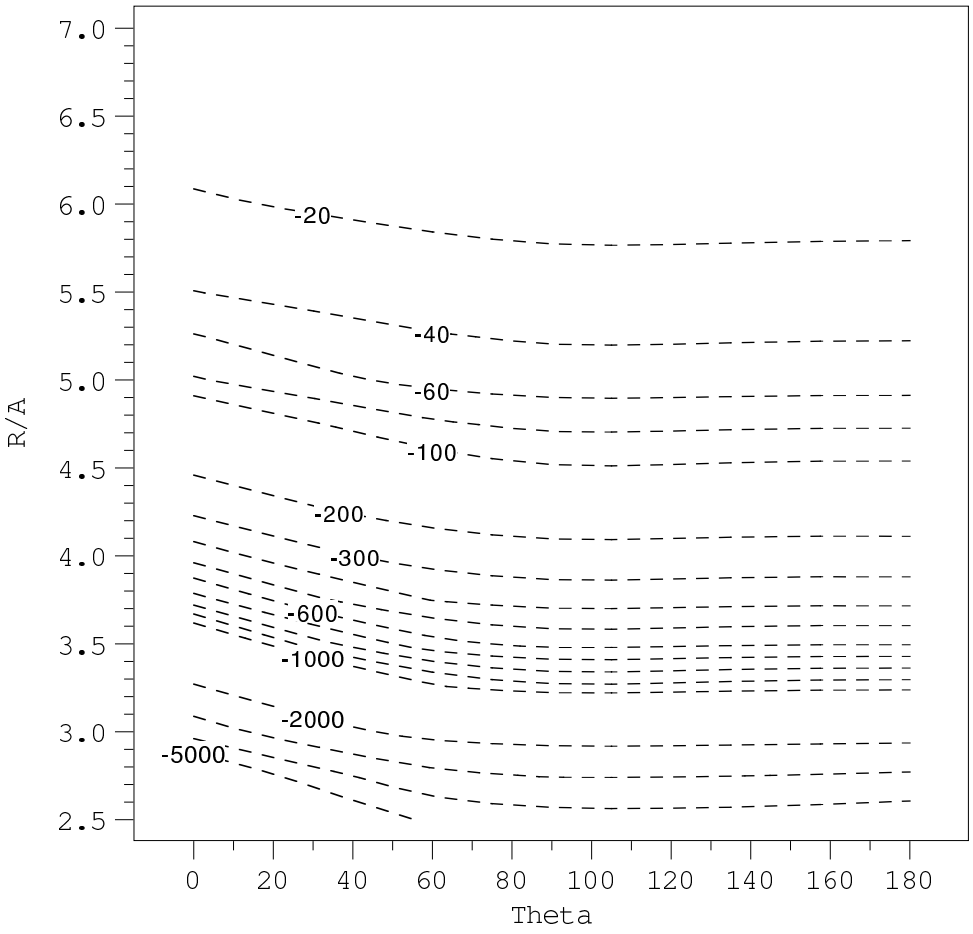

Figure 6.7: Contour plot of the second-order dispersion correction for the 1A′ state. Energy unit [cm^{-1}]

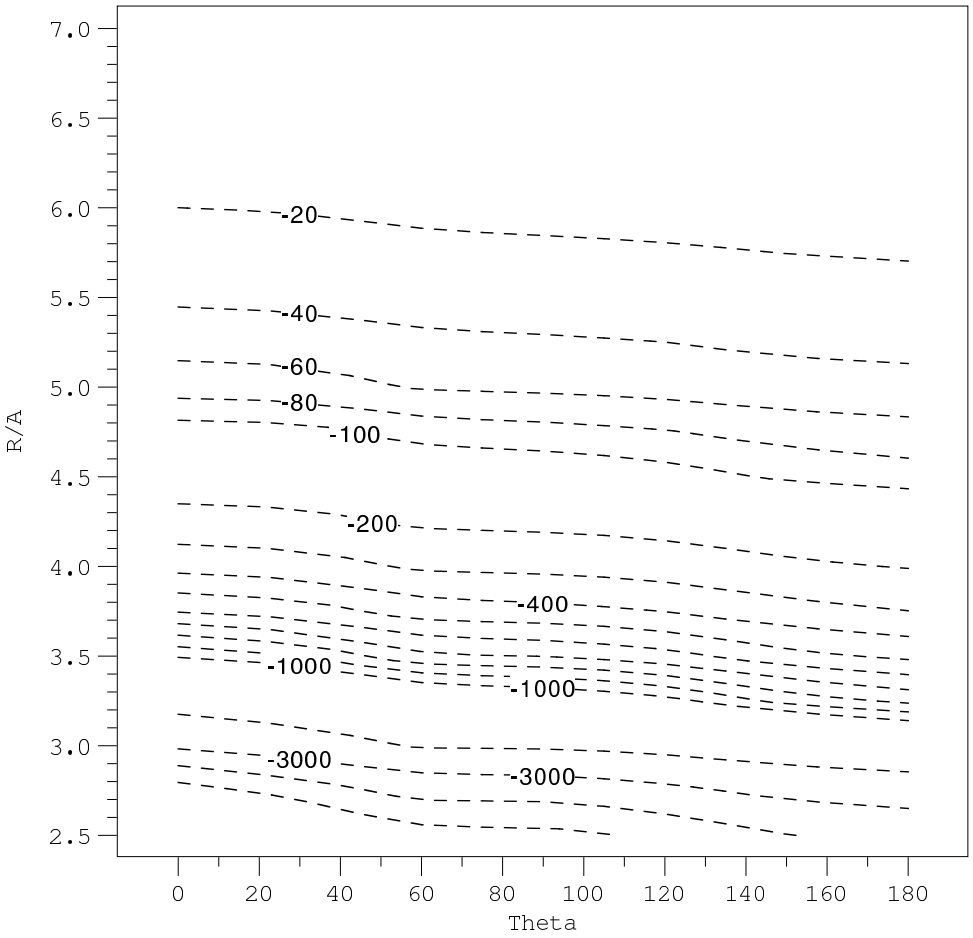

Figure 6.8: Contour plot of the second-order dispersion correction for the 2A′ state. Energy unit [cm^{-1}]

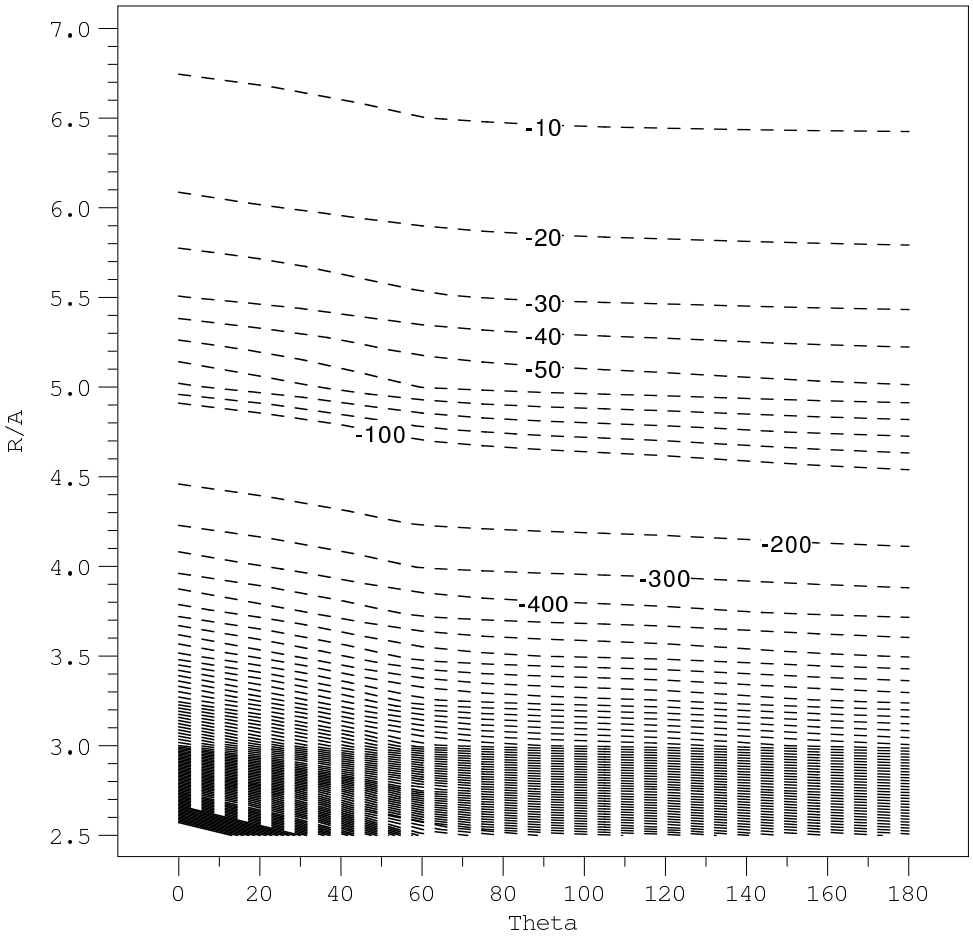

Figure 6.9: Contour plot of the second-order dispersion correction for the A″ state. Energy unit [cm^{-1}]

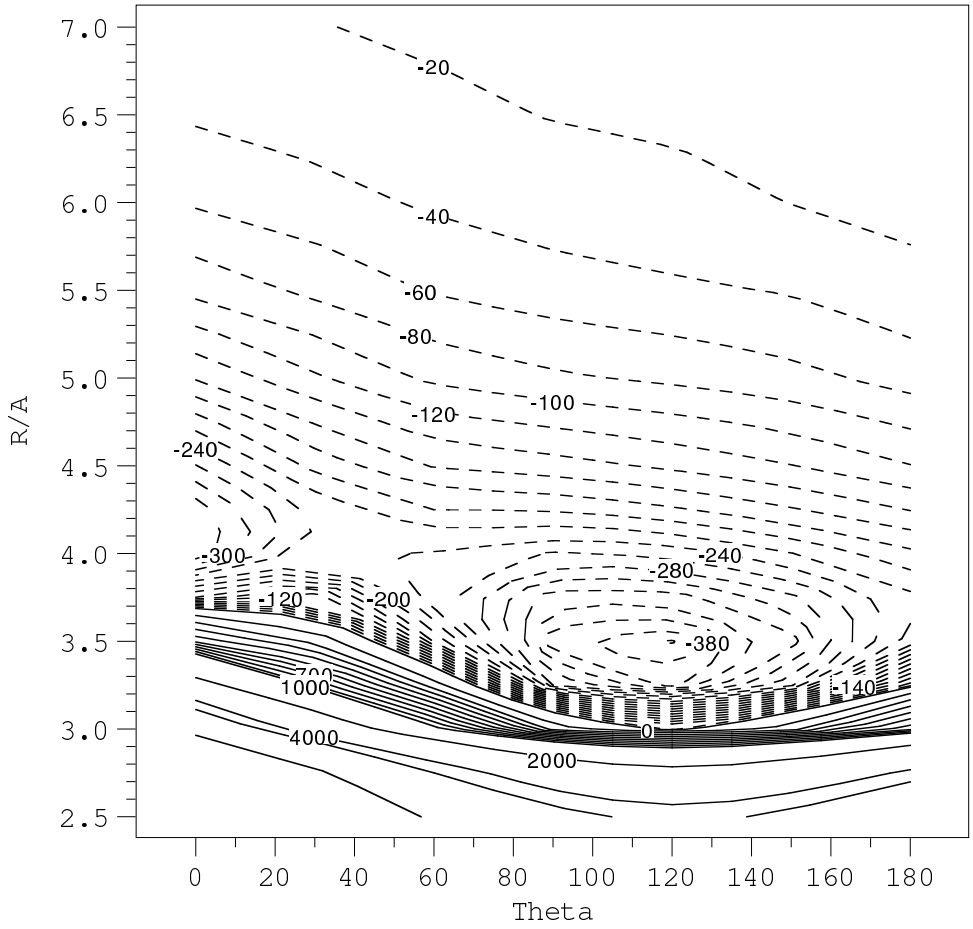

Figure 6.10: Contour plot of the sum of HL energy and the second-order dispersion correction for the $1A'$ state. Energy unit [cm^{-1}]

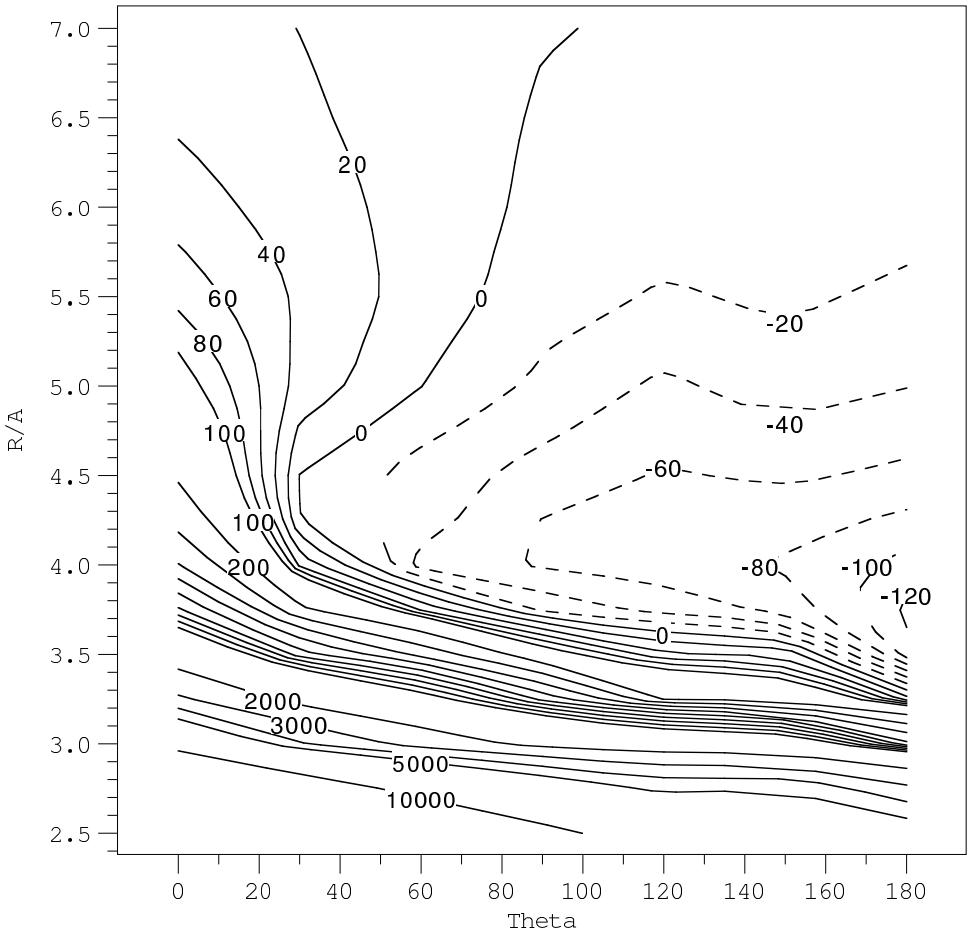

Figure 6.11: Contour plot of the sum of HL energy and the second-order dispersion correction for the 2A′ state. Energy unit [cm^{-1}]

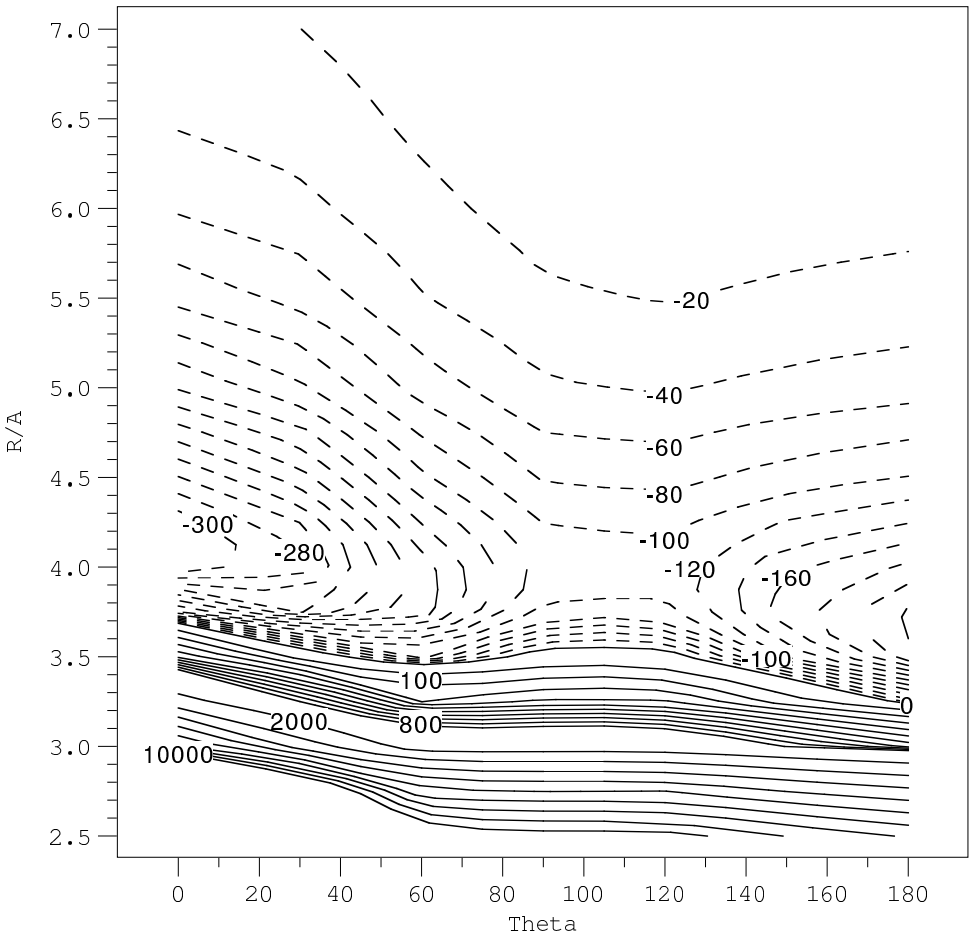

Figure 6.12: Contour plot of the sum of HL energy and the second-order dispersion correction for the A″ state. Energy unit [cm^{-1}]

CHAPTER VII

Ab initio calculations and modeling of 3-dimensional adiabatic and diabatic potential energy surfaces of $F(^2P)\cdots H_2(^1\Sigma^+)$ Van der Waals complex

7.1 Preface

The CCSD(T) methodology as applied to Cl-HCl in Chapter V proved to be very successful. However, it may be applied to systems where the manifold of surfaces ralated to the ground state Cl atom is well separated. This is not the case for H_2-halogen complexes which reveal wide areas of avoided crossing. In this and the following Chapters the Author has proposed a novel model approach to such complexes. It takes advantage of relatively simple electron charge density of the hydrogen molecule and interpolates the total PESs from very accurate CCSD(T) calculations at the highly symmetric configurations: collinear and T-shaped. The MRCI calculations are also necessary, but only to evaluate the nonadiabatic coupling between the adiabatic surfaces. Both adiabatic and diabatic PESs are obtained.' The intra-monomer stretch coordinate is incorporated and the spin-orbit coupling accounted for.

7.2 Introduction

Because of its experimental accessibility, the reaction of F with H_2 and its isotopomers has become the paradigm for exothermic triatomic reactions.[97,128] The high-quality *ab initio* potential energy surface of Stark and Werner (SW) [96] has been used in a number of quantum-scattering calculations [129–136] quasiclassical trajectory studies[130,137] and other investigations of the properties of the F-H_2 system.[138–140] This theoretical work has successfully reproduced the major features seen in both the photodetachment spectrum of the FH_2^- ion[129,138] and the molecular-beam scattering studies of the reaction of F with H_2,,[135] D_2,[141] and HD .[142] Recently, full framework for the quantum treatment of reactions of the fluorine atom with molecular hydrogen was developped ,[97] which involved four potential energy surfaces (PESs) and two, coordinate-dependent *ab initio*-derived spin-orbit interaction terms. This pioneering study established small overall reactivity of the excited (^2P) spin-orbit state of F (which is not allowed adiabatically), and led to conclusion that the dynamics of the reaction will be well described by calculations on a single, electronically adiabatic PES.

Rapid and remarkable progress in quantifying the details of the F+H_2 reaction brings about the issues previously deemed of either none or secondary importance. One such issue is the

role of the Van der Waals interactions in the entrance channel. This trend has been explicitly expressed by Skouteris et al.: "The study of chemical reaction dynamics has now advanced to the stage where even comparatively weak Van der Waals interactions can no longer be neglected in calculations of the potential energy surfaces of chemical reactions" .[93] This statement was prompted by their establishing that strong preference of production DCl vs. HCl can be directly traced to the existence of a shallow Van der Waals well in the entrance channel to the reaction.

A beneficial role of the H_2 rotation in promoting the reaction was already established on the SW (Stark and Werner) surface which favors bent transition state.[143,144] Recently, Balakrishnan and Dalgarno[145] showed that in the low temperature limit its rate coefficient is controlled by the attractive Van der Waals interaction. In addition, the latter work proved the rate to be sensitive to the details of the potential energy surface in the entrance channel, especially the hights of the of the entrance channel barrier and the depth of the Van der Waals well.

To model and accurately quantify the entrance channel, it is necessary to have accurate description of the Van der Waals interaction that determines potential energy surface (PES) in this region. For closed-shell system such an accurate treatment has been achieved for many model complexes. However, for open-shell systems, necessity to consider several states at a time, some of them of the same symmetry, presents a formidable challenge. On the one hand, the multireference configuration interaction (MRCI) techniques, which are best suited for multiple-surface problems including transition states, is difficult to apply for Van der Waals interactions because of the issues of consistent evaluation of monomer and dimer energies with respect to size, one-electron basis set, and configuration selection.[17] On the other hand, the coupled cluster (CC) techniques which easily cope with the above mentioned problems, and are so successful with closed shells[16] may be helpless when it comes to several states of the same symmetry, especially when close to the avoid crossings. To alleviate these difficulties we have recently proposed a combined application of both the coupled cluster singles, doubles and non-iterative triples excitations (CCSD(T)) and MRCI approaches to obtain accurate PESs in the Van der Waals region. The approach, termed CCSD(T)-Model (CC-M), was used in the entrance channel of the Cl+H_2 [146] reaction, and provided accurate PESs for this complex.

In this paper, to provide further justification for the CC-M approach, it is used to generate a set of new *ab initio* based model potentials for three states of the F+H_2 complex in the Van der Waals region. The three states arise from the interaction of H_2 with the triply degenerate ^{2}P F atom. The electron configuration of F gives rise to $^2\Sigma^+$ and $^2\Pi$ states in the $C_{\infty v}$ configuration, to $^2A_1$, $^2B_1$, $^2B_2$ states in the triangular C_{2v} geometry, and to $1^2A'$, $2^2A'$ and $^2A''$ states in C_s geometries. Accurate PESs for all three states have been calculated by Werner and collaborators [96,97,138] and thus are available to verify the quality of our PESs.

The essence of the CC-Model approach is to calculate accurate CCSD(T) interaction energies only for two highly symmetrical configurations, the C_{2v} and $C_{\infty v}$ geometries, and then model three lowest diabatic surfaces of the C_s symmetry by means of a simple angular interpolation, which proved successful for the Cl+H_2 system. The approach takes advantage of the oblate shape of the H_2 molecule, which results in a relatively simple anisotropy of the interaction. To obtain the fourth diabatic surface (related to the nonadiabatic coupling element of the hamiltonian matrix), a separate MRCI calculations are performed over the complete range of geometries. To obtain three lowest nonrelativistic adiabatic PESs, the Hamiltonian in the diabatic basis is diagonalized. The relativistic spin-orbit coupling effects are included by using the formalism recently developed by Alexander, Manolopoulos, and Werner ,[97] assuming empirical value of the splitting parameters. The dependence of the PESs on the H_2 stretching

coordinate is also incorporated and analysed.

7.3 Computational methods and results

7.3.1 Geometries and basis sets

The F-H_2 complex is described in Jacobi coordinates (R, θ). The R variable denotes the distance between the center of the H_2 monomer and the F atom, and θ denotes the angle between the $\vec{R}$ vector and the H_2 bond axis. $\theta = 0°$ corresponds to the F$\cdots$H-H collinear arrangement. The H_2 monomer stretch is described by r coordinate. Calculations were done for r=0.8, 1.0, 1.2, 1.4, 1.6, 1.8 and 2.0 bohr and distance R ranged from 1.5 Å to 5.5 Å. The origin of the system of coordinates was placed at the center of the H_2 molecule. In the calculations of the diabatic energies, the H_2 molecule was located along the x axis, and the z axis was perpendicular to the triatomic plane. Calculations employed the augmented correlation-consistent polarized basis sets of quadruple zeta quality (aug-cc-pvqz) basis function set of Dunning et al. [99–101] CCSD(T) calculations (but not MRCI ones) included also bond functions, with the exponents:sp 0.9, 0.3, 0.1;d 0.6, 0.2 ,[36] in the form of set: [3s3p2d] denoted as (332). Bond functions were centered in the middle of the vector $\vec{R}$. Bond functions have been shown[116] to be both effective and economical for a number of Van der Waals complexes including those with an open-shell moiety .[21,24,147,148]

7.3.2 *Ab initio* adiabatic and diabatic potential energy surfaces

Building of the CC-M potentials is done in three steps:

1. accurate CCSD(T) calculations for the C_{2v} and $C_{\infty v}$ geometries, with a large basis set, to obtain benchmark interaction energies, see Sec. 7.3.3. The model diabats for the C_s-symmetry geometries are obtained by a simple Legendre-polynomial interpolation between the C_{2v} and $C_{\infty v}$ geometries.

2. MRCI calculations with smaller basis set to obtain nonadiabatic coupling (off-diagonal derivative) matrix element and the fourth diabatic (off-diagonal) surface, see Sec. 7.3.4. These calculations do not require neither the self-consistency corrections nor the counterpoise correction.

3. The adiabatic PESs are obtained by diagonalizing the Hamiltonian matrix in terms of diabatic basis set. See Sec. 7.3.5.

It should be stressed that the CC-M approach thus avoids the major pitfalls of MRCI.

All *ab initio* calculations reported in this paper were performed using MOLPRO package.[53] The supermolecular method was used in calculations of three adiabatic potential energy surfaces. This method derives the interaction energy as the difference between the energies of the dimer AB and the monomers A and B

$$\Delta E^{(n)} = E_{AB}^{(n)} - E_A^{(n)} - E_B^{(n)} \tag{7.1}$$

The superscript (n) denotes the level of *ab initio* theory. In the CCSD(T) calculations the use of the above equation is straightforward, and free from arbitrary choices, as long as the dimer

and monomer energies are calculated with the same dimer centered basis set to counterpoise the basis set extension effect.[50] The CCSD(T) method is well known to be very effective in recovering electron correlation effects in Van der Waals complexes calculations,[16,17] and is preferred as long as the single-reference approach is valid. If not, one has to use the MRCI approach. The MRCI calculations are more involved as they require the size consistency corrections and counterpoise correction at the diabatic level. We describe application of MRCI in Sec. 7.3.4.

7.3.3 Model diabatic PESs

Legendre polynomial expansion

The CCSD(T) approach can provide us with very accurate results, close to saturation with respect to basis set and correlation effects. It can be used with confidence for the lowest state of a given symmetry, but also for excited states that can be adequately represented by a single Slater determinant - e.g., when the excited state is related to a single-electron promotion from one p orbital to another, orthogonal p orbital. The latter feature was exploited in our recent study of the HCl-Cl Van der Waals complex ,[125] where two A′ states in the Van der Waals region were well separated in a wide range of geometries. However, whereas formally the situation in the H_2-F(^{2}P) case is identical, the H_2 molecule produces a much smaller splitting of the ^{2}P state of F, and a significant nonadiabatic mixing of two adiabatic A′ states takes place, which culminates in the conical intersection for the collinear arrangement.

In our previuos work on Cl-H_2, the diabatic surfaces revealed a simple and regular shape. For a given R, the θ-dependance was monotonic between the C_{2v} and $C_{\infty v}$ geometries. On this basis, we proposed the CC-M method which assumed the CCSD(T) interaction energies for the C_{2v} and $C_{\infty v}$ geometries, and derived the interaction energies for the C_s geometries from the Legendre expansion truncated at L=2, which is equilvalent to the following angular dependence:

$$H_{11}^{\text{CC-M}}(R,r,\theta) = V_{A_1}^{\text{CCSD(T)}}(R,r)\sin^2\theta + V_{\Sigma}^{\text{CCSD(T)}}(R,r)\cos^2\theta \tag{7.2}$$

$$H_{22}^{\text{CC-M}}(R,r,\theta) = V_{B_2}^{\text{CCSD(T)}}(R,r)\sin^2\theta + V_{\Pi}^{\text{CCSD(T)}}(R,r)\cos^2\theta \tag{7.3}$$

$$H_{33}^{\text{CC-M}}(R,r,\theta) = V_{B_1}^{\text{CCSD(T)}}(R,r)\sin^2\theta + V_{\Pi}^{\text{CCSD(T)}}(R,r)\cos^2\theta \tag{7.4}$$

In essence, it takes advantage of the simple elipsoidal symmetry of the electron density of the H_2 moiety in its ground state. The CC-M diabatic surfaces were prepared for the full range of geometries using *ab initio* CCSD(T) results for the A_1, B_1, and B_2 representations of the C_{2v} symmetry and Σ^+ and Π representations for the $C_{\infty v}$ symmetry.

2-D fitting

In the framework of the CC-M, the r-dependence has to be incorporated only for C_{2v} and $C_{\infty v}$ symmetries. The analytic expression is based on Taylor expansion in the r coordinate with additional exponential r-dependent terms and the R-dependence is of the Degli Esposti-Werner type:

$$V(R,r) = \left[G(R)\,e^{-a_1(R-a_2)-b_1\xi-b_2\xi^2} - T(R)\sum_{i=5}^{9}\frac{C_i}{R^i}\right]H(\xi) \tag{7.5}$$

where

$$G(R) = \sum_{j=0}^{8} g_j R^j \tag{7.6}$$

$$H(\xi) = \sum_{m=0}^{2} h_m \xi^m,$$
$$\xi = \frac{r - r_e}{r_e}, \quad r_e = 0.7408\text{Å} \tag{7.7}$$

and damping function,

$$T(R) = \frac{1}{2}\left(1 + \tanh\left(t_1 + t_2 R\right)\right) \tag{7.8}$$

The fitting procedure resulted in 2-D surfaces which represent *ab initio* data with root-mean-square ranging from 1 cm^{-1} to 8 cm^{-1}. 2-dimensional fits were applied to model 3-dimensional diabatic surfaces using equations 7.2, 7.3 and 7.4.

Contour plots of $H_{11}^{\text{CC-M}}$, $H_{22}^{\text{CC-M}}$, and $H_{33}^{\text{CC-M}}$ for $r = 0.7408$ Å are shown in Figures 7.1, 7.2, and 7.3, respectively.

In Figures 7.1 and 7.2, a bold line indicates the crossing of diabats, $H_{11}^{\text{CC-M}}$=$H_{22}^{\text{CC-M}}$. It originates at the region of Σ^+-Π conical intersection, at $\theta = 0°$).

7.3.4 MRCI calculations and fitting of fourth diabatic potential

MRCI calculations

MRCI calculations began with the determination of the state-averged CASSCF orbitals which included all the F-moiety-related orbitals (except for 1s) as well as the σ_g and $\sigma_u^\star$ molecular orbitals of hydrogen molecule in the active space. The state averaged CASSCF orbitals allowed for all three states, 1A′, 2A′, and 1A″ .[122,123] The subsequent internally contracted MRCI calculations[112,113] included all single and double excitations relative to the full-valence CASSCF reference wave functions. Calculations were performed for several values of interhydrogen distance r and in wide range of R and θ variables. In the case of two A′ states, the excitations relative to both reference states were included, and both states were optimized simultanously. This guarantees a balanced treatment in the regions of the conical intersections.[149]

The diabatic surfaces provide more convenient representations for simulations of the Van der Waals spectra of the system. These potentials contain information about couplings between the adiabatic wavefunctions of the same symmetry. The adiabatic-diabatic transformation yields diabatic states for which the non-adiabatic coupling matrix elements approximately vanish. The diabatic states are obtained by an unitary orthogonal transformation of adiabatic states[108,109]

$$\begin{bmatrix} \Psi_1^d \\ \Psi_2^d \end{bmatrix} = \begin{bmatrix} \cos\gamma & \sin\gamma \\ -\sin\gamma & \cos\gamma \end{bmatrix} \begin{bmatrix} \Psi_1^a \\ \Psi_2^a \end{bmatrix}, \tag{7.9}$$

where the transformation angle γ depends on the nuclear coordinates. The resulting diabatic wavefunctions are no longer eigenstates of the electronic Hamiltonian. The Hamiltonian in the

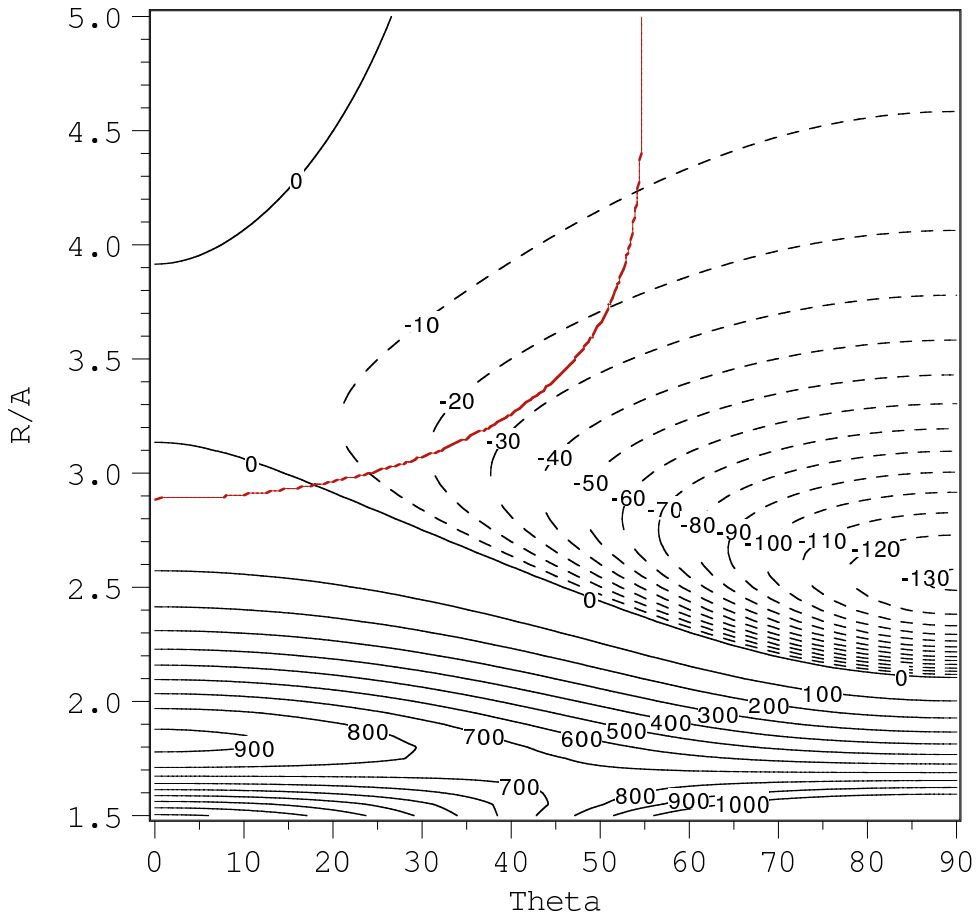

Figure 7.1: Contour plot of the modeled H_{11}^{CC-M} diabat. Values in cm^{-1}, $r = 0.7408$ Å.

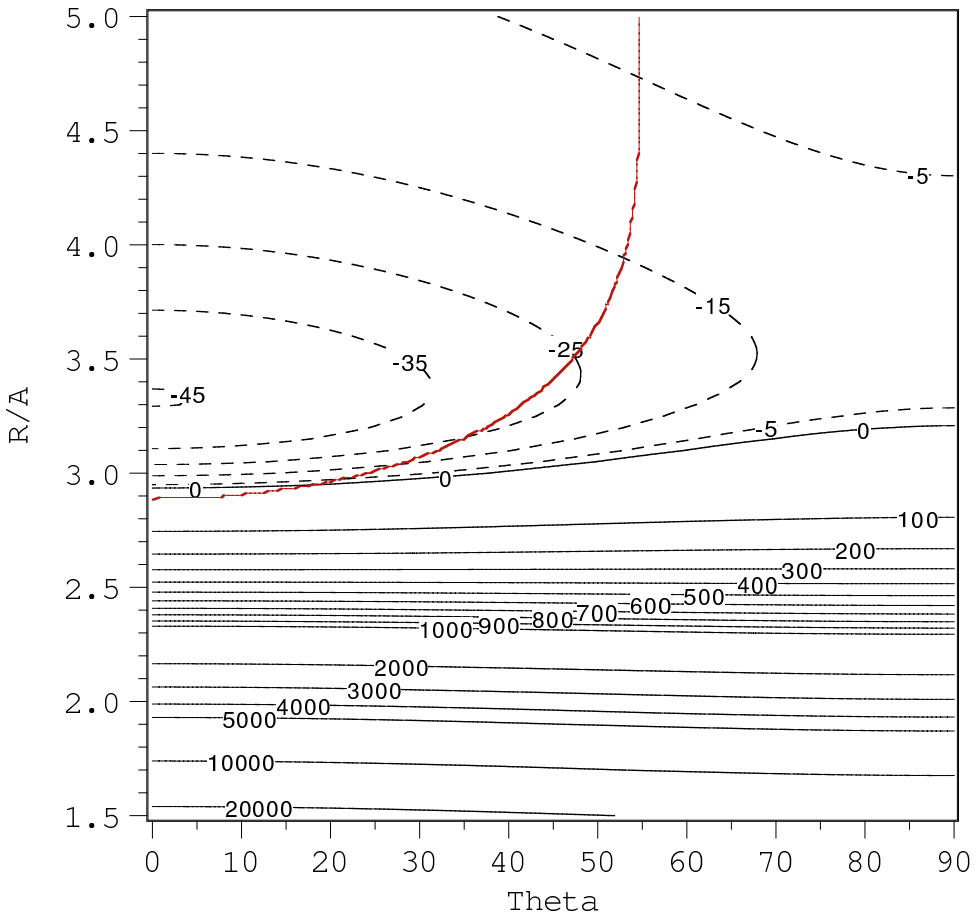

Figure 7.2: Contour plot of the modeled H_{22}^{CC-M} diabat. Values in cm^{-1}, $r = 0.7408$ Å.

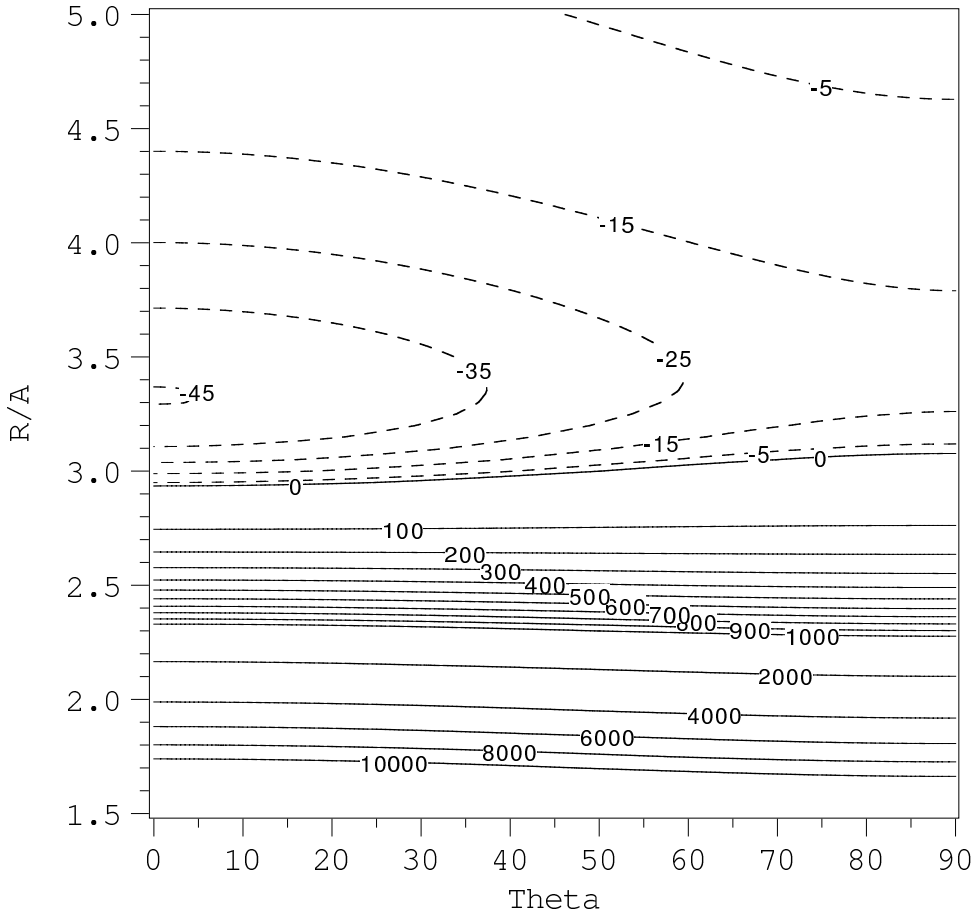

Figure 7.3: Contour plot of the modeled H_{33}^{CC-M} diabat. Values in cm^{-1}, $r = 0.7408$ Å.

diabatic (p_x, p_y, p_z) basis is not diagonal and the matrix elements are modeled as:

$$\begin{aligned} H_{11} &= H_{11}^{\text{CC-M}} \\ H_{22} &= H_{22}^{\text{CC-M}} \\ H_{33} &= H_{33}^{\text{CC-M}} \\ H_{12} &= \left(V_{1A'}^{\text{MRCI}} - V_{2A'}^{\text{MRCI}}\right) \cos\gamma \sin\gamma \end{aligned} \tag{7.10}$$

The transformation angle γ, so-called 'mixing angle', is defined as the angle between the vector of the singly occupied p orbital and the $\vec{R}$ vector. It is a function of Jacobi coordinates of the system. Within a two-state model the mixing angle can in principle be obtained by numerical integration of the non-adiabatic coupling matrix elements (NACMEs). We used the method which uses the maximal overlap with orbitals of the reference geometry to calculate mixing angle. This method calculates NACME in a approximate way using two slightly displaced geometries and method of finite differences.

Since it is convenient to perform diabatic transformation in a system of coordinates with one axis along the $\vec{R}$ vector, the actual γ was redefined as:

$$\gamma_R = \gamma + \theta - \frac{\pi}{2} \tag{7.11}$$

The plot of γ_R is shown in Figure 7.4. This figure clearly shows the region where the A′ states avoid crossing each other, and the point where the Σ^+ and Π states cross. This is the region where the mixing is the strongest and the angle in Eq. 7.9 reaches 45°. The conical intersection occurs at F···H-H, $\theta = 0°$, $R \approx 2.9$ Å. The intersection is related to the crossing of Σ^+ and Π, which switch there.

Contour plot of the H_{12} diabatic surface for $r = 0.7408$ Å is shown in Figure 2.

3-D fitting

To fit 3-dimensional set of *ab initio* data for H_{12} we used analytical expression based on the expansion in Legendre polynomials P_l^1 and Taylor expansion around $r = r_e$ interhydrogen distance:

$$H_{12}(r, R, \theta) = V_{sh}(r, R, \theta) + V_{as}(r, R, \theta) \tag{7.12}$$

where

$$V_{sh}(r, R, \theta) = \sum_{l=1}^{6} \sum_{i=0}^{3} \sum_{j=0}^{3} g_{lj} c_i R^j \xi^i e^{\sqrt{\frac{1}{2}}(a-bR)-c\xi-d\xi^2} \sqrt{\frac{4l+1}{2}} P_{2l}^1(\cos\theta) \tag{7.13}$$

and

$$V_{as}(r, R, \theta) = \sum_{n=5}^{7} \sum_{i=0}^{3} c_i \xi^i \frac{C_n}{R^n} \sqrt{\frac{2(n-4)+1}{2}} P_{2(n-4)}^1(\cos\theta),$$

$$\xi = \frac{r - r_e}{r_e}, \quad r_e = 0.7408\text{Å} \tag{7.14}$$

The fit contains 35 optimized parameters. The quality of the fit can be expressed in root-mean-square value of 9 cm^{-1}.

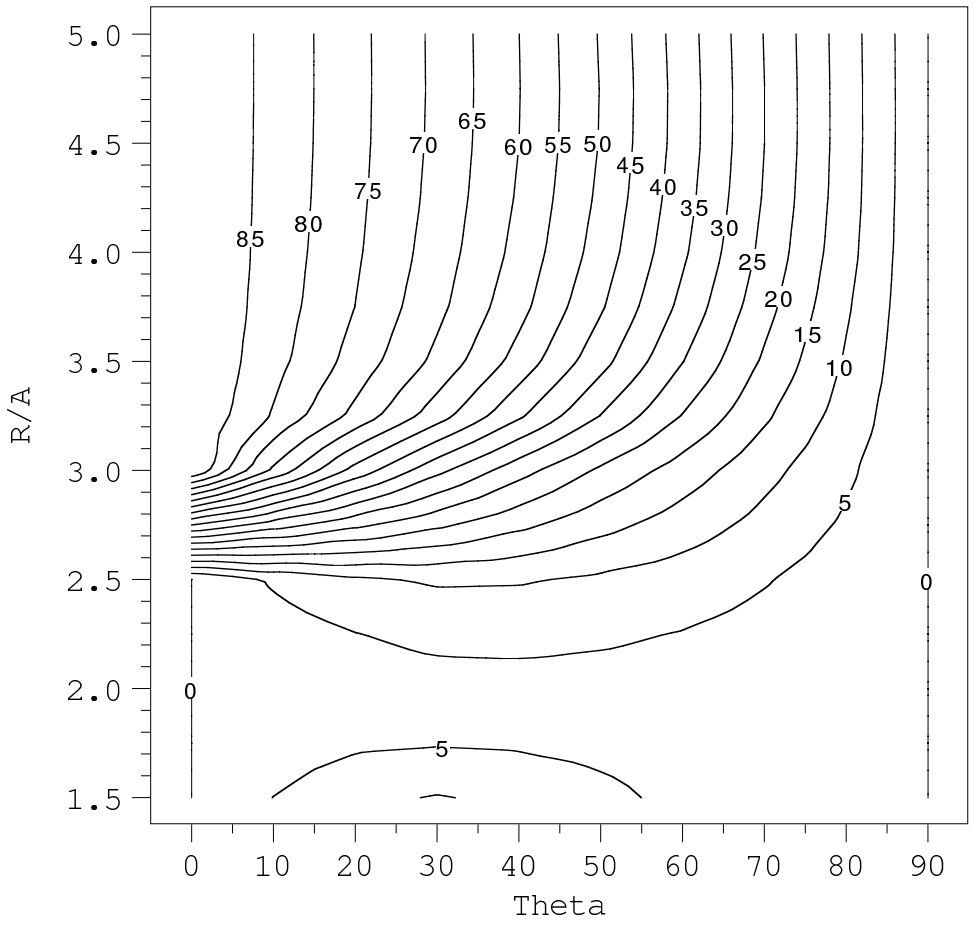

Figure 7.4: Contour plot of the γ_R mixing angle calculated in aug-cc-pvqz/tz basis set, $r = 0.7408$ Å.

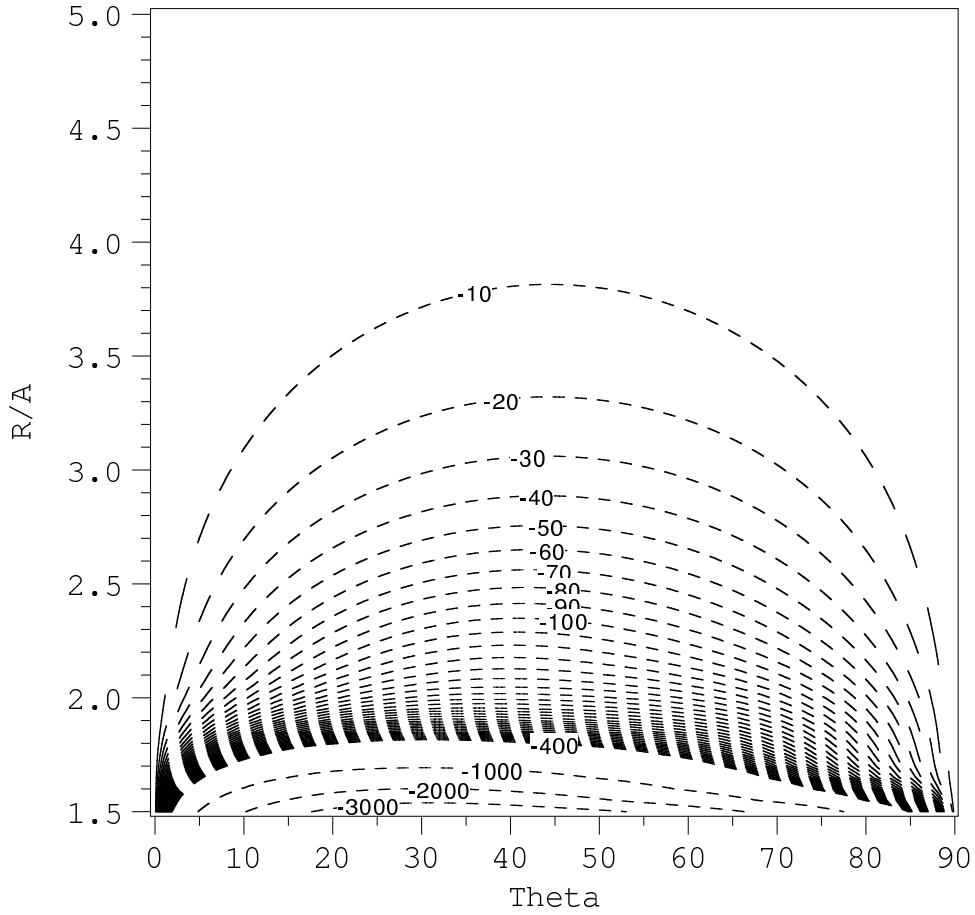

Figure 7.5: Contour plot of the MRCI+Q H_{12} coupling. Values in cm^{-1}, $r = 0.7408$ Å.

7.3.5 Model nonrelativistic adiabatic PESs

To obtain adiabatic counterparts of the diabatic surfaces, the diabatic matrix:

$$\mathbf{H}^{el} = \begin{bmatrix} H_{11} & \sqrt{2}H_{12} & 0 \\ \sqrt{2}H_{12} & H_{22} & 0 \\ 0 & 0 & H_{33} \end{bmatrix} \tag{7.15}$$

was diagonalized. Global minima and stationary points of the modeled diabatic and adiabatic surfaces are shown in Table 7.1. Contour plots of $1A'$ and $2A'$ adiabatic surfaces for $r = r_e$ are shown in Figures 7.6 and 7.7, respectively.

Table 7.1: Stationary points of modeled diabatic surfaces. Numbers in parentheses represent values of ASW[97] potential. Values in cm^{-1}.

Diabat	D_e/cm^{-1}	R_e/Å	θ_e	Type
H_{11}^{CC-M}	130.9(124.0)	2.55(2.55)	90(90)	minimum
	2.7(4.7)	3.35(3.45)	0(0)	saddle point
H_{22}^{CC-M}	45.2(47.6)	3.35(3.35)	0(0)	minimum
	10.8(9.0)	3.60(3.60)	90(90)	saddle point
H_{33}^{CC-M}	45.2(47.6)	3.35(3.35)	0(0)	minimum
	18.5(16.2)	3.45(3.5)	90(90)	saddle point

7.4 Effect of H_2 stretch

In Figures 7.8, 7.9, 7.10, 7.11 and 7.12, we show R- and r-dependent contour plots of $V(R,r)$ for the $C_{\infty v}$ symmetry (the Σ^+ and Π states, Figures 7.8 and 7.9, respectively) and for the C_{2v} symmetry (the A_1, B_1 and B_2 states, Figures 7.10, 7.11 and 7.12, respectively).

One can see that the A_1 and Σ^+ potentials, which define the ground adiabatic state, are the most sensitive functions of r, while the other $V(R,r)$ potentials weakly depend on r. The V_Σ potential reveals a weak Van der Waals minimum for large R with r close to r_e and shorter, and has a large well for small R and large r, where the reaction region is reached. The V_{A_1} potential, for large R is everywhere attractive, and fairly wide and flat with respect to r. On decreasing R and for small r, a repulsive bank is being raised, the attractive region is narrowed to larger r only, where the potential falls steeply into the reactive region.

The behavior of $V(R,r)$ determines the behavior of the diabats and adiabats, according to Eqs. 7.2, 7.3 and 7.4. The changes of r have the most significant impact on the H_{11} diabatic surface, and only a mild effect on the other two, H_{22} and H_{33}. Compared with the plot for $r = r_e$ (Figure 7.1) upon compressing H_2 to $r = 0.5292$ Å(Figure 7.13) the T-shaped geometry minimum rises from -130 cm^{-1} up to -80 cm^{-1}, the pass in the barrier at around 40° disappears, while the collinear stationary point is slightly lowered (by a few cm^{-1}). In other words, the

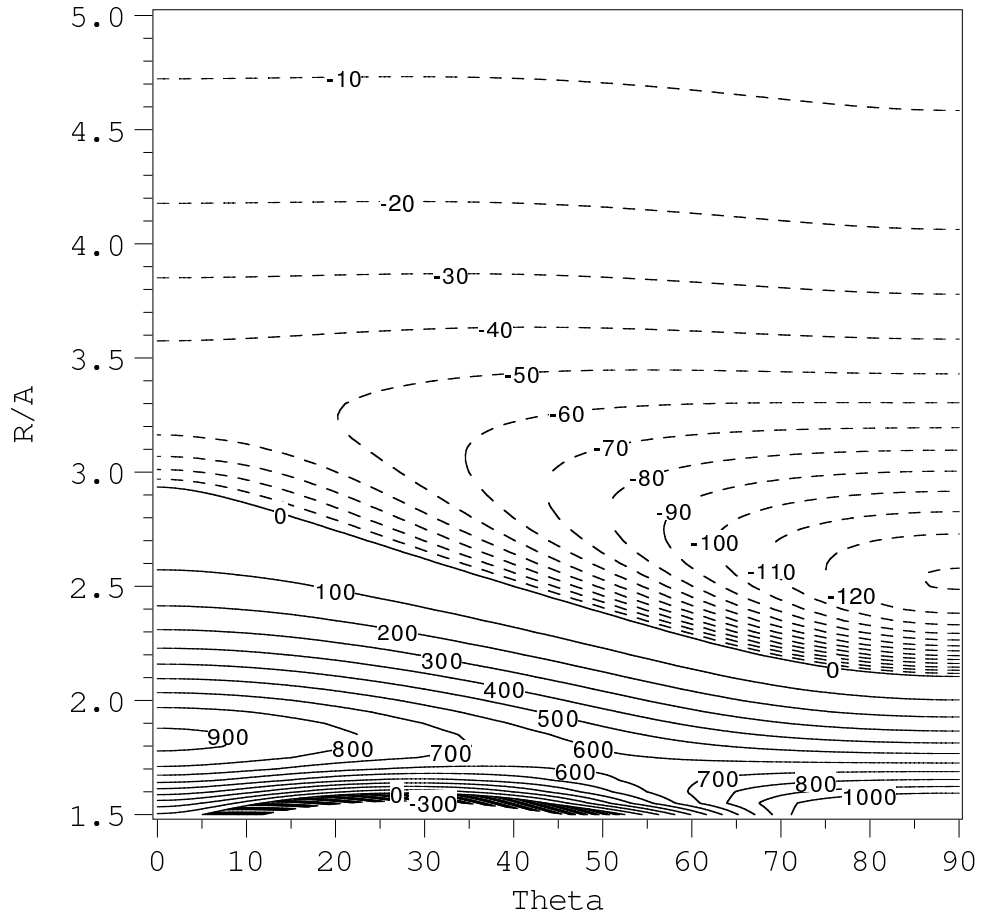

Figure 7.6: Contour plot of the modeled $1A'_{CC-M}$ adiabat. Values in cm^{-1}, $r = 0.7408$ Å.

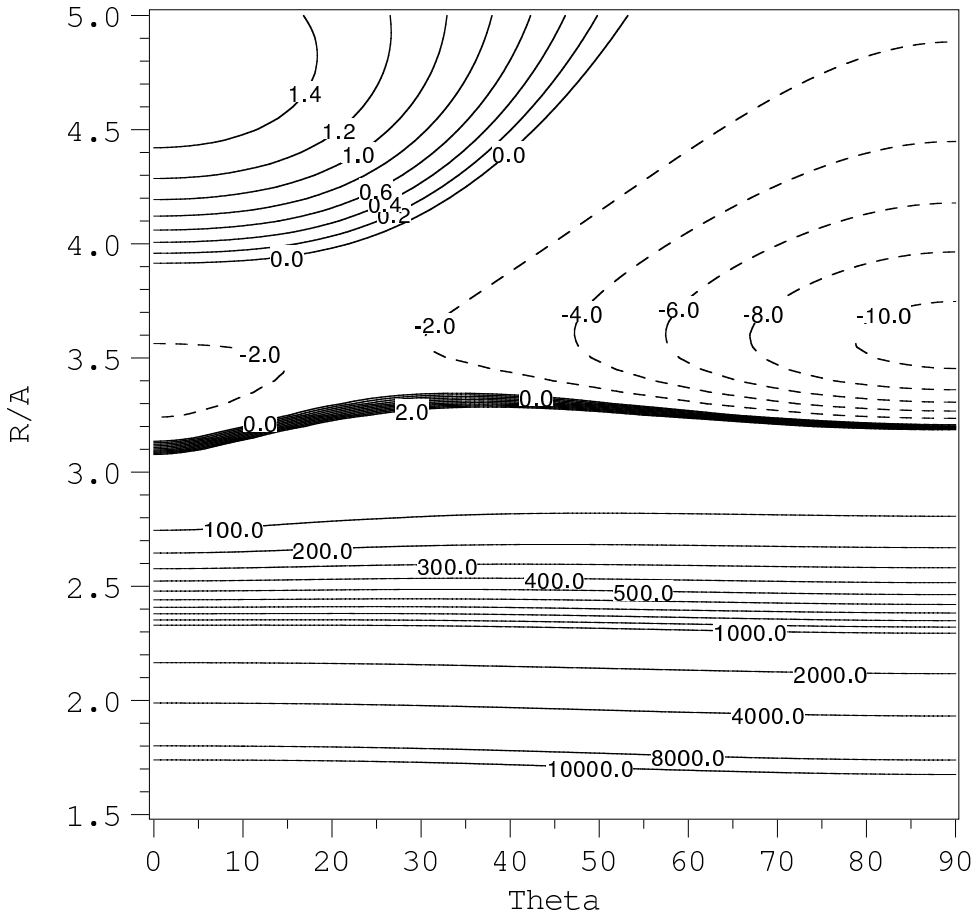

Figure 7.7: Contour plot of the modeled $2A'_{CC-M}$ adiabat. Values in cm^{-1}, $r = 0.7408$ Å.

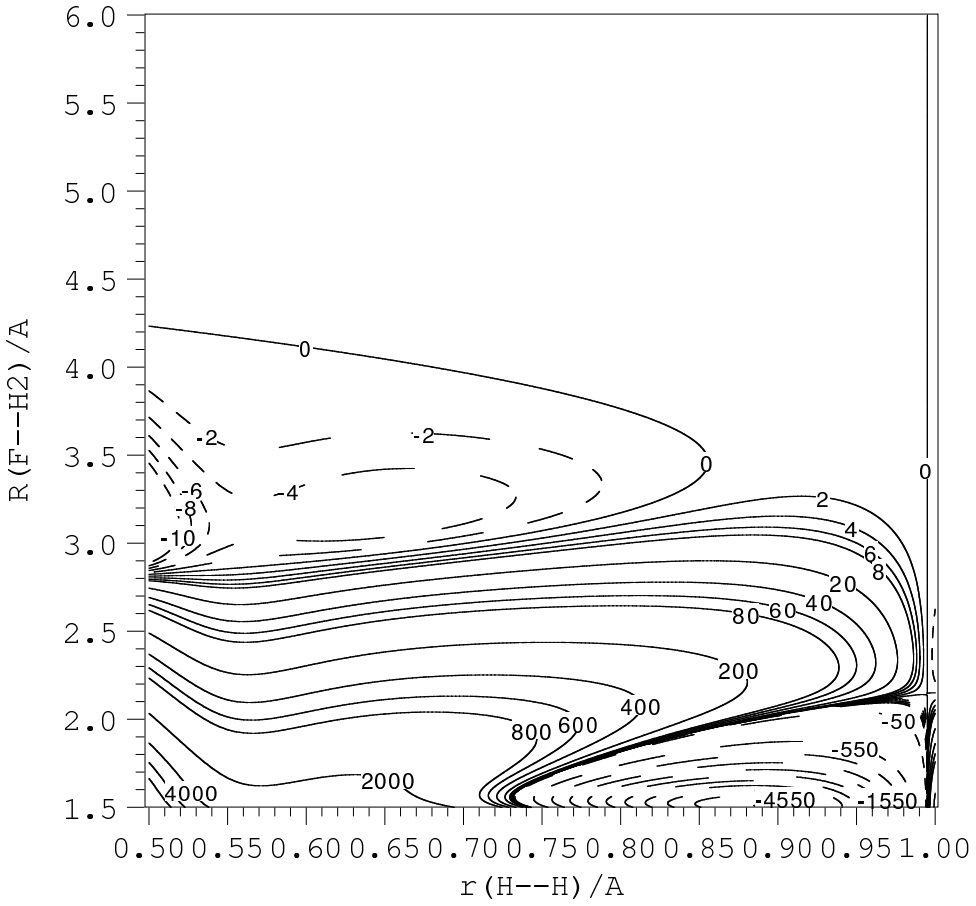

Figure 7.8: (R,r)-dependence of energies of Σ symmetry. Values in cm^{-1}.

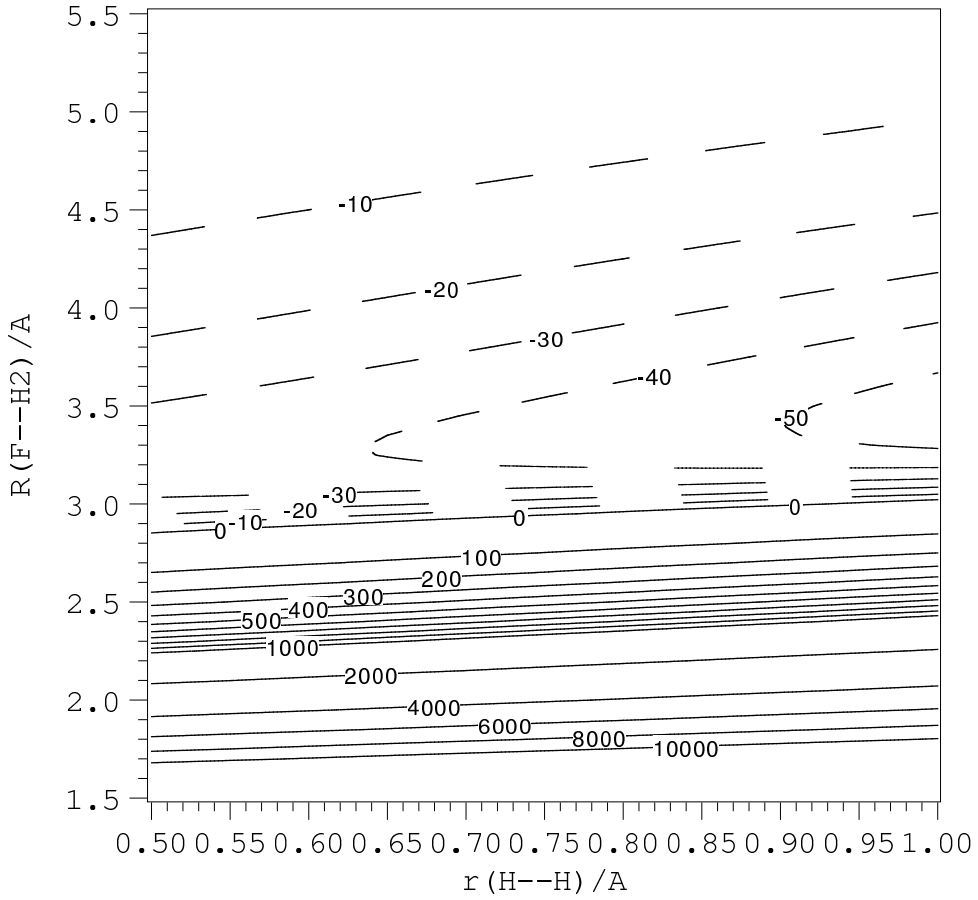

Figure 7.9: (R,r)-dependence of energies of Π symmetry. Values in cm^{-1}.

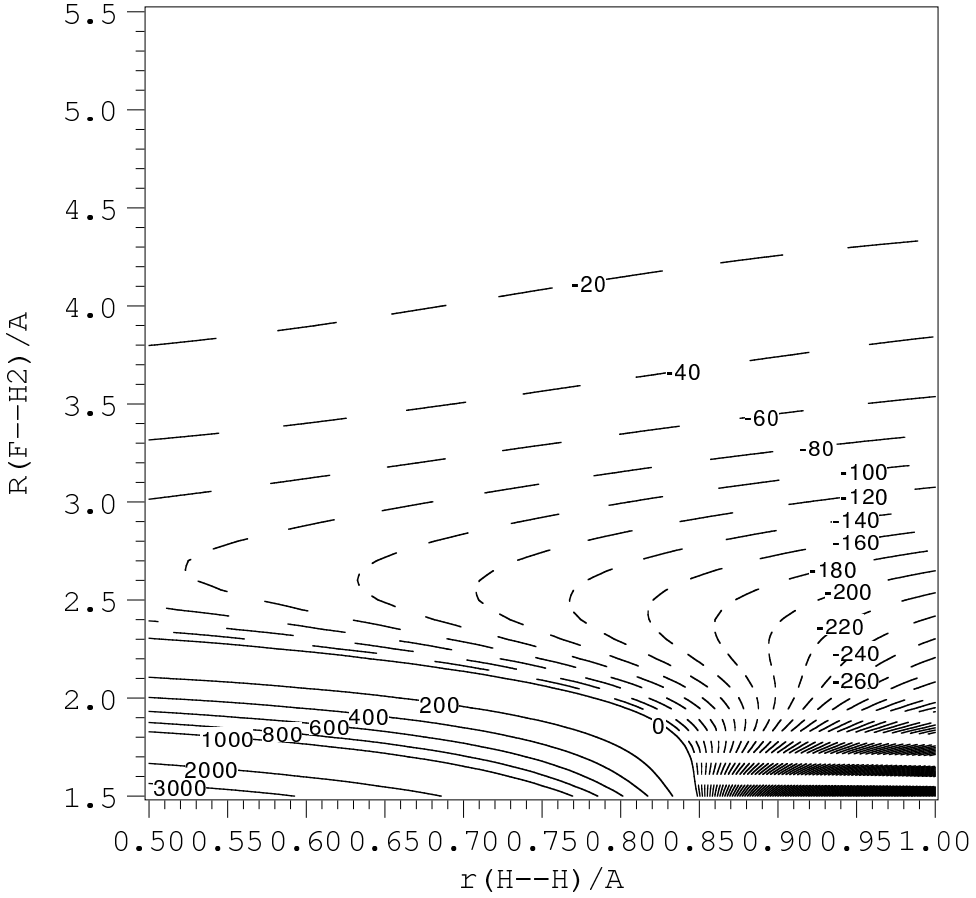

Figure 7.10: (R,r)-dependence of energies of A_1 symmetry. Values in cm^{-1}.

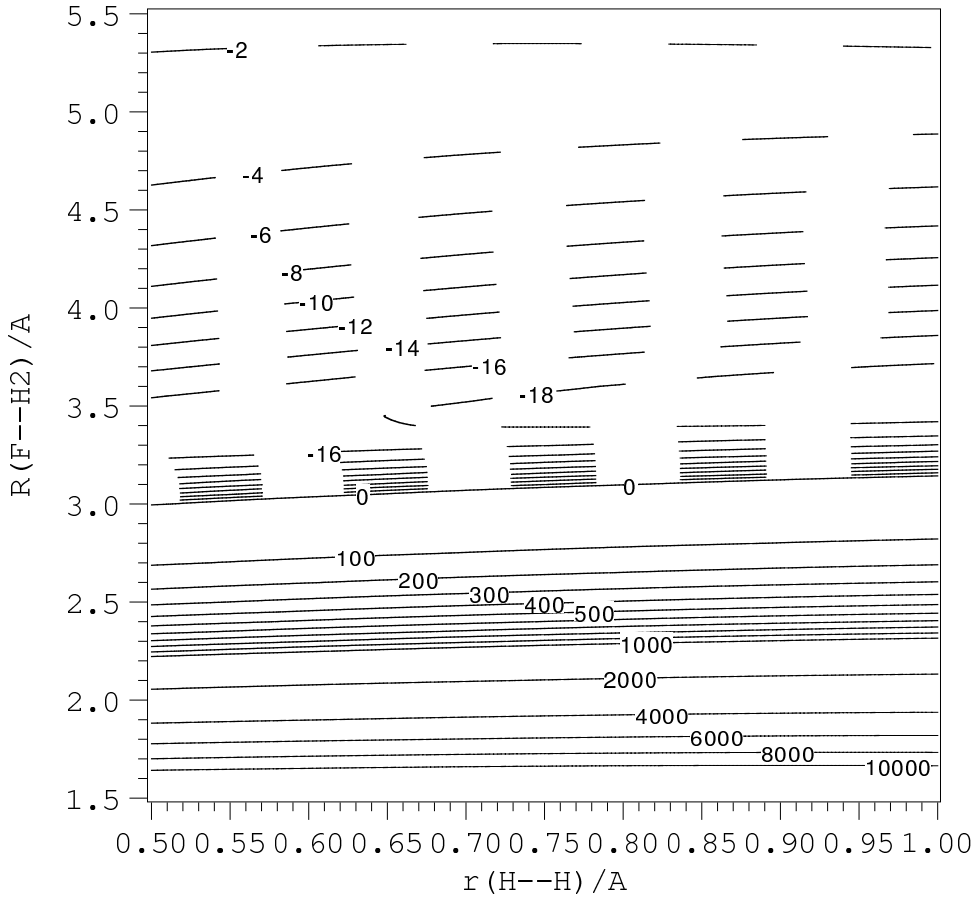

Figure 7.11: (R,r)-dependence of energies of B_1 symmetry. Values in cm^{-1}.

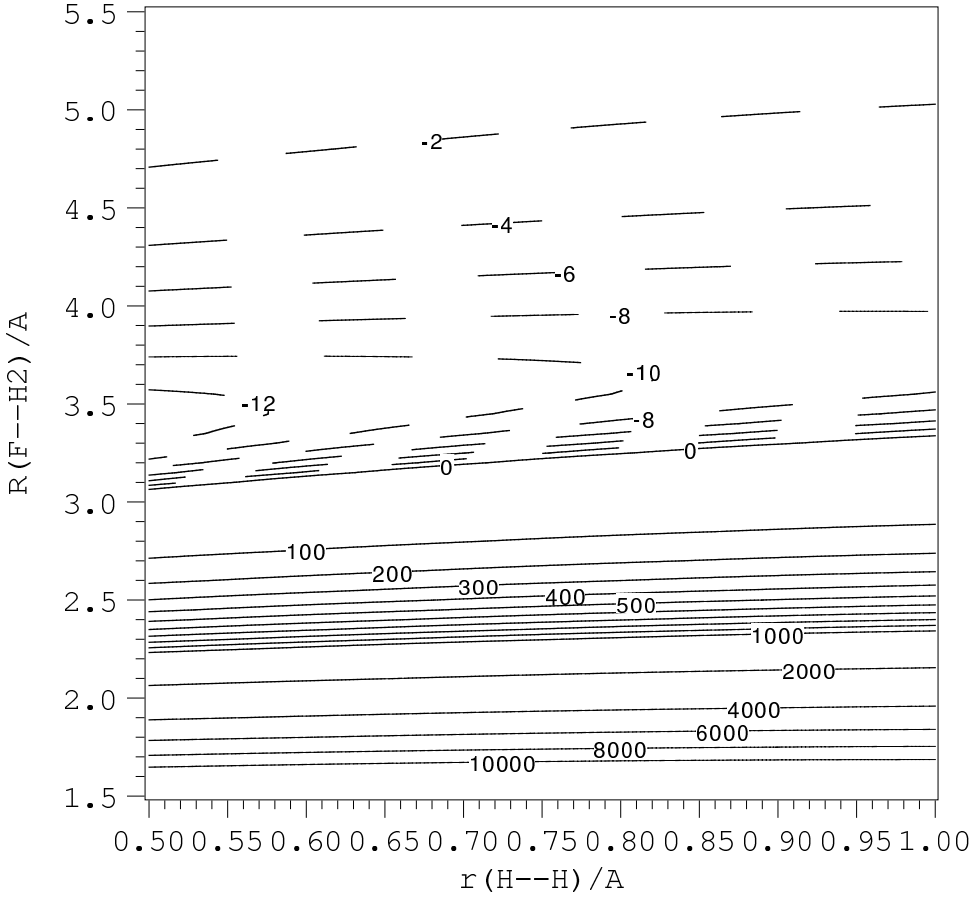

Figure 7.12: (R,r)-dependence of energies of B_2 symmetry. Values in cm^{-1}.

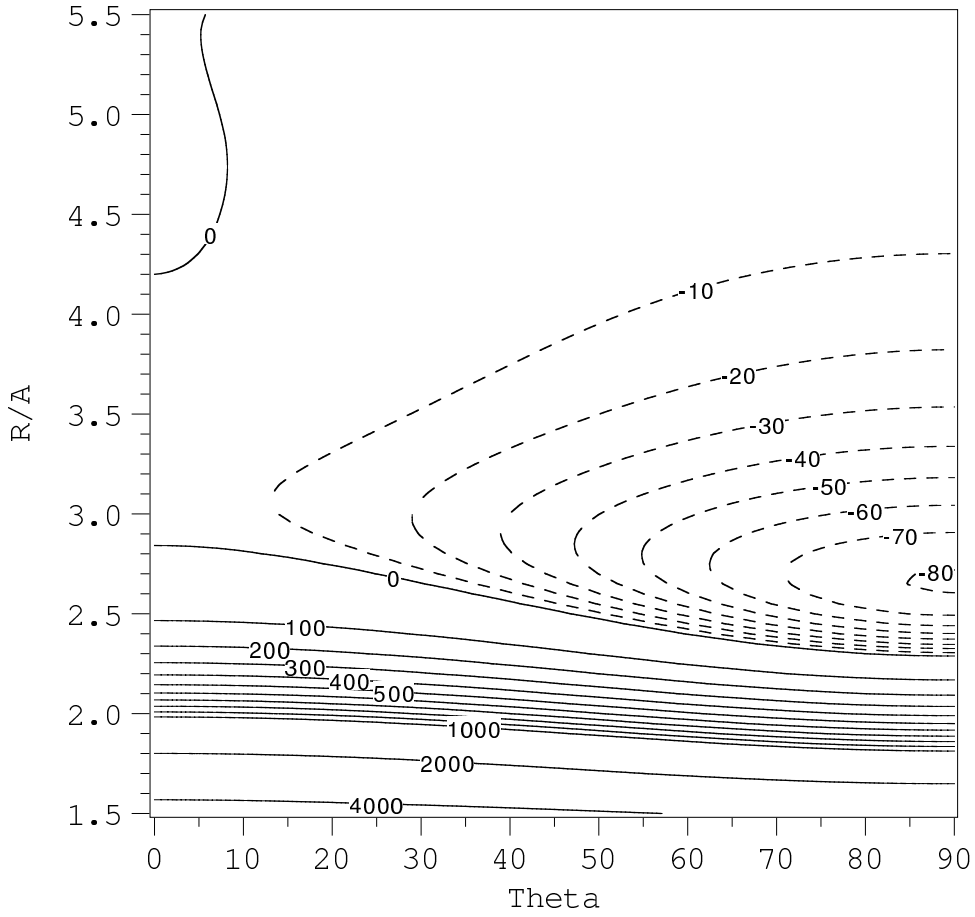

Figure 7.13: Contour plot of the modeled H_{11}^{CC-M} diabat. Values in cm^{-1}, $r = 0.529177$ Å.

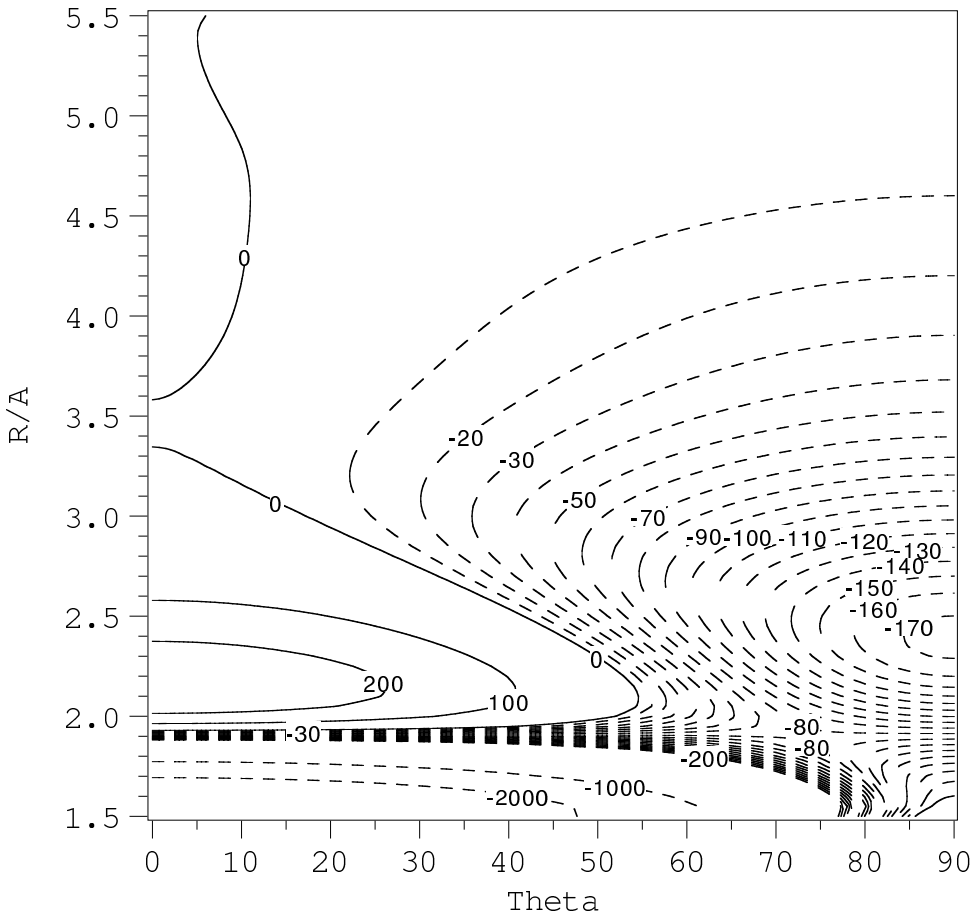

Figure 7.14: Contour plot of the modeled H_{11}^{CC-M} diabat. Values in cm^{-1}, $r = 0.846683$ Å.

minimum energy path around F is now shallower and flatter, and the pass across the reaction barrier is closed.

By contrast, stretching H_2 to $r = 0.8466$ Å (Figure 7.14) makes the T-shaped minimum deeper - from -130 down to -170 cm^{-1} - whereas the saddle in the barrier goes down to -80 cm^{-1} and widens. The collinear configuration is only slightly shallower, and at the stationary point the interaction practically vanishes. In other words, stretching H_2 deepens the entrance well but also broadens and lowers the pass across the reaction barrier.

The effect of stretching and compressing of H_2 on the H_{22} and H_{33} diabats is minor, so we do not show it in figures. The H_{22} collinear stationary point goes up by 10 cm^{-1} on squeezing and a few cm^{-1} on stretching. H_{33} is affected even less.

Since the reaction occures on the ground state adiabatic surface it is instructive to note the changes of the 1A' state. Qualitatively it is similar to the adiabat at r_e. Upon stretching this state becomes deeper, the well depth raising from 130 cm^{-1} to 170 cm^{-1}. At the same time, the barrier for the reaction is lowered from 600 cm^{-1} down to -100 cm^{-1}, and is shifted from 40° to 70°, that is closer to the T-shape geometry.

7.4.1 Spin-orbit coupling and model relativistic adiabatic PESs

Upon allowing for spin-orbit coupling of the halogen atom one obtaines two atomic terms: $^2P_{3/2}$ and $^2P_{1/2}$, separated by Δ_{SO}=404 cm^{-1}. The interaction with H_2 further splits the $^2P_{3/2}$ state into two states. To evaluate the resulting adiabatic potential energy surfaces we used the procedure described by Alexander, Manolopoulos, and Werner .[97] The matrix of the electrostatic interaction plus the spin-orbit Hamiltonian was expressed in the basis set invariant to time reversal (see Ref. [97] for details). Then the total matrix decouples:

$$\mathbf{H}^{el} + \mathbf{H}^{SO} = \begin{bmatrix} \mathbf{H} & 0 \\ 0 & \mathbf{H}^{\dagger} \end{bmatrix}, \tag{7.16}$$

where $\mathbf{H}$ is the 3x3 Hermitian matrix expressed in the basis invariant to time reversal:

$$\mathbf{H} = \begin{bmatrix} H_{11} & -V_1 - i\sqrt{2}B & V_1 \\ & V_{\Pi} + A & V_2 \\ & & V_{\Pi} - A \end{bmatrix}, \tag{7.17}$$

where $V_1 = 2^{-1/2}H_{12}$, $V_{\Pi} = (H_{33} + H_{22})/2$ and $V_2 = (H_{33} - H_{22})/2$. A and B are spin-orbit matrix elements:

$$A \equiv i\langle \Pi_y | H^{SO} | \Pi_x \rangle \tag{7.18}$$

and

$$B \equiv \langle \bar{\Pi}_x | H^{SO} | \Sigma \rangle \tag{7.19}$$

where, after Alexander et al. ,[97] we use compact Caretesian notation for diabatic states: $|\Pi_x\rangle$,$|\Pi_y\rangle$, and $|\Sigma\rangle$, related to the projections of the electronic orbital and spin momenta along the vector R. The bar above the $|\Pi_x\rangle$ state in Eq. 7.19 denotes β spin. We have found in the

Van der Waals region that A and B are practically independent of R and θ, and we fixed both at the value of $1/3\Delta_{SO}$ (in the limit of large R, A equals B). Significant changes in A and B start when the F atom approaches the H_2 molecule closer than at 2.0 Å. On diagonalizing the matrix Eq. 7.17, three adiabatic potential energy surfaces were obtained, shown in Figures 7.15, 7.16 and 7.17. They are numbered in the order of increasing energy. In the limit of large R, the first two adiabatic PESs correlate to the $^2P_{3/2}$ state of F, with the projection of j upon the R vector equal to 3/2 and 1/2 for the ground state and the first excited state, respectively. The third adiabat (Figure 7.17) correlates with the $^2P_{1/2}$ term of F atom.

One can see that the relativistic adiabatic surfaces significantly differ from non-relativistic ones. The lowest adiabatic surface is now half as deep at the T-shaped minimum (D_e=64 cm^{-1}) and considerably flattened, with a 24 cm^{-1} barrier for the H_2 rotation, around 40°, and another local minimum for the collinear arrangement (D_e=45 cm^{-1}). The other adiabatic surface related to the same $^2P_{3/2}$ asymptotic limit is shallower, with a maximum at 90° and a minimum at 0°. The third state, asymptotically separated by 404 cm^{-1} SO coupling, resembles the second in shape, but is slightly deeper.

The results for the lowest relativistic adiabatic PES may be compared with those of Werner and collaborators.[97,130] Our results of R_e=2.8 Å and D_e=64 cm^{-1} agree very well with the more accurate values from Ref.:[130] 2.85 Å and 60.3 cm^{-1}.

These results corroborate the finding of Alexander, Manolopoulos and Werner that the "spin-orbit coupling cannot be neglected in the region of the van der Waals minimum [...] and significantly alters both the depth and position of the van der Waals well". The D_e and R_e parameters of the three adiabatic PESs are listed in Table 7.2.

Table 7.2: Stationary points of modeled spin-orbit corrected adiabatic surfaces.

Adiabat	D_e/cm^{-1}	R_e/Å	θ_e	Type
adiabat 1	64	2.80	90	minimum
adiabat 1	45	3.35	0	minimum
adiabat 2	19	3.40	37	minimum
adiabat 2	18	3.35	0	saddle
adiabat 2	14	3.50	90	saddle
adiabat 3	30	3.35	0	minimum
adiabat 3	26	3.30	90	saddle

7.5 Summary and Conclusions

Model diabatic potentials CC-M for the first three states of the H_2-F complex have been derived from *ab initio* calculations for the T-shaped and collinear forms at the CCSD(T) level of theory with a large basis set. The three adiabatic surfaces are in very good agreement with those of Alexander, Stark and Werner from Ref. ,[97] as evidenced in Table 7.1, where the parameters for all stationary points are compared. In addition, the height of the barrier predicted by our model in the reaction channel is 1.66 kcal/mole, also very close to the Stark and Werner [96] best estimate of 1.45±0.25 kcal/mole. This is gratyfying, since the SW PES was obtained by different ab initio method, and different scaling was applied.

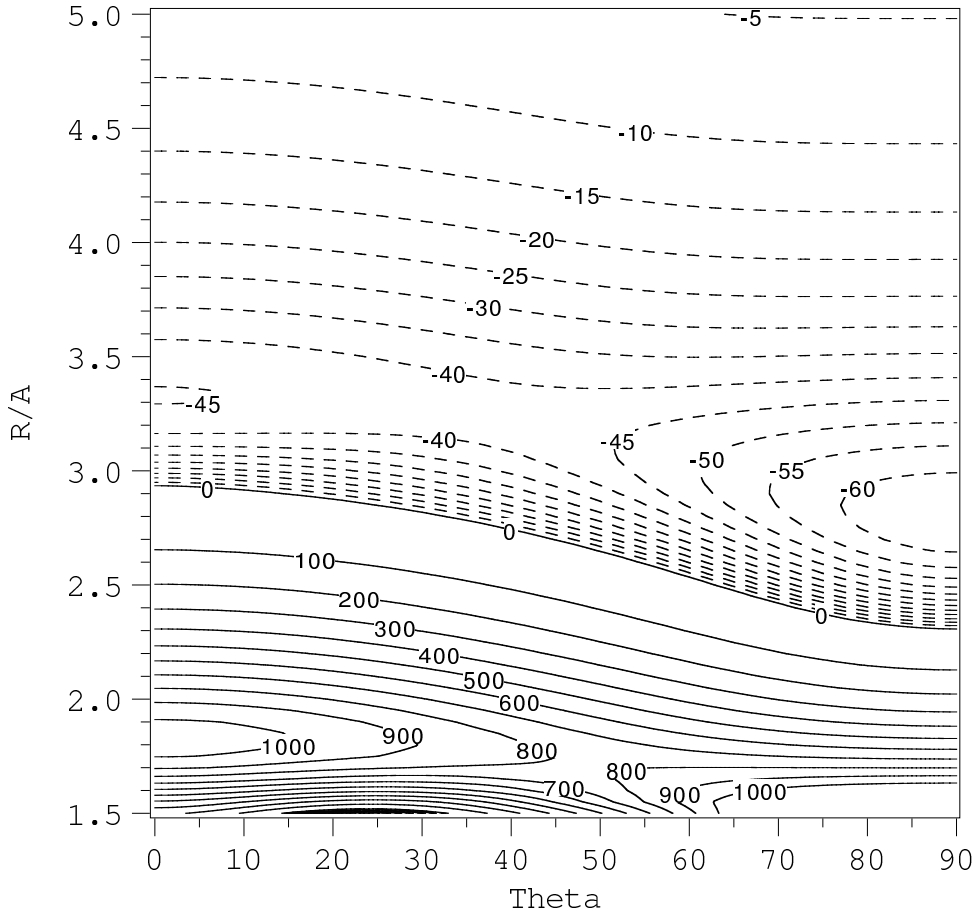

Figure 7.15: Contour plot of the spin-orbit corrected adiabat 1, which correlates to $F(^2P_{3/2})$. Values in cm^{-1}.

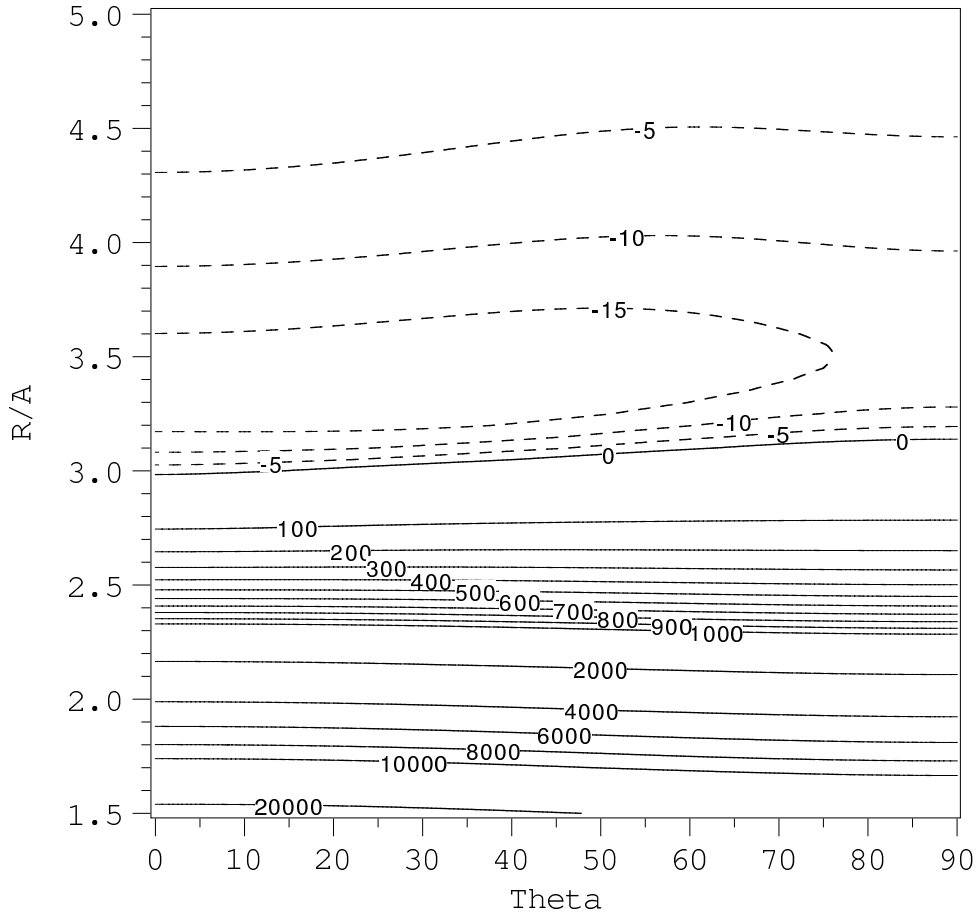

Figure 7.16: Contour plot of the spin-orbit corrected adiabat 2, which correlates to F($^2P_{3/2}$). Values in cm^{-1}.

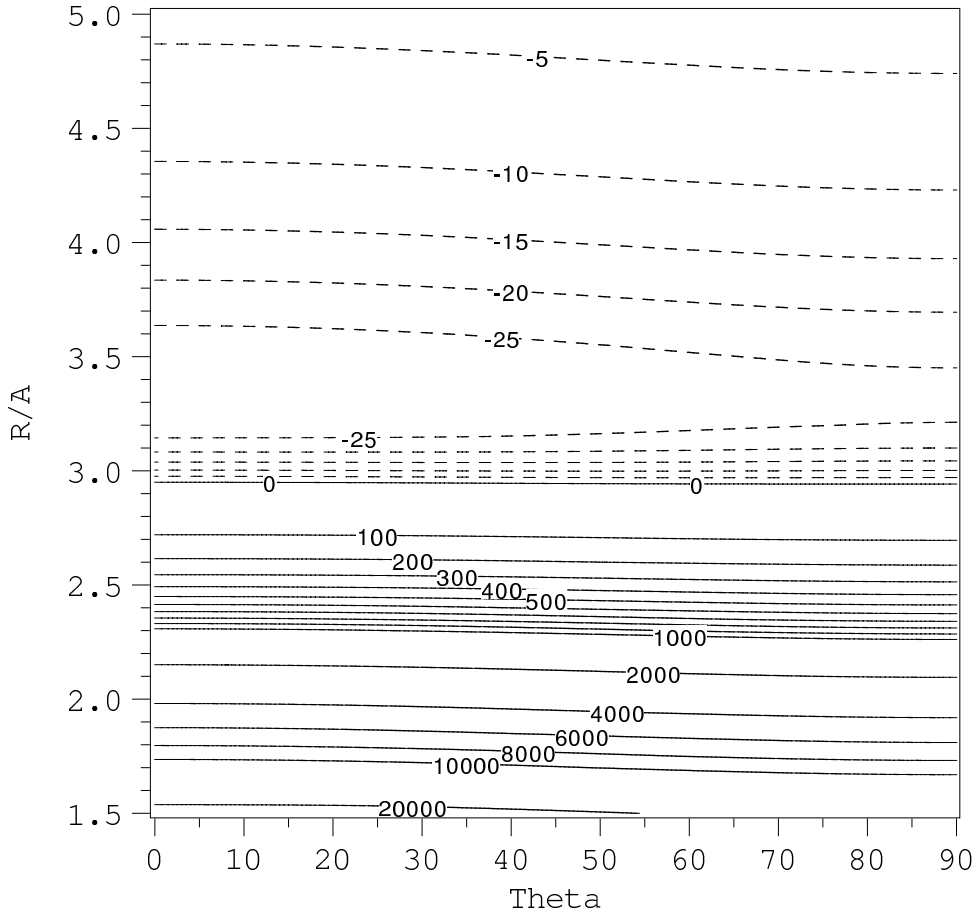

Figure 7.17: Contour plot of the spin-orbit corrected adiabat 3, which correlates to $F(^2P_{1/2})$. Values in cm^{-1}.

The 3-D CC-M PESs that includes functional dependance on the r distance have also been proposed, fitted and analyzed. It has been found that the ground state is quite sensitive to the changes in r. In particular, the height of the barrier lowers with stretching the H_2 molecule, and rises with compressing it.

The ground state diabatic nonrelativistic 1A′ PES of H_2-F may be compared with the the ground state 1A′ PES of H_2-Cl which was derived recently by us within the same CC-M framework. The intermediate and long range of these surfaces are similar, with the H_2-Cl Van der Waals well being deeper by 30 cm^{-1} (D_e of 164 cm^{-1}), but with almost the same hindrance for the H_2 rotation of ca. 85 cm^{-1}. A major qualitative difference is in the character and magnitude of the reaction barrier. The F-H_2 system with H_2 at the equilibrium r_e has a low and narrow pass in the barrier of +750 cm^{-1} at $\theta = 40 - 45°$. By way of contrast, we did not found any such pass in the Cl-H_2 short range repulsive wall.[146] In addition, Bian and Werner[150] have reported that the barrier for the reaction is collinear and more central, of 7.6 kcal/mole = 2658 cm^{-1}, with the H_2 considerably stretched.

The characteristics of the PESs is dramatically changed upon allowing for the spin-orbit effects. The relativistic ground state adiabatic PES is half as deep as the nonrelativistic one, 64 cm^{-1} vs. 131 cm^{-1}, and the barrier to the rotation of H_2 is shifted toward 40° and lowered from 86 cm^{-1} to 24 cm^{-1}, whereas the collinear saddle point transforms into a minimum. The second and third adiabatic surfaces are also considerably flattened. These results agree with the finding of Alexander, Manolopoulos and Werner that the "spin-orbit coupling cannot be neglected in the region of the van der Waals minimum [...] and significantly alters both the depth and position of the van der Waals well". Very good quantitative agreement with the results of Ref.[97] should be stressed. We also found that the spin-orbit coupling raises the reaction barrier by about 200 cm^{-1}, with respect to the F+H_2 reactants, again in fairly good accord with the more accurate result of 131 cm^{-1} of Alexander, Manolopoulos and Werner[97] .

Finally, it is worthwhile to stress that our CC-M approach is expected to provide reliable PESs for other atom-H_2 complexes as well, which are in the entry channels of many reactions, such as O+H_2, N+H_2, S+H_2, etc.

CHAPTER VIII

Ab initio calculations and modeling of adiabatic and diabatic potential energy surfaces of $Cl(^2P)\cdots H_2(^1\Sigma^+)$ Van der Waals complex

8.1 Introduction

The hydrogen-abstraction reaction $Cl + H_2 \rightarrow ClH + H$ is a fundamental reaction in chemical kinetics and hence has been the subject of a great deal of experimental and theoretical work .[93,150–164] Along with the related system $F+H_2$, they constitute important paradigms in the field of chemical reaction dynamics. The systems complement each other: while several of their characteristics are similar, they were recently shown to reveal a most puzzling difference in reactivity of the excited spin-orbit states. So far most of the *ab initio* calculations have focused upon the transition state region. The most advanced potential energy surfaces available for this reaction include semiempirical LEPS surfaces and the recent G3 surface, which resulted from an *ab initio* modification of the LEPS model in the transition state region.[156,158] Both surfaces are, however, too crude to identify a weakly-bound Van der Waals complex between $Cl(^2P)$ and $H_2(^1\Sigma^+)$. Only very recently Bian and Werner reported a globally reliable *ab initio* potential energy surfaces, BW1 and BW2, which included prediction and characterization of this complex . Not only does this complex exist - with a T-shaped minimum on a $^2A_1$ surface of 175 cm^{-1}[150] - but it also dramatically influences the reaction path and composition of products in the Cl+HD reaction.[93,165] Exact quantum mechanical calculations of reactive scattering on a PES without Van der Waals forces predict that the HCl and DCl products will be produced almost equally, whereas the same calculations on the BW2 surface show a strong preference for the production of DCl. The latter is in agreement with the experimental findings of Lee and Liu, and Dong et al. [154,155,166] These pioneering works of Bian and Werner, and Skouteris et al. demonstrated that even comparatively weak Van der Waals interactions can no longer be neglected in calculations of PESs of chemical reactions. At the same time, this is only the very beginning of a serious research in this area. The BW2 surface is a global PES which includes the entrance channel, barrier, and the exit channel regions. It was advanced using the IC-MRCI method. The authors reported that even with their largest basis set neither the barrier height nor the HCl dissociation energy was converged. To overcome this problem they resorted to empirical scaling. It is interesting to determine whether the introduction of this empirical scaling compromised the accuracy of the Van der Waals region. At the time of this writing, only ground state's adiabatic surface has been reported. A conical intersection between the ground

and the first excited states of the A′ symmetry, which for a wide range of geometries are very closely spaced and avoid crossing, increases the difficulties.

The goal of this paper was to focus on the Van der Waals region, and to provide accurate *ab initio* PES for the first three states of Cl+H_2 in the entrance channel fragment. The three states arise from the interaction of H_2 with the triply degenerate ^{2}P Cl atom. The electron configuration of Cl gives rise to $^2\Sigma$ and $^2\Pi$ states in the $C_{\infty v}$ configuration, to $^2A_1$, $^2B_1$, $^2B_2$ states in the triangular C_{2v} geometry, and to $1^2A'$, $2^2A'$ and $^2A''$ states in C_s geometries.

To calculate the interaction energies, a combination of the CCSD(T) method and the MRCISD+Q method was used. The essence of our approach is to model three lowest diabatic PES by using accurate CCSD(T) interaction energies evaluated for two highly symmetrical configurations, $C_{\infty v}$ collinear form and C_{2v} T-shaped form. The fourth diabatic PES (related to the nonadiabatic coupling matrix element) as well as the anisotropy of the interaction are evaluated from separate MRCISD+Q calculations with a medium-sized basis set over the complete range of geometries. Two templates to model anisotropy of the diabatic PESs are proposed and tested: MRCI-Scaled (CI-S) and CCSD(T)-Model (CC-M). The former employes a scaling of the MRCI interaction energies for geometries $0°<\theta<90°$, while the latter assumes a very simple linear combination of the T-shaped and collinear interaction energies with the coefficients of $\sin^2\theta$ and $\cos^2\theta$, respectively. To obtain three lowest adiabatic PESs, the hamiltonian in the diabatic basis is diagonalized. Allowing for spin-orbit coupling effects is straightforward by using the formalism recently developed by Alexander, Manolopoulos, and Werner ,[97] and assuming empirical value of the splitting parameters.

8.2 Computational methods and results

8.2.1 Geometries and basis sets

The Cl-H_2 complex is described in Jacobi coordinates (R,θ). The R variable denotes the distance between the center of the H_2 monomer and the Cl atom, and θ denotes the angle between the $\vec{R}$ vector and the H_2 bond axis. $\theta = 0°$ corresponds to the Cl$\cdots$H-H collinear arrangement. The H_2 monomer was kept rigid at the interatomic separation $r = 0.7408$ Å. The origin of the system of coordinates was placed at the center of the H_2 molecule. In the calculations of the diabatic energies, the H_2 molecule was located along the x axis , and the z axis was perpendicular to the triatomic plane. Calculations employed the augmented correlation-consistent polarized basis sets of double, triple, quadrupole and quintupole zeta quality of Dunning et al. [99–101] Some calculations included also bond functions of Tao and Pan ,[36] with the exponents:sp 0.9, 0.3, 0.1;$d\,f$ 0.6, 0.2;g 0.3, in the form of two sets: [3s3p2d] denoted as (332) and [3s3p2d 2f 1g] denoted (33221) . Bond functions were centered in the middle of the vector $\vec{R}$. Bond functions were shown to be both effective and economical for a number of Van der Waals complexes which included rare gas atoms .[21,24,147,148]

8.2.2 *Ab initio* calculations of interaction energies

All calculations reported in this paper were performed using MOLPRO package.[53] The supermolecular method was used in calculations of three adiabatic potential energy surfaces. This method derives the interaction energy as the difference between the energies of the dimer

AB and the monomers A and B

$$\Delta E^{(n)} = E_{AB}^{(n)} - E_A^{(n)} - E_B^{(n)} \tag{8.1}$$

The superscript (n) denotes the level of *ab initio* theory. In the CCSD(T) calculations the use of the above equation is straightforward, and free from arbitrary choices, as long as the dimer and monomer energies are calculated with the same dimer centered basis set. The CCSD(T) method is well known to be very effective in recovering electron correlation effects in Van der Waals complexes calculations,[16,17] and is preferred as long as the single-reference approach is valid and efficient. If not, one has to use the MRCI approach. The MRCI calculations are more involved as they require the size consistency corrections and counterpoise correction at the diabatic level. We describe application of MRCI in Sec. 8.2.3.

8.2.3 MRCI calculations of adiabatic and diabatic surfaces

MRCI calculations began with the determination of the state-averged CASSCF orbitals which assumed the Cl-moiety-related orbitals as follows: the 1s orbital frozen, the 2s and 2p orbitals doubly occupied, and the 3s and 3p orbitals active. We included also σ_g and $\sigma_u^\star$ molecular orbital in the active space. The state averaged CASSCF orbitals allowed for [122,123] all three states, 1A′, 2A′, and 1A″. The subsequent internally contracted MRCI calculations[112,113] included all single and double excitations relative to the full-valence CASSCF reference wave functions. In the case of two A′ states, the excitations relative to both reference states were included, and both states were optimized simultanously. This guarantees a balanced treatment in the regions of the conical intersections.[149]

The diabatic surfaces provide more convenient representations for simulations of the Van der Waals spectra of the system. These potentials contain information about couplings between the adiabatic wavefunctions of the same symmetry. The adiabatic-diabatic transformation yields diabatic states for which the non-adiabatic coupling matrix elements approximately vanish. The diabatic states are obtained by a unitary orthogonal transformation of adiabatic states[108,109]

$$\begin{bmatrix} \Psi_1^d \\ \Psi_2^d \end{bmatrix} = \begin{bmatrix} \cos\gamma & \sin\gamma \\ -\sin\gamma & \cos\gamma \end{bmatrix} \begin{bmatrix} \Psi_1^a \\ \Psi_2^a \end{bmatrix}, \tag{8.2}$$

where the transformation angle γ depends on the nuclear coordinates. The resulting diabatic wavefunctions are no longer eigenstates of the electronic Hamiltonian. The Hamiltonian in the diabatic (p_x, p_y, p_z) basis is not diagonal and the matrix elements are

$$\begin{aligned} H_{11} &= \cos^2\gamma V_{1A'} + \sin^2\gamma V_{2A'} \\ H_{22} &= \sin^2\gamma V_{1A'} + \cos^2\gamma V_{2A'} \\ H_{12} &= (V_{1A'} - V_{2A'})\cos\gamma\sin\gamma \end{aligned} \tag{8.3}$$

The third diabatic state, H_{33}, is exactly equal to the 1A″ adiabatic state.

The transformation angle γ, the so-called 'mixing angle', is defined as the angle between the vector of singly occupied p orbital and the $\vec{R}$ vector. This angle is a function of Jacobi coordinates of the system, and depends on the orientation of the H_2 molecule. Contour plot of the mixing angle is shown in Figure 8.1.

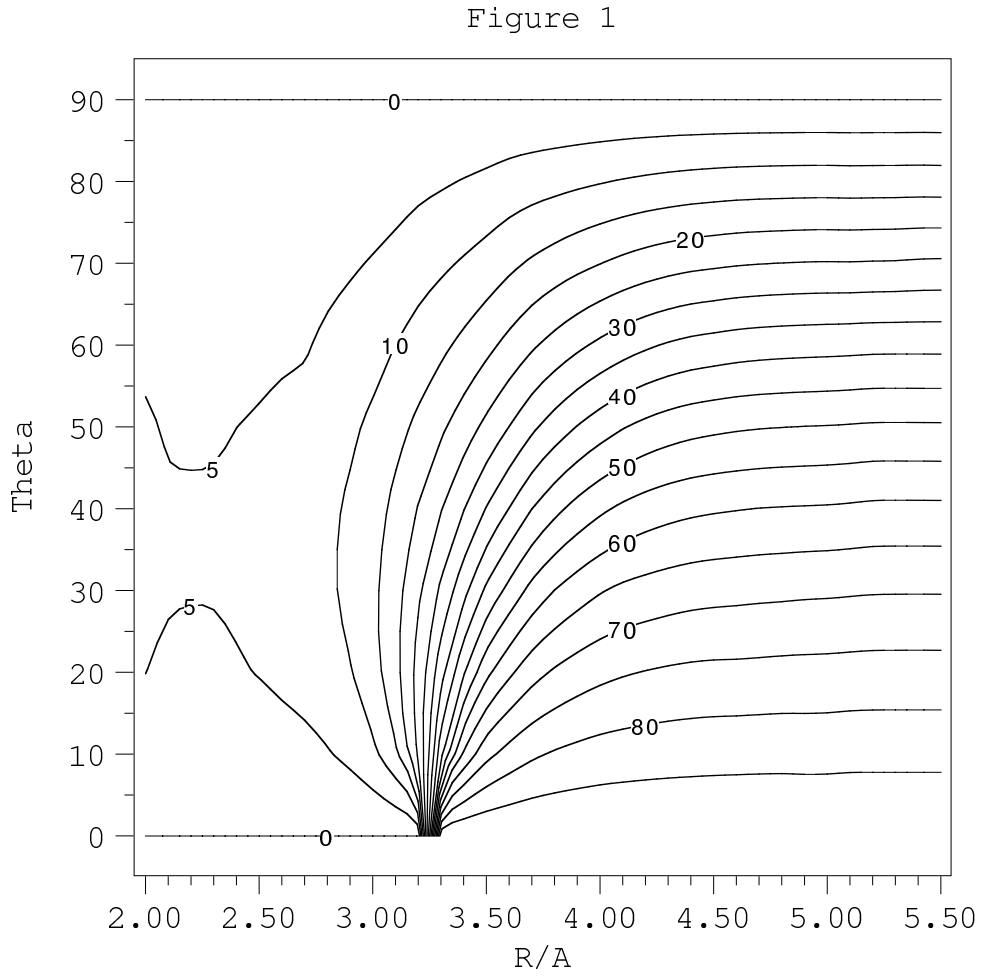

Figure 8.1: Contour plot of the γ_R mixing angle calculated in aug-cc-pvqz/tz basis set.

Within a two-state model the mixing angle can in principle be obtained by numerical integration of the non-adiabatic coupling matrix elements (NACMEs) using the relation

$$\frac{\partial \gamma\left(R,\theta\right)}{\partial q} = \left\langle 1A' \left| \frac{\partial}{\partial q} \right| 2A' \right\rangle \ . \tag{8.4}$$

This is quite computationally demanding procedure, which suffers from the fact that the NACMEs are strongly varying functions of the geometry and have poles at the conical intersections. Also, in real systems the integration is not entirely path independent, due to the admixture of further states.[110] Eq. 8.4 is only valid for the two-state model, and diabatization procedure is approximate in any case for polyatomic molecules. Therefore, we used a less expensive methods which determine the mixing angle directly with reasonable accuracy.[111] One of those methods is based on the transition angular momentum connecting the 1A″ state with two states of the A′ symmetry.

$$\gamma = \tan^{-1}\left[\frac{\left|\left\langle 1A' \left| \hat{L}_x \right| 1A'' \right\rangle\right|}{\left|\left\langle 2A' \left| \hat{L}_x \right| 1A'' \right\rangle\right|}\right] \tag{8.5}$$

The second method uses the maximal overlap with orbitals of the reference geometry to calculate mixing angle. This method calculates NACME in an approximate way using two slightly displaced geometries and method of finite differences. Both methods gave very close results, so finally we used mixing angle from the latter one.

Since it is expedient to perform diabatic transformation in a system of coordinates with one of the axis along the $\vec{R}$ vector, the actual γ was redefined as:

$$\gamma_R = \gamma + \theta - \frac{\pi}{2} \tag{8.6}$$

The plot of γ_R values is shown in Figure 1. The region where the A′ states avoid crossing each other and where the mixing is the strongest is related to the angle in Eq. 8.2 of 45°. For large R it corresponds to perpendicular approach, but around $R \approx 4$ Å it abruptly turns towards the collinear arrangement, where the conical intersection occurs at Cl$\cdots$H-H, $\theta = 0°$, $R \approx 3.25$ Å, and the crossinging of the Σ^+ and Π symmetries.

It is important to report here our finding that the γ_R angle is well reproduced by MRCISD calculations with substantially smaller basis set, of double-zeta or triple-zeta quality. This is shown in Figures 8.2, 8.3 and 8.4, where the mixing angle is plotted against θ at selected short, intermediate and long distances of 2.5 Å, 3.2 Å and 5.5 Å , respectively.

This finding is of practical importance since one may use the angle γ_R from relatively cheaper calculations. It should also be stressed that also the CASSCF calculations provided a very reasonable approximation to this angle.

Calculations of interaction energies as the difference of the dimer and monomer energies, Eq. 8.1, requires consistent evaluation of these energies. The issue of consistency is particularly challenging for the MRCI calculations since both the size consistency and the basis set consistency corrections should be included. The latter requires correcting monomer energies not only for the extension of the one-electron basis but also for the extension of many-electron configuration states. Since the configurational consistency is practically impossible to achieve (see Ref.[167]), only standard counterpoise correction is applied. To ensure consistency upon

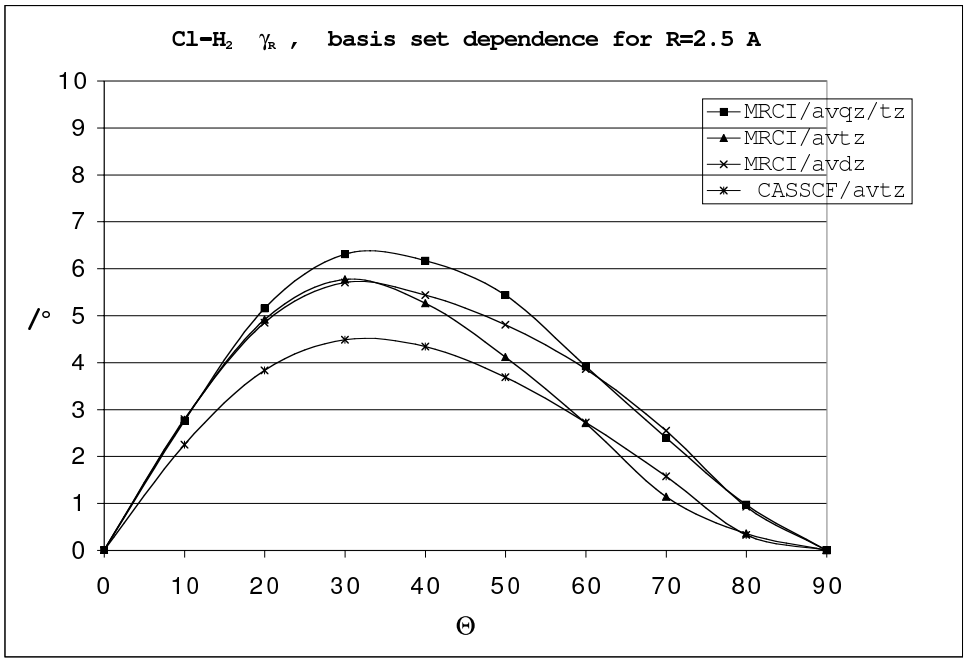

Figure 2a

Figure 8.2: Comparison of γ_R mixing angle calculated in various basis sets and methods. Distance is 2.5 Å.

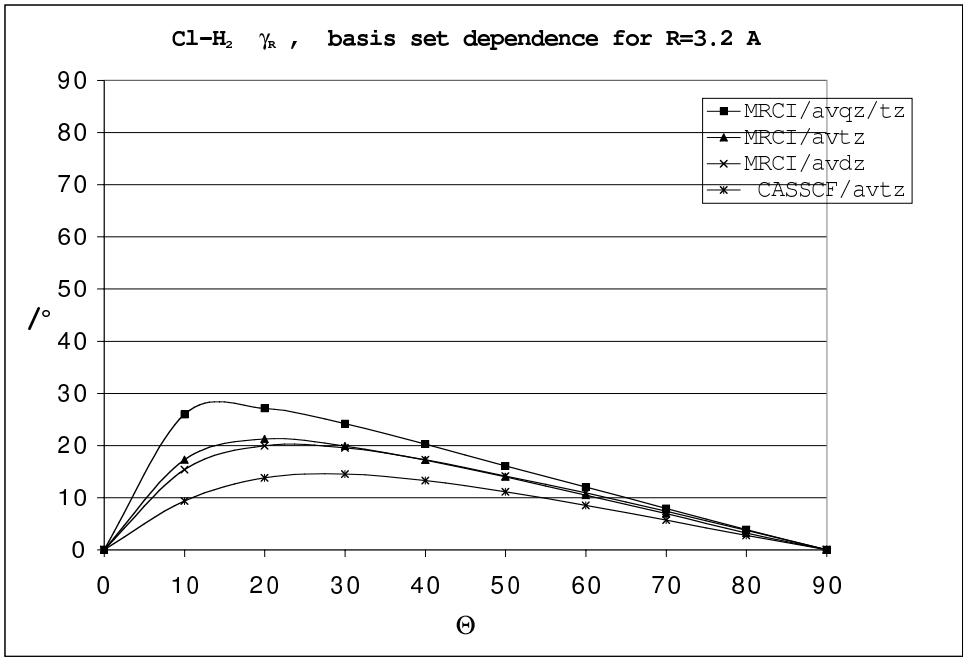

Figure 2b

Figure 8.3: Comparison of γ_R mixing angle calculated in various basis sets and methods. Distance is 3.2 Å.

dissociation at the same time, one uses the formula:[108]

$$V(R,\theta) = E_{Cl-H_2}(R,\theta) - E_{Cl}(R,\theta) - E_{H_2}(R,\theta) - \Delta_{SC} \tag{8.7}$$

where

$$\Delta_{SC} = E_{Cl-H_2}(\infty) - E_{Cl}(\infty) - E_{H_2}(\infty) \tag{8.8}$$

and all energies in Eq. 8.7 were calculated with dimer centered basis set. It is recommended, after Alexander,[108] that the CP corrections are applied for diabatic rather than adiabatic energies. To obtain CP-corrected adiabatic interaction energies one should invert the diabatic transformation.

Application of bond functions within MRCI proved to cause serious problems: the angle γ_R came out qualitatively distorted and the values of the interaction energies become suspect, see Sec. 8.2.4.

The final diabatic H_{11}, H_{22}, H_{33} and H_{12}, and adiabatic $1A'$ and $2A'$ (notice that A''=H_{33}) surfaces obtained at the MRCISD+Q/acpvqz/tz are shown in Figures 8.5, 8.6 , 8.7, 8.8, 8.9 and 8.10, respectively.

8.2.4 Benchmark CCSD(T) results for T- and L-geometries

To investigate basis set saturation in the region close to the minima for the T- and L-form, the interaction energies were obtained with a sequence of basis set, and are listed in Tables 8.1, 8.2, 8.3.

Table 8.1: Benchmark CCSD(T) results for T- and L-geometries. Results are corrected for BSSE and calculations were performed in C_{2v} symmetry. Values in cm^{-1}

Basis	A_1	Π
avtz	130.0	68.4
avqz/tz	147.6	72.0
avqz	157.1	73.8
av5z	163.1	75.6
CBS	166.5	76.7
Basis+bond functions		
avqz/tz+332	163.8	75.9
av5z+33221	167.2	76.8

Both CCSD(T) and MRCISD+Q results are compared. In the case of MRCISD+Q calculations, we also show the results uncorrected for BSSE. In addition, the MRCISD+Q values calculated both within the C_{2v} and C_s point groups of symmetry are shown, since they apparently differ. The two-exponential formula of Peterson, Woon and Dunning [168] for the CBS limit was also tested:

$$f_n = ae^{-(n-1)^2} + be^{-(n-1)} + f_{CBS} \tag{8.9}$$

Table 8.2: Benchmark CASSCF/MRCISD+Q results for T- and L-geometries. Results in parentheses are not corrected for BSSE. Calculations were performed in C_{2v} symmetry. Values in cm^{-1}

Basis	A_1	Π
avtz	136.5 (177.3)	73.7 (120.5)
avqz/tz	168.3 (185.3)	88.9 (106.2)
avqz	173.4 (193.6)	89.0 (109.3)
av5z	171.4 (192.9)	84.7 (103.2)
CBS	170.1 (192.4)	82.1 (99.6)
Basis+bond functions		
avqz/tz+332	141.5	67.5

Table 8.3: Benchmark CASSCF/MRCISD+Q results for T- and L-geometries. Results are corrected for BSSE. Calculations were performed in C_s symmetry. Values in cm^{-1}

Basis	A_1	Π
avdz	92.0	69.0
avtz	130.0	100.0
avqz/tz	154.6	100.1
Basis+bond functions		
avqz/tz+332	287.3	272.8

where three parameters: a, b and f_{CBS} were optimized and n denotes the basis set: n=2 coresponds to double-zeta, n=3 to triple-zeta, and so on.

The CCSD(T) energies converge smoothly and monotonically along the sequence of basis sets: avtz, avqz, av5z and av5z+33221. In addition, the CBS limit for the avtz, avqz and av5z sequence is extremely close to the av5z+33221 results . One can see that the values with bond function and the values of the CBS limit nicely corroborate each other.

The MRCI results, however, reveal a less satisfactory behavior. The convergence along the sequence of basis sets: avtz, avqz and av5z, is less smooth and not monotonic. The best results are somewhat larger than the CCSD(T) results, and so are the related CBS limits. Since the CP-correction, which is a correction for using one-electron dimer centered basis set rather than monomer centered basis set for monomers, does not cover all basis set inconsistencies in the MRCI case (because of configuration state functions inconsistncies in the monomer and dimer calculations) one expects a larger BSSE error still present here than in the CCSD(T) case. One can also see that the CBS limit of the CP-uncorrected energies is substantially larger than that for the CP-corrected - a clear indication of a more serious basis set error.

An important observation, repeatedly reported in the literature before,[18,169,170] is that Molpro's MRCI gives different results when constrained to the C_{2v} or $C_{\infty v}$ geometry, from those left unconstrained within the C_s symmetry. The differences are far from negligible and not regular. For example, avtz basis set leads to 136 cm^{-1} for the A_1 minimum and 74 cm^{-1} for

the Π minimum when the calculations use the C_{2v} symmetry. When the calculations use the C_s symmetry the related values are 130 cm^{-1} and 100 cm^{-1}, respectively. We treat here the C_s results as less reliable.

A final remark pertains the use of bond functions. The CCSD(T) energies in Table 8.1 are nicely and rationally improved after including bond functions. By way of contrast, the MRCI results are erratic. For instance, the C_{2v} MRCI avqz/tz+332 calculations gave much too small interaction energies, whereas the C_s MRCI avqz/tz+332 calculations yielded nonsensically large energies. A plausible reason is that bond functions produce large BSSE, which, as already mentioned, in the MRCI case cannot be fully counterpoised. We conclude that the bond function should not be used within the MRCI framework.

Overall, very consistent results of CCSD(T) method and a good agreement with the best MRCI energies give us confidence that the CCSD(T) interaction energies provide a reliable benchmark to scale the MRCI PESs. The latter will be done in the next Sec. 8.2.5.

8.2.5 Model diabatic PESs

In the previous Sec., the CCSD(T) results for the T-shaped and collinear complexes were shown to provide excellent benchmarks for the interaction energies in these particular arrangements. Indeed, the CCSD(T) approach can provide us with very accurate results, close to saturation with respect to basis set and correlation effects. It can be used with confidence for the lowest state of a given symmetry, but also for excited states that can be adequately represented by a single Slater determinant - for instance when the excited state is related to a single-electron promotion from one p orbital to another, orthogonal p orbital. The latter feature was exploited in our recent study of the HCl-Cl Van der Waals complex ,[125] where two A′ states in the Van der Waals region were for a wide range of geometries are well separated.

By way of contrast, for the H_2-Cl(^{2}P) complex the CCSD(T) proved to be unreliable for the C_s geometries. The plausible reason is that the interaction of the ^{2}P Cl with H_2 is three times as weak as with HCl (the 1A′ well depth is 163 cm^{-1} for H_2-Cl(^{2}P) vs. 586 cm^{-1} for HCl-Cl(^{2}P)[125]), and hence also the splitting 1A′-2A′ is much smaller. Consequently, nonadiabatic mixing and multireference treatment of two adiabatic A′ states are more important in the regions where the configurations are allowed to mix.

Therefore, in the area between the collinear and perpendicular arrangements the MRCI method was used (see Sec. 8.2.3, which provided us with 3 surfaces and their nonadiabatic coupling. Despite a smaller basis set without bond functions, the resulting adiabatic energies and the mixing angle were accurate enough to reliably reproduce the anisotropy of the interaction caused by rotation of the H_2 molecule.

Next, the highly accurate CCSD(T) results for the collinear and perpendicular geometries were combined with the less saturated MRCI results to provide *ab initio* based model PESs of much higher accuracy. Two models of such merging have been tested: a CI-S model and a CC-M model.

CI-S PES was abtained by scaling the MRCISD+Q diabatic surfaces to the CCSD(T) diabatic surfaces:

$$H_{11}^{\text{CI-S}}(R,\theta) = H_{11}^{\text{MRCI}}(R,\theta)\left[\frac{V_{A_1}^{\text{CCSD(T)}}(R)}{V_{A_1}^{\text{MRCI}}(R)}\sin^2\theta + \frac{V_{\Sigma}^{\text{CCSD(T)}}(R)}{V_{\Sigma}^{\text{MRCI}}(R)}\cos^2\theta\right] \tag{8.10}$$

$$H_{22}^{\text{CI-S}}(R,\theta) = H_{22}^{\text{MRCI}}(R,\theta)\left[\frac{V_{B_2}^{\text{CCSD(T)}}(R)}{V_{B_2}^{\text{MRCI}}(R)}\sin^2\theta + \frac{V_{\Pi}^{\text{CCSD(T)}}(R)}{V_{\Pi}^{\text{MRCI}}(R)}\cos^2\theta\right] \tag{8.11}$$

where the superscript CCSD(T) denotes energies obtained at the CCSD(T)/avqz/tz+332 level of theory and the subscripts refer electronic states. The coupling between states of A′ symmetry was not scaled and kept at the MRCI level of theory. Figures 8.11 and 8.12 show contour plots of the $H_{11}^{\text{CI-S}}$ and $H_{22}^{\text{CI-S}}$, respectively.

Since we noticed a particularly simple shape of the diabatic surfaces, we proposed a simpler model termed CC-M which describes the C_s geometries with a simple angular interpolation. The CC-M is defined:

$$H_{11}^{\text{CC-M}}(R,\theta) = V_{A_1}^{\text{CCSD(T)}}(R)\sin^2\theta + V_{\Sigma}^{\text{CCSD(T)}}(R)\cos^2\theta \tag{8.12}$$

$$H_{22}^{\text{CC-M}}(R,\theta) = V_{B_2}^{\text{CCSD(T)}}(R)\sin^2\theta + V_{\Pi}^{\text{CCSD(T)}}(R)\cos^2\theta \tag{8.13}$$

$$H_{33}^{\text{CC-M}}(R,\theta) = V_{B_1}^{\text{CCSD(T)}}(R)\sin^2\theta + V_{\Pi}^{\text{CCSD(T)}}(R)\cos^2\theta \tag{8.14}$$

It is worthwhile to note that the 2-D potentials defined by the above equations may be formally generalized to 3-D potentials, by including dependence of the H-H distance and replacing V(R) by V(R, r).

In the essence, it takes advantage of the simple elipsoidal symmetry of the electron density of the H_2 moiety in its ground state. The CC-model diabatic surfaces were prepared for the full range of geometries using *ab initio* CCSD(T) results for T and L arrangements for the A_1, B_1, B_2, Σ and Π symmetries. Contour plots of $H_{11}^{\text{CC-M}}$, $H_{22}^{\text{CC-M}}$, $H_{33}^{\text{CC-M}}$ and *ab initio* A″ surface are shown in Figures 8.13, 8.14, 8.15 and 8.16, respectively. In the Figures 8.13 and 8.14 we plot bold contour line (bold line starting from the region of Σ-Π conical intersection for $\theta = 0°$), where two diabats cross fulfilling condition $H_{11}^{\text{CC-M}}$=$H_{22}^{\text{CC-M}}$.

For the sake of comparison with model $H_{33}^{\text{CC-M}}$ surface, we calculated the whole A″ surface at the CCSD(T) level. As the lowest state of the A″ symmetry, this states is amenable to the CCSD(T) treatment. The differences proved to be on the order of several tenths of wavenumbers in the very short range, which is 1-4% of the repulsive energy values, and in the medium and long range, on the order of 1 or less than 1 cm^{-1}. The agreement is thus perfect, confirming the high quality of the model surfaces.

8.2.6 Model nonrelativistic adiabatic PESs

To obtain adiabatic counterparts of the diabatic surfaces, the diabatic 2x2 matrix:

$$\mathbf{H}^{el} = \begin{bmatrix} H_{11} & \sqrt{2}H_{12} \\ \sqrt{2}H_{12} & H_{22} \end{bmatrix} \tag{8.15}$$

was diagonalized. The adiabatic PESs for the CC-M are compared with the *ab initio* adiabatic MRCI PESs in Figures 8.9, 8.10 , 8.17 and 8.18. Figures 8.9 and 8.10 show the MRCI adiabatic surfaces and Figures 8.17 and 8.18 show the CC-model adiabatic surfaces.

It turned out that both models, CI-S and CC-M provided very similar PES, both at adiabatic and the diabatic levels of theory. The reason seems clear: the elipsoidal shape of H_2 electron density is faithfuly modeled by the simplest angular expansion Eqs. 8.12, 8.13, and 8.14.

Global minima and stationary points of the modeled diabatic and adiabatic surfaces are shown in Tables 8.4 and 8.5.

Table 8.4: Minima of modeled diabatic surfaces.

Diabat	D_e/cm^{-1}	$R_e/Å$	θ_e
H_{11}^{CC-M}	163.8	3.0	90
H_{22}^{CC-M}	75.9	3.75	0
H_{33}^{CC-M}	75.9	3.75	0

Table 8.5: Minima of modeled adiabatic surfaces. Adiabats 1, 2, 3 include relativistic spin-orbit effect.

Adiabat	D_e/cm^{-1}	$R_e/Å$	θ_e
1A′	163.8	3.00	90
1A′	75.9	3.75	0
2A′	24.0	4.00	90
2A′	23.7	3.50	0
1A″	75.9	3.75	0
adiabat 1	87.9	3.30	90
adiabat 1	76.2	3.70	0
adiabat 2	41.7	3.65	0
adiabat 3	57.9	3.65	0

Positions and well depths of minima of modeled surfaces are also valid for scaled $H_{ii}^{\text{CI-S}}$ surfaces.

It is worthwhile to point out that for other diatoms as e.g. for Cl_2 or HCl such extrapolation may not work due to more elaborate electron density shapes of these molecules. Yet, all atom+H_2 complexes, which are in the entry channels of many reactions, such as O+H_2, N+H_2, S+H_2, etc. are expected to be easily amenable to our treatment.

8.2.7 Spin-orbit coupling and model relativistic adiabatic PESs

Allowing for spin-orbit coupling of the halogen atom one obtaines two atomic terms: $^2P_{3/2}$ and $^2P_{1/2}$, separated by Δ_{SO}=882.4 cm^{-1}. The interaction with H_2 further splits the $^2P_{3/2}$ state into two states. To evaluate the resulting adiabatic potential energy surfaces we used the procedure described by Alexander, Manolopoulos, and Werner .[97] The matrix of the electrostatic interaction plus the spin-orbit Hamiltonian was expressed in the basis set invariant to time reversal (see Ref. [97] for details). Then the total matrix decouples:

$$\mathbf{H}^{el} + \mathbf{H}^{SO} = \begin{bmatrix} \mathbf{H} & 0 \\ 0 & \mathbf{H}^{\dagger} \end{bmatrix}, \tag{8.16}$$

where **H** is the 3x3 Hermitian matrix expressed in the basis invariant to time reversal:

$$\mathbf{H} = \begin{bmatrix} H_{11} & -V_1 - i\sqrt{2}B & V_1 \\ & V_\Pi + A & V_2 \\ & & V_\Pi - A \end{bmatrix}, \tag{8.17}$$

where $V_1 = 2^{-1/2} H_{12}$, $V_\Pi = (H_{33} + H_{22})/2$ and $V_2 = (H_{33} - H_{22})/2$. A and B are spin-orbit matrix elements:

$$A \equiv i\langle \Pi_y | H^{SO} | \Pi_x \rangle \tag{8.18}$$

and

$$B \equiv \langle \bar{\Pi}_x | H^{SO} | \Sigma \rangle \tag{8.19}$$

We have found in the Van der Waals region that A and B are practically independent of R and of the angle, and we fixed both at the value of $1/3\Delta_{SO}$ (in the limit of large R, A equals B). Significant changes in A and B start when the Cl atom approaches the H_2 molecule closer than at 2.0 Å. On diagonalizing the matrix Eq. 8.17 three adiabatic potential energy surfaces were obtained, shown in Figures 8.19, 8.20 and 8.21. They are numbered in the order of increasing energy.

In the limit of large R, the first two adiabatic PESs correlate to the $^2P_{3/2}$ state of Cl, with the projection of j upon the R vector equal to 3/2 and 1/2 for the ground state and the first excited state, respectively. The third adiabat (Figure 8.21) correlates with $^2P_{1/2}$ term of Cl atom.

One can see that the relativistic adiabatic surfaces significantly differ from non-relativistic ones. The lowest adiabatic surface is now half as deep at the T-shaped minimum (D_e=88 cm^{-1}) and considerably flattened, with a 15 cm^{-1} high barrier for the H_2 rotation, around 40°, and another local minimum for the collinear arrangement (D_e=76 cm^{-1}). The other adiabatic surface related to the same $^2P_{3/2}$ asymptotic limit is shallower, with a maximum at 90° and a minimum at 0°. The third state, asymptotically separated by 882 cm^{-1} SO coupling, resembles the second in shape, but is slightly deeper. These results are in qualitative agreement with the finding of Alexander, Manolopoulos and Werner[97] that the "spin-orbit coupling cannot be neglected in the region of the Van der Waals minimum [...] and significantly alters both the depth and position of the van der Waals well". The D_e and R_e parameters of the three adiabatic PESs are listed in Table 8.5.

8.3 Summary and Conclusions

Two model potentials for the H_2+Cl complex were constructed using accurate *ab initio* CCSD(T) and MRCI calculations: MRCI-Scaled (CI-S) and CC-Model (CC-M).

For the lowest adiabatic state, they may be compared with the globally valid potential of Bian and Werner, BW2 .[150] Our surfaces are in very good qualiatative agreement with the BW2 one. The quantitative characteristcs of the T-shaped minimum and the L saddle point somewhat differ, BW2 being 10 cm^{-1} deeper at the minimum, and revealing a 15 cm^{-1} smaller barrier for the rotation of the H_2 molecule.

We have recently adopted a similar approach for two other related complexes, F+H_2[171] and Br+H_2.[172] It is interesting to compare the depth of related stationary points, cf. Table **??**.

The stationary points were obtained at the CCSD(T) level of theory. One can see that the T-shaped minimum is 30 cm^{-1} deeper for Cl than F, but Br is only 5 cm^{-1} more bound than Cl. For the collinear arrangement, which may be identified with the barrier for rotation of H_2, one can notice that the halogen atoms differ only slightly in this respect, the barrier ranging from 82 cm^{-1} (Br) to 87 cm^{-1} (Cl). Interestingly, Werner and collaborators [97,150] predict a

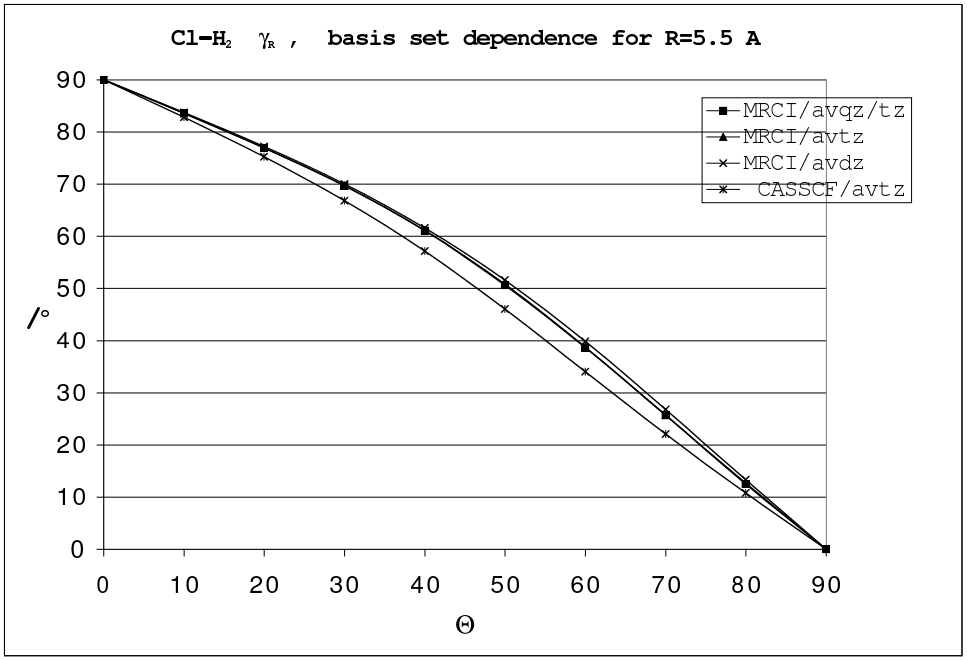

Figure 2c

Figure 8.4: Comparison of γ_R mixing angle calculated in various basis sets and methods. Distance is 5.5 Å.

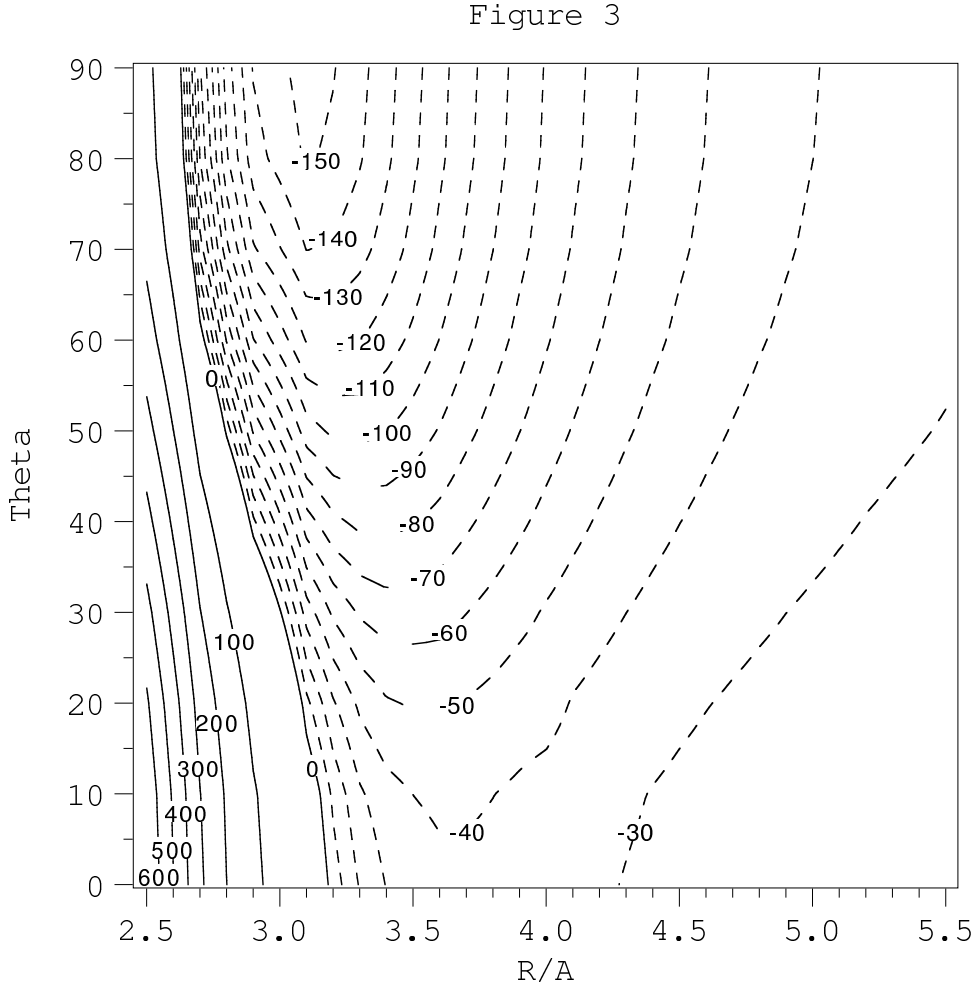

Figure 8.5: Contour plot of the MRCISD+Q H_{11} diabat. Values in cm^{-1}.

Figure 4

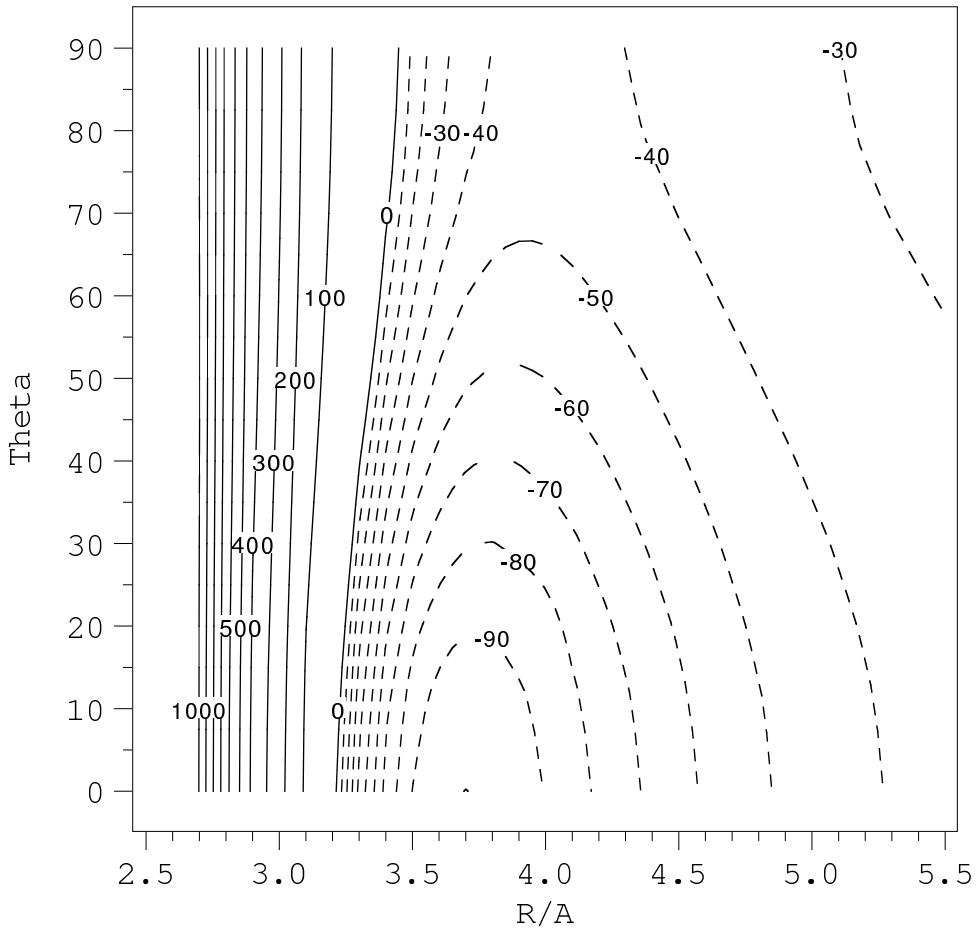

Figure 8.6: Contour plot of the MRCISD+Q H_{22} diabat. Values in cm^{-1}.

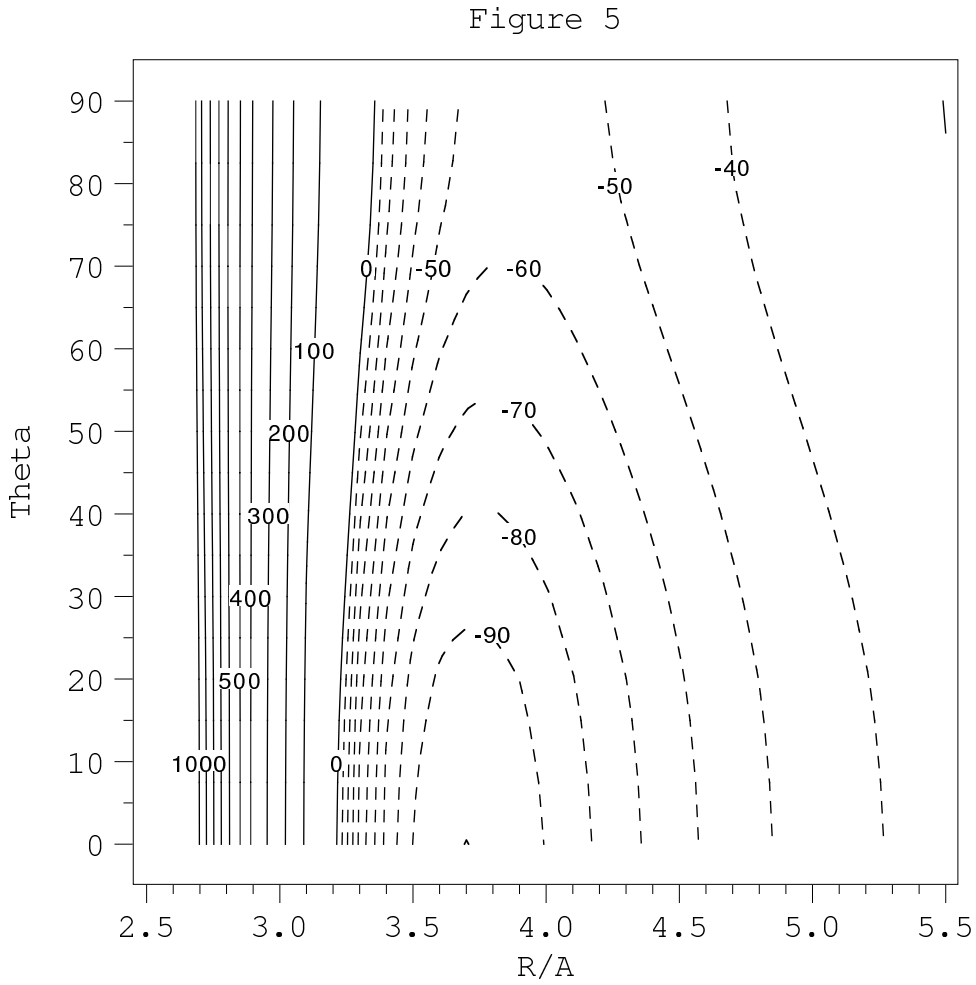

Figure 8.7: Contour plot of the MRCISD+Q H_{33} diabat. Values in cm^{-1}.

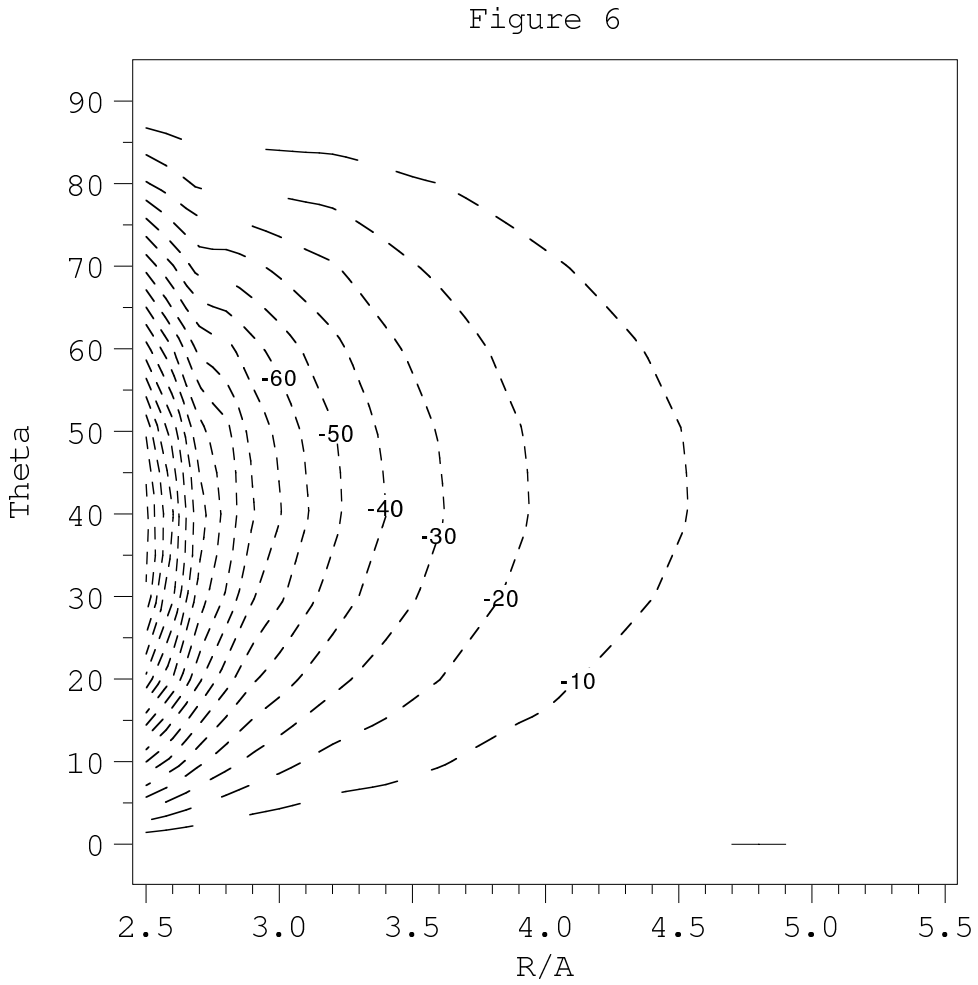

Figure 8.8: Contour plot of the MRCISD+Q H_{12} coupling. Values in cm^{-1}.

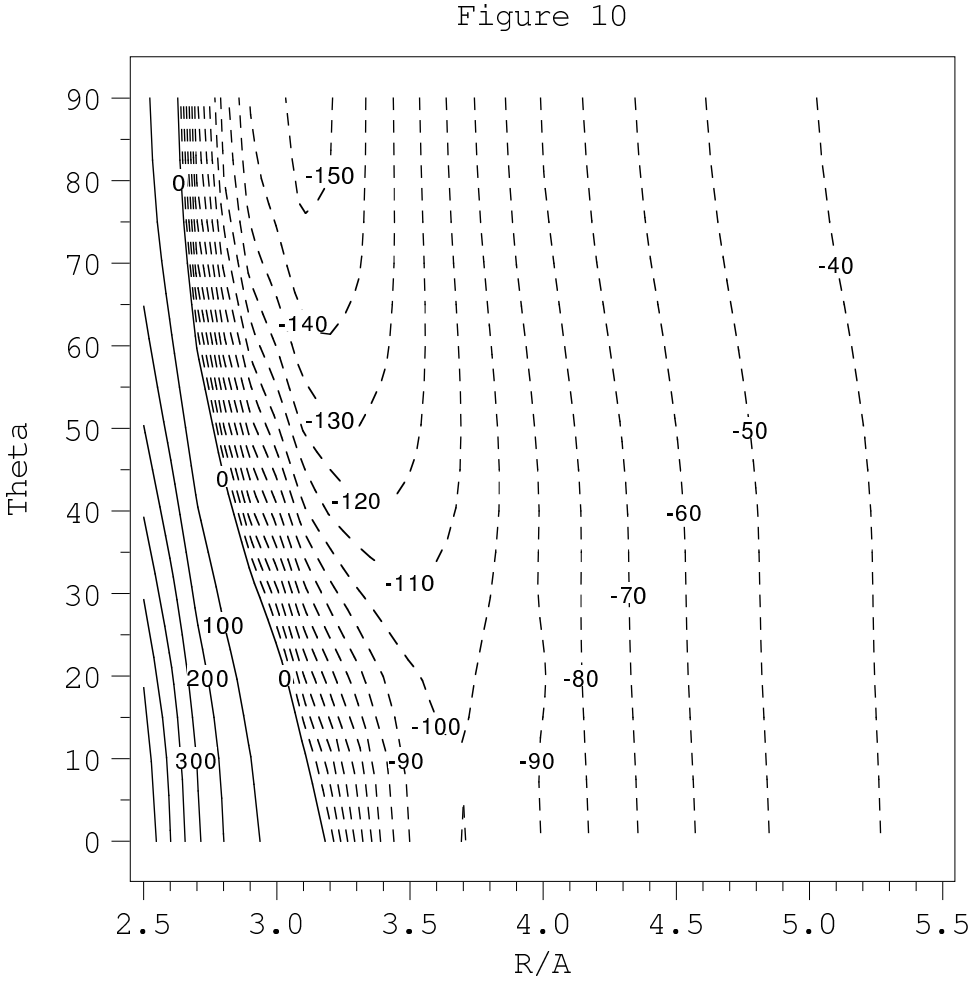

Figure 8.9: Contour plot of the 1A′ MRCISD+Q adiabat. Values in cm^{-1}.

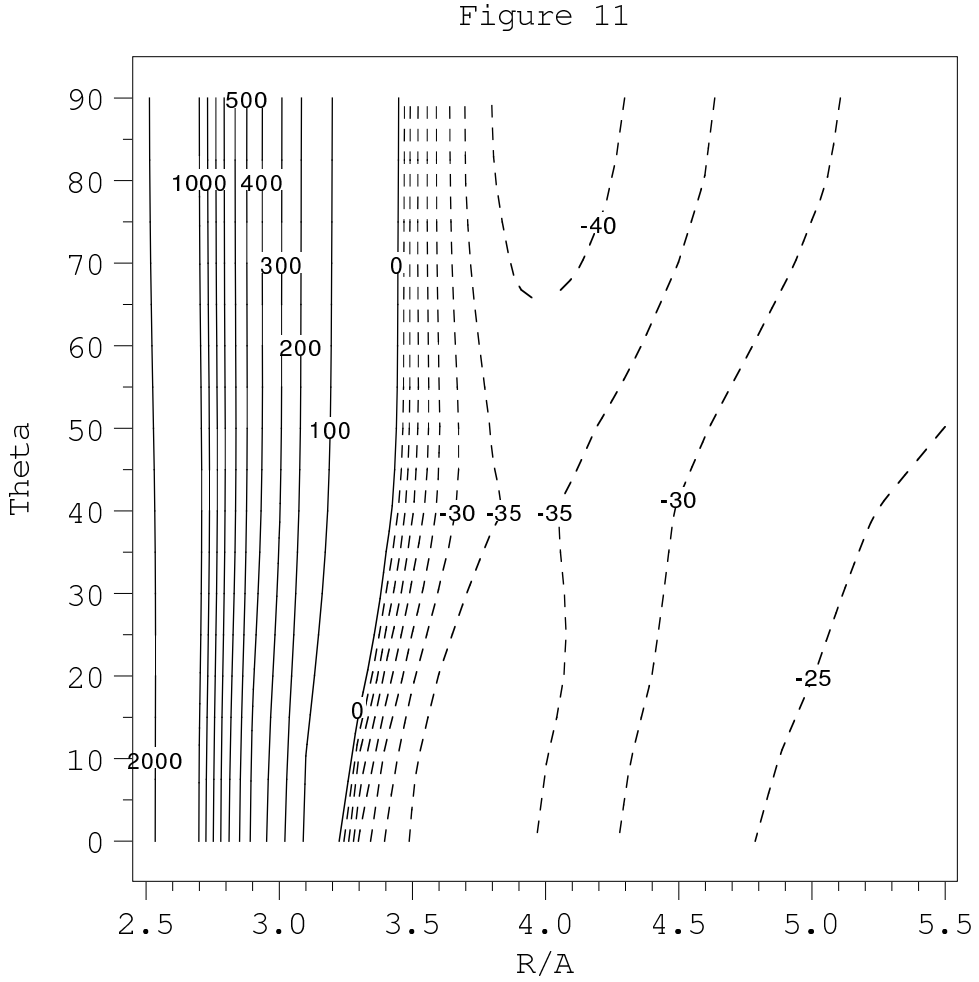

Figure 8.10: Contour plot of the 2A′ MRCISD+Q adiabat. Values in cm^{-1}.

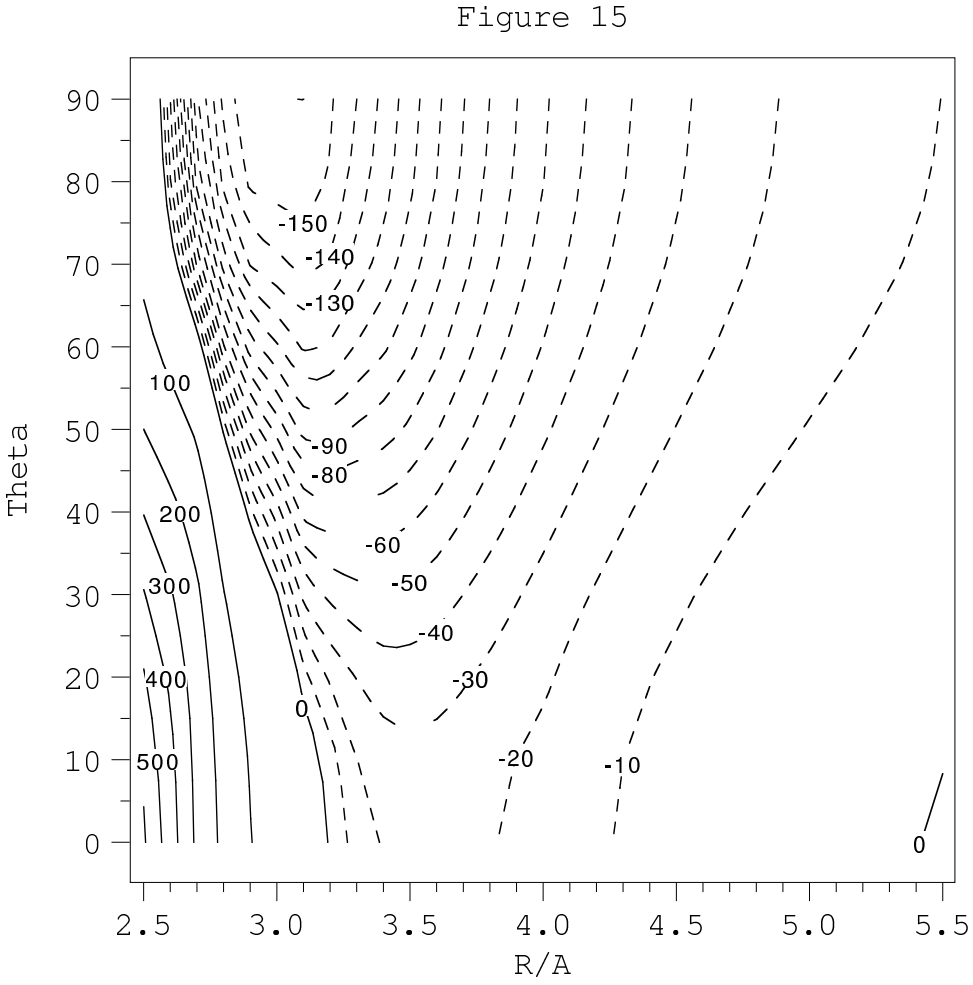

Figure 8.11: Contour plot of the scaled H_{11}^{CI-S} diabat. Values in cm^{-1}.

Figure 16

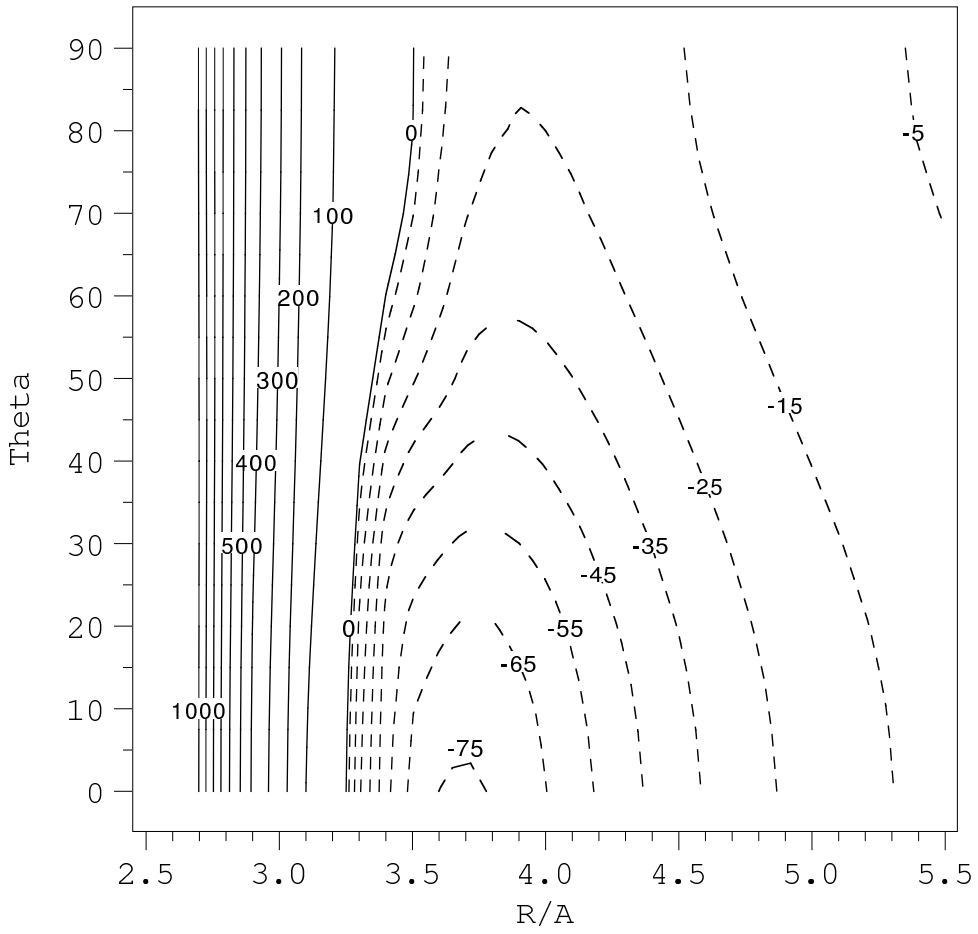

Figure 8.12: Contour plot of the scaled H_{22}^{CI-S} diabat. Values in cm^{-1}.

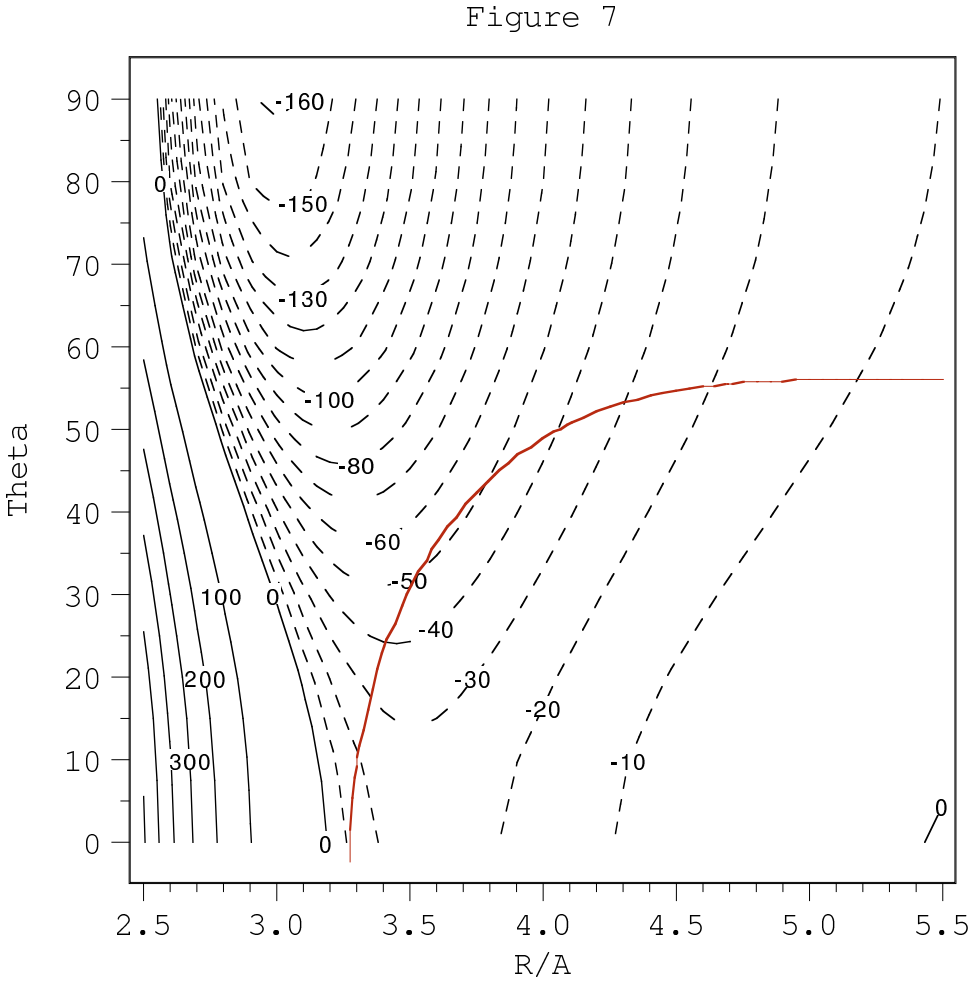

Figure 8.13: Contour plot of the modeled H_{11}^{CC-M} diabat. Values in cm^{-1}.

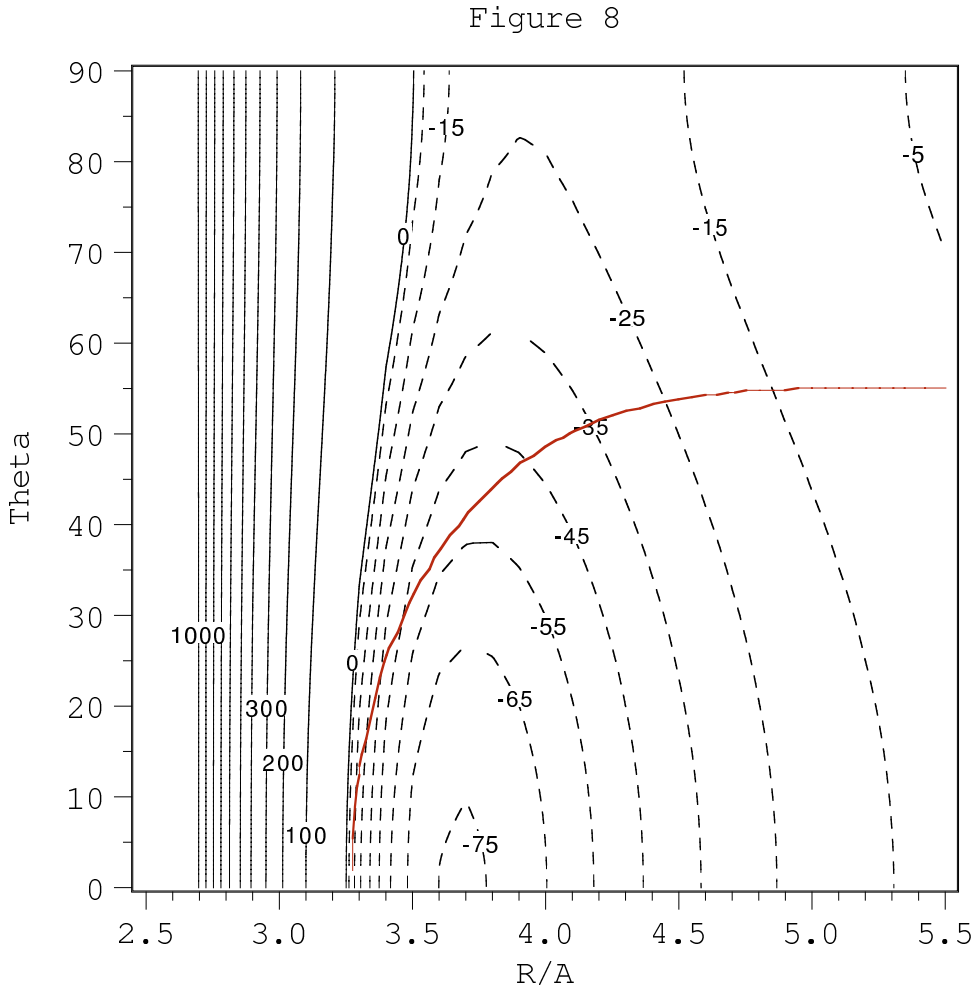

Figure 8.14: Contour plot of the modeled H_{22}^{CC-M} diabat. Values in cm^{-1}.

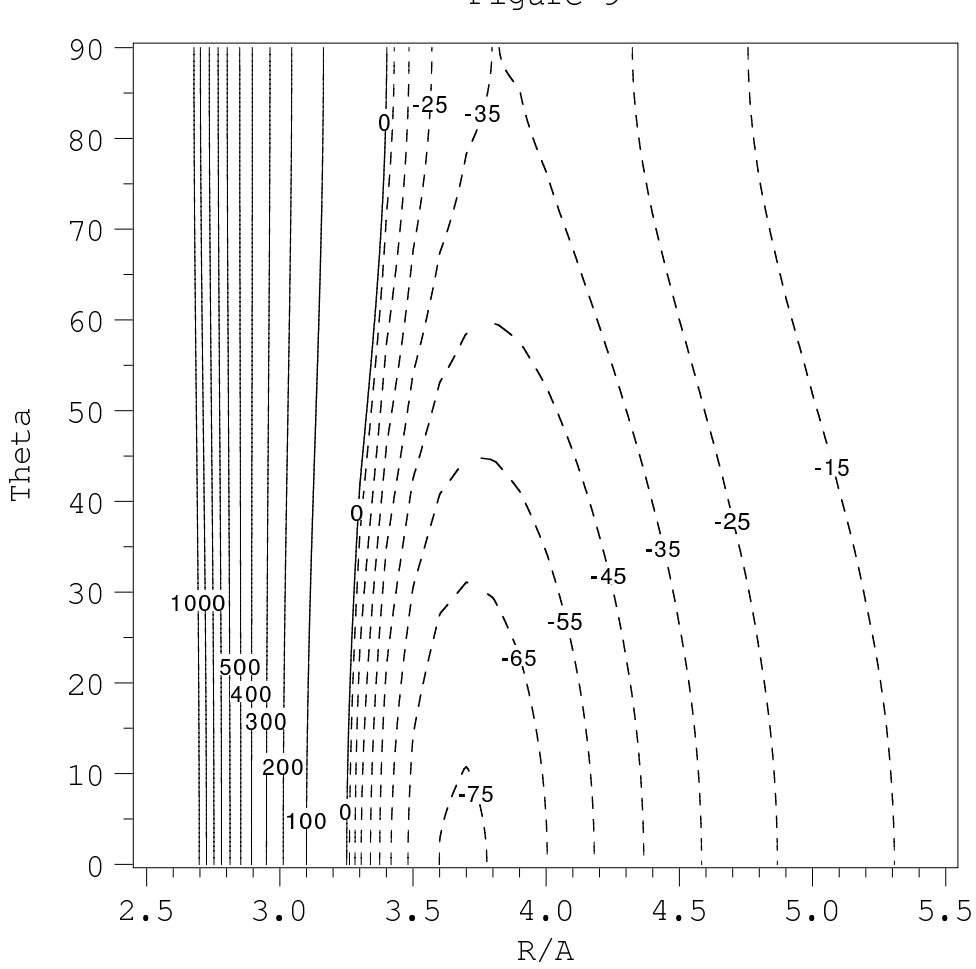

Figure 8.15: Contour plot of the modeled H_{33}^{CC-M} diabat. Values in cm^{-1}.

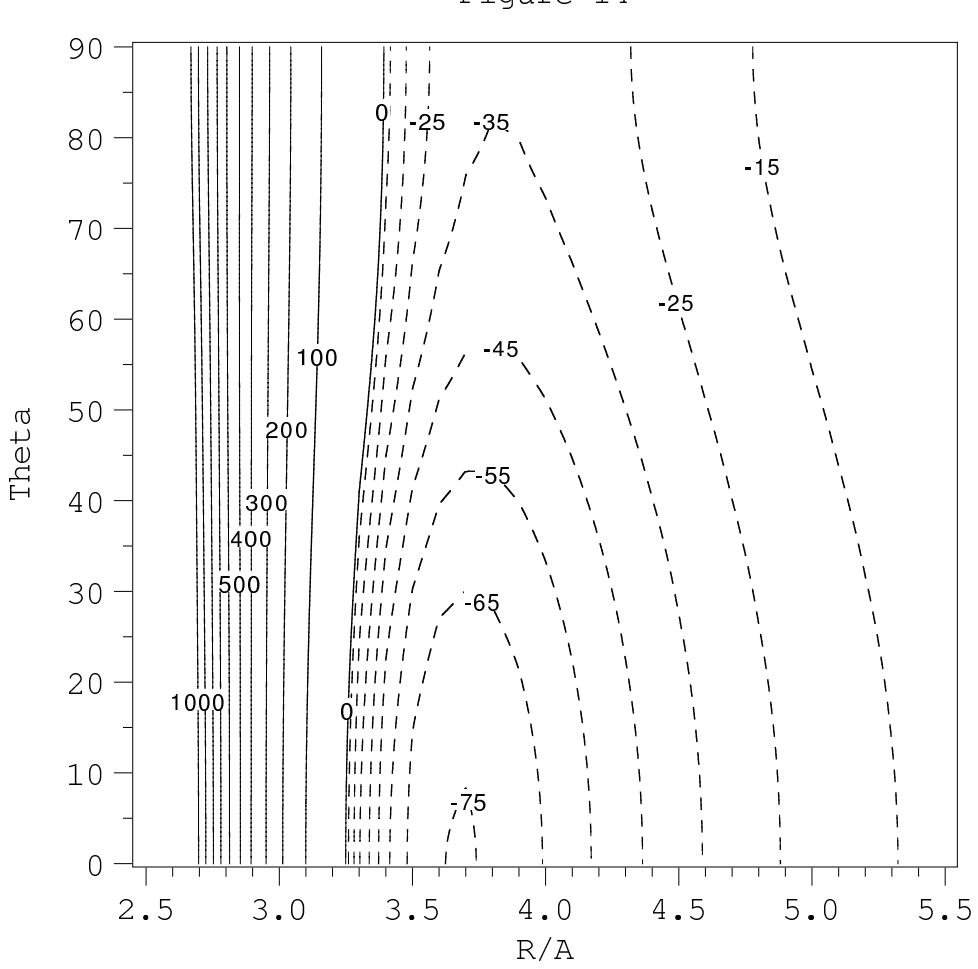

Figure 8.16: Contour plot of the fit of RCCSD(T) 1A″ adiabat. Values in cm^{-1}.

Figure 12

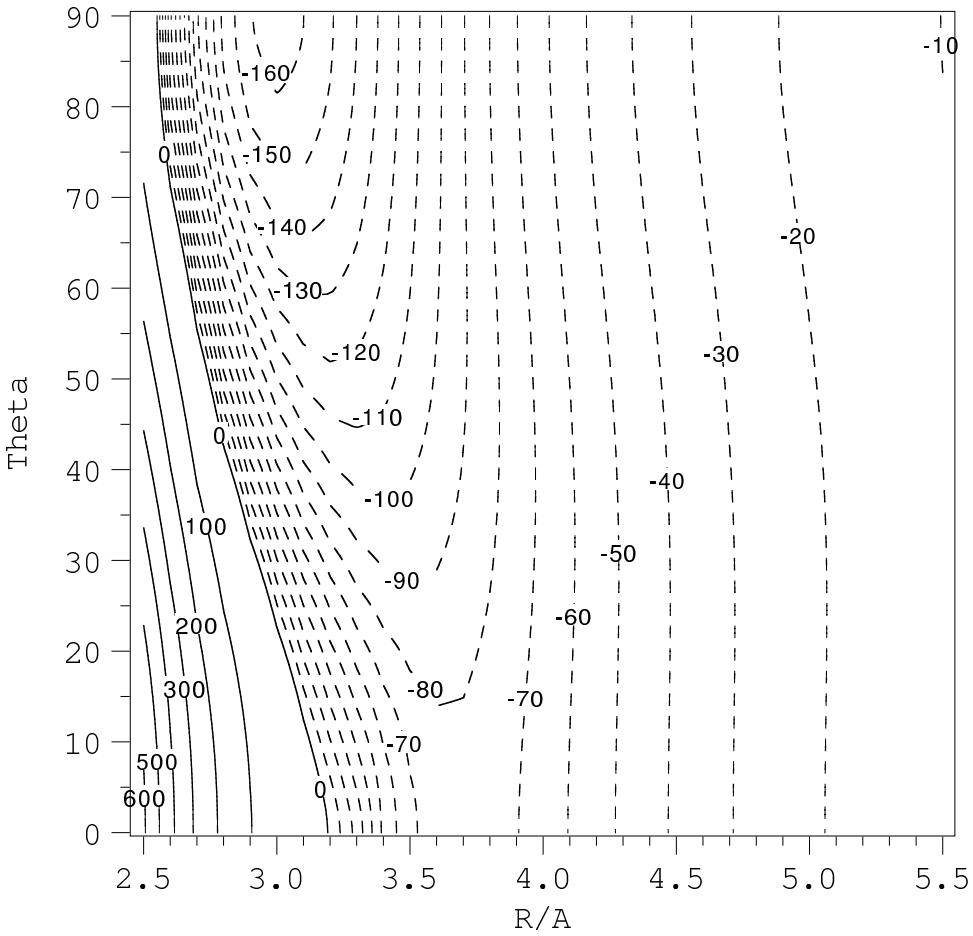

Figure 8.17: Contour plot of the modeled $1A'_{CC-M}$ adiabat. Values in cm^{-1}.

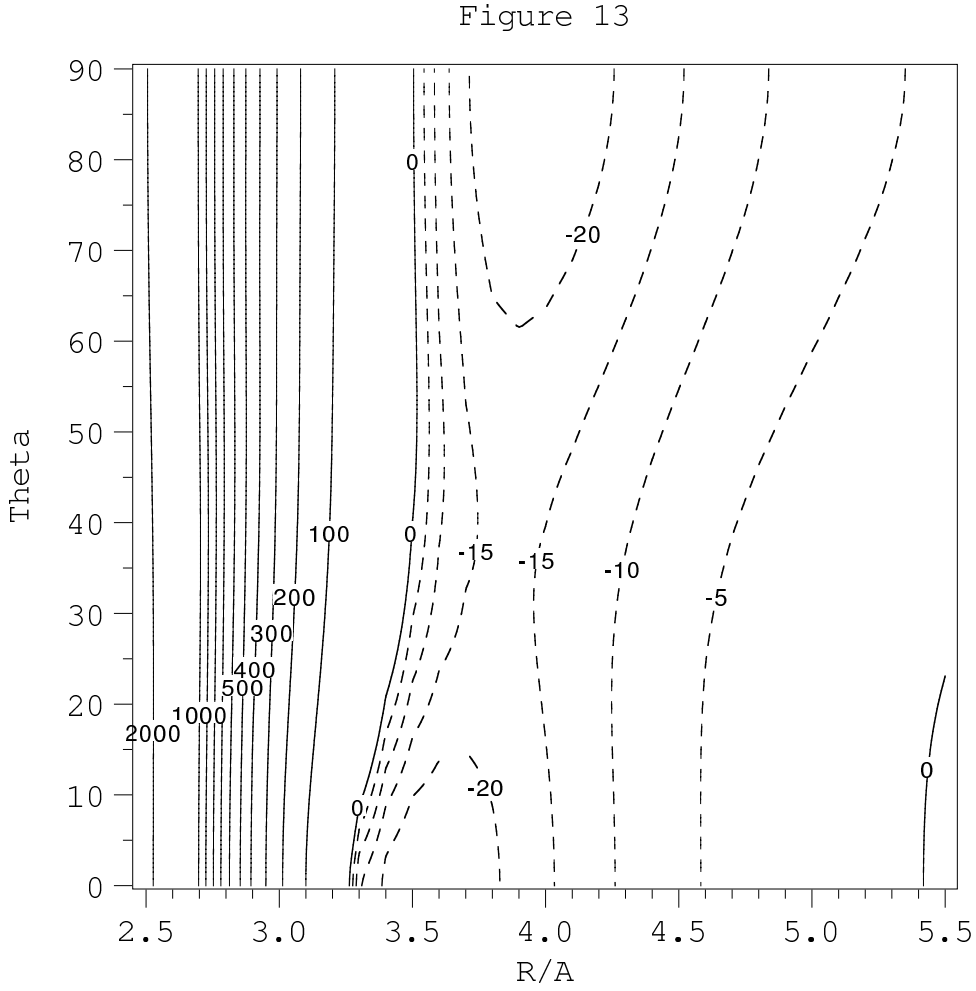

Figure 8.18: Contour plot of the modeled $2A'_{CC-M}$ adiabat. Values in cm^{-1}.

Figure 17

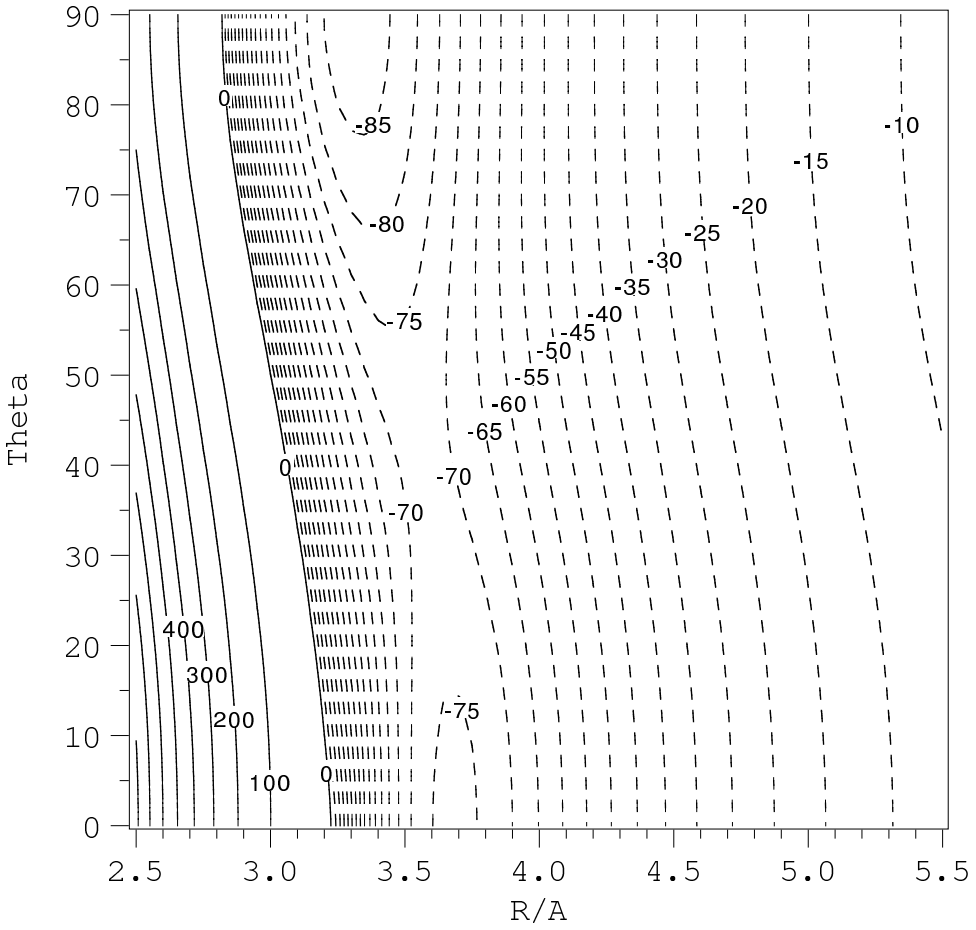

Figure 8.19: Contour plot of the spin-orbit corrected adiabat 1, which correlates to $Cl(^2P_{3/2})$. Values in cm^{-1}.

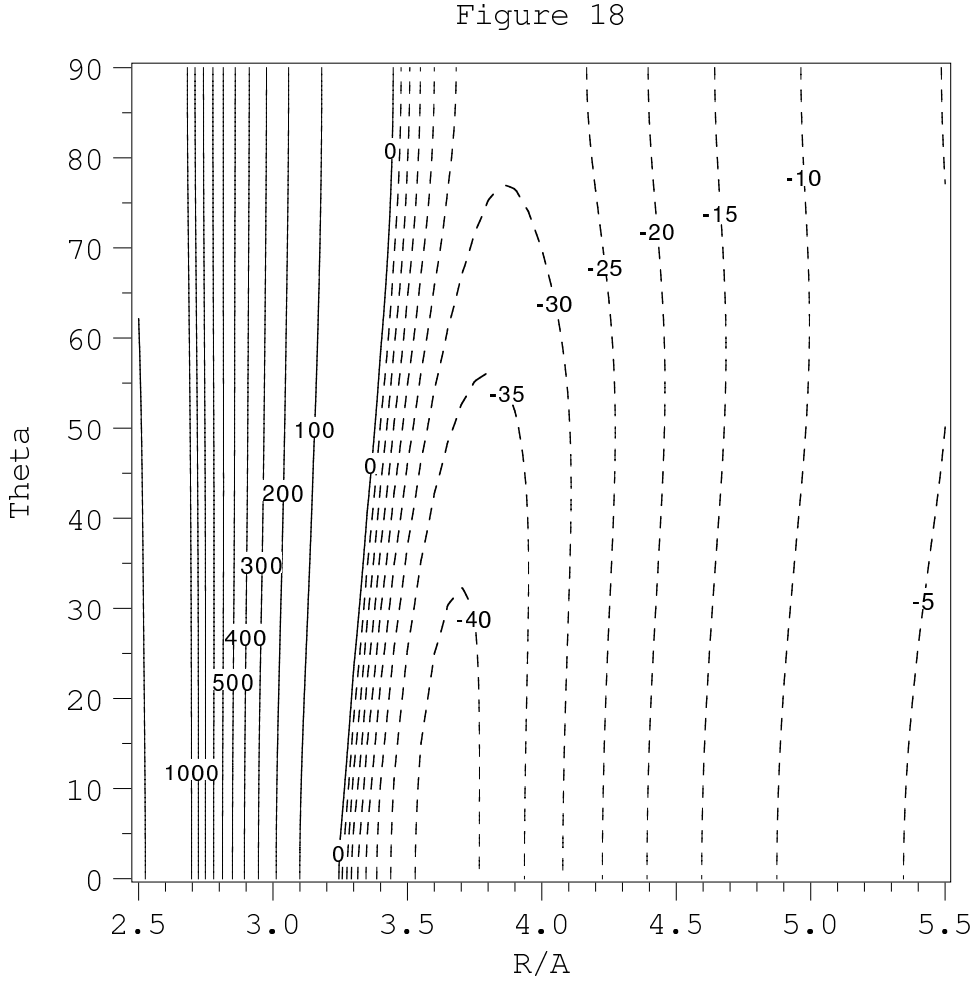

Figure 8.20: Contour plot of the spin-orbit corrected adiabat 2, which correlates to $Cl(^2P_{3/2})$. Values in cm^{-1}.

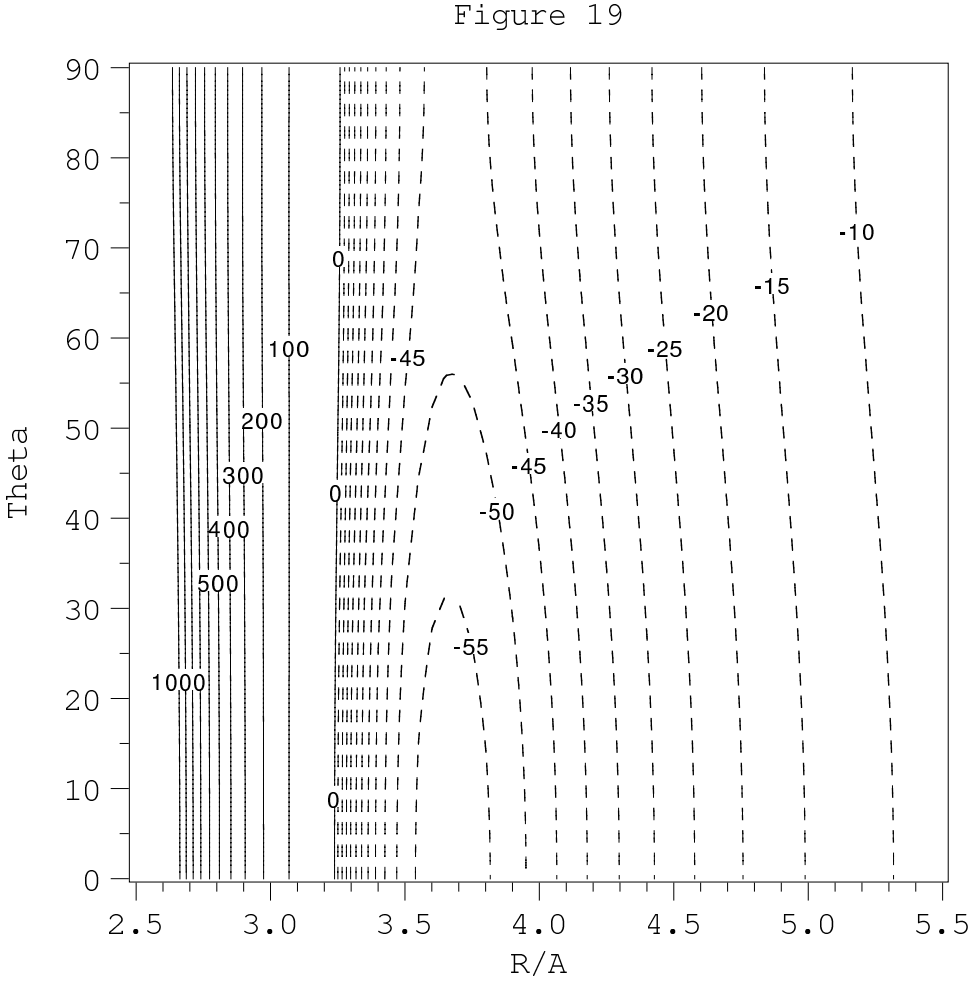

Figure 8.21: Contour plot of the spin-orbit corrected adiabat 3, which correlates to $Cl(^2P_{3/2})$. Values in cm^{-1}.

CHAPTER IX

Summary

The most important achievements of this dissertation are the following:

- Modeling of the two-dimensional PES of Ar-HCN Van der Waals complex from *ab initio* interaction energies and calculations of the ro-vibration spectra by means of the collocation method.
- Modeling of the two-dimensional PES of Ar-CO_2 from *ab initio* interaction energies and calculations of the ro-vibration spectra by means of the collocation method. Calculation of the second virial coefficient, in particular the first-order quantum correction thereto.
- *Ab initio* calculations and modeling of the PESs of Rg-S, where Rg=He, Ne, Ar, Kr, Xe. The potentials proved to be competitive to those empirically determined from the elastic and inelastic collision scattering experiments.
- *Ab initio* calculations and modeling of the PESs of the first three states: $1A'$, $2A'$, and $1A''$ related to the interaction of the ground state (^2P) atom with the ground state HCl molecule. These calculations represent the first reliable *ab initio* treatment of the HCl-Cl Van der Waals complex in the literature. Very high accuracy has been achieved due to judicious application of the CCSD(T) approach for all states, including careful elimination the BSSE by rotation of ghost monomers. The MRCI calculations have been used to provide the mixing angle of the A' symmetry states.
- A novel approach to modeling of three-dimensional PESs of the H_2-X (X stands for an open-shell atom) complexes has been designed and applied. The angular dependence of this potentials is modeled by a simple Legendre-polynomial interpolation. between the T-shaped (C_{2v}) and collinear geometries ($C_{\infty v}$), accurately calculated *ab initio* at the CCSD(T) level of theory with a large basis set. The nonadiabatic coupling (off-diagonal derivative) matrix element and the fourth, off-diagonal, diabatic surface are determined by separate multireference configuration interaction (MRCI) calculations with a medium-sized basis set. The method has been used for H_2-F, H_2-Cl and H_2-Br. Three diabatic and adiabatic potential energy surfaces (PESs) in each case have been obtained, both the nonrelativistic and relativistic (including spin-orbit coupling). Excellent agreement with the *ab initio* potentials of Stark and Werner for H_2-F has been obtained. The Author's H_2-Cl and H_2-Br are expected to be the best avialable to date for these systems.

BIBLIOGRAPHY

BIBLIOGRAPHY

[1] E. R. Bernstein (Ed.). *Chemical Reactions in Clusters*. Oxford University Press, Oxford, (1996).

[2] C. Jouvet and D. Solgadi. *Chemical Reactions in Clusters*. In ,[1] (1996).

[3] D. B. Pullman, B. Friedrich, and D. R. Herschbach. J. Chem. Phys., **93**, 3224, (1990).

[4] J. Phys. Chem. A, **101**, (1997). Issue No. 41.

[5] A. J. H. M. Meijer, G. C. Groenenboom, and A. van der Avoird. J. Phys. Chem., **101**, 7558, (1997).

[6] C. Wittig and A. H. Zewail. in Ref.[1] p. 64.

[7] J. J. Valentini. Faraday Discuss. Chem. Soc., **91**, 392, (1991).

[8] D. J. Nesbitt, J. W. Nibler, A. Schiffman, W. B. Chapman, and J. M. Hutson. J. Chem. Phys., **98**, 9513, (1993).

[9] R. J. Saykally. Acc. Chem. Res., **22**, 295, (1989).

[10] E. J. Bohac, M. D. Marshall, and R. E. Miller. J. Chem. Phys., **96**, 6681, (1992).

[11] D. T. Anderson, R. L. Schwarz, M. W. Todd, and M. I. Lester. J. Chem. Phys., **109**, 3461, (1998).

[12] V. Aquilanti, G. Liuti, F. Pirani, and F. Vecchiocattivi. J. Chem. Soc.,Faraday Trans., **2**, 85, (1989).

[13] M.-L. Dubernet, D. Flower, and J. M. Hutson. J. Chem. Phys., **94**, 7602, (1991).

[14] M. C. Heaven. J. Phys. Chem., **97**, 8567, (1993).

[15] R. A. Loomis and M. I. Lester. Annu. Rev. Phys. Chem., **48**, 643, (1997).

[16] G. Chałasiński and M. M. Szczęśniak. Chem. Rev., **94**, 1723, (1994).

[17] G. Chałasiński and M. M. Szczęśniak. Chem. Rev., **100**, 4253, (2000).

[18] Jason Williams and Millard H. Alexander. J. Chem. Phys., **112**, 5722, (2000).

[19] M. H. Alexander, A. R. Walton, M. Yang, X. Yang, E. Hwang, and P. J. Dagdigian. J. Chem. Phys., **106**, 6320, (1997).

[20] M. H. Alexander. J. Chem. Phys., **108**, 4467, (1998).

[21] S. M. Cybulski, R. Burcl, G. Chałasiński, and M. M. Szczęśniak. J. Chem. Phys., **103**, 10116, (1995).

[22] S. M. Cybulski, G. Chałasiński, and M. M. Szczęśniak. J. Chem. Phys., **105**, 9525, (1996).

[23] S. M. Cybulski, R. A. Kendall, G. Chałasiński, M. W. Severson, and M. M. Szczęśniak. J. Chem. Phys., **106**, 7731, (1997).

[24] R. A. Kendall, G. Chałasiński, J. Kłos, R. Bukowski, M. W. Severson, M. M. Szczęśniak, and S. M. Cybulski. J. Chem. Phys., **108**, 3235, (1998).

[25] J. Klos, G. Chałasiński, M. T. Berry, R. Bukowski, and S. M. Cybulski. J. Chem. Phys., **112**, 2195, (2000).

[26] J. Kłos, G. Chałasiński, M. T. Berry, R. A. Kendall, R. Burcl, M. M. Szczęśniak, and S. M. Cybulski. J. Chem. Phys., **112**, 4952, (2000).

[27] R. Toczyłowski, F. Doloresco, and S. M. Cybulski. J. Chem. Phys., **114**, 851, (2001).

[28] K. Tanaka, S. Bailleux, A. Mizoguchi, K. Harada, T. Baba, I. Ogawa, and M. Shirasaka. J. Chem. Phys., **113**, 1524, (2000).

[29] I. P. Hamilton and J. C. Light. J. Chem. Phys., **84**, 306, (1986).

[30] W. Yang and A. C. Peet. J. Chem. Phys., **92**, 522, (1990).

[31] J. M. Hutson. Adv. Mol. Vibrat. Coll. Dyn., **1A**, 1, (1991).

[32] K. T. Tang and J. P. Toennies. J. Chem. Phys., **80**, 3726, (1984).

[33] A. C. Peet and W. Yang. J. Chem. Phys., **90**, 1746, (1989).

[34] A. J. Misquita, R. Bukowski, and K. Szalewicz. J. Chem. Phys., **112**, 5308, (2000).

[35] P. J. Marshall, M. M. Szczęśniak, J. Sadlej, G. Chałasiński, M. A. ter Horst, and C. J. Jameson. J. Chem. Phys., **104**, 6569, (1996).

[36] F.-M. Tao and Y.-K. Pan. J. Chem. Phys., **97**, 4989, (1992).

[37] S. W. Sharpe, D. Reifschneider, C. Wittig, and R. A. Beaudet. J. Chem. Phys., **94**, 233, (1991).

[38] Russel T. Pack. J. Chem. Phys., **78**, 7217, (1983).

[39] J. Hutson, A. Ernesti, M. M. Law, C. F. Roche, and R. J. Wheatley. J. Chem. Phys., **105**, 9130, (1996).

[40] R. G. Newton. *Scattering THeory of Waves and Particles*. McGraw-Hill, New York, (1966).

[41] M. F. Golde and B. A. Trush. Chem. Phys. Lett., **29**, 486, (1974).

[42] P. C. Tellinghuisen, J. Tellinghuisen, J. A. Coxon, J. E. Velasco, and D. W. Setser. J. Chem. Phys., **68**, 5178, (1978).

[43] G. Lo and D. W. Setser. J. Chem. Phys., **100**, 5432, (1994).

[44] Y. Zhao, I. Yourshaw, G. Reiser, C. C. Arnold, and D. M. Neumark. J. Chem. Phys., **101**, 6538, (1994).

[45] I. Yourshaw, T. Lenzer, G. Reiser, and D. M. Neumark. J. Chem. Phys., **109**, 5247, (1998).

[46] T. Lenzer, I. Yourshaw, M. R. Furlanetto, G. Reiser, and D. M. Neumark. J. Chem. Phys., **110**, 9578, (1999).

[47] V. Aquilanti, D. Ascenzi, E. Barca, D. Cappelletti, and F. Pirani. Phys. Chem. Chem. Phys., **2**, 4081, (2000).

[48] A. V. Nemukhin, B. L. Grigorenko, and A. A. Granovsky. Chem. Phys. Lett., **301**, 287, (1999).

[49] M. Yamanishi, K. Hirao, and K. Yamashita. J. Chem. Phys., **108**, 1514, (1998).

[50] S. F. Boys and F. Bernardi. Mol. Phys., **19**, 553, (1970).

[51] P. J. Knowles, C. Hampel, and H.-J. Werner. J. Chem. Phys., **99**, 5219, (1993).

[52] P. J. Knowles, C. Hampel, and H.-J. Werner. J. Chem. Phys., **112**, (2000).

[53] MOLPRO is a package of *ab initio* programs written by H.-J. Werner and P. J. Knowles, with contributions from R. D. Amos, A. Bernhardsson, A. Berning, P. Celani, D. L. Cooper, M. J. O. Deegans, A. J. Dobbyn, F. Eckert, C. Hampel, G. Hetzer, T. Korona, R. Lindh, A. W. Lloyd, S. J. McNicholas, F. R. Manby, W. Meyer, M. E. Mura, A. Nicklass, P. Palmieri R. Pitzer, G. Rauhut, M. Schütz, H. Stoll, A. J. Stone, R. Tarroni, and T. Thorsteinsson.

[54] M. Urban, J. Noga, S. J. Cole, and R. J. Bartlett. J. Chem. Phys., **83**, 4041, (1985).

[55] E. A. Reisch and W. Meyer. J. Chem. Phys., **14**, 915, (1979).

[56] A. Degli Esposti and H.-J. Werner. J. Chem. Phys., **93**, 3351, (1990).

[57] C. E. Moore. *Atomic Energy Levels*. Nat. Bur. Stand. Gaithesburg, (1949).

[58] E. E. Nikitin and S. Ya. Umanskii. *Theory of Slow Atomic Collisions*. Springer, Berlin, (1984).

[59] A. A. Buchachenko, J. Jakowski, G. Chałasiński, M. M. Szczęśniak, and S. M. Cybulski. J. Chem. Phys., **112**, 5852, (2000).

[60] V. Aquilanti and G. Grossi. J. Chem. Phys., **73**, 1165, (1980).

[61] V. Aquilanti, P. Casavecchia, G. Grossi, and A. Laganá. J. Chem. Phys., **73**, 1173, (1980).

[62] M. H. Alexander, T. Orlikowski, and J. E. Straub. Phys. Rev. A, **28**, 73, (1983).

[63] V. Aquilanti, R. Candori, and F. Pirani. J. Chem. Phys., **89**, 6157, (1988).

[64] Z. Ma, K. Liu, L. B. Harding, M. Komotos, and G. C. Schatz. J. Chem. Phys., **100**, 8026, (1994).

[65] F. Pirani and F. Vecchiocattivi. Mol. Phys., **45**, 1003, (1987).

[66] R. V. Krems, A. A. Buchachenko, M. M. Szczęśniak, J. Kłos, and G. Chałasiński. submitted for publication.

[67] A. Nicklass, M. Dolg, H. Stoll, and H. Preuss. J. Chem. Phys., **102**, 8942, (1995).

[68] M-L. Dubernet and J. Hutson. J. Phys. Chem., **98**, 5844-5854, (1994).

[69] K. Liu, A. Kolessov, J. W. Partin, I. Bezel, and C. Wittig. Chem. Phys. Lett., **299**, 374, (1999).

[70] Z. Q. Zhao, W. B. Chapman, and D. J. Nesbitt. J. Chem. Phys., **102**, 7046, (1995).

[71] D. K. Bondi, J. N. L. Connor, J. Manz, and J. Römelt. Mol. Phys., **50**, 467, (1983).

[72] J. N. L. Connor and W. Jakubetz. In A. Laganà, editor, *Supercomputer Algorithms for Reactivity, Dynamics and Kinetics of Small Molecules*, pages 395–411. Kluwer Dordrecht, The Netherlands, (1989).

[73] Q. Sun, J. M. Bowman, G. C. Schatz, J. R. Sharp, and J. N. L. Connor. J. Chem. Phys., **92**, 1677, (1990).

[74] G. C. Schatz, B. Amaee, and J. N. L. Connor. J. Chem. Phys., **92**, 4893, (1990).

[75] J. P. Fulmer and P. M. Aker. J. Chem. Phys., **96**, 4252, (1992).

[76] W. Jakubetz, D. Sokolovski, J. N. L. Connor, and G. C. Schatz. J. Chem. Phys., **97**, 6451, (1992).

[77] M. J. Cohen, A. Willets, and N. C. Handy. J. Chem. Phys., **99**, 5885, (1993).

[78] R. B. Metz, T. Kitsopoulos, A. Weaver, and D. M. Neumark. J. Chem. Phys., **88**, 1463, (1988).

[79] R. B. Metz, A. Weaver, S. E. Bradforth, T. N. Kitsopoulos, and D. M. Neumark. J. Phys. Chem., **94**, 1377, (1990).

[80] D. M. Neumark. Annu. Rev. Phys. Chem., **43**, 153, (1992).

[81] G. C. Schatz. J. Chem. Phys., **90**, 3582, (1989).

[82] B. Gadzy and J. M. Bowman. J. Chem. Phys., **91**, 4615, (1989).

[83] G. C. Schatz, D. Sokolovski, and J. N. L. Connor. Faraday Discuss. Chem. Soc., **91**, 17, (1991).

[84] K. Yamashita and K. Morokuma. J. Chem. Phys., **93**, 3716, (1990).

[85] O. Hahn, J. M. Llorente Gomez, and S. H. Taylor. J. Chem. Phys., **94**, 2608, (1991).

[86] T. W.J. Whiteley, A. J. Dobbyn, J. N. L. Connor, and G. C. Schatz. Phys. Chem. Chem. Phys., **2**, 549, (2000).

[87] A. J. Dobbyn, J. N. L. Connor, N. A. Besley, P. J. Knowles, and G. C. Schatz. Phys. Chem. Chem. Phys., **1**, 957, (1999).

[88] M. González, J. Hijazo, J. J. Novoa, and R. Sayós. J. Chem. Phys., **108**, 3168, (1998).

[89] G. C. Schatz, P. McCabe, and J. N. L. Connor. Faraday Discuss., **110**, 139, (1998).

[90] C. S. Maierle, G. C. Schatz, M. S. Gordon, P. McCabe, and J. N. L. Connor. J. Chem. Soc., Faraday Trans., **93**, 709, (1997).

[91] M. I. Lester, B. V. Pond, D. T. Anderson, L. B. Harding, and A. F. Wagner. J. Chem. Phys., **113**, 9889, (2000).

[92] M. D. Wheeler, M. Tsiouris, M. I. Lester, and G. Lendvay. J. Chem. Phys., **112**, 6590, (2000).

[93] D. Skouteris, D. E. Manolopoulos, W. Bian, H. J. Werner, L-H. Lai, and K. Liu. Science, **286**, 1713, (1999).

[94] M. Meuwly and J. M. Hutson. J. Chem. Phys., **112**, 592, (2000).

[95] M. Meuwly and J. M. Hutson. Phys. Chem. Chem. Phys., **2**, 441, (2000).

[96] K. Stark and H.-J. Werner. J. Chem. Phys., **104**, 6515, (1996).

[97] M. H. Alexander, D. E. Manolopoulos, and H.-J. Werner. J. Chem. Phys., **113**, 11084, (2000).

[98] K. P. Huber and G. Herzberg. *Molecular Spectra and Molecular Structure IV. Constants of Diatomic Molecules.* Van Nostrand Reinhold, New York, (1979).

[99] T. H. Dunning, Jr. J. Chem. Phys., **90**, 1007, (1989).

[100] R. A. Kendall, T. H. Dunning, Jr., and R. J. Harrison. J. Chem. Phys., **96**, 6796, (1992).

[101] D. E. Woon and T. H. Dunning, Jr. J. Chem. Phys., **98**, 1358, (1993).

[102] S. M. Cybulski and J. S. Holt. J. Chem. Phys., **110**, 7745, (1999).

[103] P. G. Szalay and J. Gauss. J. Chem. Phys., **112**, 4027, (2000).

[104] F. Jensen. *Introduction to computational chemistry.* Chichester, Wiley, (1999).

[105] J. M. L. Martin. J. Chem. Phys., **100**, 8186, (1994).

[106] J. H. van Lenthe, J. G. C. M. van Duijneveldt-van de Rijdt, and F. B. van Duijneveldt. Adv. Chem. Phys, **69**, 521, (1987).

[107] M. Gutowski, M. M. Szczęśniak, and G. Chałasiński. Chem. Phys. Lett., **241**, 140, (1995).

[108] M. H. Alexander. J. Chem. Phys., **99**, 6014, (1993).

[109] H.-J. Werner, B. Follmeg, and M. H. Alexander. J. Chem. Phys., **89**, 3139, (1988).

[110] C. A. Mead and D. G. Truhlar. J. Chem. Phys., **77**, 6090, (1982).

[111] F. Rebentrost and W. A. Lester, Jr. J. Chem. Phys., **64**, 3879, (1976).

[112] H.-J. Werner and P. J. Knowles. J. Chem. Phys., **89**, 5803, (1988).

[113] P. J. Knowles and H.-J. Werner. Chem. Phys. Lett., **145**, 514, (1988).

[114] R. Bukowski, B. Jeziorski, and K. Szalewicz. (unpublished).

[115] J. O. Hirschfelder. *Intermolecular Forces, Advances in Chemical Physics Vol. 12.* John Wiley and Sons, New York-London-Sydney, (1967).

[116] R. Burcl, G. Chałasiński, R. Bukowski, and M. M. Szczęśniak. J. Chem. Phys., **103**, 1498, (1995).

[117] R. Toczyłowski and S. M. Cybulski. J. Chem. Phys., **112**, 4604, (2000).

[118] R. Burcl, R. V. Krems, A. A. Buchachenko, M. M. Szczęśniak, G. Chałasiński, and S. M. Cybulski. J. Chem. Phys., **109**, 2144, (1998).

[119] H. Koch, B. Fernandez, and O. Christiansen. J. Chem. Phys., **108**, 2784, (1998).

[120] R. J. Bartlett. In D. R. Yarkony, editor, *Modern Electronic Structure, Part II*, page 1047. World Scientific, Singapore, (1995).

[121] R. J. Bartlett and J. F. Stanton. Applications of post-hartree-fock methods: A tutorial. In K. B. Lipkowitz and D. B. Boyd, editors, *Reviews in Computational Chemistry*, volume V. VCH Publishers, New York, (1994).

[122] H.-J. Werner and P. J. Knowles. J. Chem. Phys., **82**, 5053, (1985).

[123] P. J. Knowles and H.-J. Werner. Chem. Phys. Lett., **115**, 259, (1985).

[124] R. Burcl, R. V. Krems, A. A. Buchachenko, M. M. Szczęśniak, G. Chałasiński, and S. M. Cybulski. J. Chem. Phys., **109**, 2144, (1998).

[125] J. Kłos, G. Chałasiński, M. M. Szczęśniak, and H.-J. Werner. J. Chem. Phys., **115**, 3085, (2001).

[126] GAUSSIAN 92 M. J. Frish, G. W. Trucks, M. Head-Gordon, P. M. W. Gill, M. W. Wong, J. B. Foresman, B. G. Johnson, H. B. Schlegel, M. A. Robb, E. S. Replogle, R. Gomperts, J. L. Andres, K. Raghavachari, J. S. Binkley, C. Gonzalez, R. L. Martin, D. J. Fox, D. J. Defrees, J. Baker, J. J. P. Stewart and J. A. Pople. Gaussian , Inc., Pittsburgh, (1992).

[127] S. M. Cybulski, TRURL94, Rochester, MI, 1994.

[128] D. E. Manolopoulos. J. Chem. Soc., Faraday Trans., **93**, 673, (1997).

[129] D. E. Manolopoulos, K. Stark, H.-J. Werner, D. W. Arnold, S. E. Bradforth, and D. M. Neumark. Science, **262**, 1852, (1993).

[130] J. F. Castillo, B. Hartke, H.-J. Werner, F. J. Aoiz, B. Bañares, and B. Martìnez-Haya. J. Chem. Phys., **109**, 7224, (1998).

[131] J. F. Castillo, D. E. Manolopoulos, K. Stark, and H.-J. Werner. J. Chem. Phys., **104**, 6531, (1996).

[132] M. Baer, M. Faubel, B. Martinez-Haya, L. Y. Rusin, U. Tappe, and J. P. Toennies. J. Chem. Phys., **104**, 2743, (1996).

[133] P. Honvault and J.-M. Launay. Chem. Phys. Lett., **270**, 287, (1998).

[134] P. Honvault and J.-M. Launay. Chem. Phys. Lett., **303**, 657, (1999).

[135] J. F. Castillo and D. E. Manolopoulos. Faraday Discuss. Chem. Soc., **110**, 119, (1998).

[136] R. T. Skodje, D. Skouteris, D. E. Manolopoulos, S. H. Lee, F. Dong, and K. Liu. J. Chem. Phys, **112**, 4536, (2000).

[137] F. J. Aoiz, L. Bañares, B. Martinez-Haya, J. Castillo, D. E. Manolopoulos, K. Stark, and H-J. Werner. J. Phys. Chem. A, **101**, 6403, (1997).

[138] B. Hartke and H.-J. Werner. Chem. Phys. Lett., **280**, 430, (1997).

[139] T. Takayanagi and Y. Kurosaki. Chem. Phys. Lett., **286**, 35, (1998).

[140] T. Takayanagi and Y. Kurosaki. Phys. Chem. Chem. Phys., **1**, 1099, (1999).

[141] M. Faubel, L. Rusin, S. Schlemmer, F. Sondermann, U. Tappe, and J. P. Toennies. J. Chem. Phys., **101**, 2106, (1994).

[142] F. Dong, S.-H. Lee, and K. Liu. J. Chem. Phys., **113**, 3633, (2000).

[143] F. J. Aoiz, L. Bañares, V. J. Herrero, V. Saez Rabanos, K. Stark, and H.-J. Werner. J. Chem. Phys., **102**, 9248, (1995).

[144] F. J. Aoiz, L. Bañares, V. J. Herrero, V. Saez Rabanos, K. Stark, I. Tanarro, and H.-J. Werner. Chem. Phys. Lett., **262**, 175, (1996).

[145] N. Balakrishnan and A. Dalgarno. Chem. Phys. Lett., **341**, 652, (2001).

[146] J. Kłos, G. Chałasiński, and M. M. Szczęśniak. J. Chem. Phys. in preparation.

[147] S. M. Cybulski, R. A. Kendall, G. Chałasiński, M. W. Severson, and M. M. Szczęśniak. J. Chem. Phys., **106**, 7731, (1997).

[148] S. M. Cybulski and R. Toczyłowski. J. Chem. Phys., **111**, 10520, (1999).

[149] P. J. Knowles and H.-J. Werner. Theor. Chim. Acta, **84**, 95, (1992).

[150] W. Bian and H.-J. Werner. J. Chem. Phys., **112**, 220, (2000).

[151] M. Alagia, N. Balucani, and L. Cartechini *et al.* Science, **273**, 1519, (1996).

[152] M. Alagia, N. Balucani, and L. Cartechini *et al.* Phys. Chem. Chem. Phys., **2**, 599, (2000).

[153] N. Balucani, L. Cartechini, P. Casavecchia, G. G. Volpi, F. J. Aoiz, L. Bañares, M. Menéndez, W. Bian, and H.-J. Werner. Chem. Phys. Lett., **328**, 500, (2000).

[154] S.-H. Lee, K. Liu, and H. Chang. J. Chem. Phys., **110**, 8229, (1999).

[155] S.-H. Lee and K. Liu. J. Chem. Phys., **111**, 6253, (1999).

[156] T. C. Allison, G. C. Lynch, D. G. Truhlar, and M. S. Gordon. J. Phys. Chem., **100**, 13575, (1996).

[157] H. Wang, W. H. Thompson, and W. H. Miller. J. Chem. Phys., **107**, 7194, (1997).

[158] T. C. Allison, G. C. Lynch, D. G. Truhlar, and M. S. Gordon. J. Phys. Chem., **100**, 13588, (1996).

[159] F. J. Aoiz and L. Bañares. Chem. Phys. Lett., **247**, 232, (1995).

[160] F. J. Aoiz and L. Bañares. J. Phys. Chem., **100**, 18108, (1996).

[161] U. Manthe, W. Bian, and H.-J. Werner. Chem. Phys. Lett., **313**, 647, (1999).

[162] D. Skouteris, H.-J. Werner, F. J. Aoiz, L. Bañares, M. Menéndez J. F. Castillo, N. Balucani, L. Cartechini, and P. Casavecchia. J. Chem. Phys., **114**, 10662, (2001).

[163] S.-H. Lee and K. Liu. J. Chem. Phys., **115**, 1197, (2001).

[164] A. Hanf, A. Lauter, D. Suresh, H.-R. Volpp, and J. Wolfrum. Chem. Phys. Lett., **340**, 71, (2001).

[165] F. J. Aoiz, L. Bañares, J. F. Castillo, M. Menéndez, D. Skouteris, and H.-J. Werner. J. Chem. Phys., **115**, 2074, (2001).

[166] F. Dong, S.-H. Lee, and K. Liu. J. Chem. Phys., **115**, 1197, (2001).

[167] F. B. van Duijneveldt, J. G. C. M. van Duijneveldt-van de Rijdt, and J. van Lenthe. Chem. Rev., **94**, 1873, (1994).

[168] K. A. Peterson, D. E. Woon, and T. H. Dunning, Jr. J. Chem. Phys., **100**, 7410, (1994).

[169] C. W. Bauschlicher, S. P. Walch, S. R. Langhoff, P. R. Taylor, and R. L. Jaffe. J. Chem. Phys., **88**, 1743, (1988).

[170] Zhiming Li, V. A. Apkarian, and L. B. Harding. J. Chem. Phys., **106**, 42, (1997).

[171] J. Kłos, G. Chałasiński, and M. M. Szczęśniak. , submitted for publication.

[172] J. Kłos, G. Chałasiński, and M. M. Szczęśniak. , to be published.